UC Berkeley
UC Berkeley Electronic Theses and Dissertations

Title
Redox control of iron biomineralization in Magnetospirillum magneticum AMB-1

Permalink
https://escholarship.org/uc/item/1935b8kv

Author
Jones, Stephanie Rhianon

Publication Date
2015

Peer reviewed|Thesis/dissertation

Redox control of iron biomineralization in *Magnetospirillum magneticum* AMB-1

by

Stephanie Rhianon Jones

A dissertation submitted in partial satisfaction of the

requirements for the degree of

Doctor of Philosophy in

Chemistry

in the

Graduate Division

of the

University of California, Berkeley

Committee in charge:

Professor Michelle C. Y. Chang, Chair
Professor Christopher J. Chang
Professor Arash Komeili

Spring 2015

Redox control of iron biomineralization in *Magnetospirillum magneticum* AMB-1

© 2015

by Stephanie Rhianon Jones

Abstract

Redox control of iron biomineralization in *Magnetospirillum magneticum* AMB-1

by

Stephanie Rhianon Jones

Doctor of Philosophy in Chemistry

University of California, Berkeley

Professor Michelle C. Y. Chang, Chair

Magnetotactic bacteria have evolved complex subcellular machinery to construct linear chains of magnetite nanocrystals that allow the host cell to sense direction. Each mixed-valent iron nanoparticle is mineralized from soluble iron within a membrane-encapsulated vesicle termed the magnetosome, which serves as a specialized compartment that regulates the iron, redox, and pH environment of the growing mineral. In order to dissect the biological components that control this process, we have carried out genetic and biochemical studies of proteins proposed to function in iron mineralization in *Magnetospirillum magneticum* AMB-1. As iron biomineralization by magnetotactic bacteria represents a particularly interesting case for understanding how the production of nanomaterials can be programmed at the genetic level, we also apply synthetic biology techniques towards the production of new cellular materials and new cellular functions.

As the production of magnetite requires both the formation of Fe(II) and Fe(III), the redox components of the magnetosome play an essential role in this process. Using genetic complementation studies, we show that the redox cofactors or heme sites of the two putative redox partners, MamP and MamT, are required for magnetite biomineralization *in vivo* and that removal of one or both sites leads to defects in mineralization. We develop and optimize a heterologous expression method in the *E. coli* periplasm to cleanly isolate fully heme-loaded MamP for biochemical studies. Spectrochemical redox titrations show that the reduction potential of MamP lies in a different range than other *c*-type cytochrome involved in either Fe(III) reduction or Fe(II) oxidation. Nonetheless, *in vitro* mineralization studies with MamP and Fe(II) show that it is able to catalyze the formation of mixed-valent Fe(II)/Fe(III) oxides such as green rust.

Biomineralization also requires lattice-templating proteins that guide the growth of the functional crystalline material. We use *in vitro* binding and synthesis studies with putative magnetite-templating proteins, the Mms6 family proteins, to show that they are competent to bind and stabilize non-thermodynamically stable faces of magnetite. We also use *in vitro* iron mineralization to show that the Mms6 family proteins can work together with the redox protein MamP to produce mixed-valent iron oxides from soluble Fe(II) species and to control mineral structure. Further studies with Mms7ct indicate that it and other Mms6 family proteins may play a more significant role in controlling magnetite mineral structure than previously hypothesized. Beyond simple control of size and shape of magnetite, it may also template the crystal lattice of the mineral itself similar to what has been observed with calcium biomineralization, where

unstable crystal forms and phases of the mineral are stabilized by interaction with peptides and other macromolecules.

We next set up and begin testing systems to engineer magnetotactic bacteria for the production of new functional materials. We replace the metal-binding C-terminus of native Mms6 family proteins in AMB-1 with peptides known to precipitate metal oxides *in vitro* under mild conditions. Initial characterization of the behavior of these constructs in AMB-1 has been carried out, although additional experiments are required to test whether they can enable formation of new materials *in vivo*. We also discuss developing a cellular biosensor based on the formation of a magnetic material in response to an analyte.

i

Table of Contents

Chapter 1: Introduction – Control of iron oxide mineralization in magnetotactic bacteria

Chapter 2: Genetic and biochemical characterization of two heme-containing proteins encoded by the magnetosome island of *M. magneticum* AMB-1

List of Figures, Schemes, and Tables

Chapter 1

Chapter 2

Chapter 3

Chapter 4

List of Abbreviations

ALA	5-aminolevulinic acid
AMB-1	*Magnetospirillum magneticum* AMB-1
Amp	ampicillin
Cb	carbenicillin
Cm	chloramphenicol
C_{mag}	cellular magnetization
DAP	diaminopimelic acid
DLS	dynamic light scattering
DMSO	dimethyl sulfoxide
DNase	deoxyribonuclease
dNTP	deoxynucleotide triphosphate
DTT	diothiothreitol
EDTA	ethylenediaminetetraacetic acid
ESI-MS	electrospray ionization mass spectrometry
Fe_3O_4	magnetite
FPLC	fast protein liquid chromatraphy
GFP	green fluorescent protein
HEPES	4-[(2-hydroxyethyl)piperazin-1-yl]ethanesulfonic acid
HPLC	high performance liquid chromatography
HRTEM	high resolution transmission electron microscopy
ICP-OES	inductively coupled plasma-optical emission spectrometry
IPTG	isopropyl β-D-1-thiogalactopyranoside
Km	kanamycin
LB	Luria-Bertani broth
MAI	magnetosome genetic island
MALDI	matrix assisted laser desorption/ionization
$MamP_{ox}$	oxidized MamP
$MamP_{red}$	reduced MamP
MBP	maltose binding protein
MG	Magnetic Growth (media)
MM	magnetosome membrane
MO-1	Magnetic ovoid bacterium strain MO-1

MOCR	monomeric mutant of the Ocr protein
MTB	magnetotactic bacteria
MWCO	molecular weight cut off
OD	optical density
ODQ	1*H*-[1,2,4]oxadiazolo[4,3-a]quinoxalin-1-one
ORFs	open reading frames
PCR	polymerase chain reaction
PDTC	pyrrolidine dithiocarbamate
PMSF	phenylmethanesulfonyl fluoride
PVDF	polyvinylidene fluoride
rpm	revolutions per minute
R_z	Reinheitzahl ratio
SDS-PAGE	sodium dodecyl sulfate- polyacrylamide gel electrophoresis
SEC	size exclusion chromatography
SLIC	sequence and ligation independent cloning
SUMO	small ubiquitin-like modifier protein
TB	Terrific broth
TBS	tris-buffered saline
TBST	Tween-20 tris-buffered saline
TEM	transmission electron microscopy
TEMED	N,N,N′,N′-Tetramethylethane-1,2-diamine
TEV	Tobacco Etch Virus
Tris	trisaminomethane
TRX	Thioredoxin protein
XRD	X-ray diffraction

Acknowledgments

Chapter 1: *Control of iron oxide mineralization in magnetotactic bacteria*

1.1. Introduction

Living organisms are capable of carrying out many sophisticated and coordinated operations, such as sensing, directional movement, self-organization, and transformations of small molecules. However, the scope of innovation found in natural systems is typically limited to naturally abundant elements in their immediate environment. In contrast, human chemists have discovered many novel and tunable properties of matter by extending reaction space beyond the small subset of elements used in biology to the entire periodic table. This diversity in function and composition is especially striking for the chemistry of inorganic elements and materials, which have transformed society by harnessing d-block-accessible functions such as semiconduction and photon upconversion, functions that are currently orthogonal to biology. We seek to open new doors between synthetic biology and inorganic nanoscience with the overall goal of designing and exploiting novel hybrid functions for living cells at the biotic-abiotic interface.

The transformation of soluble metal ions to form various biological nanostructures, from the intricately patterned diatom frustule to the unusually strong mollusk shell, provides important function at the organism level [1-3] and has inspired new methods for the preparation of synthetic materials [4-7]. The mineralization of calcium and silica is the best understood as it produces the largest classes of biominerals [8-12]. In these systems, biological macromolecules are self-assembled to produce an array of functional groups that bind the material and shift the equilibrium from soluble ions to ion clusters while also templating product composition and lattice structure (*Figure 1.1*) [1, 13-17]. This model for biomineralization is based mainly on fixed oxidation-state biomineralization of calcium, which also takes place exterior to the cell. However, the controlled mineralization of redox-capable elements such as iron [18-20], copper [21, 22], and manganese [23-25] are also observed, although they are less broadly distributed. Of the latter group, iron biomineralization by magnetotactic bacteria represents a particularly interesting case for understanding how the production of nanomaterials can be programmed at the genetic level.

Magnetotactic bacteria house a sophisticated system to sense the earth's magnetic field for magnetoaerotaxis using linear chains of biological magnets, consisting of membrane-encapsulated magnetite ($Fe^{2+}Fe^{3+}_2O_4$) nanoparticles of various sizes (35-120 nm) and shapes with several unusual properties [26]. First, these nanoparticles are generated as a single magnetic domain [27], suggesting that they have naturally evolved to maximize the magnetic contribution of each iron atom. In addition, the magnetite is synthesized as an internally pure material with surface-passivating proteins [28] rather than as a composite material with organic layers, as is often observed in calcium-based biominerals [29]. Also, in contrast to the structural biomaterials built from calcium and silicon, the production of magnetite requires redox chemistry to produce the mixed-valent Fe(II)/Fe(III) product and could allow us to access large classes of functional transition metal-based materials using synthetic biology approaches.

The genes encoding the formation of the membrane and its encapsulated nanoparticle, together called the magnetosome, are found on an island (~100 kB) bordered by repetitive DNA sequences [30, 31]. Previous work has showed that magnetosome formation in magnetotactic bacteria species *Magnetospirillum magneticum* AMB-1 proceeds by invagination of the inner membrane aided by actin-like proteins to align vesicles followed by mineralization of Fe within the vesicles [32-35]. Under iron starvation conditions, magnetosomes are produced as empty vesicles but are still competent to catalyze mineralization. Many classes of essential genes have been identified from a

detailed genetic knockout study of AMB-1 [*36*]. However, detailed biochemical characterization and functional analysis have yet to be performed on many of the protein products of the genes directly involved in controlling mineral composition and redox state.

As a result of their materials properties and genetic characteristics, magnetotactic bacteria offer a genetic system for expanding the range of elements, oxidation states, and synthetic routes to inorganic materials while tuning nanoscale properties, such as size and shape homogeneity. Also, the magnetosome architecture results in embedding of the nanocrystals within the cell itself so that new hybrid cellular functions can be achieved (*Figure 1.2*).
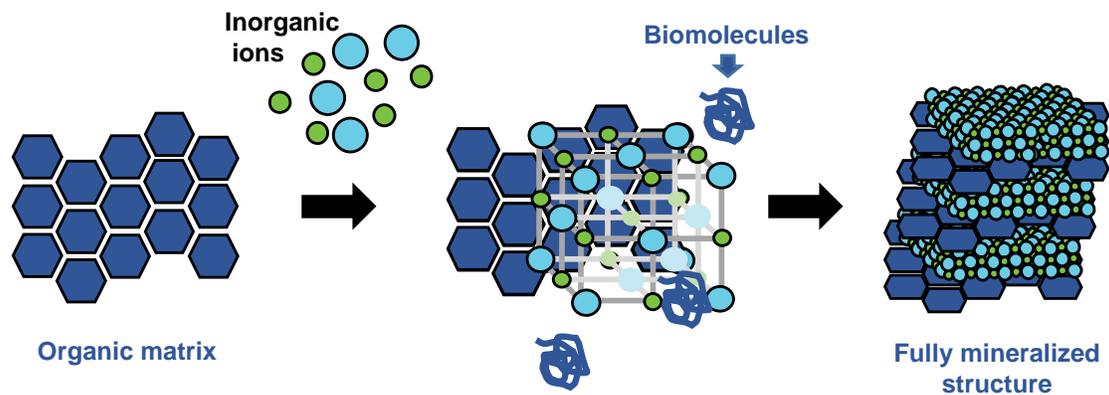
Figure 1.1. *Mechanism of templated biomineralization for composite nanomaterials. Biological macromolecules are self-assembled to produce an array of functional groups (organic matrix) that bind the material and shift the equilibrium from soluble ions to ion clusters while also templating product composition and lattice structure. The organic matrix remains embedded in the lattice structure in the fully mineralized structure. This imparts the ability for synthesis under mild conditions and the ability to grow and self-repair.*
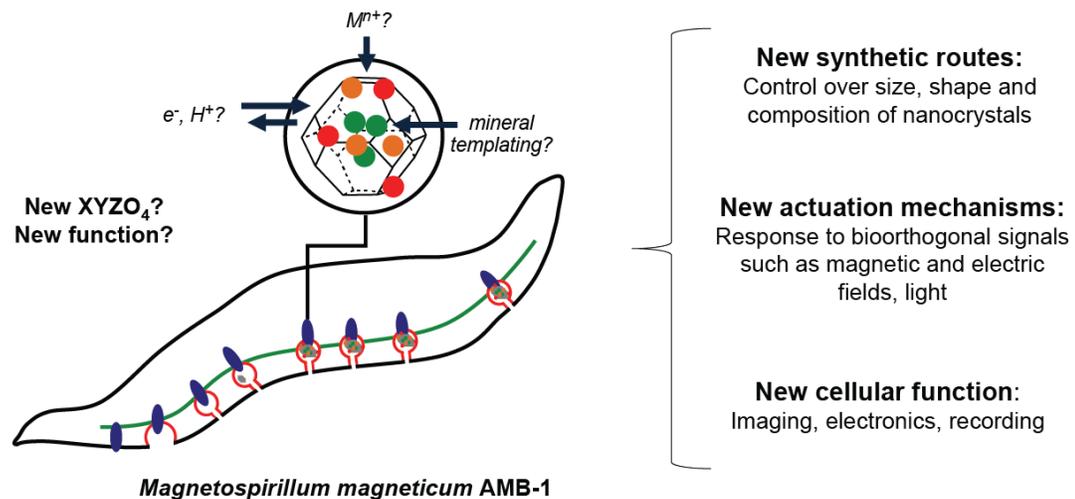
Figure 1.2. *Synthetic biology and hybrid inorganic-organic materials. We aim to combine the synthetic specificity of biological systems with the broad functionality of inorganic materials. As a result of their materials properties and genetic characteristics, magnetotactic bacteria offer a genetic system for expanding the range of elements, oxidation states, and synthetic routes to inorganic materials while tuning nanoscale properties, such as size and shape homogeneity. Also, the magnetosome architecture results in embedding of the nanocrystals within the cell itself, potentially allowing the cell to respond to bioorthogonal signals and thus gain new cellular function.*

1.2. Biologically induced mineralization by iron-respiring bacteria

Biologically induced mineralization. In magnetotactic bacteria, magnetite biominerals provide a critical function to the cell: they allow the microaerophilic cell to passively align to the earth's magnetic field and limit the degrees of freedom of search for an ideal oxygen concentration. In order to maximize the utility of the product, magnetotactic bacteria tightly control the formation of the material. In contrast, inorganic biominerals can be deposited by adventitious precipitation, called biologically induced mineralization, which arises from secondary interactions between various metabolic processes and the surrounding environment. For example, bacteria and fungi can transform Mn^{3+} to insoluble Mn^{4+} minerals due to their extracellular generation of superoxides [25]. Other bacteria have the ability to precipitate uranium, lead, cadmium, or even gold ions as a detoxification mechanism [37]. As precipitation is a byproduct of cellular activities, mineralization is not under strict control. Therefore, the morphology, lattice structure, and composition of the inorganic particles are heterologous and poorly defined [38]. However, biologically-induced iron oxide mineralization by iron-respiring bacteria can provide valuable insight into how electron transfer in biological systems can precipitate nanomaterials from redox-capable precursors.

Microorganisms from both Archaea and Bacteria are capable of metabolically exploiting the favorable redox potential of the Fe^{3+} / Fe^{2+} redox couple and various electron donors or acceptors [19]. Iron-oxidizing organisms under both aerobic and anaerobic conditions can use Fe^{2+} as an electron source for producing the reducing equivalents necessary for biomass production. Iron-reducing organisms under anaerobic conditions can use Fe^{3+} as a terminal electron acceptor in energy-generating electron transport chains. As a byproduct of these electron-transfer metabolisms, soluble and insoluble iron substrates can be transformed into new iron-based materials. The utilization of iron as an electron source or sink and the formation of these materials is subject to both thermodynamic and kinetic constraints.

Biologically-accessible aqueous iron chemistry. The standard reduction potential of the Fe^{3+} / Fe^{2+} couple (+ 770 mV) only applies in strongly acidic solutions in which both oxidation states have high solubility [39]. The reducing power of ferrous iron increases dramatically at neutral pH due to the formation of insoluble iron oxides and oxyhydroxides, effectively removing Fe^{3+} from solution. For example, values for amorphous and more soluble ferrihydrite and the $Fe(OH)_3$ / Fe^{2+} couple are reported between -200 mV to + 100 mV whereas the potentials for less soluble crystalline iron oxides reside between -88 mV (lepidocrocite) and -314 mV (magnetite) (*Figure 1.3*) [19, 23, 39]. Indeed, the reduction potential values for iron oxides decrease by ~ 59 mV per unit increase in pH [23]. The reduction potential also decreases with increasing size of solid iron oxide particulates, with the most dramatic effects for sub-micron grain sizes [40, 41]. Also, both Fe^{2+} and Fe^{3+} form complexes with species other than H_2O and OH^-, which can drastically change the redox potential of the complexed iron due to the preferential chelation of one oxidation state [42]. This wide variation in iron redox potential due to solubility, pH, nanoparticle size, and complexation affects the thermodynamic feasibility of bacterial oxidation/reduction of specific iron compounds for metabolic purposes.

Iron-reducing bacteria. *Shewanella putrifaciens* and *Geobacter metallireducens* are two well-studied iron-reducing bacteria that produce magnetite as a by-product of respiring upon iron. Under anaerobic conditions, the bacteria utilize poorly crystalline ferric oxyhydroxides such as ferrihydrite as a terminal electron acceptor, reducing Fe^{3+} to Fe^{2+} [19, 39]. The mechanism of

magnetite formation in this manner is well-characterized: after reduction of ferrihydrite Fe^{3+} to soluble Fe^{2+}, the Fe^{2+} aquo species binds the surface of the excess ferric oxides, mixed-valent hydroxo-complexes dissolute and are released off the surface, and then the complexes subsequently reprecipitate as the mixed-valent magnetite material [19, 43, 44]. This mineralization is not regulated, and subsequently the magnetite nanoparticles are irregular in shape and size, have poor magnetic properties, and often remain in close contact with the host cell.

However, the biochemistry and physiology of electron transfer to iron oxides is well characterized in these organisms. Both *Geobacter* and *Shewanella* are able to grow heterotrophically by conserving energy from the catabolism of organic molecules [19, 39]. The electrons from the carbon source are passed to a redox-active small molecule such as NAD^+. The redox-active small molecule then passes the electrons to the proton-translocating complex NADH1, which generates a proton gradient for energy production. The electrons next enter the menaquinone pool and then travel through the periplasm and the outer membrane through a series of multiheme cytochromes with overlapping midpoint reduction potentials around 0 to -350 mV, delivering electrons to the terminal electron acceptor Fe^{3+} [45-49].

This last step, the transfer of electrons from a biomolecule embedded in a bacterial membrane to a solid substrate, is non-trivial. Several mechanisms have been proposed, though none are mutually exclusive. The observations that *Geobacter metallireducens* must be in direct contact with iron oxides to grow and form pili that attach to the iron oxide lead to the theory that electrons are passed directly from outer-membrane c-type cytochromes to the iron oxide substrate [50, 51]. When the genes for pili formation were deleted, *Geobacter* could no longer reduce insoluble metal oxides but could reduce soluble forms of Fe^{3+} such as Fe^{3+}-citrate. Though mutants could not grow on the iron oxides, they could still attach to them [50]. Follow-up studies showed that OmcS, the most abundant cytochrome required for Fe^{3+} reduction and one with the lowest measured reduction potential, was localized to the pili [51]. However, other critical cytochromes to the iron-reduction pathway were not. In both *Shewanella* and *Geobacter*, pili are able to conduct electrons [52]. A second mechanism for electron transfer to solid iron minerals is based on the observation that secreted flavins and riboflavins are critical to growth on iron oxides in *Shewanella* species [53, 54]. These exogenous electron shuttles are reduced at the cell surface by membrane-bound cytochromes and oxidized extracellularly by Fe^{3+}. *Geobacter* species have not been shown to produce endogenous electron shuttles, but Fe(III) reduction can be greatly stimulated by the addition of exogenous electron shuttles such as flavins or humic substances [55]. A third and final mechanism suggests that the secretion of organic chelators allows for the solubilization of Fe^{3+} for easy transfer of electrons from the cell surface [56].

Iron-oxidizing bacteria. Bacteria can also transform iron materials by using Fe^{2+} as an electron source for producing the reducing equivalents necessary for biomass production. Iron-oxidizing bacteria transform iron minerals by precipitating insoluble iron oxides rather than by the dissolution of iron oxides and re-precipitation of mixed-valent species (as in the case of iron-reducing bacteria). Iron(II) oxidation can be coupled to O_2 reduction at acidic pH, to O_2 (aerobic) or nitrate/perchlorate (anaerobic) reduction at neutral pH, or even coupled to CO_2 reduction in photosynthetic organisms. Iron oxidation has particular challenges, as organisms must be able to oxidize various forms of Fe^{2+} found at neutral pH, transfer electrons (potentially uphill) to redox-capable small molecules, and deal with the rapid precipitation of the Fe^{3+} products [19, 39].

6

The biomolecular details of iron oxidation are not well understood, though some progress has been made to elucidate iron oxidation by phototrophic bacteria. A three-gene operon (*pioABC*) from the phototrophic iron(II)-oxidizer *Rhodopseudomonas palustris* has been found to be critical for iron oxidation [*57*]. These genes encode a periplasmic decaheme cytochrome *c*-type protein, an outer membrane porin, and a periplasmic high-potential iron protein (~0 to +0.4 V). It is the high-potential iron protein and the cytochrome transfer electrons from Fe^{2+} to their destination in the cell, whereas the outer-membrane porin could be involved in Fe transport. A three-gene operon (*foxEYZ*) from another phototrophic iron(II)-oxidizer *Rhodobacter ferrooxidans* SW2 has also been characterized [*58*]. The genes encode a decaheme c-type cytochrome (FoxE), an inner membrane transport protein, and a quinone-binding protein. The hemes of FoxE have positive reduction potentials (+207 and +270 mV at pH 7) that could allow downhill electron transfer from many geochemically relevant ferrous iron forms to the photosynthetic reaction center [*59*].

Iron oxidation coupled to anaerobic nitrate (NO_3^-) reduction is of particular interest due to its ability to form mixed-valent iron oxides in *vivo* and in *vitro* as well as its potential metabolic similarity to magnetotactic bacteria. The oxidation of Fe^{2+} (soluble and insoluble) coupled to nitrate reduction is energetically favorable at neutral pH and should yield enough energy to support carbon fixation and microbial growth [*19, 39*]. However, only a couple pure bacterial cultures have been isolated that are nitrate-dependent iron-oxidizers. Therefore, it has been postulated that nitrate-reduction coupled to iron-oxidation is primarily an adventitious process or detoxification strategy [*60*]. In fact, several such strains, including *Acidovorax* strain BoFeN1, has been shown to precipitate intracellular iron minerals in the periplasm. Evidence supports the suggestion that the important site of Fe(II) oxidation is the same as the site of NO_2^-, NO, and N_2O reduction (i.e., the redox-active proteins Nar, Nir, Nor, and Nos and other redox-active components of the periplasm) and thus the periplasmic components of all nitrate-reducers should be capable of iron oxidation [*60, 61*].
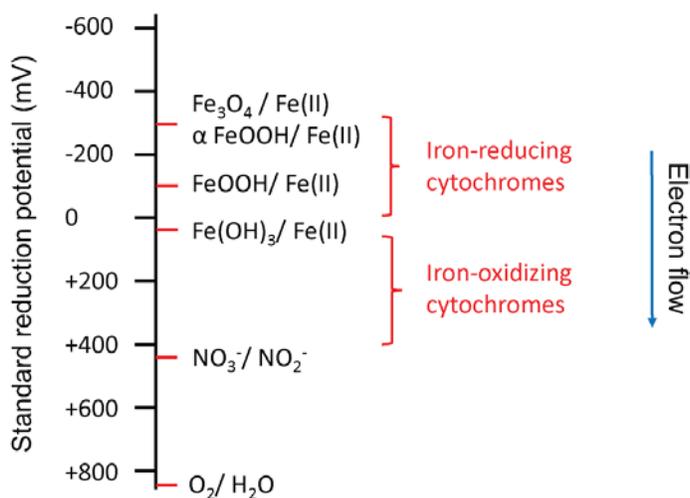
Figure 1.3. Common reduction potentials for iron species in water at pH 7.0 and their accessibility by redox-active proteins from iron respiring bacteria.

7

1.3. Models for magnetite formation in magnetotactic bacteria

A conserved set of magnetosome-associated genes is organized in a large genomic island called the Magnetosome Island (MAI). Many classes of essential genes have been identified from a detailed genetic knockout study of the MAI in *Magnetospirillum magneticum* AMB-1 [*36*]. The study suggests a stepwise assembly of the magnetosome, with a set of gene products responsible for each part of the process acting to (1) invaginate the cell membrane and form the magnetosome membrane, (2) sort and process proteins responsible for magnetite formation, (3) align the magnetosomes into a chain, and (4) take up iron, prime the environment of the magnetosome, and mineralize the magnetic material [*36, 62*]. In recent years, incredible progress has been made in detailing the functions of individual genes as well as in describing the overall chemical transformation of the iron material. In this section, current knowledge on the chemical mechanism of magnetite crystallization in magnetotactic bacteria is summarized.

Mechanisms for magnetite synthesis. There exists experimental evidence for two distinct and mutually exclusive mechanisms for magnetite synthesis in magnetotactic bacteria (*Figure 1.4*) [*26*]. The first mechanism is similar to the transformation of iron oxides by iron-reducing bacteria, in which Fe^{3+} accumulates in the magnetosome and forms an amorphous high-density hydrous ferric oxide (ferrihydrite) precursor, which is then partially reduced to $Fe^{2+}Fe_2^{3+}O_4$ (magnetite). In a detailed study by Frankel *et al.* in 1983 [*63*], Mössbauer spectroscopy was performed on whole and fractionated early-growth (red cell pellets) versus late-growth (black cell pellets) *Magnetospirillum magnetotacticum* MS-1 cells. The study identified a low-density ferrous hydroxide followed by a high-density ferrous hydroxide (ferrihydrite) and then magnetite. The authors suggested the Fe^{3+}-quinate added to solution was taken up by the cell, reduced to $Fe^{2+,}$ and the chelator released. Fe^{2+} is then re-oxidized in the magnetosome and accumulates as a low-density hydrous iron oxide. Dehydration of the low-density hydrous iron oxide results in a high-density hydrous iron oxide (ferrihydrite). Finally, partial reduction and further dehydration results in magnetite. This mechanism is analogous to the better-understood mineralization mechanisms of calcium or silica, which often make use of amorphous precursor phases that are molded into the final morphology before crystallization [*1, 12, 38*]. The mechanism also falls in line with what is known of iron biomineralization in chiton teeth [*20, 64, 65*]. Chiton are molluscs with rows of iron oxide teeth used to scrape microscopic algae off of rocks. The teeth are built in a sequential process involving ferritin delivering iron to the cells that build the tooth, the deposition of ferrihydrite on a pre-formed organic matrix, and the formation of an outer layer of magnetite by partial reduction of the ferrihydrite. Though the analogous biomineralization mechanism lends even more credence to this mechanism of formation, it has become clearer in recent years that cellular fractionation of magnetotactic bacteria is non-trivial in terms of both separations of components as well as abiotic oxidation of iron species. Also, modern tools in molecular biology can allow for better characterization of the early-growth and mutant cells.

The partial reduction mechanism has also been used to explain the layer of hematite (α-Fe_2O_3) discovered by a combination of electron microscopy and real-time X-ray magnetic circular dichroism in immature (though full-sized) magnetite crystals within 15 min of transferring iron-depleted *Magnetospirillum gryphiswaldense* MSR-1 cells into Fe-containing media [*66*]. The crystalline ferric oxide hematite is considered the precursor material, which surrounds and protects the magnetite which grows from it. However, a recent study using electron microscopy in combination with Fe K-edge X-ray absorption near edge structure found that iron is accumulated

in *Magnetospirillum gryphiswaldense* MSR-1 in the form of a high-phosphorus-content ferrihydrite from bacterioferritin cores and is subsequently rapidly transformed to crystalline magnetite [*67*]. Therefore, both the presence of the precursor material and its identification have yet to be confirmed.

The second proposed mechanism for magnetite synthesis in magnetotactic bacteria, the co-precipitation mechanism, is the controlled transport and rapid mixing of Fe^{2+} and Fe^{3+} in the magnetosome. In a study by Faivre *et al*. [*68*], Mössbauer spectroscopy was also performed on whole and fractionated early-growth versus late-growth *Magnetospirillum gryphiswaldense* MSR-1 cells. However, early-growth versus late-growth magnetite can be analyzed more carefully: magnetite mineralization is induced by transferring iron-depleted cells into Fe-containing media. In this study, no precursor phase was identified. The group found that MSR-1 cells took up either or both Fe^{2+} or Fe^{3+}, an observation validated by microbiological experiments. Iron is then converted to a ferrous high-spin species predominantly located in the membrane and a membrane-associated ferritin, and magnetite crystallization proceed by rapid co-precipitation of Fe^{2+} and Fe^{3+} ions in the correct 1 Fe^{2+}: 2 Fe^{3+} ratio for the magnetite lattice. At all stages, magnetosome particles consisted exclusively of magnetite, although the authors suggest that ferrihydrite might have escaped detection by electron diffraction owing to its poor crystallinity. As synthesis by co-precipitation lacks an amorphous precursor phase, crystalline magnetite can be built ion by ion to yield crystals with well-defined facets consistent with the underlying crystal structure [*69*]. Although biological systems often rely on their ability to mold amorphous precursor phases into the final crystalline material, co-precipitation might better explain the materials properties that distinguish magnetotactic bacteria from other biomineralizing organisms: defectless crystal lattices and the lack of lattice-embedded biomolecules.

A recent report has attempted to reconcile the conflicting experimental evidence by characterizing material transformation with several modern microscopy techniques for both Fe and phosphorus in time-resolved experiments where magnetite mineralization is induced by transferring iron-depleted cells into Fe-containing media [*70*]. The study found that upon uptake, Fe is stored in a phosphate-rich ferric hydroxide phase which also contained some particles of another poorly crystalline iron oxyhydroxide phase as well as of hematite. The study suggests that Fe and P are separated during the transfer to the magnetosome vesicle, leading to the formation of nanometric ferrihydrite, which can then be transformed into magnetite upon partial reduction of Fe^{3+} to Fe^{2+}. However, ferrihydrite is again not directly observed, though it is suggested that the irregular morphology of the nascent magnetite crystals supports the notion of a solid-phase transformation from the precursor, despite the lack of a bulk amorphous phase as is the case in calcium or silica biomineralization.

In all mechanisms of formation, redox-active proteins are necessary to regulate and monitor the oxidation state of iron species within the magnetosome.

Regulation of pH in the magnetosome. A potential-pH diagram, or Pourbaix diagram, can be used to map out thermodynamically stable phases of iron in an aqueous electrochemical system. At an environmentally-relevant iron concentration (10 μM) and standard temperature and pressure, the chemical stability of magnetite is limited to small region centered at pH = 10 and a standard electrode potential of -0.5 V [*26*]. This suggests that the product of magnetite biosynthesis, however it is formed, only exists stably at limited redox potential and pH values. Consequently,

the magnetosome must also control pH in addition to metal ion transport into the vesicle and shuttling of redox equivalents during synthesis. The magnetosome must also regulate pH during the formation of magnetite. In all mechanisms of formation, protons are released due to the formation of the oxide bridges in magnetite, which are known to be derived from water rather than from molecular oxygen [71]. The putative Na^+/H^+ antiporter MamN, whose genetic knockout produces enormous defects in cellular magnetization, is currently believed to pump protons out of the magnetosome to maintain the pH of the compartment [72]. However, detailed biochemical studies have yet to determine the function of the protein.

Partial reduction
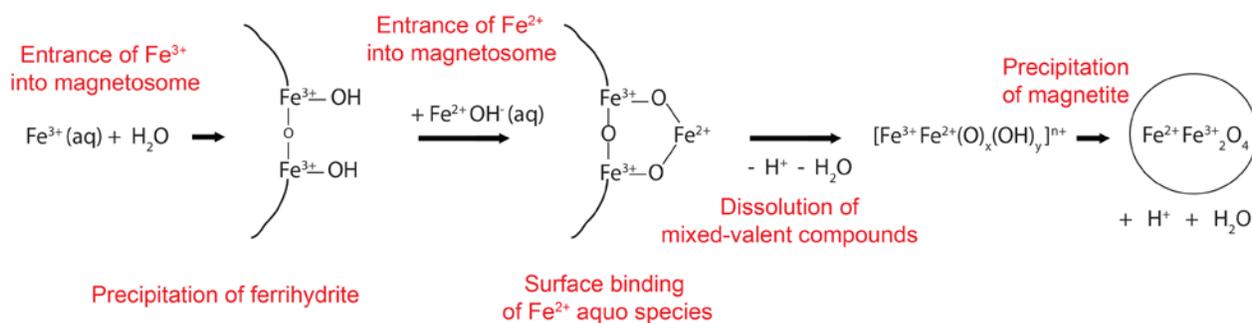
Co-precipitation
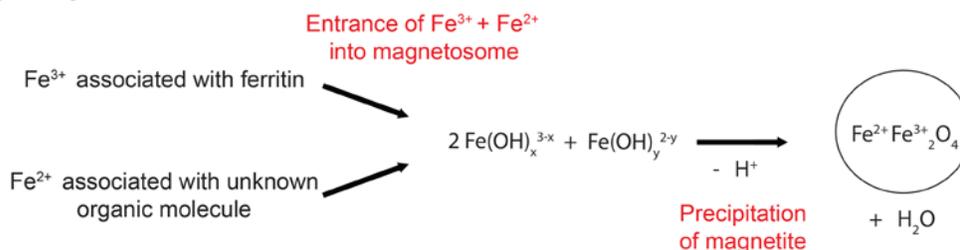
Figure 1.4. *Models for magnetite mineralization in magnetotactic bacteria. In the partial reduction mechanism, Fe(III) accumulates as a low-density hydrous iron oxide in the magnetsome. Dehydration of the low-density hydrous iron oxide results in a high-density hydrous iron oxide (ferrihydrite). Fe(II)-aquo species bind the surface of the magnetite and mixed-valent compounds dissolute off the surface. Finally, re-precipitation and further dehydration results in magnetite. In the co-precipitation mechanism, Fe(II) and Fe(III) accumulates in the correct ratio (1:2) in the magnetosome for the ion-by-iron crystallization of magnetite. Both mechanisms result in the formation of protons which need to be removed from the magnetosome to maintain a pH at which magnetite is thermodynamically stable.*

1.4. Control of iron redox state in magnetotactic bacteria

A class of essential genes have been identified from a detailed genetic knockout study of *Magnetospirillum magneticum* AMB-1 that are necessary for the precipitation of magnetite but do not affect membrane biogenesis or chain alignment [*36, 73*]. These genes encode putative ion transporters such as MamM which has homology to the cation diffusion facilitator protein family as well as the potential pH-controlling Na^+/H^+ antiporter MamN [*36*]. Another set of genes, *mamCFDC* and the *mms6* cluster, encode proteins which have been implicated in size and shape control of the magnetite nanocrystals [*74*]. Two genes implicated in protein sorting due to their homology to HtrA/DegP family proteases as well as their lack of magnetite formation are *mamE* and *mamO* [*75, 76*]. There are also several genes that are critical for magnetite biomineralization but have no homology to characterized proteins: *mamT*, *mamP*, *mamS*, and *mamR* [*36*]. Genetic knockouts of the magnetosome island genes *mamH*, *mamX*, and *mamZ* also appear to have some, though mild, defects in crystal formation [*73*].

In contrast to biomaterials built from calcium and silicon, the production of magnetite requires redox chemistry to produce the mixed-valent Fe^{2+} / Fe^{3+} product. Therefore, it has been suggested that one or more of these proteins of unknown function are capable of electron transfer to or from the growing iron mineral. Of these proteins, MamE, MamT, MamP, and MamX have two c-type cytochrome heme-binding CXXCH motifs in domains that are homologous to each other but not to other c-type cytochromes, leading to the proposal that they constitute a new class of heme-binding electron transfer proteins termed "magnetochromes" [*77*]. The C-terminal domain of MamZ is also postulated to be involved in redox chemistry as it exhibits similarities to a ferric reductase-like transmembrane protein [*78*]. Since many of these genes have protein-interaction motifs in the form of PDZ domains, it has been suggested that they assemble into an electron transport chain in the magnetosome membrane and magnetosome space [*77*].

The magnetochrome MamE is a critical player in magnetite formation. The deletion of *mamE* results in the mislocalization of other proteins and severe downstream magnetic defects [*36, 75, 76*]. MamE consists of two closely-spaced CXXCH heme-binding motifs flanked by an N-terminal HtrA/DegP protease domain and two C-terminal PDZ domains. Time-course experiments showed that although the MamE heme-binding mutant is capable of synthesizing large fixed single-domain magnetite crystals, this process is slowed from wild type and forms a significant number of smaller crystals similar to those found in the MamE protease mutant [*75*]. Due to this data, it was suggested that this MamE's CXXCH motifs may serve to activate or enhance proteolysis required for crystal size transition or they may act independently of the protease domain in another electron transfer function [*75*].

MamP and MamT are also magnetochromes as interest [*77, 79*]. MamP consists of a N-terminal signal or transmembrane sequence followed by a PDZ domain with a C-terminal di-heme magnetochrome domain. A genetic knockout of *mamP* reveals small, flaky particles in the magnetosomes with 1-2 wild type or larger than wild type crystals per cell [*36*]. MamT is a small magnetochrome protein with a N-terminal transmembrane segment, which may interact with PDZ domains through a putative PDZ-binding C-terminal segment. A genetic knockout of *mamT* shows small, elongated crystals of wild type number [*36*]. Recent progress has been made in determining the iron oxidoreductase functions of these proteins (*Chapter 2*) [*79, 80*].

A tempting explanation is that magnetite formation in AMB-1 is a controlled inside-out Fe^{2+} oxidation similar to anaerobic nitrate-dependent iron-oxidizing bacteria. It is known that *Magnetosprillum gryphiswaldense* MSR-1 has a complete denitrification (nitrate reduction) pathway and that the pathway is necessary for the anaerobic growth of MSR-1 [*81*]. It has been postulated that the periplasmic components of all nitrate-reducing bacteria are innately capable of ferrous iron oxidation and that their growth is dependent on overcoming toxicity of iron and radical byproducts [*60, 61*]. In fact, several such non-biomineralizing strains, including *Acidovorax* strain BoFeN1, have been shown to precipitate intracellular iron minerals in the periplasm. A nitrite reductase from magnetotactic bacteria species *Magnetospirillum magnetotacticum* MS-1 has also been shown to oxidize Fe^{2+} *in vitro* [*82*]. Indeed, over the last decade several periplasmic protein components from *Magnetospirillum* species have been isolated and implicated in iron redox control [*83, 84*].

The denitrification pathway is also linked to proper magnetite formation in species of magnetotactic bacteria. For example, deletion of the magnetochrome mamX or its heme-binding domains as well as mamZ or is C-terminal ferric-reductase domain resulted in mild mineralization defects with mostly wild type crystals flanked by small, flaky crystals. However, the severity of the defects increased markedly in the absence of nitrate in the solution or in the absence of the periplasmic nitrate reductase Nap [*78*].

1.5. Lattice templation of magnetite in magnetotactic bacteria

Magnetite nanocrystals are co-localized in the magnetosome vesicle with several magnetosome island-derived proteins, including a set of tightly bound small proteins that can only be removed from the mineral upon boiling under denaturing conditions [*85*]. This set of proteins, called the Mms proteins are located within two adjacent gene clusters (*mamCDFG* and *mms6*) in the *Magnetospirillum* species' magnetosome island [*86*]. Sequence analysis of the Mms proteins indicate that several of these proteins share common properties including an N-terminal hydrophobic portion comprising a putative transmembrane segment and self-assembly related sequence as well as a C-terminal acidic portion that likely interacts with the mineral (*Figure 1.5*). *In vitro* magnetite synthesis studies with Mms6 have shown that the inclusion of the Mms6 protein in a colloidal synthesis leads to tighter size distributions of nanocrystals [*87*]. Changes in crystal size and morphology compared to purely synthetic magnetite can be observed with high-resolution TEM [*88, 89*]. The critical function of the Mms proteins in magnetite biomineralization is also supported by genetic studies, which have demonstrated that disruption of these genes lead to shape and size defects in mineralization [*36, 74*]. It has been suggested that members of the family share some redundant function and control the morphology of the crystal in a cumulative manner [*90*], a theory which recently has been confirmed by expressing different subsets of the *mms* genes *in vivo* and analyzing their crystal facets by HRTEM [*91*]. Based on their sequence characteristics and *in vitro* and *in vivo* mineralization function, it seems likely that the Mms proteins play an analogous role to templating proteins involved in calcium or silica biomineralization, which can self-assemble using one domain to provide a multimeric array of functional groups on another domain to bind the growing mineral and stabilize its growth [*92, 93*].

Through a careful genetic study, it has emerged that one gene, *mmsF*, is the major regulator of magnetite biomineralization in *Magnetospirillum magneticum* AMB-1 [*74*]. In the 8-gene deletion

mutant ΔR3 consisting of both *mamCDFG* and the *mmsF*-containing *mms6* clusters, the expression of MmsF alone is sufficient to restore the synthesis of mature magnetite crystal. Deletion of the *mmsF* gene results in the stalling of magnetite crystal growth at smaller sizes than wild type. Though, some interesting differences between expressing *mmsF* in the ΔR3 background strain versus the *mms6* cluster deletion strain suggests that one or several of the MamFDC proteins negatively regulate MmsF in the absence of Mms6. Examining the MmsF amino acid sequence reveals that MmsF does not have the same basic structure as Mms6 or other peptides found to be tightly bound to magnetite *in vivo*, but is thought to have three transmembrane helices as opposed to one. MmsF proteins assembles into large oligomeric structures *in vitro* which narrow and enlarge the crystal size distribution in magnetite precipitation reactions [*94*].

It should be noted that the *mamCDFG* and *mms6* clusters are not conserved among magnetotactic bacteria species. In fact, *Desulfovibrio magneticus* RS-1 contains neither clusters and forms unique bullet-shaped magnetite crystals [*95-97*]. Therefore, there must be overlapping factors that include the Mms proteins which stabilize crystal facets during magnetite synthesis.
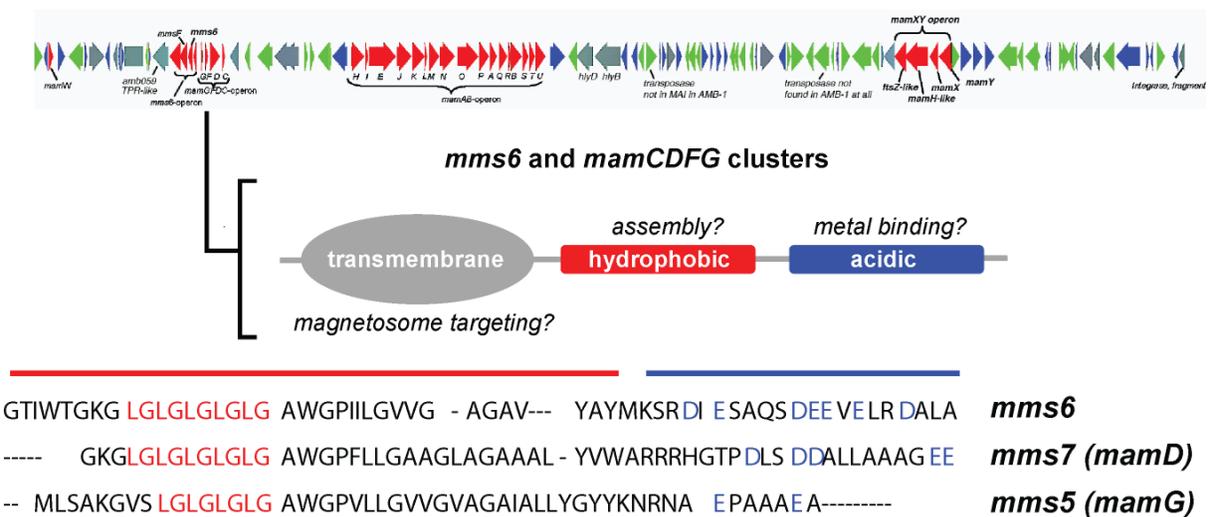
Figure 1.5. *The structure of templating proteins from the MamCDFG and Mms6 clusters. Sequence analysis of the Mms proteins indicate that these proteins share common properties including an N-terminal hydrophobic portion comprising a putative transmembrane segment and self-assembly related sequence. The C-terminal segment is highly acidic and likely interacts with the mineral.*

1.6. Specific aims and thesis organization

In order to explore new strategies for inorganic nanoparticle synthesis and engineering biorthogonal cellular functions, we have initiated studies aimed at the discovery and characterization of magnetosome protein components critical for the formation of the mixed-valent magnetite biomaterial. We have focused on studying the magnetotactic bacteria species *Magnetospirillum magneticum* AMB-1 as a model for redox-controlled biomineralization of transition metal-based materials.

Towards this goal, this thesis will be structured as follows: Chapter 2 discusses the genetic and biochemical characterization of two heme-containing proteins, MamP and MamT, which are thought to be involved in controlling Fe(II):Fe(III) ratio and which are encoded by the magnetosome island of *M. magneticum* AMB-1. Chapter 3 describes the purification of putative iron mineral-templating peptides from magnetotactic bacteria and their interaction with magnetite and magnetite precursors. Finally, Chapter 4 discusses using synthetic biology approaches to build new cellular nanomaterials and new cellular functions in AMB-1.

1.7. References

1.   S. Weiner and L. Addadi (2011) Crystallization pathways in biomineralization. *Annu. Rev. Mater. Res.* 41:21-40.
2.   F. H. Wilt (2005) Developmental biology meets materials science: morphogenesis of biomineralized structures. *Dev. Biol.* 280(1):15-25.
3.   C. E. Hamm, R. Merkel, O. Springer, P. Jurkojc, C. Maier, K. Prechtel, and V. Smetacek (2003) Architecture and material properties of diatom shells provide effective mechanical protection. *Nature* 421:841-843.
4.   C. Mao, D. J. Solis, B. D. Reiss, S. T. Kottmann, R. Y. Sweeney, A. Hayhurst, G. Georgiou, B. Iverson, and A. M. Belcher (2004) Virus-based toolkit for the directed synthesis of magnetic and semiconducting nanowires. *Science* 303(5655):213-217.
5.   J. E. Yang, S. Y. Choi, J. H. Shin, S. J. Park, and S. Y. Lee (2013) Microbial production of lactate-containing polyesters. *Microbial Biotech.* 6(6):621-636.
6.   A. Y. Chen, Z. Deng, A. N. Billings, U. O. Seker, M. Y. Lu, R. J. Citorik, B. Zakeri, and T. K. Lu (2014) Synthesis and patterning of tunable multiscale materials with engineered cells. *Nat. Mater.* 13(5):515-523.
7.   M. M. Tomczak, J. M. Slocik, M. O. Stone, and R. R. Naik (2007) Bio-based approaches to inorganic material synthesis. *Biochem. Soc. Trans.* 35(3):512-515.
8.   C. A. Orme, A. Noy, A. Wierzbicki, M. T. McBride, M. Grantham, H. H. Teng, P. M. Dove, and J. J. DeYoreo (2001) Formation of chiral morphologies through selective binding of amino acids to calcite surface steps. *Nature* 411(6839):775-779.
9.   A. M. Belcher, X. Wu, R. J. Christensen, P. K. Hansma, G. D. Stucky, and D. E. Morse (1996) Control of crystal phase switching and orientation by soluble mollusc-shell proteins. *Nature* 381:56-58.
10.   G. K. Hunter, P. V. Hauschka, A. R. Poole, L. C. Rosenberg, and H. A. Goldberg (1996) Nucleation and inhibition of hydroxyapatite formation by mineralized tissue proteins. *Biochem. J.* 317:59-64.

11. H. A. Currie and C. C. Perry (2007) Silica in plants: biological, biochemical and chemical studies. *Ann. Bot.* 100(7):1383-1389.
12. M. Hildebrand (2008) Diatoms, biomineralization processes, and genomics. *Chem. Rev.* 108(11):4855-4874.
13. G. Falini, S. Albeck, S. Weiner, and L. Addadi (1996) Control of aragonite or calcite polymorphism by mollusk shell macromolecules. *Science* 271(5245):67-69.
14. H. H. Teng, P. M. Dove, C. A. Orme, and J. J. De Yoreo (1998) Thermodynamics of calcite growth: baseline for understanding biomineral formation. *Science* 282(5389):724-727.
15. S. Weiner, A. Veis, E. Beniash, T. Arad, J. W. Dillon, B. Sabsay, and F. Siddiqui (1999) Peritubular dentin formation: crystal organization and the macromolecular constituents in human teeth. *J. Struct. Biol.* 126(1):27-41.
16. G. He, T. Dahl, A. Veis, and A. George (2003) Nucleation of apatite crystals in vitro by self-assembled dentin matrix protein 1. *Nat Mater* 2(8):552-558.
17. G. Fu, S. Valiyaveettil, B. Wopenka, and D. E. Morse (2005) $CaCO_3$ biomineralization: acidic 8-kDa proteins isolated from aragonitic abalone shell nacre can specifically modify calcite crystal morphology. *Biomacromolecules* 6(3):1289-1298.
18. E. C. Theil (2013) Ferritin: the protein nanocage and iron biomineral in health and in disease. *Inorg. Chem.* 52(21):12223-12233.
19. K. A. Weber, L. A. Achenbach, and J. D. Coates (2006) Microorganisms pumping iron: anaerobic microbial iron oxidation and reduction. *Nat. Rev. Microbiol.* 4(10):752-764.
20. K. M. Towe, and H. A. Lowenstam (1967) Ultrastructure and development of iron mineralization in the radular teeth of *Cryptochiton stelleri* (*Mollusca*). *J. Ultrastruct. Res.* 17(1):1-13.
21. H. C. Lichtenegger, T. Schoberl, M. H. Bartl, H. Waite, and G. D. Stucky (2002) High abrasion resistance with sparse mineralization: copper biomineral in worm jaws. *Science* 298(5592):389-392.
22. A. Manceau, K. L. Nagy, M. A. Marcus, M. Lanson, N. Geoffroy, T. Jacquet, and T. Kirpichtchikova (2008) Formation of metallic copper nanoparticles at the soil-root interface. *Environ. Sci. Technol.* 42(5):1766-1772.
23. B. Thamdrup (2000) Bacterial manganese and iron reduction in aquatic sediments. *Advances in Microbial Ecology* 16:41-84.
24. B. M. Tebo, H. A. Johnson, J. K. McCarthy, and A. S. Templeton (2005) Geomicrobiology of manganese(II) oxidation. *Trends Microbiol.* 13:421-428.
25. D. R. Learman, B. M. Voelker, A. I. Vazquez-Rodriguez, and C. M. Hansel (2011) Formation of manganese oxides by bacterially generated superoxide. *Nat. Geosci.* 4:95-98.
26. D. Faivre and D. Schuler (2008) Magnetotactic bacteria and magnetosomes. *Chem. Rev.* 108(11):4875-4898.
27. R. B. Frankel, J.-P. Zhang, and D. A. Bazylinski (1998) Single magnetic domains in magnetotactic bacteria. *J. Geophys. Res.* 103:30601-30604.
28. A. Fischer, M. Schmitz, B. Aichmayer, P. Fratzl, and D. Faivre (2011) Structural purity of magnetite nanoparticles in magnetotactic bacteria. *J. R. Soc. Interface* 8(60):1011-1018.
29. F. C. Meldrum and H. Colfen (2008) Controlling mineral morphologies and structures in biological and synthetic systems. *Chem. Rev.* 108(11):4332-4432.
30. S. Schubbe, M. Kube, A. Scheffel, C. Wawer, U. Heyen, A. Meyerdierks, M. H. Madkour, F. Mayer, R. Reinhardt, and D. Schuler (2003) Characterization of a spontaneous

nonmagnetic mutant of *Magnetospirillum gryphiswaldense* reveals a large deletion comprising a putative magnetosome island. *J. Bacteriol.* 185(19):5779-5790.

31. T. Matsunaga, Y. Okamura, Y. Fukuda, A. T. Wahyudi, Y. Murase, and H. Takeyama (2005) Complete genome sequence of the facultative anaerobic magnetotactic bacterium *Magnetospirillum* sp. strain AMB-1. *DNA Res.* 12(3):157-166.

32. A. Komeili, Z. Li, D. K. Newman, and G. J. Jensen (2006) Magnetosomes are cell membrane invaginations organized by the actin-like protein MamK. *Science* 311(5758):242-245.

33. O. Draper, M. E. Byrne, Z. Li, S. Keyhani, J. C. Barrozo, G. Jensen, and A. Komeili (2011) MamK, a bacterial actin, forms dynamic filaments in vivo that are regulated by the acidic proteins MamJ and LimJ. *Mol. Microbiol.* 82(2):342-354.

34. D. Schuler and E. Baeuerlein (1998) Dynamics of iron uptake and Fe_3O_4 biomineralization during aerobic and microaerobic growth of *Magnetospirillum gryphiswaldense*. *J. Bacteriol.* 180(1):159-162.

35. A. Komeili, H. Vali, T. J. Beveridge, and D. K. Newman (2004) Magnetosome vesicles are present before magnetite formation, and MamA is required for their activation. *Proc. Natl. Acad. Sci. U. S. A.* 101(11):3839-3844.

36. D. Murat, A. Quinlan, H. Vali, and A. Komeili (2010) Comprehensive genetic dissection of the magnetosome gene island reveals the step-wise assembly of a prokaryotic organelle. *Proc. Natl. Acad. Sci. U. S. A.* 107(12):5593-5598.

37. S. K. Checa, M. Espariz, M. E. Audero, P. E. Botta, S. V. Spinelli, and F. C. Soncini (2007) Bacterial sensing of and resistance to gold salts. *Mol Microbiol* 63(5):1307-1318.

38. S. Mann (2001) *Biomineralization: principles and concepts in bioinorganic materials chemistry*. Oxford University Press, Oxford.

39. L. J. Bird, V. Bonnefoy, and D. K. Newman (2011) Bioenergetic challenges of microbial iron metabolisms. *Trends Microbiol.* 19(7):330-340.

40. D. Langmuir (1971) Particle size effect on the reaction goerthite = hematite + water. *Am. J. Sci.* 271:147-156.

41. U. Schwertmann and R. M. Cornell (2000) *Iron oxides in the laboratory : preparation and characterization* (Wiley-VCH, Weinheim ; New York) 2nd completely rev. and extended Ed pp xviii, 188 p.

42. W. Stumm and G. F. Lee (1960) The chemistry of aqueous iron. *Schweizerische Zeitschrift für Hydrologie* 22:295-319

43. J. E. Kostka and K. H. Nealson (1995) Dissolution and reduction of magnetite by bacteria. *Environ. Sci. Technol.* 29(10):2535-2540.

44. K. R. Abhilash and B. D. Pandey (2011) Microbial synthesis of iron-based nanomaterials - a review. *Bull. Mater. Sci.* 34(2):191-198.

45. M. Firer-Sherwood, G. S. Pulcu, and S. J. Elliott (2008) Electrochemical interrogations of the Mtr cytochromes from *Shewanella*: opening a potential window. *J. Biol. Inorg. Chem.* 13(6):849-854.

46. J. R. Lloyd, C. Leang, A. L. Hodges Myerson, M. V. Coppi, S. Cuifo, B. Methe, S. J. Sandler, and D. R. Lovley (2003) Biochemical and genetic characterization of PpcA, a periplasmic c-type cytochrome in *Geobacter sulfurreducens*. *Biochem. J.* 369(Pt 1):153-161.

47. X. Qian, T. Mester, L. Morgado, T. Arakawa, M. L. Sharma, K. Inoue, C. Joseph, C. A. Salgueiro, M. J. Maroney, and D. R. Lovley (2011) Biochemical characterization of purified OmcS, a c-type cytochrome required for insoluble Fe(III) reduction in *Geobacter sulfurreducens*. *Biochim. Biophys. Acta* 1807(4):404-412.

48. T. S. Magnuson, N. Isoyama, A. L. Hodges-Myerson, G. Davidson, M. J. Maroney, G. G. Geesey, and D. R. Lovley (2001) Isolation, characterization and gene sequence analysis of a membrane-associated 89 kDa Fe(III) reducing cytochrome c from *Geobacter sulfurreducens*. *Biochem. J.* 359(Pt 1):147-152.

49. L. Shi, D. J. Richardson, Z. Wang, S. N. Kerisit, K. M. Rosso, J. M. Zachara, and J. K. Fredrickson (2009) The roles of outer membrane cytochromes of *Shewanella* and *Geobacter* in extracellular electron transfer. *Environ. Microbiol. Rep.* 1:220-227.

50. G. Reguera, K. D. McCarthy, T. Mehta, J. S. Nicoll, M. T. Tuominen, and D. R. Lovley (2005) Extracellular electron transfer via microbial nanowires. *Nature* 435(7045):1098-1101.

51. C. Leang, X. Qian, T. Mester, and D. R. Lovley (2010) Alignment of the c-type cytochrome OmcS along pili of *Geobacter sulfurreducens*. *Appl. Environ. Microbiol.* 76(12):4080-4084.

52. M. Y. El-Naggar, G. Wanger, K. M. Leung, T. D. Yuzvinsky, G. Southam, J. Yang, W. M. Lau, K. H. Nealson, and Y. A. Gorby (2010) Electrical transport along bacterial nanowires from *Shewanella oneidensis* MR-1. *Proc. Natl. Acad. Sci. U. S. A.* 107(42):18127-18131.

53. H. von Canstein, J. Ogawa, S. Shimizu, and J. R. Lloyd (2008) Secretion of flavins by *Shewanella* species and their role in extracellular electron transfer. *Appl. Environ. Microbiol.* 74(3):615-623.

54. M. E. Hernandez and D. K. Newman (2001) Extracellular electron transfer. *Cell. Mol. Life Sci.* 58(11):1562-1571.

55. D. R. Lovley and E. L. Blunt-Harris (1999) Role of humic-bound iron as an electron transfer agent in dissimilatory Fe(III) reduction. *Appl Environ Microbiol* 65(9):4252-4254.

56. M. Taillefert, J. S. Beckler, E. Carey, J. L. Burns, C. M. Fennessey, and T. J. DiChristina (2007) *Shewanella putrefaciens* produces an Fe(III)-solubilizing organic ligand during anaerobic respiration on insoluble Fe(III) oxides. *J. Inorg. Biochem.* 101(11-12):1760-1767.

57. Y. Jiao and D. K. Newman (2007) The *pio* operon is essential for phototrophic Fe(II) oxidation in *Rhodopseudomonas palustris* TIE-1. *J. Bacteriol.* 189:1765–1773.

58. L. R. Croal, Y. Jiao, and D. K. Newman (2007) The fox operon from Rhodobacter strain SW2 promotes phototrophic Fe(II) oxidation in *Rhodobacter capsulatus* SB1003. *J. Bacteriol.* 189(5):1774-1782.

59. I. H. Saraiva, D. K. Newman, and R. O. Louro (2012) Functional characterization of the FoxE iron oxidoreductase from the photoferrotroph *Rhodobacter ferrooxidans* SW2. *J. Biol. Chem.* 287(30):25541-25548.

60. H. K. Carlson, I. C. Clark, S. J. Blazewicz, A. T. Iavarone, and J. D. Coates (2013) Fe(II) oxidation is an innate capability of nitrate-reducing bacteria that involves abiotic and biotic reactions. *J. Bacteriol.* 195(14):3260-3268.

61. H. K. Carlson, I. C. Clark, R. A. Melnyk, and J. D. Coates (2012) Toward a mechanistic understanding of anaerobic nitrate-dependent iron oxidation: balancing electron uptake and detoxification. *Front. Microbiol.* 3:57.

62. S. E. Greene and A. Komeili (2012) Biogenesis and subcellular organization of the magnetosome organelles of magnetotactic bacteria. *Curr. Opin. Cell. Biol.* 24(4):490-495.

63. R. B. Frankel, G. S. Papaefstathiou, R. P. Blakemore, and W. O'Brien (1983) Fe_3O_4 precipitation in magnetotactic bacteria. *Biochim. Biophys. Acta* 763:147-159.

64. Y. Han, C. Liu, D. Zhou, F. Li, Y. Wang, and X. Han (2011) Magnetic and structural properties of magnetite in radular teeth of chiton *Acanthochiton rubrolinestus*. *Bioelectromagnetics* 32(3):226-233.

65. M. Nemoto, Q. Wang, D. Li, S. Pan, T. Matsunaga, and D. Kisailus (2012) Proteomic analysis from the mineralized radular teeth of the giant Pacific chiton, *Cryptochiton stelleri* (Mollusca). *Proteomics* 12(18):2890-2894.

66. S. Staniland, B. Ward, A. Harrison, G. van der Laan, and N. Telling (2007) Rapid magnetosome formation shown by real-time x-ray magnetic circular dichroism. *Proc. Natl. Acad. Sci. U. S. A.* 104(49):19524-19528.

67. M. L. Fdez-Gubieda, A. Muela, J. Alonso, A. Garcia-Prieto, L. Olivi, R. Fernandez-Pacheco, and J. M. Barandiaran (2013) Magnetite biomineralization in *Magnetospirillum gryphiswaldense*: time-resolved magnetic and structural studies. *ACS Nano* 7(4):3297-3305.

68. D. Faivre, L. H. Bottger, B. F. Matzanke, and D. Schuler (2007) Intracellular magnetite biomineralization in bacteria proceeds by a distinct pathway involving membrane-bound ferritin and an iron(II) species. *Angew. Chem. Int. Ed. Engl.* 46(44):8495-8499.

69. C. Lang, D. Schuler, and D. Faivre (2007) Synthesis of magnetite nanoparticles for bio- and nanotechnology: genetic engineering and biomimetics of bacterial magnetosomes. *Macromol. Biosci.* 7(2):144-151.

70. J. Baumgartner, G. Morin, N. Menguy, T. Perez Gonzalez, M. Widdrat, J. Cosmidis, and D. Faivre (2013) Magnetotactic bacteria form magnetite from a phosphate-rich ferric hydroxide via nanometric ferric (oxyhydr)oxide intermediates. *Proc. Natl. Acad. Sci. U. S. A.* 110(37):14883-14888.

71. K. W. Mandernack, D. A. Bazylinski, W. C. Shanks III, and T. D. Bullen (1999) Oxygen and iron isotope studies of magnetite produced by magnetotactic bacteria. *Science* 285(5435):1892-1896.

72. L. Rahn-Lee and A. Komeili (2013) The magnetosome model: insights into the mechanisms of bacterial biomineralization. *Front. Microbiol.* 4:352.

73. A. Lohsse, S. Borg, O. Raschdorf, I. Kolinko, E. Tompa, M. Posfai, D. Faivre, J. Baumgartner, and D. Schuler (2014) Genetic dissection of the mamAB and mms6 operons reveals a gene set essential for magnetosome biogenesis in *Magnetospirillum gryphiswaldense*. *J. Bacteriol.* 196(14):2658-2669.

74. D. Murat, V. Falahati, L. Bertinetti, R. Csencsits, A. Kornig, K. Downing, D. Faivre, and A. Komeili (2012) The magnetosome membrane protein, MmsF, is a major regulator of magnetite biomineralization in *Magnetospirillum magneticum* AMB-1. *Mol. Microbiol.* 85(4):684-699.

75. A. Quinlan, D. Murat, H. Vali, and A. Komeili (2011) The HtrA/DegP family protease MamE is a bifunctional protein with roles in magnetosome protein localization and magnetite biomineralization. *Mol. Microbiol.* 80(4):1075-1087.

76. W. Yang, R. Li, T. Peng, Y. Zhang, W. Jiang, Y. Li, and J. Li (2010) *mamO* and *mamE* genes are essential for magnetosome crystal biomineralization in *Magnetospirillum gryphiswaldense* MSR-1. *Res. Microbiol.* 161(8):701-705.

77. M. I. Siponen, G. Adryanczyk, N. Ginet, P. Arnoux, and D. Pignol (2012) Magnetochrome: a c-type cytochrome domain specific to magnetotatic bacteria. *Biochem. Soc. Trans.* 40(6):1319-1323.

78. O. Raschdorf, F. D. Muller, M. Posfai, J. M. Plitzko, and D. Schuler (2013) The magnetosome proteins MamX, MamZ and MamH are involved in redox control of magnetite biomineralization in *Magnetospirillum gryphiswaldense*. *Mol. Microbiol.* 89(5):872-886.

79. M. I. Siponen, P. Legrand, M. Widdrat, S. R. Jones, W. J. Zhang, M. C. Chang, D. Faivre, P. Arnoux, and D. Pignol (2013) Structural insight into magnetochrome-mediated magnetite biomineralization. *Nature* 502(7473):681-684.

80. A. Taoka, Y. Eguchi, S. Mise, Z. Oestreicher, F. Uno, and Y. Fukumori (2014) A magnetosome-associated cytochrome MamP is critical for magnetite crystal growth during the exponential growth phase. *FEMS Microbiol. Lett.*

81. Y. Li, E. Katzmann, S. Borg, and D. Schuler (2012) The periplasmic nitrate reductase Nap is required for anaerobic growth and involved in redox control of magnetite biomineralization in *Magnetospirillum gryphiswaldense*. *J. Bacteriol.* 194(18):4847-4856.

82. T. Yamazaki, H. Oyanagi, T. Fujiwara, and Y. Fukumori (1995) Nitrate reductase from the magnetotactic bacterium: a novel cytochrome *cd1* with Fe(II):nitrate oxidoreductase activity. *Eur. J. Biochem.* 233:665–671.

83. A. Taoka, K. Yoshimatsu, M. Kanemori, and Y. Fukumori (2003) Nitrate reductase from the magnetotactic bacterium *Magnetospirillum magnetotacticum* MS-1: purification and sequence analyses. *Can. J. Microbiol.* 49(3):197-206.

84. Y. Noguchi, T. Fujiwara, K. Yoshimatsu, and Y. Fukumori (1999) Iron reductase for magnetite synthesis in the magnetotactic bacterium *Magnetospirillum magnetotacticum*. *J. Bacteriol.* 181(7):2142-2147.

85. A. Arakaki, J. Webb, and T. Matsunaga (2003) A novel protein tightly bound to bacterial magnetic particles in *Magnetospirillum magneticum* strain AMB-1. *J. Biol. Chem.* 278(10):8745-8750.

86. C. Jogler, W. Lin, A. Meyerdierks, M. Kube, E. Katzmann, C. Flies, Y. Pan, R. Amann, R. Reinhardt, and D. Schuler (2009) Toward cloning of the magnetotactic metagenome: identification of magnetosome island gene clusters in uncultivated magnetotactic bacteria from different aquatic sediments. *Appl. Environ. Microbiol.* 75(12):3972-3979.

87. T. Prozorov, P. Palo, L. Wang, M. Nilsen-Hamilton, D. Jones, D. Orr, S. K. Mallapragada, B. Narasimhan, P. C. Canfield, and R. Prozorov (2007) Cobalt ferrite nanocrystals: out-performing magnetotactic bacteria. *ACS Nano* 1(3):228-233.

88. A. Arakaki, F. Masuda, Y. Amemiya, T. Tanaka, and T. Matsunaga (2010) Control of the morphology and size of magnetite particles with peptides mimicking the Mms6 protein from magnetotactic bacteria. *J. Colloid Interface Sci.* 343(1):65-70.

89. Y. Amemiya, A. Arakaki, S. S. Staniland, T. Tanaka, and T. Matsunaga (2007) Controlled formation of magnetite crystal by partial oxidation of ferrous hydroxide in the presence of recombinant magnetotactic bacterial protein Mms6. *Biomaterials* 28(35):5381-5389.

90. A. Scheffel, A. Gardes, K. Grunberg, G. Wanner, and D. Schuler (2008) The major magnetosome proteins MamGFDC are not essential for magnetite biomineralization in *Magnetospirillum gryphiswaldense* but regulate the size of magnetosome crystals. *J. Bacteriol.* 190(1):377-386.

91. A. Arakaki, A. Yamagishi, A. Fukuyo, M. Tanaka, and T. Matsunaga (2014) Co-ordinated functions of Mms proteins define the surface structure of cubo-octahedral magnetite crystals in magnetotactic bacteria. *Mol. Microbiol.* 93(3):554-567.

92. C. Groger, K. Lutz, and E. Brunner (2008) Biomolecular self-assembly and its relevance in silica biomineralization. *Cell. Biochem. Biophys.* 50(1):23-39.

93. G. He, S. Gajjeraman, D. Schultz, D. Cookson, C. Qin, W. T. Butler, J. Hao, and A. George (2005) Spatially and temporally controlled biomineralization is facilitated by interaction between self-assembled dentin matrix protein 1 and calcium phosphate nuclei in solution. *Biochemistry* 44(49):16140-16148.

94. A. E. Rawlings, J. P. Bramble, R. Walker, J. Bain, J. M. Galloway, and S. S. Staniland (2014) Self-assembled MmsF proteinosomes control magnetite nanoparticle formation in vitro. *Proc. Natl. Acad. Sci. U. S. A.* 111(45):16094-16099.

95. T. Sakaguchi, A. Arakaki, and T. Matsunaga (2002) *Desulfovibrio magneticus* RS-1, a novel sulfate-reducing bacterium that produces intracellular single-domain-sized magnetite particles. *Int. J. Syst. Evol. Microbiol.* 52(Pt 1):215-221.

96. T. Matsunaga, M. Nemoto, A. Arakaki, and M. Tanaka (2009) Proteomic analysis of irregular, bullet-shaped magnetosomes in the sulphate-reducing magnetotactic bacterium *Desulfovibrio magneticus* RS-1. *Proteomics* 9(12):3341-3352.

97. H. Nakazawa, A. Arakaki, S. Narita-Yamada, I. Yashiro, K. Jinno, N. Aoki, A. Tsuruyama, Y. Okamura, S. Tanikawa, N. Fujita, H. Takeyama, and T. Matsunaga (2009) Whole genome sequence of *Desulfovibrio magneticus* strain RS-1 revealed common gene clusters in magnetotactic bacteria. *Genome Res.* 19(10):1801-1808.

Chapter 2: *Genetic and biochemical characterization of two heme-containing proteins encoded by the magnetosome island of* M. magneticum *AMB-1*

Portions of this work were performed in collaboration with the following persons:

Spectroelectrochemical titrations were performed with the assistance of Dr. Margaret Brown. The development of MamP purification protocols and characterization of MamP were performed in close collaboration with Dr. Tiffany Wilson. The ΔmamTΔR9 strain was made by Dr. Lilah Rahn-Lee. Dr. Ertan Ozyamak and Professor Arash Komeili were instrumental in the development of this work. Cloning was performed in close collaboration with Laura Fredriksen.

Portions of this work were published in the following scientific journal:

2.1. Introduction

The unparalleled ability of living systems to evolve new chemistry taps into both organic and inorganic reaction space as well homogeneous and heterogeneous catalysis. Indeed, the transformation of soluble metal ions to form various biological nanostructures, from the intricately patterned diatom frustule to the unusually strong mollusk shell, provides important function at the organism level [1-6] and has inspired new methods for the preparation of synthetic materials [7-11]. The mineralization of calcium is the most well understood as it produces perhaps the largest class of biominerals [12-16]. However, the controlled mineralization of elements such as silicon [17-19], iron [20-26], copper [27, 28], and manganese [29-32] are also observed although less broadly distributed. Of the latter group, iron biomineralization by magnetotactic bacteria represents a particularly interesting case for understanding how the production of nanomaterials can be programmed at the genetic level.

Magnetotactic bacteria house a sophisticated system to sense the earth's magnetic field for magnetoaerotaxis using linear chains of biological magnets, consisting of membrane-encapsulated magnetite ($Fe(II)Fe(III)_2O_4$) nanoparticles of various sizes (35-120 nm) and shapes with several unusual properties [33]. First, these nanoparticles are generated as a single magnetic domain [34], suggesting that they have naturally evolved to maximize the magnetic contribution of each iron atom. In addition, the magnetite is synthesized as an internally pure material with surface-passivating proteins [35] rather than as a composite material with organic layers, as is often observed in calcium-based biominerals [4]. Also in contrast to the structural biomaterials built from calcium and silicon, the production of magnetite requires redox chemistry to produce the mixed-valent Fe(II)/Fe(III) product and could allow us to access large classes of functional transition metal-based materials using synthetic biology approaches.

The magnetite nanocrystals are grown by the cell under genetically-controlled conditions within a subcellular vesicle, called the magnetosome, to produce defectless nanocrystals with a narrow size and shape distribution [36]. Based on its Pourbaix diagram, magnetite remains stable only at select redox potentials and pHs which thereby implies that the magnetosome forms a compartment that has been optimized for synthesis of these materials. Interestingly, an analysis of the magnetosome island (MAI) of *Magnetospirillum magneticum* AMB-1, which houses a large part of the genetic material encoding this process, reveals that several essential genes are annotated as potential iron transporters, proton transporters, and redox proteins and could serve to tune these different parameters. Our group is interested in identifying and characterizing the components involved directly in mineral synthesis to facilitate efforts to engineer the magnetosome for new synthetic functions. In this study, we focus on MamP and MamT, which are predicted *c*-type cytochromes in the MAI proposed to participate in redox reactions of iron in the magnetosome [37, 38]. We show that the double CXXCH heme motifs are essential for physiological function for both proteins, which supports a primary role *in vivo* involving redox chemistry. This finding is also consistent with the recently reported crystal structure of the MamP ortholog from the MO-1 strain that shows that it comprises a novel "magnetochrome" fold involving the minimal association of 23 amino acids around each heme cofactor [39]. We further carry out *in vitro* biochemical experiments on purified MamP and demonstrate that it is competent to catalytically oxidize Fe(II) to Fe(III) despite its relatively unusual reduction potential compared to other cytochromes reported to carry out Fe(II) oxidation or Fe(III) reduction. Finally, *in vitro* iron mineralization show that MamP is capable of producing mixed-valent iron oxides from soluble

22

Fe(II) species and can work synergistically with mineral-templating proteins from the Mms family to control mineral structure.

2.2. Materials and methods

Reagent information. Luria-Bertani (LB) Broth Miller, $2 \times$ YT Media, Terrific Broth, LB Agar Miller, sodium thiosulfate, sodium nitrate, and glycerol were purchased from EMD Biosciences (Darmstadt, Germany). Carbenicillin (Cb), isopropyl-β-D-thiogalactopyranoside (IPTG), phenylmethanesulfonyl fluoride (PMSF), tris(hydroxymethyl)aminomethane base (Tris), sodium chloride, dithiothreitol (DTT), 4-(2-hydroxyethyl)-1-piperazineethanesulfonic acid (HEPES), magnesium chloride hexahydrate, potassium chloride, potassium phosphate monobasic, potassium phosphate dibasic, D-sucrose, kanamycin (Km), ethylene glycol, ethylene diamine tetraacetic acid disodium dihydrate (EDTA), bromophenol blue sodium salt, anhydrous sodium acetate, methanol, L-ascorbic acid, sodium acetate, guanidine hydrochloride, and 30% hydrogen peroxide were purchased from Fisher Scientific (Pittsburgh, PA). Chloramphenicol (Cm), methylsulfoxide (DMSO), hydrochloric acid, glacial acetic acid, ammonium hydroxide, potassium hydroxide, and sodium hydroxide were purchased from EMD Millipore (Billerica, MA). β-mercaptoethanol, ammonium bicarbonate, sodium dithionite, sodium phosphate dibasic hepthydrate, N,N,N',N'-tetramethyl-ethane-1,2-diamine (TEMED), ammonium iron(II) sulfate hexahydrate, 3,3′,5,5′-tetramethylbenzidine, toluylene blue, hexaammineruthenium(III) chloride, *p*-benzoquinone, methyl viologen, anthraquinone-2-sulfonic acid, 2-hydroxy-1,4-naphthoquinone, magnesium sulfate heptahydrate, manganese(II) sulfate monohydrate, cobalt(II) chloride hexahydrate, calcium chloride, zinc sulfate heptahydrate, copper(II) sulfate pentahydrate, aluminum potassium sulfate dodecahydrate, boric acid, sodium molybdate dehydrate, succinic acid, biotin, folic acid, pyridoxine hydrochloride, thiamine hydrochloride, riboflavin, calcium D-(+)-pantothenate, vitamin B-12, *p*-aminobenzoic acid, thioctic acid, nicotinic acid, d-desthiobiotin, 5-aminolevulinic acid (ALA) and diaminopimelic acid (DAP) were purchased from Sigma-Aldrich (St. Louis, MO). Imidazole and formic acid were purchased from Acros Organics (Morris Plains, NJ). Nitrilotriacetic acid was purchased from Eastman Organic Chemicals. 3′-chloroindophenol was purchased from TCI-SU (Tokyo, Japan). ODQ was purchased from Cayman Chemical Company (Ann Arbor, MI). Acrylamide/Bis-acrylamide (30%, 37.5:1), electrophoresis grade sodium dodecyl sulfate (SDS) and ammonium persulfate were purchased from Bio-Rad Laboratories (Hercules, CA). Restriction enzymes, T4 DNA ligase, Antarctic phosphatase, Phusion DNA polymerase, T5 exonuclease, and Taq DNA ligase were purchased from New England Biolabs (Ipswich, MA). Deoxynucleotides (dNTPs) and Platinum Taq High-Fidelity polymerase (Pt Taq HF) were purchased from Invitrogen (Carlsbad, CA). PageRuler™ Plus prestained protein ladder was purchased from Fermentas (Glen Burnie, Maryland). Oligonucleotides were purchased from Integrated DNA Technologies (Coralville, IA), resuspended at a stock concentration of 100 µM in 10 mM Tris-HCl, pH 8.5, and stored at either 4°C for immediate use or -20°C for longer term use. DNA purification kits and Ni-NTA agarose were purchased from Qiagen (Valencia, CA). Recombinant RNAse-free DNAse I and Complete EDTA-free protease inhibitor were purchased from Roche Applied Science (Penzberg, Germany). TEV protease was purchased from the QB3 MacroLab at UC Berkeley. Amicon Ultra 3,000 MWCO and 10,000 MWCO centrifugal concentrators and 5,000 MWCO and 10,000 MWCO regenerated cellulose ultrafiltration membranes were purchased from EMD Millipore (Billerica,

MA). Mass spectral analyses were carried out at the College of Chemistry Mass Spectrometry Facility at UC Berkeley.

Bacterial strains. *E. coli* DH10B-T1^R was used for DNA construction. *E. coli* BL21(DE3) and C43(DE3) were used for heterologous protein production of Mms7ct and MamP, respectively. *E. coli* WM3064 was used for conjugative transfer of plasmids into *M. magneticum* AMB-1 wild-type (AK30) and knockout (Δ*mamP*, AK69; ΔR9, AK57; Δ*mamT*ΔR9, AK155) strains as previously described [*40*]. Since the Δ*mamT* gene falls between two repeating regions of the *mamQRB* locus and its deletion frequently lead to *mamQRB* recombination, the Δ*mamT* strain was made in the ΔR9 genetic background in which the downstream *mamQRB* has been removed from the MAI without causing a detectable phenotype in wild-type *M. magneticum* AMB-1.

***Magnetospirillum magneticum* AMB-1 cell culture.** AMB-1 was grown using Magnetic Growth (MG) media [*40*] with Wolfe's mineral solution omitting tartaric acid, Wolfe's vitamin solution, and iron malate (100× stock made from 3 mM FeCl$_3$ and 9 mM DL-malic acid). Solid media was generated by the addition of agar (0.7% w/v) to MG media. For antibiotic selection, kanamycin (Km) was supplied at a final concentration of 10 µg/mL in liquid cultures and 15 µg/mL in solid media. Carbenicillin (Cb) was used at a final concentration of 20 µg/mL in both liquid and solid media. Plasmids were introduced into AMB-1 strains by conjugative transfer with an *E. coli* WM3064 donor strain using literature methods as described [*40*]. Cultures for mutant screens, C$_{mag}$ measurements, and TEM/HRTEM characterization were grown in MG media (10 mL) at 30°C without agitation in seal-capped anaerobic culture tubes (20 mL) after degassing the headspace with Ar.

Plasmid construction. Standard molecular biology techniques were used to carry out plasmid construction. All PCR amplifications were carried out with Phusion DNA polymerase. For amplification of GC-rich sequences from *M. magneticum* AMB-1 (AMB-1), PCR reactions were supplemented with DMSO (5%) with primer annealing temperatures 8-10°C below the melting temperature (T$_m$) calculated using OligoCalc [*41*]. Plasmids were assembled either using the Gibson method [*42*] or restriction digest and ligation. All constructs were verified by sequencing (Quintara Biosciences; Berkeley, CA).

Plasmids for *mamP* and *mamT* complementation studies. Plasmids for *mamP* and *mamT* complementation with AMB-1 were derived from the pAK22-derived plasmid pAK262 [*43*].

pAK262Amp-MamP. To avoid known problems with magnetite formation related to the kanamycin resistance cassette (Km^R) [*43*], the Km^R marker was first replaced with the ampicillin marker (Amp^R) to generate the *mamP* complementation plasmid pAK262Amp-MamP. The plasmid backbone containing *mamP* and Amp^R cassette were amplified respectively from pAK262 (pAK F1/R1 primers) and pCWori (pAK F2/R2 primers) for Gibson assembly.

pAK262Amp-MamP$_{Δheme1}$, pAK262Amp-MamP$_{Δheme2}$, pAK262Amp-MamP$_{Δheme}$. The *mamP*$_{Δheme1}$ and *mamP*$_{Δheme2}$ complementation plasmids were then constructed from pAK262Amp-MamP by QuikChange site-directed mutagenesis of the CXXCH motif to AXXAA. The residues C224, C227, and H228 were mutated to alanine to generate pAK262Amp-MamP$_{Δheme1}$ by amplification of pAK262Amp-MamP with the MamP QC F2/R2 primers. The residues C268, C272, and H273 were mutated to alanine to generate

24

pAK262Amp-MamP$_{\Delta heme2}$ using the MamP QC F1/R1 primers. The *mamP*$_{\Delta heme}$ complementation plasmid, pAK262Amp-MamP$_{\Delta heme}$, was then generated from pAK262Amp-MamP$_{\Delta h2}$ by amplification with the MamP QC F2/R2 primers.

pAK262Amp-MamT$_{\Delta heme1}$,   pAK262Amp-MamT$_{\Delta heme2}$,   pAK262Amp-MamT$_{\Delta heme}$. pAK262Amp-MamT was constructed by Gibson assembly of *mamT* (residues 1-176) amplified from AMB-1 genomic DNA (MamT SF1/MamT SR1 primers) and the pAK262Amp backbone amplified from pAK262Amp-MamP plasmid (pAK MamT F1/R1 primers) to remove *mamP*.

The *mamT*$_{\Delta heme1}$ and *mamT*$_{\Delta heme2}$ complementation plasmids were then constructed from pAK262Amp-MamT by QuikChange site-directed mutagenesis of the CXXCH to AXXAA as described above for MamP. Plasmid pAK262Amp-MamT$_{\Delta heme1}$ was constructed by mutagenesis of residues C103, C106, and H107 to alanine using the MamT QC F1/R1 primers. Plasmid pAK262Amp-MamT was constructed by mutagenesis of residues C154, C157, and H158 to alanine using the MamT QC F2/R2 primers. Finally, plasmid pAK262Amp-MamT$_{\Delta heme}$ was generated by amplifying pAK262Amp-MamT$_{\Delta heme2}$ with the MamT QC F1/R1 primers.

pAK262Amp-MamP.FLAG. The pAK262Amp-MamP.FLAG plasmid was made by amplifying *mamP* from pAK262Amp-MamP with the primers MamP Flag F1/R1 and the pAK262Amp vector from pAK262Amp-MamP with the primers MamP Flag F2/R2 The two pieces were assembled by the Gibson method.

pAK262Amp-FLAG.MamP. The pAK262Amp-FLAG.MamP plasmid was made by amplifying *mamP* from pAK262Amp-MamP with the primers Flag MamP F1/R1 and by amplifying the pAK262Amp vector from pAK262Amp-MamP with the primers Flag MamP F2/R2. The two pieces were assembled by the Gibson method.

pAK262-MamP.GFP$_{sf}$. The pAK262-MamP.GFP$_{sf}$ plasmid was made by amplifying MamP from pAK262Amp-MamP with primers P GFPsf F1/R1 and by amplifying GFP$_{sf}$ with P GFPsf F2/R2 from pBK-GFP-superfold plasmid (Molecular Foundry, Lawrence Berkeley National Laboratory) [*44*]. The genes were inserted into the EcoRI-SpeI restriction sites of pAK262 vector by Gibson assembly.

pAK262-GFP$_{sf}$.MamP. The pAK262-GFP$_{sf}$.MamP plasmid was made by amplifying GFPsf from pBK-GFP-superfold with GFPsf P F1/R1 and by amplifying MamP from pAK262Amp-MamP with GFPsf P F2/R2. The genes were inserted into the EcoRI-SpeI restriction sites of pAK262 vector by Gibson assembly.

Plasmids for heterologous expression of MamP in *E. coli*. The initial plasmid for the heterologous expression of MamP in *E. coli* was constructed in a series of steps designed to make intermediates for testing MamP expression.

pCWori-OmpA.MamP. The sequence encoding the mature MamP sequence (residues 29-275) predicted by TMHMM program [*45*] was amplified from pAK262 with the MamP Ex F1/R1 primers and inserted into the NcoI-HindIII site of pCWori-OmpA.sLipA, which contains an N-terminal *ompA* periplasmic targeting sequence between the NdeI and NcoI restriction sites.

pCWori-OmpA.His₆.SUMOtev.MamP. The pCWori-OmpA.His$_6$.SUMOtev.MamP vector was constructed by amplification of the His$_6$.SUMOtev.MamP cassette from pSUMO-MamP with the MamP Ex F2/R2 primers and insertion into the NcoI-HindIII site of pCWori-OmpA.MamP. The plasmid pSUMO-MamP was constructed by sequence and ligation independent cloning (SLIC). The SLIC-compatible pSUMO plasmid was linearized through SSpI digestion and assembled with MamP amplified from pAK262 with MamP LIC F1/R1 (QB3 Macrolab, UC Berkeley).

pCWori-OmpA.His₆.NusAtev.MamP. The pCWori-OmpA.His$_6$.NusAtev.MamP vector was constructed by amplification of the His$_6$.NusAtev.MamP cassette from pNusA-MamP with the MamP Ex F3/R2 primers and insertion into the NcoI-HindIII site of pCWori-OmpA.MamP. The plasmid pNusA-MamP was constructed by SLIC. The SLIC-compatible pNusA plasmid was linearized through SspI digestion and assembled with MamP amplified from pAK262 with MamP LIC F1/R1 (QB3 Macrolab, UC Berkeley).

pCWori-OmpA.His₆.MOCRtev.MamP. The pCWori-OmpA.His$_6$.MOCRtev.MamP vector was made by amplifying the His$_6$.MOCRtev.MamP cassette from pMOCR-MamP with the MamP Ex F4/R2 primers and inserting into the NcoI-HindIII site of pCWori-OmpA.MamP. The plasmid pMOCR-MamP was constructed by SLIC. The SLIC-compatible pMOCR plasmid was linearized through SspI digestion and assembled with MamP amplified from pAK262 with MamP LIC F1/R1 (QB3 Macrolab, UC Berkeley).

pCWori-OmpA.His₆.TRXtev.MamP. The pCWori-OmpA.His$_6$.TRXtev.MamP vector was constructed by amplification of the His$_6$.TRXtev.MamP cassette from pET-His$_6$.TRXtev.MamP with the MamP Ex F5/R2 primers and insertion into the NcoI-HindIII site of pCWori-OmpA.sLipA. The plasmid pET-His$_6$.TRXtev.MamP was constructed by SLIC. A SLIC-compatible pTRX vector was linearized through SspI digestion and ligated with MamP was amplified from pAK262 from MamP LIC F1/R1. (QB3 Macrolab, UC Berkeley).

pCWori-OmpA.His₆.MBPtev.MamP. An MBP domain was fused to MamP by gene splicing by overlap extension (SOE). The His$_6$.MBPtev fragment was amplified from pSV272.1 using the MamP Ex F6/R3 primers and the MamP fragment was amplified from pMocr-MamP using the MamP Ex F7/R1 primers. The individual pieces were assembled using the MamP Ex F6/MamP Ex R1 primers. The product was then inserted into the NcoI-HindIII site of the pCWOri-OmpA.MamP vector.

pET29a-OmpA.His₆.MOCRtev.MamP. The pET29a-OmpA.His$_6$.MOCRtev.MamP vector was constructed by amplification of the OmpA.His$_6$.Mocr.MamP cassette from pCWori-OmpA.His$_6$.MOCRtev.MamP with the MamP Ex F8/R4 primers and inserting into the XbaI-XhoI site of pET29a..

pET29a-OmpA.His₆.MBPtev.MamP. The pET29a-OmpA.His$_6$.MBPtev.MamP vector was constructed by amplification of the OmpA.His$_6$.MBPtev.MamP cassette from pCWori-OmpA.His$_6$.MBPtev.MamP with the MamP Ex F8/R4 primers and insertion into the XbaI-XhoI site of pET29a-OmpA.His$_6$.MOCRtev.MamP.

Transformation of *M. magneticum* AMB-1. Plasmids for complementation or gene disruption were introduced into AMB-1 by conjugative transfer from an *E. coli* WM3064 donor strain using literature methods as described [*40*]. The plasmid to be transferred was first

transformed into *E. coli* WM3064 by electroporation and plated for growth overnight at 37ºC on LB agar supplemented with the appropriate antibiotic (Km, 100 µg/mL; Cb, 100 µg/mL) and DAP (300 µM). Individual colonies were inoculated into LB (5 mL) containing antibiotic and DAP and grown overnight at 37ºC with rotary shaking (200 rpm). *E. coli* cell cultures (500 µL) were then pelleted by brief centrifugation (14,000 × g) for 1 min at room temperature. The pellets were washed twice with LB DAP (0.5 mL) before resuspending in LB DAP (200 µL). The AMB-1 recipient strain was prepared by inoculation of cells from a freezer stock into a sealed-cap conical tube (50 mL) containing Magnetic Growth media (MG media, 50 mL). All MG media described in this document is prepared according to literature methods and supplemented with iron malate solution (100× stock made from 3 mM $FeCl_3$ and 9 mM DL-malic acid) and Wolfe's vitamin solution [*40*]. After 2 d growth at 30ºC without agitation, the entire culture volume was pelleted by centrifugation (14,000 × g) for 15 min at 4ºC and resuspended in MG (600 µL). One-third of the resuspended AMB-1 pellet was added to the resuspended *E. coli* pellet (200 µL), the cells were mixed gently, pelleted by brief centrifugation (14,000 × g) for 10 min at room temperature, and resuspended in MG (200 µL). The cells were plated together onto MG DAP agar. The plates were first incubated at room temperature for 1 h before transferring into a sealed microaerobic jar (Oxoid, Ltd.; Basingstoke, UK) at 30ºC for an additional 2-4 h. The jar was evacuated with vacuum until the pressure valve read -0.6 bar and was then refilled with N_2 to a pressure of +0.2 bar. The positive pressure was relieved by venting before the jar was sealed at 0 bar. After this incubation, cell mixtures were scraped off the MG DAP agar plates with a sterile inoculating loop and streaked onto fresh MG agar plates supplemented with the appropriate antibiotic (Km, 15 µg/mL; Cb, 20 µg/mL). These plates were incubated in the microaerobic jar for 4-6 d until colonies could be visualized. Single colonies were inoculated into microcentrifuge tubes (1.5 mL, Eppendorf) completely filled with MG (1.5 mL) and supplemented with the appropriate antibiotic (Km, 10 µg/mL; Cb, 20 µg/mL) to yield primary cultures within 4-8 d of growth at 30ºC with no agitation. After a cell pellet developed in the primary culture, an aliquot of the primary culture (10 µL) was diluted (1:1000) into sealed anaerobic tubes (20 mL) with MG containing 20 mM HEPES pH 7.2 supplemented with the appropriate antibiotic (10 mL) and grown at 30ºC with no agitation until $OD_{400 \text{ nm}}$ = 0.1-0.25 (approximately 2 d) for the secondary culture.

Construction of *M. magneticum* AMB-1 Δ*mamT*ΔR9. The Δ*mamT* gene falls between two repeating regions of the *mamQRB* locus, which is known to cause recombination and subsequent loss from from the magnetosome island. Since the deletion of *mamT* alone appeared unstable to complementation, the Δ*mamT*ΔR9 strain (AK155) was used for further experiments in this study. The Δ*mamT*ΔR9 strain was generated by introduction of the non-replicating pAK334 gene disruption plasmid [*46*] via conjugative transfer from *E. coli* WM3064 in the ΔR9 genetic background (AK57) [*43*]), in which the downstream *mamQRB* has been removed from the MAI without causing a detectable phenotype in wild-type AMB-1. After initial selection of parental strains on kanamycin, primary cultures containing kanamycin and secondary cultures without antibiotic were prepared. For counterselection using the *sacB* gene, aliquots of the secondary cultures (100 µL and 1 mL) were plated on MG supplemented with sucrose (1% w/v) without antibiotic by spreading with glass beads on MG plates. After incubation for 4-6 d at 30ºC, individual colonies were inoculated into new primary cultures and screened for deletion of gene of interest without loss of the MAI using colony PCR [*46*].

Characterization of cellular magnetization (C_{mag}). Secondary AMB-1 cultures were grown in MG (10 mL) containing 20 mM HEPES pH 7.2 without agitation at 30°C in seal-capped anaerobic culture tubes (20 mL) with Ar-evacuated headspace to $OD_{400\,nm} = 0.2$ (~2 d). The culture C_{mag} was determined as previously described [*47*]. Briefly, $OD_{400\,nm}$ was measured on an Agilent 8000 UV-Visible spectrophotometer with a magnet parallel or perpendicular to the spectrometer beam and the ratio ($C_{mag} = A_{400\,nm,\,perpendicular}/A_{400\,nm,\,parallel}$) was calculated. The C_{mag} measurements were performed in biological triplicates with two technical replicates per colony using cultures from three independent growths or conjugations.

Transmission electron microscopy. Secondary AMB-1 cultures were grown in MG (10 mL) containing 20 mM HEPES pH 7.2 without agitation at 30°C in seal-capped anaerobic culture tubes (20 mL) with the headspace evacuated with Ar to $OD_{400\,nm} = 0.25$–0.3 (~2-3 d). An aliquot of cell culture (100–500 µL) was pelleted by brief centrifugation ($14,000 \times g$) for 10 min aerobically at room temperature and resuspended in MG (~10 µL). The cells were adsorbed onto 400-mesh copper grid coated with Formvar/Carbon (TedPella Inc.) and analyzed using a TECNAI 12 TEM (FEI) operating at 120 kV with a charge-coupled device camera (Gatan UltraScan, University of California at Berkeley Electron Microscope Laboratory). In each case, 20–50 cells, each containing 1–20 crystals, were analyzed. For each strain, >300 particles from >20 cells was analyzed for three different colonies from each biological replicate.

Fluorescence microscopy. Secondary AMB-1 cultures were grown in MG (10 mL) containing 20 mM HEPES pH 7.2 without agitation at 30°C in seal-capped anaerobic culture tubes (20 mL) with an Ar-evacuated headspace to $OD_{400\,nm} = 0.1$–0.2 (~ 1.5 d). An aliquot of cell culture (0.5 – 1.0 mL) was pelleted by brief centrifugation ($14,000 \times g$) for 5 min aerobically at room temperature and resuspended in MG (~200 µL). The cells were adsorbed onto pads of MG agarose (2% w/v) and GFP fluorescence was imaged on an API DeltaVision Elite deconvolution microscope (Applied Precision; Issaquah, WA) using the 100× oil objective with the FITC filter sets.

Immunostaining. Antibodies to MamP were raised by ProSci Inc. (Poway, CA) in rabbits using a synthetic peptide from MamP (QLEGAPMILAGPRPHGYR) conjugated to a carrier protein. Testing of these antibodies indicated that MamP could be detected to < 20 ng/lane using a 1:1000 dilution (*Figure 2.5*). AMB-1 cultures were grown without agitation in MG (10 mL) containing 20 mM HEPES pH 7.2 at 30°C in seal-capped anaerobic culture tubes (20 mL) evacuated with Ar to $OD_{400\,nm} = 0.2$ (~ 2d). Cells were pelleted by centrifugation ($9,800 \times g$) for 15 min and resuspended in 2×Laemmli buffer containing BME (5% v/v) (125 µL for 10 mL of culture at $OD_{400\,nm} = 0.2$). The cell suspension was heated at 70ºC for 15 min and centrifuged ($14,000 \times g$) for 10 min at room temperature to remove particulate matter. Samples (15 uL) were run on a 12% Bis-Tris SDS-PAGE gel at 150 V at 4ºC for 45-80 min. The gel was equilibrated in transfer buffer (50 mM Tris, 192 mM glycine, 20% v/v methanol, 0.05% w/v SDS) for 25 min before transferring at 50 V for 2 h to a pre-wetted PVDF membrane (Bio-Rad) using a BioRad Trans-Blot. All subsequent steps utilized a rocking agitator to provide mixing. The membrane was blocked for 2 h at room temperature in 5% w/v milk (Apex BioResearch Products, Research Triangle Park, NC) in TBST buffer (50 mM Tris, pH 8.0, 150 mM NaCl, 0.1% w/v Tween-20) followed by incubation with MamP primary antibodies (1:1000 dilution in TBST containing 5% w/v milk) at room temperature for 1.5 h. The membrane was washed in TBST (3×15 min) before incubating with Goat Anti-Rabbit IgG-HRP (Bio-Rad Laboratories,1:5000) at room temperature

for 1 h. The membrane was washed again TBST (3 × 15 min) before visualization with a Western Lightning Plus ECL kit (PerkinElmer; Waltham, MA) using a Bio-Rad Mini Trans-Blot Cell and Quantity One software.

Immunostaining of MamP.FLAG and FLAG.MamP was performed by growing $\Delta mamP$ + pAK262Amp-MamP.FLAG and $\Delta mamP$ + pAK262Amp-FLAG.MamP AMB-1 cultures without agitation in MG (1 L) containing 20 mM HEPES pH 7.2 and 20 μg/mL Cb at 30°C in seal-capped buffer bottle (1 L) evacuated with Ar to $OD_{400\,nm} = 0.2$ (~ 2d). Cells were pelleted by centrifugation ($9,800 \times g$) for 15 min for a total of 0.5 g of cells. The cells were resuspended in AMB-1 lysis buffer (5 mL of 50 mM Tris pH 7.4, 150 mM NaCl, 1 mM EDTA, 0.1% Triton X-100, 0.1 mM PMSF, 1 Complete tablet). The cells were passed twice through a French Pressure cell (Thermo Scientific; Waltham, MA) at 14,000 psi. The lysate was centrifuged at $15,300 \times g$ for 20 min at 4°C to separate the soluble and insoluble fractions. The soluble fraction was applied to ANTI-FLAG M2 affinity gel (Sigma-Aldrich, 100 μL) equilibrated with ANTI-FLAG resin wash buffer (50 mM Tris-HCl pH 7.4, 150 mM NaCl, 1 mM EDTA) and incubated with gentle shaking at 4ºC for 1 hr. The resin was washed with 3 × 1 mL of wash buffer by spinning and resuspending in 1.5 mL microfuge tubes for 1 min at $5,000 \times g$. Protein was eluted from the column by incubating for 10 min in 3× FLAG peptide (Sigma-Aldrich, 150 ng/μL in ANTI-FLAG resin wash buffer). Samples were resuspended in 2× Laemmli buffer containing BME (5% v/v). The cell suspension was heated at 70ºC for 15 min and centrifuged ($14,000 \times g$) for 10 min at room temperature to remove particulate matter. Samples (15 uL) were run on a 12% Bis-Tris SDS-PAGE gel at 150 V at 4ºC for 45-80 min. The gel was equilibrated in transfer buffer (50 mM Tris, 192 mM glycine, 20% v/v methanol, 0.05% w/v SDS) for 25 min before transferring at 50 V for 2 h to a pre-wetted PVDF membrane (Bio-Rad) using a BioRad Trans-Blot. All subsequent steps utilized a rocking agitator to provide mixing. The membrane was blocked for 2 h at room temperature in 5% w/v milk (Apex BioResearch Products, Research Triangle Park, NC) in TBST buffer (50 mM Tris, pH 8.0, 150 mM NaCl, 0.1% w/v Tween-20) followed by incubation with Monoclonal ANTI-FLAG M2 (Sigma-Aldrich, 1:8500 dilution) in TBST containing 5% w/v milk at room temperature for 1.5 h. The membrane was washed in TBST (3 × 15 min) before incubating with Goat Anti-Mouse IgG-HRP (Bio-Rad Laboratories,1:5000 dilution) at room temperature for 1 h. The membrane was washed again TBST (3 × 15 min) before visualization with a Western Lightning Plus ECL kit (PerkinElmer; Waltham, MA) using a Bio-Rad Mini Trans-Blot Cell and Quantity One software.

Heterologous expression of His_6.MBP.MamP. 2 × YT (4 × 1 L) containing Km (50 μg/mL) and Cm (35 μg/mL) in a 2.8 L Fernbach baffled shake flask was inoculated with 10 mL of an overnight 50 mL LB culture of freshly transformed *E. coli* C43(DE3) containing the appropriate overexpression plasmid and the cytochrome *c* maturation plasmid, pEC86 [*48*]. The cultures were grown at 30°C and 200 rpm to $OD_{600} = 0.8$ to 0.9, at which point cultures were induced to express protein with IPTG (10-50 μM) and shaken overnight at 30°C and 200 rpm. Cell pellets were harvested by centrifugation at $5,524 \times g$ for 7 min at 4°C and immediately lysed for protein purification.

Purification of MamP. Harvested cell pellets were thoroughly resuspended (5 mL/g wet cell paste) by gentle pipetting in Periplasmic Lysis Buffer (20% w/v sucrose, 1 mM EDTA, 50 mM potassium phosphate, pH 8.0) supplemented with a Complete EDTA-free protease inhibitor cocktail (1 tablet/50 mL buffer, Roche) and PMSF (0.5 mM). A combined lysozyme/osmotic shock strategy was employed to prepare the periplasmic fraction by addition of lysozyme (0.5

mg/mL) and incubation at room temperature for 15 min, followed by the addition ice-cold water (1 vol) and mild shaking (100 rpm) for 15 min in tubes resting horizontally on ice. The soluble periplasmic fraction was separated from the remaining cellular debris by centrifugation at 10,414 $\times$ g for 15 min at 4°C. All subsequent steps were carried out at 4°C.

Isolation of the His$_6$.MBPtev.MamP fusion. Periplasmic fractions from the different flasks were then pooled and stirred with DNase (~ 3 units/g wet cell paste) for 1 h. MgCl$_2$ (5 mM) was added to the combined periplasmic fraction to reduce stripping of the Ni-NTA resin by EDTA, while sodium chloride (150 mM) was added to minimize non-specific binding. The periplasmic lysate was applied to Ni-NTA Agarose (Qiagen, 20-25 mL), equilibrated with Ni-NTA Buffer A (50 mM potassium phosphate, pH 8.0, 300 mM NaCl, 10 mM imidazole), by batch binding for 30 min on a rocking agitator. The resin was then transferred into a column (2.5 $\times$ 10 cm, BioRad) and washed with Ni-NTA Buffer A (3 column vol), with subsequent elution with Ni-NTA Buffer B (50 mM potassium phosphate, pH 8.0, 300 mM NaCl, 250 mM imidazole; 2-3 column vol). The eluate was concentrated to <10 mL in an Amicon Ultrafiltration Stirred Cell (Millipore) fit with a 10 kD MWCO YM regenerated cellulose membrane (Millipore).

TEV cleavage. To the concentrated Ni-NTA eluate, His-tagged TEV protease (~ 1 mg TEV per 40-50 mg of His$_6$-MBP-MamP fusion) and the resulting mixture was dialyzed (Spectra/Por Biotech Cellulose Ester Dialysis Membrane, 3,500-5,000 MWCO; Spectrum Laboratories) against 50 mM potassium phosphate, 300 mM NaCl, 1 mM DTT, pH 8.0 overnight (3 $\times$ 1:75 dilution).

MamP isolation. The dialyzed mixture was then applied to the same Ni-NTA agarose column, washed and re-equilibrated with Ni-NTA Buffer A (~ 10 column vol). MamP was washed from the column with Ni-NTA Buffer A (3 column vol) and concentrated to <10 mL in an Amicon Ultrafiltration Stirred Cell using a 10 kD MWCO YM regenerated cellulose membrane (Millipore). To remove residual and endogenous untagged MBP, the MamP sample was then applied to an Amylose column (2 mL), equilibrated with 50 mM potassium phosphate, 300 mM NaCl, 1 mM EDTA, pH 8.0. MamP was recovered from this column by washing with the same buffer (3-5 column vol). The MamP solution was concentrated further (<2 mL) in a 3 kD MWCO Amicon Ultra-15 Centrifugal Filter Unit (Millipore) by centrifugation (5,000 $\times$ g) at 4°C before loading onto a HiLoad 16/20 Superdex 200 column (GE Healthcare) attached to an ÄKTApurifier FPLC (1 mL/min; GE Healthcare). The column was equilibrated with and run in 50 mM potassium phosphate, pH 8.0, 150 mM NaCl. Fractions (2 mL) were monitored by A$_{407\,nm}$ and those with A$_{407\,nm}$ > 0.1 were further characterized by their Rz value (A$_{407\,nm}$/A$_{280\,nm}$) using a Beckman Coulter DU-800 spectrophotometer before pooling. Fractions with Rz $\geq$ 7.0 were concentrated five-fold using 3 kD MWCO Amicon Ultra-0.5 Centrifugal Filter Unit and stored at -80°C with the addition of glycerol (60% v/v stock) to a final concentration to 10% v/v without further purification. Those fractions with Rz values between 5.0 and 7.0 were pooled and exchanged into Q buffer (100 mM Tris, pH 8.0) by overnight dialysis (Spectra/Por Biotech Cellulose Ester Dialysis Membrane, 3,500-5,000 MWCO, 3 $\times$ 1:75 dilution). for an additional purification step. The sample (~5 mL) was chromatographed on a HiTrap Q HP column (GE Healthcare, 5 mL) using a linear gradient from 0 to 0.5 M NaCl over 40 column volumes (1 mL/min). These fractions were then concentrated and stored at -80°C as described above. The extinction coefficient of the MamP

monomer (Rz = 7.1) at 280 nm was measured to be 46,100 $M^{-1}cm^{-1}$ (AAA Service Laboratory; Damascus, OR) and is used to calculate the MamP concentration. The extinction coefficient for the Soret peak of the diheme-loaded $MamP_{ox}$ monomer was measured to be 331,100 $M^{-1}cm^{-1}$ at 407 nm using the protein concentration determined by acidolysis.

Heme staining of SDS-PAGE gels. Samples were prepared for loading onto a gel by incubation for 15 min at room temperature with a Laemmli sample buffer with β-mercaptoethanol omitted (4× stock: 0.25 M Tris-HCl, 2% SDS, 40% glycerol, 0.04% bromophenol blue). The sample was analyzed by SDS-PAGE at room temperature following literature protocol [10] on a standard 12 w/v% acrylamide gel at 150 V for approximately 60-80 min. The gel was then soaked at room temperature in the dark with 3,3′,5,5′-tetramethylbenzidine (2 mM) in 0.25 M sodium acetate, pH 5.0 containing 30% v/v methanol for 2 h on an orbital shaker. H_2O_2 (60 mM) was added to initiate the development of blue bands within 15 min and stopped by rinsing with ddH_2O. The gels were then stained with Coomassie using standard protocols to visualize total protein content.

Preparation of MamP for nanoelectrospray ionization mass spectroscopy (Nano-ESI-MS). Purified MamP (10-15 μM; 15 μL) was exchanged into 50 mM ammonium bicarbonate, pH 8.0, by repeated concentration/dilution cycles in an 3 kDa MWCO Amicon Ultra-0.5 Centrifugal Filter Unit (14,000 × g) at 4°C, until the estimated non-volatile salt concentration was in the sub-micromolar range (typically 10-12 cycles). On the final concentration/dilution cycle, ddH_2O was used to dilute the protein to a final ammonium bicarbonate concentration of 10 mM before concentrating MamP to a final concentration of ~5 μM. The buffer-exchanged protein samples were immediately submitted for nano-ESI-MS analysis in the QB3/Chemistry Mass Spectrometry Facility at UC Berkeley. The samples were acidified just prior to collecting spectra by addition of 10× formic acid stock to a final concentration of 1% v/v.

Inductively-coupled plasmon resonance-atomic emission spectroscopy (ICP-AES) of MamP. Serial dilutions of a ferric nitrate stock solution (1,000 mg/L) in ddH_2O were used to prepare six solutions between 50 μg/L and 1,000 μg/L, from which a standard curve was generated. MamP was dialyzed (3×10^{-2}, for a 10^{-6} final dilution of the original buffer) overnight in 50 mM potassium phosphate, 150 mM NaCl, pH 7.5 at 4°C. The protein was diluted to a concentration intended to yield ~300 μg iron/L (assuming 100% cofactor occupancy). Samples were analyzed on an Optima 7000 DV ICP-OES (Perkin Elmer; Fremont, CA) using Ar as the carrier gas at a sample flow rate of 1 mL/min (RF power, 1200 watts; plasma gas flow, 15 L/min; auxiliary gas flow; 0.2 L/min; nebulizer gas flow, 0.8 L/min). From this experiment, the extinction coefficient of the Soret band for the diheme-loaded $MamP_{ox}$ monomer was determined to be 348,700 $M^{-1}cm^{-1}$ at 407 nm and the extinction coefficient for the protein absorption band was determined to be 48,200 $M^{-1}cm^{-1}$ at 280 nm.

Structural comparison between MamP from AMB-1 and homolog from MO-1. Phyre2 [49] was used to predict the structure of MamP based on the structure of the MO-1 homolog [39]. UCSF Chimera was used to visualize the protein structural comparison [50]. Protein BLAST was used to compare the full length structure of both proteins (MamP AMB-1, 275 residues; MamP MO-1, 260 residues) [51] and determine the percent homology of the proteins.

Spectrochemical titration of MamP. Spectrochemical titrations were carried out on MamP in a 1.6 mL cell consisting of a 1 cm semi-micro quartz magnetic stir cell with an anaerobic seal

and cap (Starna Cells, Inc; Atascadero, CA) and stir bar using literature methods [52]. MamP was deoxygenated in an anaerobic glove box (Controlled Atmosphere Chamber; Plas Labs; Lansing, MI) under a 90:10 Ar:H_2 atmosphere by passing an aliquot of protein (400 µL) over a PD-10 desalting column (GE Healthcare Life Sciences) equilibrated with titration buffer (Ar-sparged 20 mM Tris, 50 mM KCl, 5% (v/v) ethylene glycol, pH 7.5). MamP (1 mL of ~ 22 µM) was transferred into the cell followed by the Ar-sparged redox mediator cocktail (toluylene blue, 5 µM; hexaammineruthenium(III) chloride, 16.5 µM; p-benzoquinone, 16.5 µM; 3′-chloroindophenol, 10 µM; methyl viologen, 7.5 µM; anthraquinone-2-sulfonic acid, 10 µM; 2-hydroxy-1,4-naphthoquinone, 10 µM). The cuvette was then outfitted with the electrodes and sealed from air before removing from the glove box. The reaction was maintained under N_2 (g) for the duration of the experiment. The oxidant solution was prepared in the glove box by dissolving solid ODQ in Ar-sparged DMSO (10 mM) and then diluting into titration buffer (0.5 mM). The potential of the protein solution was measured using an oxidation-reduction potential microelectrode (MI-800, Microelectrodes, Inc.; Bedford, NH) and Ag/AgCl reference microelectrode (MI-402, Microelectrodes, Inc.) connected to a basic pH/mV/ORP meter (Orion 420Aplus, Thermo Scientific; Waltham, MA). Protein was initially reduced step-wise using excess sodium dithionite introduced via syringe until the potential stabilized and UV-Vis spectrum showed the protein to be fully reduced. After reduction, ODQ (0.2-1 µL; 0.5 mM) was titrated in with stirring to oxidize MamP. The reaction was allowed to equilibrate for 15 min after each addition. UV-visible spectra were collected at each potential on an Agilent 8453 diode-array spectrophotometer equipped with an Agilent 8909A stirring module (Santa Clara, CA). The fraction of reduced MamP was monitored by ΔA 551 nm, and the midpoint reduction potential was determined by fitting to the following equation [53]:

$$Y = \frac{e^{-96500 \times (m_0 - m_1)/2477.572}}{1 + e^{-96500 \times (m_0 - m_1)/2477.572}}$$

Titration of MamP$_{red}$ with oxygen. Oxygen titration of MamP was carried out in a 1.6 mL cell consisting of a 1 cm semi-micro quartz magnetic stir cell with an anaerobic seal and cap (Starna Cells, Inc; Atascadero, CA) and stir bar. MamP was deoxygenated in an anaerobic glove box (Controlled Atmosphere Chamber; Plas Labs; Lansing, MI) under a 90:10 Ar:H_2 atmosphere by passing an aliquot of protein (90 µL) over a PD-10 desalting column (GE Healthcare Life Sciences) equilibrated with titration buffer (Ar-sparged 50 mM HEPES, pH 7.5). The protein solution was brought up to a volume of 1 mL with titration buffer to a final concentration of 1.3 µM (based on heme content). The protein was transferred to the cell and sealed from air before removing from the glove box. The reaction was maintained under N_2 for the duration of the experiment. Protein was initially reduced step-wise using excess sodium dithionite introduced via syringe until the potential stabilized and UV-Visible spectrum showed the protein to be fully reduced. After reduction, air-saturated 50 mM HEPES, pH 7.5 solution (O_2 concentration 260 µM) was titrated in with stirring to oxidize MamP. The reaction was allowed to equilibrate for 1 min after each addition. UV-visible spectra were collected at each addition on an Agilent 8453 diode-array spectrophotometer equipped with an Agilent 8909A stirring module (Santa Clara, CA). The MamP was considered completely oxidized when the $A_{551\ nm}$ and $A_{407\ nm}$ bands remained unchanged with the addition of O_2.

Reduction of MamP$_{ox}$ by iron(II). Resting MamP (MamP$_{ox}$) was deoxygenated in an anaerobic glove box (Controlled Atmosphere Chamber; Plas Labs; Lansing, MI) under a 90:10 Ar:H$_2$ atmosphere by passing an aliquot of protein (23 µM based on heme content, 100 µL) over a PD-10 desalting column (GE Healthcare Life Sciences) equilibrated with buffer (Ar-sparged 50 mM HEPES, pH 7.5). Ammonium iron(II) sulfate (25 mM) was dissolved in the glove box in the same buffer and used as the stock solution for iron(II) addition. MamP was diluted to a final volume of 1 mL and transferred into an anaerobic quartz cuvette. The MamP and iron(II) solutions were sealed from air before removing from the glove box. The UV-Visible spectrum of MamP$_{ox}$ was collected on an Agilent 8453 diode-array spectrophotometer before collecting the UV-visible spectrum of MamP$_{red}$ after the addition of the iron solution to a final concentration of 1 mM.

***In vitro* iron mineralization.** MamP (5-25 µM, 500 µL) was exchanged from the phosphate storage buffer into HEPES reaction buffer (50 mM HEPES pH 8.0, 100 mM NaCl) by concentrating and diluting the protein five times in 3,000 MWCO Amicon centrifuge filters (0.5 mL) for a total dilution of ~1:3,125 of the original buffer, as the autooxidation of Fe(II) in phosphate buffer is high [*54*]. Additional reaction buffer (15 mL) was transferred into a 20 mL borosilicate scintillation vial (Fisherbrand), sealed with a septum (Sigma-Aldrich Suba-Seal #33), and degassed by bubbling Ar gently through the solution with a needle (21G × 1.5 in, BD PrecisionGlide) with a second needle as a purge. Evaporation was minimized by passing Ar through a bubbler filled with ddH$_2$O between the gas tank and the reaction vial. Ammonium Fe(II) sulfate hexahydrate (125 mg) was used the ferrous iron source because of its air stability in salt form and transferred as a solid into a glass vial (15 × 45 mm borosilicate threaded vials, Fisherbrand) and sealed with a septum (Sigma-Aldrich Suba-Seal #13). The headspace of the vial was then evacuated with Ar using a needle. After 80 min of degassing both the reaction buffer and the solid Fe(II), degassed reaction buffer (2 mL) was introduced to the vial containing the ammonium Fe(II) sulfate solid using an argon-purged glass syringe to a final concentration of 160 mM and dissolved with gentle agitation.

Empty glass reaction vials (15 × 45 mm borosilicate threaded vials, Fisherbrand) were sealed with septa (Sigma-Aldrich Suba-Seal #9) and degassed with Ar for 30 min using a needle. Reaction buffer (425 µL) was then added with an Argon-purged airtight glass syringe, followed by Fe(II) (150 µL, 40 mM final concentration). All vials were kept under partial Ar pressure after introduction of Fe(II) by delaying the removal of the Ar needle for an additional min after removal of the venting needles from the reaction vials. At this time, undegassed MamP (25 µL) or reaction buffer (25 µL) was immediately introduced via Ar-purged glass syringe to a final concentration of 2.5 µM to initiate the reaction (t = 0 min) and agitated gently to mix. Over the course mineralization reaction, the vials were agitated gently at 10 min intervals and with ambient air (20 µL) was introduced via a glass syringe at t = 10 min and 20 min to turn over MamP.

Mineralization reactions at different pH values (6.0, 7.5, 9.0) were performed exactly as described above with the following modification: MamP for all three reactions was buffer exchanged into pH 7.5 reaction buffer and subsequently distributed into HEPES reaction buffer at pH 6.0, 7.5, or 9.0.

2.3. Results and discussion

Genetic characterization of the physiological function of mamP and mamT in AMB-1. The genetic analysis of the MAI of AMB-1 implicate both *mamP* and *mamT* as key components

involved in the mineralization of iron [46]. Based on the essential but distinct roles of the MamP and MamT proteins revealed by these knockout studies [43], we were interested in further exploring their physiological and biochemical function. Towards this goal, we sought to probe the *in vivo* role of the heme-binding sites of MamP and MamT, which are proposed to enable the transfer of redox equivalents to or from mineralizing iron species within the magnetosome [38]. As such, each of the two CXXCH *c*-type cytochrome motifs found within both MamP and MamT were either individually or doubly mutated to AXXAA by sequential site-directed mutagenesis to remove the two cysteines required for covalent heme attachment as well as the coordinating histidine. The corresponding $mamP_{\Delta heme1}$, $mamP_{\Delta heme2}$, $mamP_{\Delta heme}$, $mamT_{\Delta heme1}$, $mamT_{\Delta heme2}$, and $mamT_{\Delta heme}$ mutants were then expressed from a constitutive *tac* promoter on a pAK(Amp^R)-derived plasmid in the appropriate $\Delta mamP$ or $\Delta mamT\Delta R9$ background.

Initial characterization of the *mamP* and *mamT* heme mutant strains was carried out using a qualitative assay for cellular magnetization (C$_{mag}$), which measures the ability of an oblong cell to turn in the presence of an external magnetic field using the ratio of light scattered when this field is placed parallel or perpendicular to the axis of the spectrophotometric cell. The parental $\Delta mamP$ and $\Delta mamT\Delta R9$ strains exhibit a strong magnetic defect with C$_{mag}$ measurements of 1.2 ± 0.1 and 1.2 ± 0.05 respectively, where 1.0 indicates no cellular magnetization and 2.0 represents the characteristic C$_{mag}$ observed for wild-type *M. magneticum* AMB-1 with full magnetite chains [47] (*Figure 2.1*). Complementation of the chromosomal deletion of *mamP* or *mamT* with the corresponding plasmid-borne wild-type gene subsequently rescues cellular magnetization to wild-type levels ($\Delta mamP$ + *mamP*, C$_{mag}$ = 2.0 ± 0.2; $\Delta mamT\Delta R9$ + *mamT*, C$_{mag}$ = 1.97 ± 0.04). In contrast, we found that deletion of one or both of the hemes was sufficient to impair magnetite formation with little to no recovery of magnetic response compared to wild-type upon complementation (*Figure 2.1*).

Transmission electron microscopy (TEM) was then used to analyze the iron oxide particles produced by these strains in more detail. Previous studies have shown that deletion of either *mamP* or *mamT* from AMB-1 causes a severe iron mineralization defect, although the expected number of magnetosome vesicles are observed and remain arranged in a linear fashion [46]. Interestingly, the morphology of the crystals formed in $\Delta mamP$ and $\Delta mamT$ cells differ considerably, suggesting that these two redox proteins play different roles in magnetosome biogenesis [37, 38]. Ablation of one or more of the heme sites of MamP yields a phenotype indistinguishable from the $\Delta mamP$ strain with mostly small, flake-like crystals of uncertain iron oxide phase along with 1-2 wild type or larger-sized crystals per cell (*Figure 2.2* and *Figure 2.3*). Although the MamT heme mutants behave similarly to the corresponding MamP mutants with respect to cellular magnetization, the TEM images reveal key differences with regard to iron mineralization as the crystals observed only in the MamT mutants are small, elongated, and dumbbell-shaped, which suggests twinning (*Figure 2.2 and Figure 2.3*). Overall, these results are consistent with a model where the heme redox sites of both MamP and MamT are critical for mineralization as the mutation of a single site yields a phenotype that cannot be differentiated from the deletion strain. The difference in the crystal morphologies between the MamP and MamT heme mutants further suggests that the changes in mineralization behavior related to the ablation of the heme sites is related more to the loss of MamP or MamT function, respectively, rather than a more general defect in magnetosome biogenesis.

As the loss of MamP and MamT function could lead to a variety of complex biological outcomes, we have carried out additional control experiments as a simple check for large-scale changes in magnetosome resulting from these mutations. For example, the deletion of certain magnetosome proteins, such as MamE, can result in the mislocalization of other proteins and severe downstream magnetic defects in the deletion strains [55]. To test whether the *mamP* or *mamT* deletions cause a similar mislocalization of key magnetosome proteins, C-terminal GFP fusions of MamC, MmsF, MamF, and MamI were expressed in wild type, ΔR9, Δ*mamP*, and Δ*mamT*ΔR9 strains. Fluorescence microscopy studies showed that all GFP fusions localized as a filament at midcell in Δ*mamP* and Δ*mamT*ΔR9 as consistent with wild-type *M. magneticum* AMB-1, which suggests that localization of these proteins to the magnetosome is not altered (*Figure 2.4*). In addition, variation in MamP expression levels has been observed to lead to differences in iron mineralization [56]. To examine this possibility, antibodies to MamP were raised for immunostaining experiments, which indicated that MamP mutants are expressed at levels consistent with or higher than wild-type protein (*Figure 2.5*). While we cannot eliminate the possibility that removal of the heme sites of MamP and MamT results in misprocessing, mislocalization, or structurally destabilization of MamP, MamT, or other essential magnetosome components, we hypothesize that the CXXCH motifs serve a critical function in the mineralization process of AMB-1.
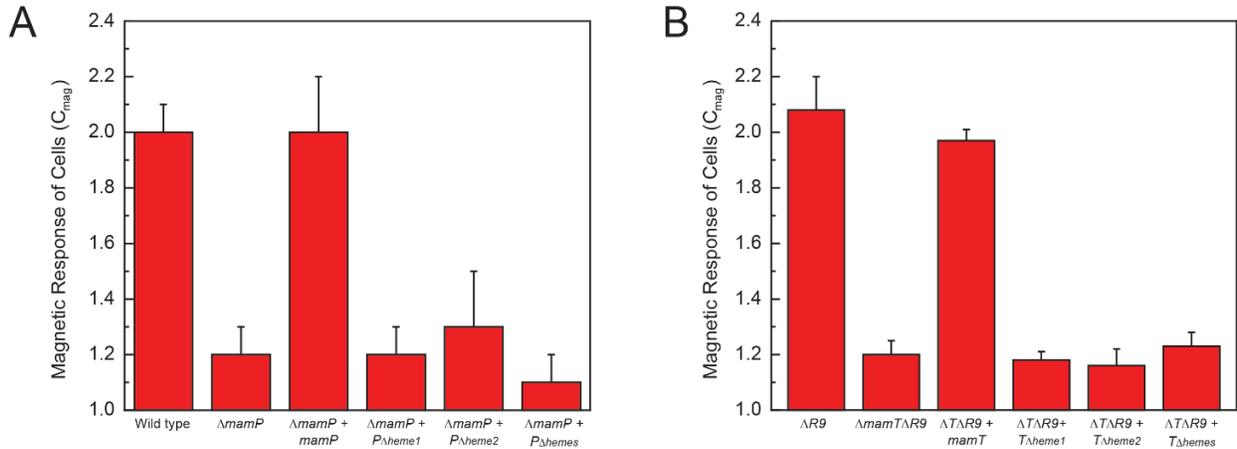
Figure 2.1. *Analysis of the magnetic response (C_{mag}) of MamP and MamT heme mutants in vivo. (A) C_{mag} measurements of M. magneticum AMB-1 wild-type (2.0 ± 0.1) and ΔmamP (1.2 ± 0.1) strains compared to the ΔmamP strains complemented with wild-type mamP (2.0 ± 0.2), mamP$_{Δheme1}$ (1.2 ± 0.1), mamP$_{Δheme2}$ (1.3 ± 0.2), and mamP$_{Δheme}$ (1.1 ± 0.1) plasmids. (B) C_{mag} measurements of M. magneticum AMB-1 ΔR9 (2.1 ± 0.1) and ΔmamTΔR9 (1.2 ± 0.05) strains compared to the ΔmamTΔR9 strains complemented with wild-type mamT (1.97 ± 0.04), mamT$_{Δheme1}$ (1.18 ± 0.03), mamT$_{Δheme2}$ (1.16 ± 0.06), and mamT$_{Δheme}$ (1.23 ± 0.05) plasmids. All data are reported as the mean ± s.d. of three biological replicates of technical duplicates (n = 6).*
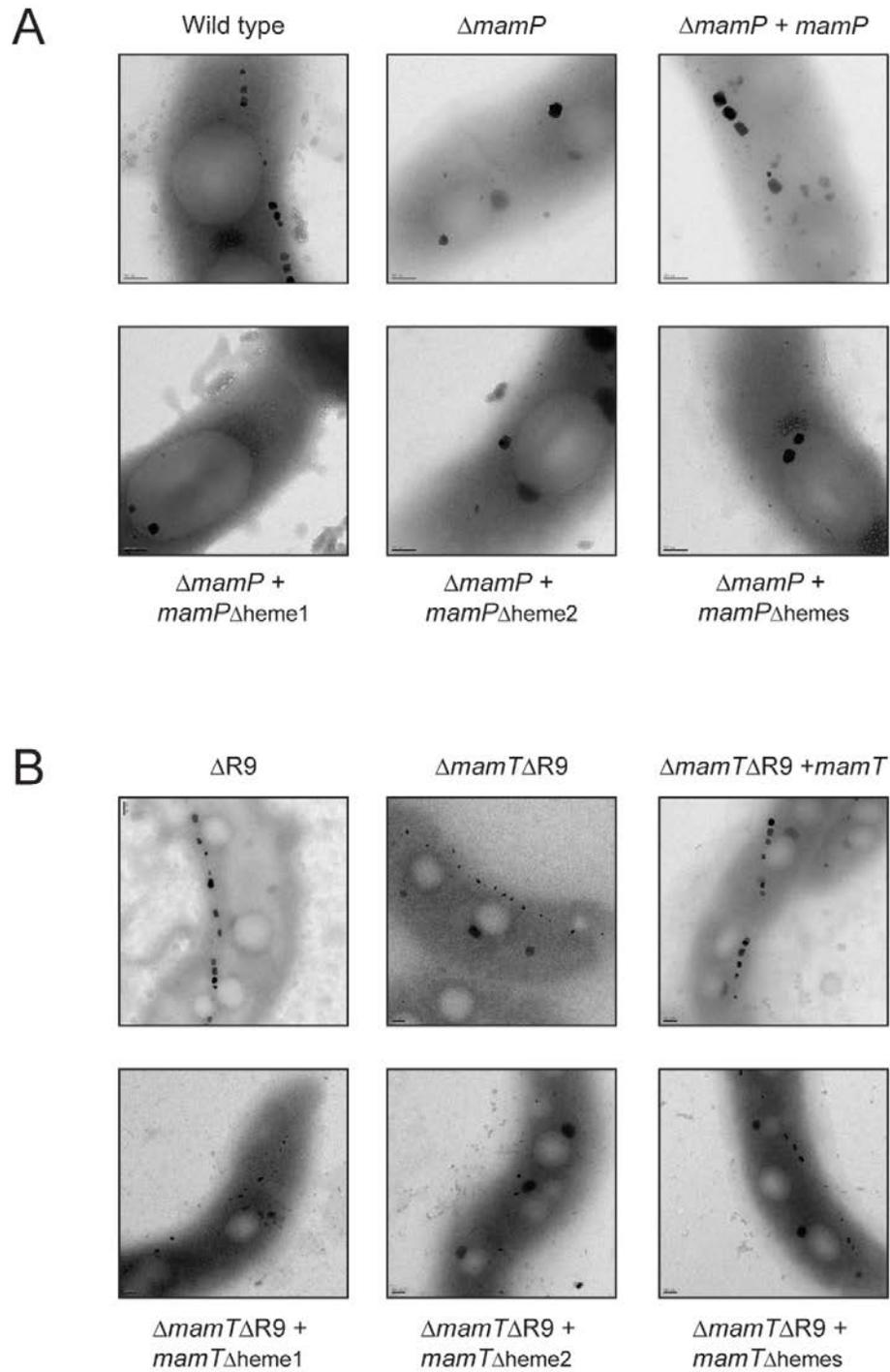
Figure 2.2. *TEM images of iron oxide particles produced by MamP and MamT heme mutants* in vivo. *(A) Representative TEM images of* M. magneticum *AMB-1 wild-type and ΔmamP strains compared to the ΔmamP strain complemented with wild-type mamP, mamP$_{Δheme1}$, mamP$_{Δheme2}$, and mamP$_{Δheme}$ genes. (B) Representative TEM images of* M. magneticum *AMB-1 wild-type and ΔmamP strains compared to the ΔmamTΔR9 strain complemented with wild-type mamT, mamT$_{Δheme1}$, mamT$_{Δheme2}$, and mamT$_{Δheme}$ genes.*
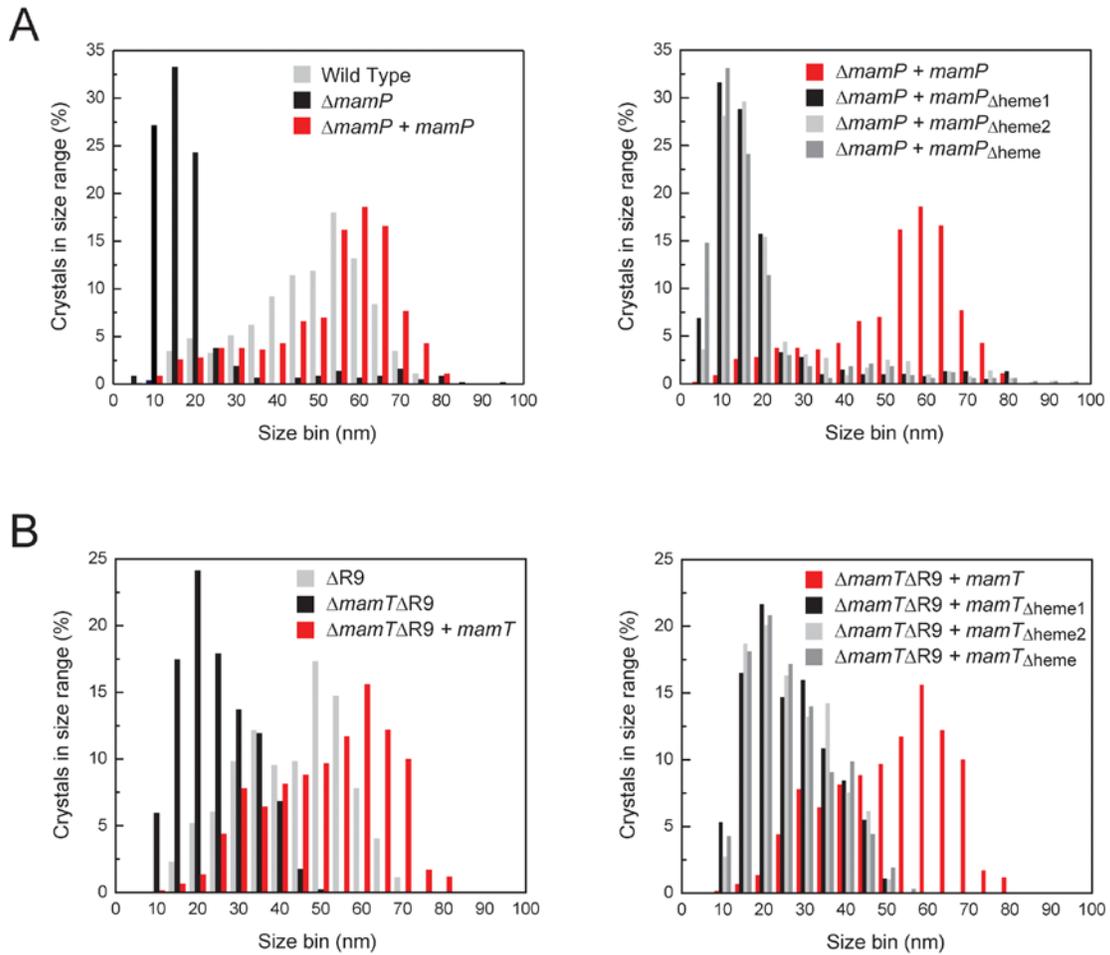
Figure 2.3. *Statistical analysis of iron oxide particles produced by MamP and MamT heme mutants in vivo. (A) Histograms of crystal sizes observed in the* M. magneticum *AMB-1 control strains (wild-type, 455 particles in 30 cells; ΔmamP, 425 particles in 38 cells; ΔmamP + mamP, 469 particles in 40 cells) strains compared to the ΔmamP mutant complemented with the different MamP heme variants (ΔmamP + mamP$_{\Delta heme1}$; 389 particles, 31 cells; ΔmamP + mamP$_{\Delta heme2}$; 638 particles, 41 cells; ΔmamP + mamP$_{\Delta hemes}$, 332 particles, 34 cells). Histograms are separated into two different plots for clarity. (B) Histograms of crystal sizes observed in the* M. magneticum *AMB-1 control strains (ΔR9, 346 particles in 28 cells; ΔmamTΔR9, 452 particles in 21 cells; ΔmamTΔR9 + mamT, 589 particles in 35 cells) compared to the ΔmamTΔR9 mutant complemented with the different MamT heme variants (ΔmamTΔR9 + mamT$_{\Delta heme1}$, 545 particles in 34 cells; ΔmamT + mamT$_{\Delta heme2}$, 583 particles in 37 cells; ΔmamTΔR9 + mamT$_{\Delta hemes}$, 629 particles in 31 cells). Histograms are separated into two different plots for clarity.*
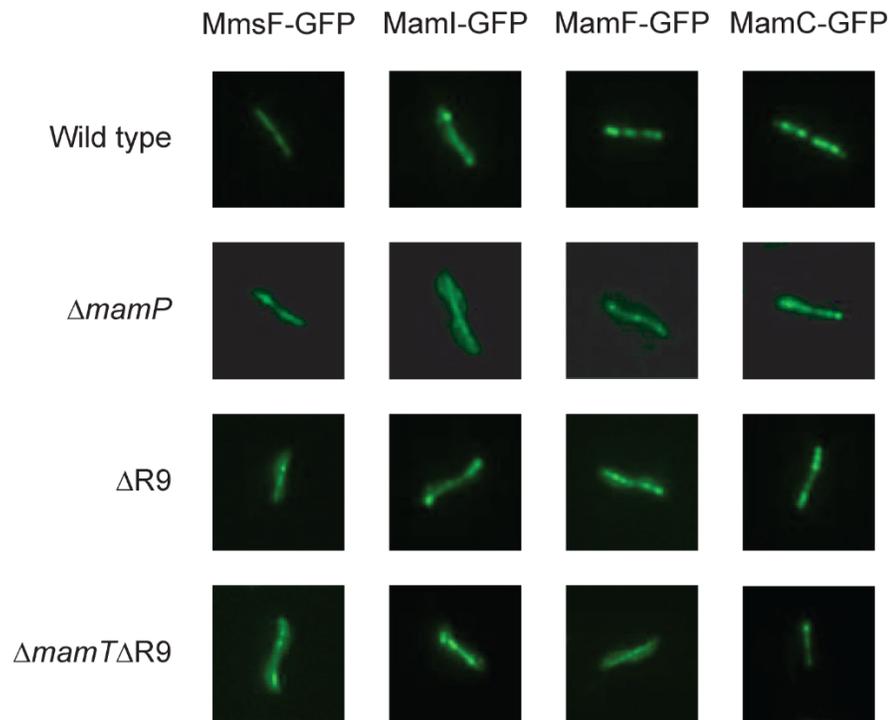
Figure 2.4. *Monitoring the localization of key magnetosome proteins in M. magneticum AMB-1 deletion strains using fluorescence microscopy of GFP fusions. Plasmids expressing MmsF-GFP, MamI-GFP, MamF-GFP, and MamC-GFP were introduced into M. magneticum AMB-1 wild type, ΔmamP, ΔR9 and ΔmamTΔR9 strains by conjugation. Secondary cultures were imaged by fluorescence microscopy to visualize the GFP fusion proteins. The midcell localization of these proteins as a filament is consistent with localization to the magnetosome.*
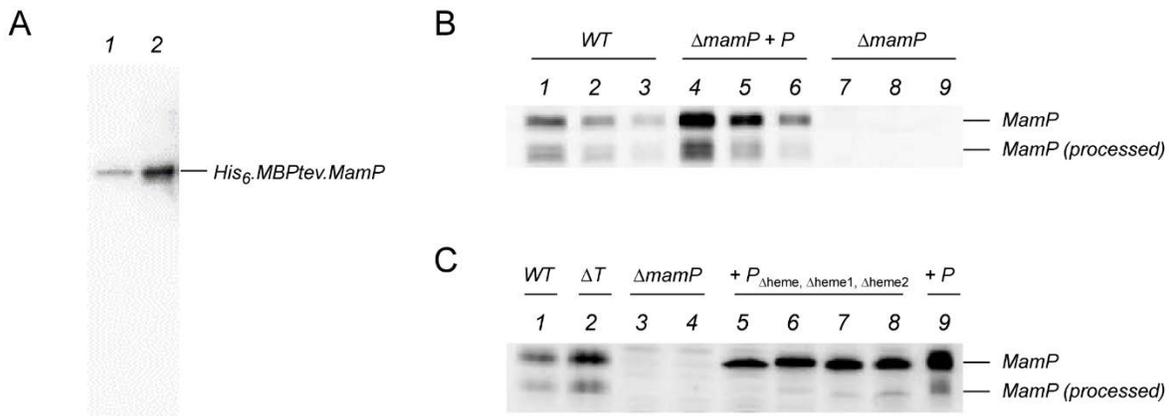
Figure 2.5. *Analysis of MamP expression in* M. magneticum *AMB-1 by immunostaining with αMamP. (A) Characterization of the αMamP serum with His$_6$.MBPtev.MamP. Periplasmic preparation (lane 1), Ni-NTA eluate (lane 2). Based on the concentrations of these samples estimated using the absorption of the Soret peak, the detection limit is < 20 ng per lane for the MamP fusion. (B) Western blot comparing expression of MamP in wild type, ΔmamP, and ΔmamP complemented with wild-type MamP strains. Wild-type undiluted (lane 1), wild type 1:1 dilution (lane 2), wild-type 1:3 dilution (lane 3), ΔmamP + mamP undiluted (lane 4), ΔmamP + mamP 1:1 dilution (lane 5), ΔmamP + mamP 1:3 dilution (lane 6), ΔmamP undiluted (lane 7), ΔmamP 1:1 dilution (lane 8), ΔmamP 1:3 dilution (lane 9). (C) Western blot comparing expression of MamP in wild-type, ΔmamP, ΔmamT, and ΔmamP complemented with wild-type MamP and different heme mutants. Wild-type (lane 1), ΔmamT (lane 2), ΔmamP 1 (lane 3), ΔmamP colony 2 (lane 4), ΔmamP + mamP$_{Δheme1}$ (lane 5), ΔmamP + mamP$_{Δheme2}$ colony (lane 6), ΔmamP + mamP$_{Δheme2}$ colony 2 (lane 7), ΔmamP + mamP$_{Δheme}$ (lane 8), ΔmamP + mamP 1:2 dilution (lane 9).*
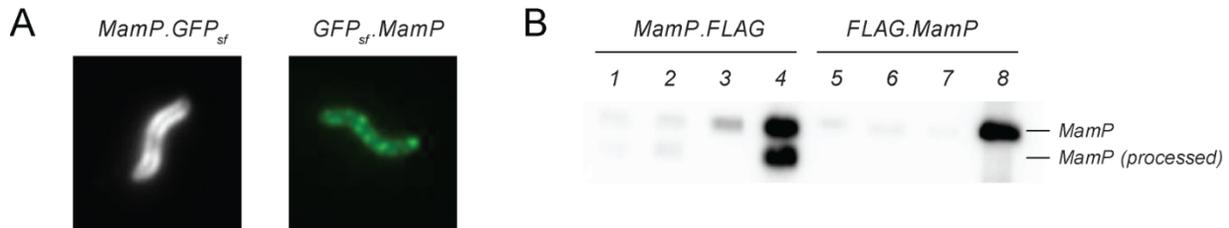
Figure 2.6. *Analysis of MamP localization and processing in* M. magneticum *AMB-1. (A) Fluorescence microscopy of GFP fusion with MamP: ΔmamP + mamP.GFP$_{sf}$ and ΔmamP + GFP$_{sf}$.mamP. Both constructs were imaged the same way but the GFP$_{sf}$.MamP image was processed for color while MamP.GFP$_{sf}$ was not processed for color. (B) Immunostaining of FLAG-tagged MamP native AMB-1 expression and purification. FLAG-tagged MamP was partially purified from both ΔmamP + mamP.FLAG and ΔmamP + FLAG.mamP and immunostained with anti-FLAG antibodies. ΔmamP + mamP.FLAG lysate (lane 1), ΔmamP + mamP.FLAG soluble fraction (lane 2), ΔmamP + mamP.FLAG insoluble fraction (lane 3), ΔmamP + mamP.FLAG anti-FLAG affinity gel eluate (lane 4), ΔmamP + FLAG.mamP lysate (lane 5), ΔmamP + FLAG.mamP soluble fraction (lane 6), ΔmamP + FLAG.mamP insoluble fraction (lane 7), ΔmamP + FLAG.mamP anti-FLAG affinity gel eluate (lane 8). All samples (18 µL) were loaded without dilution.*

We also made an attempt to determine the localization of MamP by constructing N-terminal and C-terminal GFP superfold (GFP$_{sf}$) fusions of the protein and expressing the constructs in Δ*mamP*. It has been suggested that MamP could be a component of the periplasm, a component of the magnetosome, or a component of both [*38, 56*]. In our experiments, fluorescence localization in neither construct indicated MamP localization at midcell, but showed widespread cellular distribution, possibly with higher accumulation in the periplasm or cell membrane (*Figure 2.6A*). However, we still cannot eliminate the possibility that functional MamP is localized to the magnetosome. Fluorescence analysis of GFP$_{sf}$ fusions to MamP are complicated by indications that MamP is processed *in vivo*. We first noticed such processing in comparing Δ*mamP* with wild type and Δ*mamP* + *mamP* AMB-1 pellets in Western blots immunostained with αMamP (*Figure 2.5B*). The expected MamP band appeared at 28.9 kDa as well as a lower molecular weight band. In order to further investigate this processing, we sought to isolate MamP from its native host. Therefore, we expressed MamP.FLAG and FLAG.MamP, respectively, from constitutive *tac* promoters on a pAK(Amp^R)-derived plasmid in the Δ*mamP* background and partially isolated the tagged MamP with a small amount of anti-FLAG affinity resin (*Figure 2.6B*). Immunostaining shows only the full length form of FLAG.MamP is isolated by the resin while both full length and processed forms of MamP.FLAG are isolated, suggesting that processing occurs close to the N-terminus of MamP (*Figure 2.6B, lanes 4 and 8*).

Using genetic complementation studies, we have shown that the redox cofactors or heme sites of the two putative redox partners, MamP and MamT, are required for this process *in vivo* and that removal of one or both sites leads to defects in mineralization that are nearly indistinguishable from the phenotypes of the *mamP* and *mamT* deletion strains. Although we cannot rule out other effects caused by mutation of the heme sites, TEM studies show the heme mutants retain the crystallization phenotypes that are a signature of either *mamP* or *mamT* loss of function while controls indicate both that the processed forms of the mutant proteins are present in the complementation strains and that key magnetosome proteins retain their proper localization. The difference in the defects does suggest that MamP and MamT do not have redundant functions in magnetite formation.

Heterologous expression and isolation of MamP. Based on the essential role of the heme redox sites of these two cytochromes *in vivo*, we turned our attention to the *in vitro* biochemical characterization of MamP, which is both predicted to be localized to the magnetosome as well as proposed to directly interact with the iron oxide particle [*38, 56*]. Towards this goal, we constructed a series of plasmids for the heterologous expression of the MamP protein from AMB-1 in *Escherichia coli* (*E. coli*). All of these plasmids contain the native *mamP* gene encoding the predicted mature sequence of MamP (residues 29-275) as well as an N-terminal OmpA tag [*57*] to direct the protein to the periplasm of *E. coli*, which provides an oxidizing compartment needed for the maturation of *c*-type cytochromes [*58*]. These constructs also included a solubilization tag consisting of a fused protein (NusA; TRX, thioredoxin; SUMO, small ubiquitin-like modifier; MOCR, monomeric Ocr protein; MBP, maltose-binding protein) flanked by an N-terminal His$_6$-affinity tag and C-terminal Tobacco Etch Virus (TEV) protease cleavage site (*Appendix 1*). MamP expression was initially screened in pCWori backbone, in which the protein is expressed from a double *tac* promoter with a dual ribosome-binding site that has been found to frequently increase the functional expression of heme proteins [*59*]. Overall, we found that proteolysis of MamP was

problematic in many of these variants, which could possibly be related to the accompanying observation that the second heme site was often unoccupied.

After significant optimization, we found that the OmpA.His$_6$.MBPtev.MamP fusion protein could be produced as the full-length protein with high heme content and that total MamP levels could be improved using a T7 promoter to drive its expression without losing significant heme incorporation. The optimal strain determined from these screens consisted of *E. coli* c43(DE3) [*60*] co-expressing the pEC86 cytochrome *c* maturation plasmid [*48*] with pET29a-OmpA.His$_6$.MBPtev.MamP. Since lower inducer concentrations ([IPTG] ~ 10-50 μM) have been reported to improve yields of *c*-type cytochromes expressed from a T7 promoter [*61*], we further screened IPTG levels in this range to optimize production of the heme-loaded His$_6$.MBPtev.MamP fusion (*Figure 2.7*). In this study, we found that IPTG concentrations between 25 and 40 μM yielded the highest levels of heme incorporation as determined by the intensity of the Soret absorbance band in the periplasmic lysate (*Figure 2.7*). Thus, we chose a concentration in the middle of this range (35 μM IPTG) for all subsequent expressions.

The His$_6$.MBPtev.MamP fusion protein (~73 kD) was isolated along with contaminating His$_6$.MBP (~45 kD) from the periplasmic lysate using a Ni-NTA affinity column (Supporting Appendix *Fig. S5*). After cleaving the His$_6$.MBPtev.MamP fusion by incubation with His$_6$.TEV protease, the sample was subjected to a second passage over a Ni-NTA column and an amylose column to remove His$_6$.TEV, His$_6$.MBP, and other cellular proteins enriched by Ni-NTA affinity chromatography. The lingering minor contaminants were then removed by size-exclusion chromatography, yielding MamP which is >95% pure as judged by an overloaded reducing gel (*Figure 2.8A*). More importantly, the size-exclusion step allows the separation of MamP of differential heme content. MamP was found to elute from the size-exclusion column in a single asymmetric peak, with fractions exhibiting Reinheitzahl ratios (Rz = A$_{Soret, 407 nm}$/A$_{280 nm}$) ranging between 2 and 8. The fractions at the leading edge to the center of the peak exhibit the highest Rz values (typically 7.0-7.2) and are then collected and pooled for downstream biochemical experiments (*Figure 2.8B*).

The heme content of the heterologously expressed MamP was characterized by a combination of protein acidolysis, inductively-coupled plasma atomic emission spectroscopy (ICP-AES), and electrospray ionization mass spectrometry (ESI-MS). Based on the low expected molar extinction coefficient of MamP and overlap with the heme absorption bands at 280 nm (*Figure 2.8B*), protein acidolysis was used to measure MamP concentration and determine ε$_{280 nm}$ after amino acid analysis (46,100 M^{-1} cm^{-1} per MamP monomer, *Figure 2.9*) MamP was then subjected to iron analysis by ICP-AES, which revealed that, within error, each MamP monomer contained two equivalents of iron as expected for diheme-loaded MamP (2.0 ± 0.4, *Figure 2.9*). The molar extinction coefficients calculated by these two methods are in good agreement with each other despite being based on different measurements of either protein or iron content, suggesting that both experiments provide fairly accurate quantification (*Figure 2.9*). MamP was also analyzed by ESI-MS as the hemes should be covalently attached via the cysteines in the *c*-type cytochrome CXXCH motif. The major peak in the ESI mass spectrum of MamP is centered at 27,503 Da (*Figure 2.8C*), as expected for the diheme-loaded protein (calculated: 27,505 Da). The other minor peak in the spectrum corresponds to half of the weight of the major peak, and is an artifact of the deconvolution process from the raw mass-to-charge data. Finally, size exclusion chromatography compared to standards shows that MamP forms a stable dimer in solution, giving a value of 75 ±

24 kD (Figure *2.8DE*). This is consistent with the crystal structure of the ortholog from Marine magnetotactic ovoid bacterium MO-1 (*Figure 2.10*) [*39*].

To gain more insight into the structural character of MamP, we built a structural homology model in Phyre2 with the MamP homolog crystallized from Marine magnetotactic ovoid bacterium MO-1 (*Figure 2.10*). The N-termini of the proteins are quite different, possibly due to the fact that the putative transmembrane segment at the N-terminus are residing in two very different species. The PDZ domains have 42% identity while the c-type cytochrome motifs and their linker region have 57% identity. This is reflected in the similarity of our structural model. Two main differences occur in the extra four-residue loop (loop 2) surrounding the second heme in AMB-1, as well as several differences in the PDZ domain (loop 1) which could contribute to species-specific protein-protein interactions. Interestingly, despite the structural similarity at the putative functional end of the protein, the MO-1 MamP fails to complement the Δ*mamP* phenotype when expressed off a pAK262-Amp plasmid in *M. magneticum* AMB-1 [*39*]. We attempted to express both the full MO-1 MamP homolog in AMB-1 as well as a MO-1 MamP fusion where the AMB-1 N-terminus is substituted for the MO-1 N-terminus. However, we cannot eliminate the possibility that the MO-1 MamP is poorly expressed in AMB-1 or that critical protein-protein interactions necessary for localization or processing are eliminated by expressing a protein from a highly divergent species. Therefore, based on the similar structure and c-type cytochrome domains, it is likely that the MO-1 and AMB-1 MamPs are functionally equivalent.

Biochemical characterization of MamP from *M. magneticum* AMB-1. In order to investigate the electron transfer capabilities of MamP, spectroelectrochemical titrations were performed to measure the Fe(III)/Fe(II) redox couple in both the oxidative and reductive directions. The Fe(III)-MamP resting state was initially reduced stepwise with sodium dithionite until the potential stabilized and the UV-visible spectrum showed the protein to be fully reduced to the Fe(II) state. Reduced MamP was then titrated with an oxidant and absorbance spectra were collected at each potential so that the fraction of reduced and oxidized MamP could be quantified (*Figure 2.11A*). Because of the steepness of the potential curve at the midpoint, the fully oxidized MamP was subsequently re-reduced to collect the reductive curve, with MamP demonstrating reversible, Nernstian behavior in both directions. The average Fe(III)/Fe(II) midpoint reduction potential was fit to a value of -89 ± 11 mV at pH 7.5, where the width of the transition predicts a two-electron redox process with very similar if not identical redox potentials for each of the heme sites within the MamP monomer (*Figure 2.11B*). This observation is consistent with the crystal structure, which shows that the cofactors are bound to a minimal domain of approximately 23 amino acids and likely enables rapid and reversible electron transfer to and from the iron center without significant perturbation from the protein environment [*62*].

Interestingly, the measured midpoint reduction potential for MamP is quite different from other putative iron oxidoreductases and falls between the ranges of the measured potentials for iron-reducing and iron-oxidizing cytochromes known to be involved in iron transformations. For example, the Fe(III)/Fe(II) couple for iron oxidases from either *Rhodobacter ferrooxidans SW2* [*63*] or *Ferrobacillus ferrooxidans* [*64*, *65*] were reported to be in the +200 to +300 mV range. In contrast, iron-reducing organisms, such as *Shewanella oneidensis*, contain *c*-type cytochromes such as OmcA with reduction potentials ranging from -234 to -324 mV [*66*]. However, some *c*-type cytochromes do have more positive reduction potentials, such as an extracellular electron carrier found in *Geobacter sulfurreducins* (-167 mV) [*67*].

While different, the MamP Fe(III)/Fe(II) couple remains slightly higher than the reduction potentials for various reactions between insoluble iron oxides and soluble, complexed Fe(II) [68]. For example, values for ferrihydrite and the Fe(III)(OH)$_3$/Fe(II) couple are between -200 mV to + 100 mV whereas the potentials for crystalline iron oxides reside between -88 mV (lepidocrocite) and -314 mV (magnetite). The standard reduction potential of the Fe(III)/Fe(II) couple (+770 mV) applies only to strongly acidic solutions in which both oxidation states have high solubility [69]. Indeed, the reducing power of ferrous iron increases dramatically at neutral pH due to the formation of insoluble iron oxides and oxyhydroxides [70]. As such, the measurement of reduction potentials of insoluble iron minerals is quite complex, as chelated iron oxide forms have higher potentials than ferric iron oxides and are dependent on pH and even particle size [71, 71, 70]. Thus, at circumneutral pH, reduction potentials for these species can range from -300 mV to +400 mV and the MamP couple is found in the middle of this range. This could suggest that MamP is tuned to transform very specific iron species at specific pH values.

As the reduction potential of MamP falls directly in between characterized iron-reducing and iron-oxidizing cytochromes, we decided to investigate its chemical competence to carry out redox chemistry with iron. In the absence of additional mediators, we found that the resting Fe(III)-MamP could be reduced by the addition of iron(II) salts (*Figure 2.11C*). Interestingly, this reaction introduced scattering into the spectroscopic measurements by the precipitation of iron species resulting from the formation of Fe(III) in solution. Reduced Fe(II)-MamP could further be rapidly and stoichiometrically oxidized by the titration of one equivalent of molecular oxygen (*Figure 2.11C*). These results demonstrate that Fe(II) and oxygen enable the formation of a closed catalytic cycle for overall oxidation of Fe(II) to Fe(III) catalyzed by MamP.

The ability of MamP to oxidize Fe(II) at a lower overpotential provides a mechanism for the generation of Fe(II) and Fe(III) within the magnetosome for magnetite formation, while preventing the re-reduction of Fe(III) to Fe(II). In this manner, MamP could be optimized for controlling the stoichiometry of Fe(II) and Fe(III) so that the magnetite nanoparticle can be grown without defects.
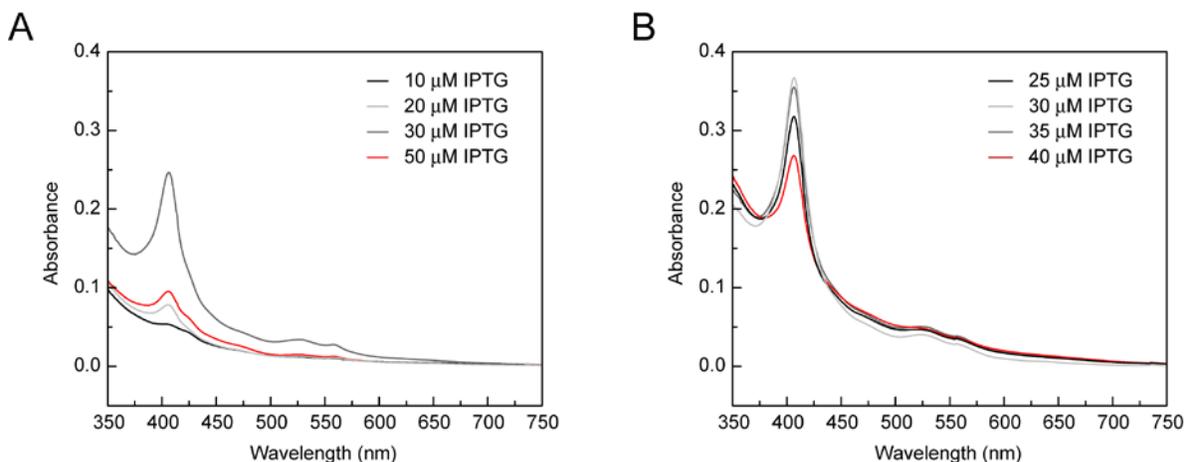
Figure 2.7. *Optimization of induction conditions for heterologous MamP expression. (A) Preliminary optimization. (B) Final optimization. In these experiments, E. coli C43(DE3) cells co-expressing pET29a-OmpA.His$_6$.MBP.MamP and pEC86 were induced at various concentrations of IPTG. After preparation of the periplasmic lysate, UV-visible spectra were collected to visualize the relative level of the MamP Soret peak.*
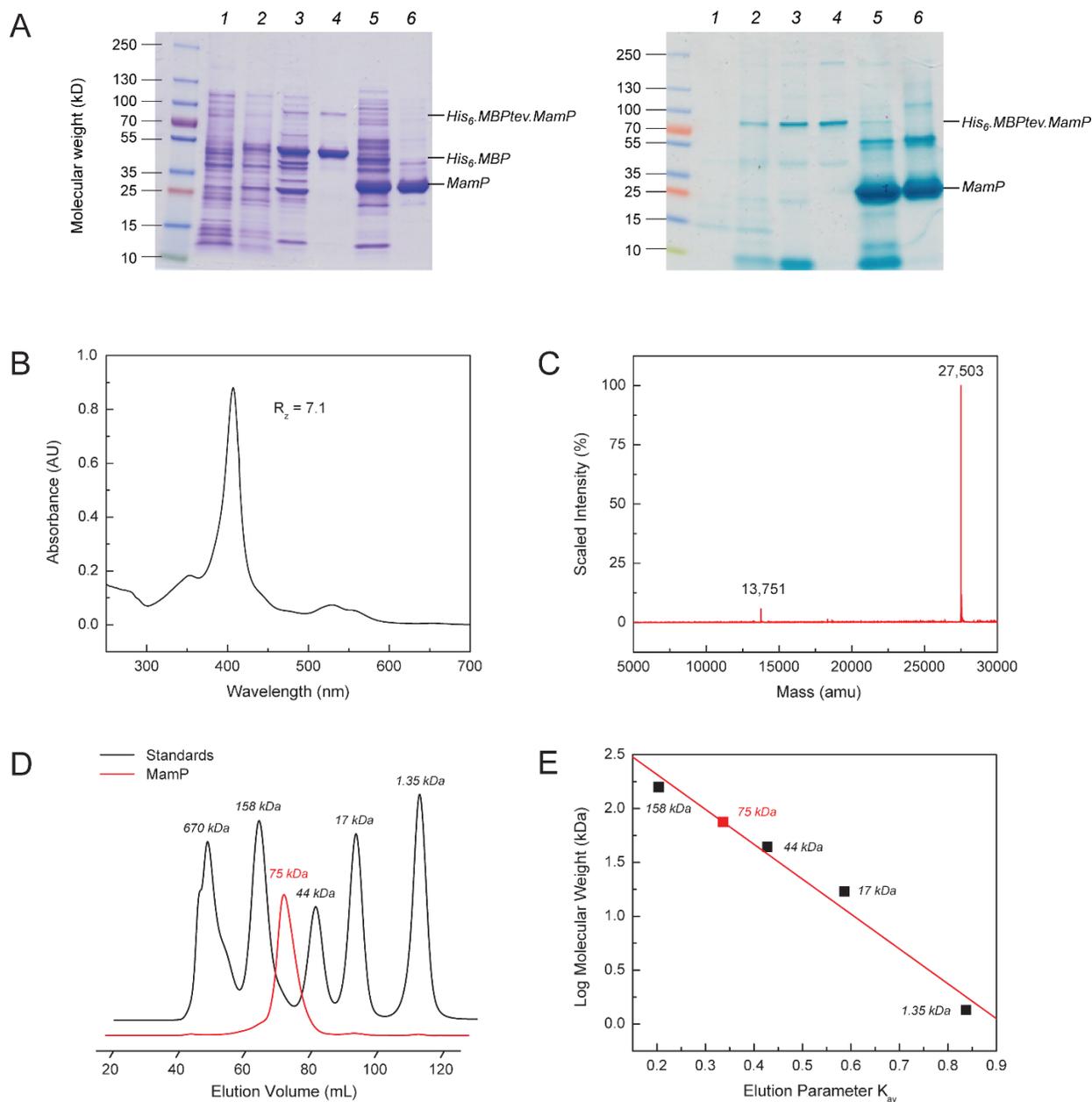
Figure 2.8. *Purification and characterization of heterologously-expressed MamP (A) Coomassie-stained gel using samples prepared under reducing conditions (right) and heme-stained gel with the same samples prepared under non-reducing conditions. Pre-induction sample (lane 1), post-induction sample (lane 2), periplasmic lysate (lane 3), Ni-NTA eluate (lane 4), amylose-purified (lane 5) SEC-purified (lane 6). Molecular weights: His6-MBPtev-MamP, 73 kDa; His6-MBP, 45 kDa; MamP, 27.5 kDa. (B) UV-Visible spectrum of MamP with the Soret peak at 407 nm. (C) ESI mass spectrum of MamP showing covalent modification by two heme prosthetic groups (MW$_{calc}$ = 27,505 Da). (D) Size-exclusion chromatogram of MamP compared to standards monitoring A280 nm. (E) Standard curve generated from a linear fit of the log molecular weight of the protein standards versus their elution parameter K$_{av}$ where K$_{av}$ = (V$_e$ - V$_0$)/(V$_{col}$ – V$_0$). The MW$_{app}$ of MamP was estimated to be 75 ± 24 kD based on a linear fit to the molecular weight standards.*

44

A

	Composition (mol %)		
Amino acid	Analyzed	Expected	% Error
Asp	21.51	21	2.4
Thr	13.98	14	-0.1
Ser	9.78	9	8.7
Glu	17.09	22	-22.3
Pro	24.00	27	-11.1
Gly	23.56	24	-1.8
Ala	29.54	31	-4.7
Val	18.66	21	-11.1
Met	5.67	6	-5.5
Ile	8.20	8	4.0
Leu	22.46	22	2.1
Tyr	4.93	3	64.3
Phe	8.62	7	23.1
His	5.67	5	13.4
Lys	7.82	7	11.7
Arg	15.91	17	-6.4
MamP concentration (μM)			13.3

B

$R^2 = 0.9977$

137 ± 29 μg/L

C

Method	$\varepsilon_{280\ nm}$ ($M^{-1}cm^{-1}$)	$\varepsilon_{407\ nm}$ ($M^{-1}cm^{-1}$)
Acidolysis	46,100	331,100
ICP	48,200	348,700

Figure 2.9. *Determination of the extinction coefficient of MamP. (A) Analysis of MamP amino acid composition after acidolysis. For predicted amino acid concentrations, N and Q were converted to D and E, respectively. Please note that error in Y and F is expected based on the small number of amino acids per protein molecule. (B) ICP-AES analysis of MamP. The calibration curve was generated with standard solution of Fe(NO₃)₃ (black squares) and the value measured for MamP (red square). Based on a linear fit of the standards, the concentration of Fe in the MamP sample was calculated to be 137 ± 29 µg/L. (C) Comparison of the extinction coefficients measured for the protein absorption and Soret peaks of Fe(III)-MamP by acidolysis and ICP-AES. The extinction coefficient at 280 nm for the MamP protein absorption (Δ280 nm) was calculated directly from acidolysis data with A280 nm and the experimentally-determined MamP concentration. The extinction coefficient for the Soret peak at 407 nm (Δ407 nm) was then calculated from A₄₀₇ ₙₘ of the same sample using the concentration of MamP and the assumption of 100% heme occupancy. The extinction coefficient for the Soret peak of a single diheme-loaded Fe(III)-MamP monomer was calculated directly from concentration of Fe in the MamP sample. The Δ280 nm was then calculated from A280 nm and the assumption of 100% heme occupancy. The expected Rz value for diheme-loaded MamP is calculated to be 7.2 based on the ratio of Δ407 nm and Δ280 nm.*

A

B

Loop 2

Loop 1

Loop 2

Loop 1

C

Loop 1
*

MO-1 73 PALSDANGGFVAPNVQFSEAHWQGMEALPLSIELKRKLKLPLDLEGLLIDETSLNAAVSGLLAGDVLVAINGRKVKTLKKMQKETRRVQMDRRASLTVYRKG--------RLLTLTLSE- 183
           PA   FV   ++ E HWQGM+   ++ EL RKL P L+G+L+ E +LNAA SGLLAGD++V I+   V ++ + +R V   A ++V RK   R LT+ L E
AMB-1 76 PATESPLPNFVPRKLKVFEGHWQGMDGRLMTEELARKLNYPRGLQGVLLGEVTLNAAFSGLLAGDLIVRIDDTPVTDMESFKAASRTVANRSDARISVLRKDNRPGAPVVRKLTVVLREA 195

                                                                                                      PDZ domain

Loop 2
*

MO-1 184 EKNLGLAQVETAPMILPGDIMPHPYRGPCTQCHAIGTTGHITPDPDGIVLPPGPIR----AGAKMPHRDRGPCAACHAI 258
           E LG AQ+E APMIL GD PH YRG CT CH IG   +TPDPD I LPP I   A + PH RGPC ACH I
AMB-1 196 EGGLGFAQLEGAPMILAGDPRPHGYRGACTDCHPIGQGFELTPDPDLISLPPPTITRDMVARSVNPHEVRGPCEACHVI 274

                        C-type cytochrome domain

Figure 2.10. *Structural comparison of MamP from marine magnetic ovoid MO-1 and* Magnetospirillum magneticum *AMB-1. (A) View of the MO-1 MamP dimer (blue) with the Phyre2 AMB-1 MamP dimer model overlaid (yellow). (B) Structural model of protein looking down between the dimer and heme sites. The MamP MO-1 structure is in blue and the MamP AMB-1 model is in yellow. (C) BLAST comparison of the MO-1 and AMB-1 amino acid sequences with extra loops in AMB-1 structure marked with *.*

Figure 2.11. *Characterization of MamP redox behavior. (A) Changes in the electronic absorption spectrum showing the stepwise oxidation of Fe(II)–MamP (MamP_red, red) to Fe(III)–MamP (MamP_ox, black). (B) Three individual redox titrations of MamP monitored by $\Delta A551$ nm. The curve fit is shown as a red line. (C) Redox cycle of MamP-catalyzed oxidation of Fe(II). Changes in the electronic absorption spectrum of MamP showing the reduction of Fe(III)-MamP by ammonium iron(II) sulfate followed by re-oxidation of Fe(II)-MamP by titration of one equivalent of molecular oxygen.*

47

Mineralization of iron oxides from Fe(II) with MamP. The ability of MamP to rapidly generate Fe(III) from Fe(II) should also enable catalysis of the formation of mixed-valent iron oxides related to magnetite since they can be made by mixing of Fe(II) and Fe(III) salts [*72*]. Indeed, we observed that reaction of Fe(II) with resting Fe(III)-MamP, while introducing oxygen as the terminal oxidant, led to the formation of a green mineral within 10 min and reached high levels within 20 min (*Figure 2.12A*). In comparison, little to no mineralization takes place above background in the control reaction with no MamP, as it was not observed to significantly increase within the timeframe of the reaction (30 min, *Figure 2.12A*). Furthermore, the mineralization reaction catalyzed by MamP is significantly faster than the formation of iron(III) oxides or hydroxides in the reaction with no MamP, even with the introduction of oxygen (*Figure 2.12A*). The formation of a green rust-like mineral in the MamP reaction is consistent with a mixed Fe(II)-Fe(III) oxyhydroxide green rust (2-4 Fe(II): 1 Fe(III)), which is a possible precursor to magnetite (1 Fe(II): 2 Fe(III)) that is incompletely oxidized [*72*]. Given the variation of the reduction potential of green rust with Fe(II):Fe(III) ratio (-210 to +270 mV) [*73*], the rates of mineralization and Fe(II) oxidation can affect the identity of the mineral formed as MamP would be competent to further oxidize some of these species. Thus, the bulk formation of green rust rather than magnetite under these *in vitro* conditions may indicate that the stoichiometry of Fe(II) to MamP may be controlled *in vivo* such that Fe(II) and Fe(III) are formed in the appropriate ratio for direct formation of magnetite or that other components could be involved in the oxidation of green rust to magnetite.

It has been suggested that magnetotactic bacteria tightly control the pH as well as the reducing potential of the magnetosome in order to crystallize thermodynamically-stable magnetite [*36*]. In order to investigate the extent of environmental control over MamP-induced mineralization, we performed similar mineralization reactions at pH 6.0, environmental conditions well below the thermodynamic stability of magnetite, as well as at pH 9.0, a pH in the middle of the range for the thermodynamic stability of magnetite but well above typical cellular conditions. We saw rapid mineralization of green rust at pH 7.5 and pH 9.0 and slow mineralization of fully oxidized ferrihydrite at pH 6.0 (*Figure 2.12B*). Mineralization conditions above pH 7.5 will lead to the formation of magnetic material after a significant amount of time (> 60 min) (*Figure 2.12C*). However, it has not been determined whether this is due to the slow introduction of O_2 through the caps or due to the action of MamP. As pH contributes to both solubility and solubility differences between Fe(II) and Fe(III) as well as to the stability of different iron oxide species, it seems likely that the magnetosome has specific proteins which control pH as well as proteins which control redox potential, such as MamP and other magnetochromes.

In vitro mineralization studies with MamP and Fe(II) show that it is able to catalyze the formation of mixed-valent Fe(II)/Fe(III) oxides such as green rust. While we utilize oxygen as the terminal oxidant for this reaction, other small-molecule oxidants, such as nitrate or perchlorate, could also be used for anaerobic mineralization based on the MamP reduction potential. The formation of the incompletely oxidized mineral under these conditions is likely a result of kinetic competition between the rates of mineralization versus Fe(II) oxidation and could be controlled *in vivo* by local Fe(II) concentration, iron:MamP stoichiometry, or pH inside the magnetosome.
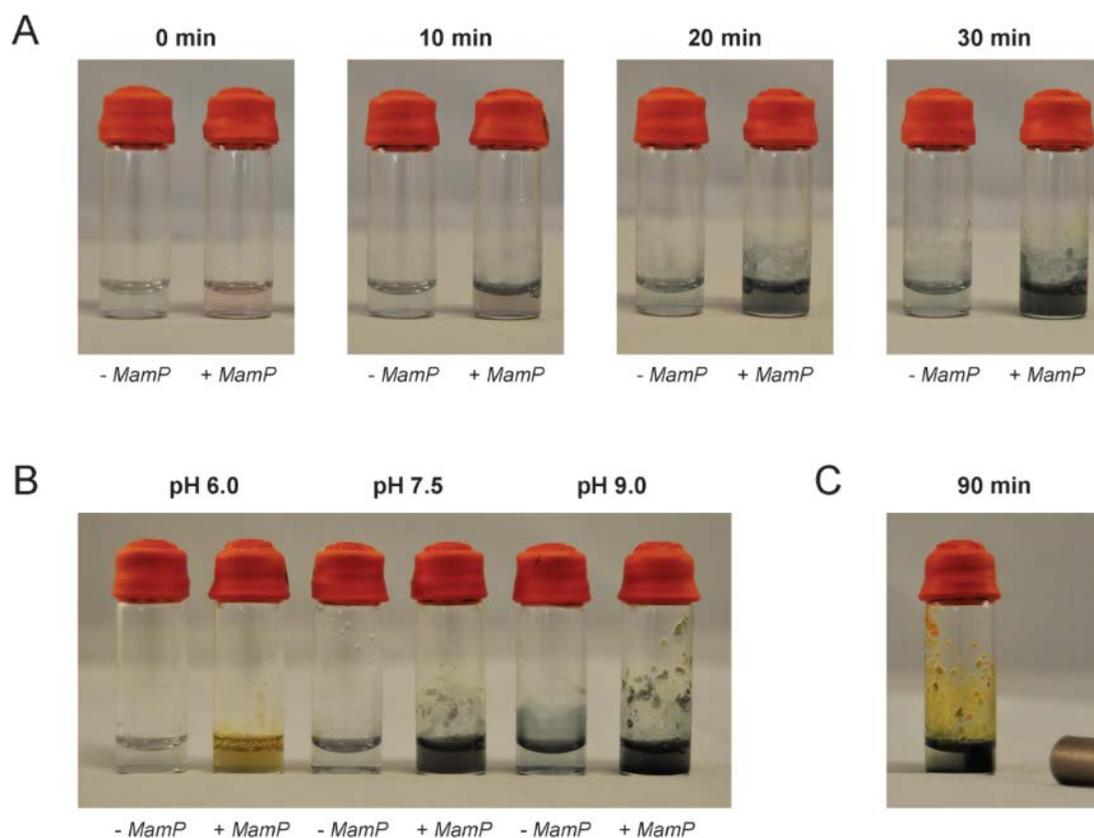
Figure 2.12. In vitro *mineralization of iron by MamP. (A) In vitro iron mineralization reactions containing ammonium Fe(II) sulfate (40 mM) in 50 mM HEPES pH 8.0, 100 mM NaCl with and without MamP (2.5 µM). Air was introduced through undegassed MamP or reaction buffer (for the no MamP control) by syringe at 10 and 20 min to provide oxygen as a terminal oxidant at an approximate final concentration of 2.5 µM. (B) In vitro iron mineralization reactions performed at pH 6.0, 7.5, and 9.0 with and without MamP after 30 minutes of reaction.. (C) In vitro mineralization reaction at pH 9.0 after 90 minutes. After more than an hour, reactions at pH 7.5 and above develop iron oxides in solution that are attracted to a magnet.*

49

2.4. Conclusion

Magnetotactic bacteria have evolved a remarkable organelle that serves to genetically control the size, shape, and identity of the iron oxide nanoparticles that are used for passive sensing of direction. As the production of magnetite requires both the formation of Fe(II) and Fe(III), the redox components of the magnetosome play an essential role in this process.

Using genetic complementation studies, we have shown that the redox cofactors or heme sites of the two putative redox partners, MamP and MamT, are required for this process *in vivo* and that removal of one or both sites leads to defects in mineralization that are nearly indistinguishable from the phenotypes of the Δ*mamP* and Δ*mamT* deletion strains, respectively. Although we cannot rule out other effects caused by mutation of the heme sites, controls indicate both that the processed forms of the mutant proteins are present in the complementation strains and that key magnetosome proteins retain their proper localization. We have developed and optimized a heterologous expression method in the *E. coli* periplasm to cleanly isolate fully heme-loaded MamP for biochemical studies, as shown by amino acid analysis, iron analysis, and MALDI-TOF MS. Spectrochemical redox titrations show that the reduction potential of MamP (-89 ± 11 mV) lies in a different range than other *c*-type cytochrome involved in either Fe(III) reduction or Fe(II) oxidation. Nonetheless, Fe(III)-MamP remains competent to oxidize soluble Fe(II) species and can be re-oxidized to the Fe(III)-resting state in order to form a closed catalytic cycle leading to overall formation of Fe(III) from Fe(II). *In vitro* mineralization studies with MamP and Fe(II) show that it is able to catalyze the formation of mixed-valent Fe(II)/Fe(III) oxides such as green rust. The formation of the incompletely oxidized mineral under these conditions is likely a result of kinetic competition between the rates of mineralization versus Fe(II) oxidation and could be controlled *in vivo* by local Fe(II) concentration, iron:MamP stoichiometry, or pH inside the magnetosome.

Our results suggest that the biological mechanism for iron mineralization in *M. magneticum* AMB-1 involves the transport of iron into the magnetosome in the Fe(II) oxidation state and its subsequent oxidation to Fe(III) to form magnetite in a process that is controlled by magnetosome redox (MamP and MamT) and components (*Figure 2.13*). Biomineralization in magnetotactic bacteria may be directly related to Fe(II) oxidation by anaerobic nitrate-dependent bacteria and by analogy, ultimately coupled to the respiratory chain. In this regard, it has been postulated that periplasmic components of these nitrate-reducing bacteria enable Fe(II) oxidation in order to overcome toxicity of iron and radical byproducts [74] based on the observation that several strains can precipitate iron minerals within the periplasm. Furthermore, nitrate reduction has been shown to be linked to biomineralization in other species of magnetotactic bacteria and is mediated by key periplasmic proteins [37, 75, 76]. Since the magnetosome is ultimately derived from the periplasmic compartment of the host, it would be interesting to hypothesize that magnetite nanoparticle formation represents an inside-out respiratory process, in which the electron transport chain provides not only energy to the cell but also oxidizing equivalents to the tightly-controlled biomineralization process.
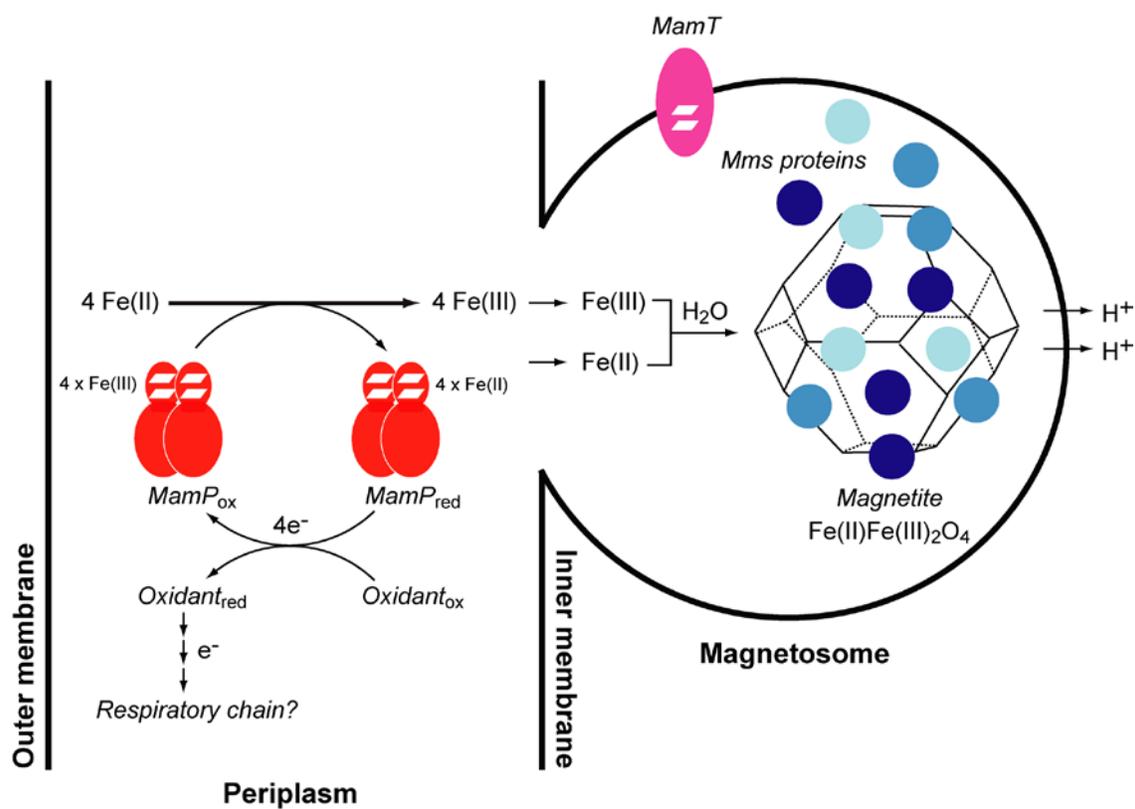
Figure 2.13. Model for redox-controlled magnetite formation in M. magneticum AMB-1. Soluble Fe(II) is oxidized to Fe(III) either in the periplasm or magnetosome through a redox chain involving magnetosome-specific cytochromes, MamP and MamT (and potentially MamE and MamX), as well as other general electron transport proteins in the periplasmic compartment. The overall oxidation of Fe(II) leads to the formation of 4 reducing equivalents per MamP dimer, which could potentially be passed to the respiratory chain for energy metabolism. The localization of MamP and MamT to either the periplasm or magnetosome have yet to be determined, but their respective sequences are predicted to contain a signal sequence and transmembrane segment. A mixture of Fe(II) and Fe(III) is generated in the magnetsome either by direct oxidation with a magnetosome-localized MamP or MamT or through transport from the periplasm (Fe(II) or Fe(III)) or cytoplasm (Fe(II)) via predicted cation diffusion facilitors (MamB and/or MamM). The Fe(II) and Fe(III) ions are templated by Mms6 family proteins to form the magnetite (Fe(II)Fe(III)2O4) mineral lattice with oxide bridges derived from water. Based on our data, we hypothesize that the Fe(II):Fe(III) ratio in the magnetosome is set by MamP while the Fe(II):Fe(III) ratio in the mineral lattice may be further controlled by templating components (Mms6 family proteins). The in vivo product of MamP has yet to be determined and could possibly be magnetite itself or a Fe(II)-Fe(III) oxide precursor that is further oxidized by other redox components while being stabilized and protected by Mms6 family proteins from over-oxidation to Fe(III) oxides. The protons lost during mineralization from the bridging water molecules are concomitantly transported out of the magnetosome by a predicted Na+/H+ antiporter (MamN) to maintain the pH required for stable magnetite formation.

2.5. References

1.   L. Addadi and S. Weiner (1997) Biomineralization - a pavement of pearl. *Nature* 389:912.
2.   S. Weiner and L. Addadi (2011) Crystallization pathways in biomineralization. *Annu. Rev. Mater. Res.* 41:21-40.
3.   F. H. Wilt (2005) Developmental biology meets materials science: morphogenesis of biomineralized structures. *Dev. Biol.* 280(1):15-25.
4.   F. C. Meldrum and H. Colfen (2008) Controlling mineral morphologies and structures in biological and synthetic systems. *Chem. Rev.* 108(11):4332-4432.
5.   E. P. Katz, E. Wachtel, M. Yamauchi, and G. L. Mechanic (1989) The structure of mineralized collagen fibrils. *Connect. Tissue Res.* 21:149-154.
6.   C. E. Hamm, R. Merkel, O. Springer, P. Jurkojc, C. Maier, K. Prechtel, and V. Smetacek (2003) Architecture and material properties of diatom shells provide effective mechanical protection. *Nature* 421:841-843.
7.   C. Mao, D. J. Solis, B. D. Reiss, S. Kottmann, R. Sweeney, G. Georgiou, B. Iverson, and A. M. Belcher (2004) Virus-based genetic toolkit for the directed synthesis of magnetic and semiconducting nanowires. *Science* 303:213-215.
8.   C. Mao, C. E. Flynn, A. Hayhurst, R. Sweeney, J. Qi, G. Georgiou, B. Iverson, and A. M. Belcher (2003) Viral assembly of oriented quantum dot nanowires. *Proc. Natl. Acad. Sci. U. S. A.* 100(12):6946-6951.
9.   J. E. Yang, S. Y. Choi, J. H. Shin, S. J. Park, and S. Y. Lee (2013) Microbial production of lactate-containing polyesters. *Microbial Biotech.* 6(6):621-636.
10.   A. Y. Chen, Z. Deng, A. N. Billings, U. O. Seker, M. Y. Lu, R. J. Citorik, B. Zakeri, and T. K. Lu (2014) Synthesis and patterning of tunable multiscale materials with engineered cells. *Nat. Mater.* 13(5):515-523.
11.   M. M. Tomczak, J. M. Slocik, M. O. Stone, and R. R. Naik (2007) Bio-based approaches to inorganic material synthesis. *Biochem. Soc. Trans.* 35(3):512-515.
12.   M. Suzuki, K. Saruwatari, T. Kogure, Y. Yamamoto, T. Nishimura, T. Kato, and H. Nagasawa (2009) An acidic matrix protein, Pif, is a key macromolecule for nacre formation. *Science* 325:1388-1390.
13.   C. A. Orme, A. Noy, A. Wierzbicki, M. T. McBride, M. Grantham, H. H. Teng, P. M. Dove, and J. J. DeYoreo (2001) Formation of chiral morphologies through selective binding of amino acids to calcite surface steps. *Nature* 411(6839):775-779.
14.   J. J. De Yoreo, A. Wierzbicki, and P. M. Dove (2007) New insights into mechanisms of biomolecular control on growth of inorganic crystals. *Cryst. Eng. Comm.* 9:1144-1152.
15.   A. M. Belcher, X. Wu, R. J. Christensen, P. K. Hansma, G. D. Stucky, and D. E. Morse (1996) Control of crystal phase switching and orientation by soluble mollusc-shell proteins. *Nature* 381:56-58.
16.   G. K. Hunter, P. V. Hauschka, A. R. Poole, L. C. Rosenberg, and H. A. Goldberg (1996) Nucleation and inhibition of hydroxyapatite formation by mineralized tissue proteins. *Biochem. J.* 317:59-64.
17.   D. J. Belton, O. Deschaume, and C. C. Perry (2012) An overview of the fundamentals of the chemistry of silica with relevance to biosilicification and technological advances. *FEBS J.* 279(10):1710-1720.

18.   H. A. Currie and C. C. Perry (2007) Silica in plants: biological, biochemical and chemical studies. *Ann. Bot.* 100(7):1383-1389.

19.   M. Hildebrand (2008) Diatoms, biomineralization processes, and genomics. *Chem. Rev.* 108(11):4855-4874.

20.   L. J. Bird, V. Bonnefoy, and D. K. Newman (2011) Bioenergetic challenges of microbial iron metabolisms. *Trends Microbiol.* 19(7):330-340.

21.   C. T. Lefevre and D. A. Bazylinski (2013) Ecology, diversity, and evolution of magnetotactic bacteria. *Microbiol. Mol. Biol. Rev.* 77(3):497-526.

22.   L. Shi, D. J. Richardson, Z. Wang, S. N. Kerisit, K. M. Rosso, J. M. Zachara, and J. K. Fredrickson (2009) The roles of outer membrane cytochromes of *Shewanella* and *Geobacter* in extracellular electron transfer. *Environ. Microbiol. Rep.* 1:220-227.

23.   E. C. Theil (2013) Ferritin: the protein nanocage and iron biomineral in health and in disease. *Inorg. Chem.* 52(21):12223-12233.

24.   K. A. Weber, L. A. Achenbach, and J. D. Coates (2006) Microorganisms pumping iron: anaerobic microbial iron oxidation and reduction. *Nat. Rev. Microbiol.* 4(10):752-764.

25.   R. Wiltschko and W. Wiltschko (2013) The magnetite-based receptors in the beak of birds and their role in avian navigation. *J. Comp. Physiol. A Neuroethol. Sens. Neural Behav. Physiol.* 199(2):89-98.

26.   K. M. Towe and H. A. Lowenstam (1967) Ultrastructure and development of iron mineralization in the radular teeth of *Cryptochiton stelleri* (*Mollusca*). *J. Ultrastruct. Res.* 17(1):1-13.

27.   H. C. Lichtenegger, T. Schoberl, M. H. Bartl, H. Waite, and G. D. Stucky (2002) High abrasion resistance with sparse mineralization: copper biomineral in worm jaws. *Science* 298(5592):389-392.

28.   A. Manceau, K. L. Nagy, M. A. Marcus, M. Lanson, N. Geoffroy, T. Jacquet, and T. Kirpichtchikova (2008) Formation of metallic copper nanoparticles at the soil-root interface. *Environ. Sci. Technol.* 42(5):1766-1772.

29.   C. N. Butterfield, A. V. Sodatova, S. W. Lee, T. G. Spiro, and B. M. Tebo (2013) Mn(II, III) oxidation and MnO_2 mineralization by an expressed bacterial multicopper oxidase. *Proc. Natl. Acad. Sci. U. S. A.* 110:11731-11735

30.   B. M. Tebo, H. A. Johnson, J. K. McCarthy, and A. S. Templeton (2005) Geomicrobiology of manganese(II) oxidation. *Trends Microbiol.* 13:421-428.

31.   C. M. Hansel, C. A. Zeiner, C. M. Santelli, and S. M. Webb (2012) Mn(II) oxidation by an ascomycete fungus is linked to superoxide production during asexual reproduction. *Proc. Natl. Acad. Sci. U. S. A.* 109:12621-12625

32.   D. R. Learman, B. M. Voelker, A. I. Vazquez-Rodriguez, and C. M. Hansel (2011) Formation of manganese oxides by bacterially generated superoxide. *Nat. Geosci.* 4:95-98.

33.   D. A. Bazylinski and R. B. Frankel (2004) Magnetosome formation in prokaryotes. *Nat. Rev. Microbiol.* 2(3):217-230.

34.   R. B. Frankel, J.-P. Zhang, and D. A. Bazylinski (1998) Single magnetic domains in magnetotactic bacteria. *J. Geophys. Res.* 103:30601-30604.

35.   A. Fischer, M. Schmitz, B. Aichmayer, P. Fratzl, and D. Faivre (2011) Structural purity of magnetite nanoparticles in magnetotactic bacteria. *J. R. Soc. Interface* 8(60):1011-1018.

36.   D. Faivre and D. Schuler (2008) Magnetotactic bacteria and magnetosomes. *Chem. Rev.* 108(11):4875-4898.

37. L. Rahn-Lee and A. Komeili (2013) The magnetosome model: insights into the mechanisms of bacterial biomineralization. *Front. Microbiol.* 4:352.

38. M. I. Siponen, G. Adryanczyk, N. Ginet, P. Arnoux, and D. Pignol (2012) Magnetochrome: a c-type cytochrome domain specific to magnetotatic bacteria. *Biochem. Soc. Trans.* 40(6):1319-1323.

39. M. I. Siponen, P. Legrand, M. Widdrat, S. R. Jones, W. J. Zhang, M. C. Chang, D. Faivre, P. Arnoux, and D. Pignol (2013) Structural insight into magnetochrome-mediated magnetite biomineralization. *Nature* 502(7473):681-684.

40. A. Komeili, H. Vali, T. J. Beveridge, and D. K. Newman (2004) Magnetosome vesicles are present before magnetite formation, and MamA is required for their activation. *Proc. Natl. Acad. Sci. U. S. A.* 101(11):3839-3844.

41. W. A. Kibbe (2007) OligoCalc: an online oligonucleotide properties calculator. *Nucleic Acids Res.* 35(Web Server issue):W43-46.

42. D. G. Gibson, L. Young, R. Y. Chuang, J. C. Venter, C. A. Hutchison, and H. O. Smith (2009) Enzymatic assembly of DNA molecules up to several hundred kilobases. *Nat. Methods* 6(5):343-345.

43. D. Murat, A. Quinlan, H. Vali, and A. Komeili (2010) Comprehensive genetic dissection of the magnetosome gene island reveals the step-wise assembly of a prokaryotic organelle. *Proc. Natl. Acad. Sci. U. S. A.* 107(12):5593-5598.

44. J. D. Pedelacq, S. Cabantous, T. Tran, T. C. Terwilliger, and G. S. Waldo (2006) Engineering and characterization of a superfolder green fluorescent protein. *Nat. Biotechnol.* 24(1):79-88.

45. A. Krogh, B. Larsson, G. von Heijne, and E. L. Sonnhammer (2001) Predicting transmembrane protein topology with a hidden Markov model: application to complete genomes. *J. Mol. Biol.* 305(3):567-580.

46. D. Murat, V. Falahati, L. Bertinetti, R. Csencsits, A. Kornig, K. Downing, D. Faivre, and A. Komeili (2012) The magnetosome membrane protein, MmsF, is a major regulator of magnetite biomineralization in *Magnetospirillum magneticum* AMB-1. *Mol. Microbiol.* 85(4):684-699.

47. D. Schuler, R. Uhl, and E. Bauerlein (1995) A simple light scattering method to assay magnetism in *Magnetospirillum gryphiswaldense*. *FEMS Microbiol. Lett.* 132:139-145.

48. E. Arslan, H. Schulz, R. Zufferey, P. Kunzler, and L. Thony-Meyer (1998) Overproduction of the *Bradyrhizobium japonicum* c-type cytochrome subunits of the cbb3 oxidase in *Escherichia coli*. *Biochem. Biophys. Res. Commun.* 251(3):744-747.

49. L. A. Kelley and M. J. Sternberg (2009) Protein structure prediction on the Web: a case study using the Phyre server. *Nat. Protoc.* 4(3):363-371.

50. E. F. Pettersen, T. D. Goddard, C. C. Huang, G. S. Couch, D. M. Greenblatt, E. C. Meng, and T. E. Ferrin (2004) UCSF Chimera - a visualization system for exploratory research and analysis. *J. Comput. Chem.* 25(13):1605-1612.

51. S. F. Altschul, T. L. Madden, A. A. Schaffer, J. Zhang, Z. Zhang, W. Miller, and D. J. Lipman (1997) Gapped BLAST and PSI-BLAST: a new generation of protein database search programs. *Nucleic Acids Res.* 25(17):3389-3402.

52. R. Makino, S. Y. Park, E. Obayashi, T. Iizuka, H. Hori, and Y. Shiro (2011) Oxygen binding and redox properties of the heme in soluble guanylate cyclase: implications for the mechanism of ligand discrimination. *J. Biol. Chem.* 286(18):15678-15687.

53. P. L. Dutton (1978) Redox potentiometry: determination of midpoint potentials of oxidation-reduction components of biological electron-transfer systems. *Methods Enzymol.* 54:411-435.

54. K. D. Welch, T. Z. Davis, and S. D. Aust (2002) Iron autoxidation and free radical generation: effects of buffers, ligands, and chelators. *Arch. Biochem. Biophys.* 397(2):360-369.

55. A. Quinlan, D. Murat, H. Vali, and A. Komeili (2011) The HtrA/DegP family protease MamE is a bifunctional protein with roles in magnetosome protein localization and magnetite biomineralization. *Mol. Microbiol.* 80(4):1075-1087.

56. A. Taoka, Y. Eguchi, S. Mise, Z. Oestreicher, F. Uno, and Y. Fukumori (2014) A magnetosome-associated cytochrome MamP is critical for magnetite crystal growth during the exponential growth phase. *FEMS Microbiol. Lett.*

57. M. P. Pritchard, R. Ossetian, D. N. Li, C. J. Henderson, B. Burchell, C. R. Wolf, and T. Friedberg (1997) A general strategy for the expression of recombinant human cytochrome P450s in *Escherichia coli* using bacterial signal peptides: expression of CYP3A4, CYP2A6, and CYP2E1. *Arch. Biochem. Biophys.* 345(2):342-354.

58. C. Sanders and H. Lill (2000) Expression of prokaryotic and eukaryotic cytochromes c in *Escherichia coli*. *Biochim. Biophys. Acta* 1459(1):131-138.

59. S. G. Rupasinghe, H. Duan, H. L. Frericks Schmidt, D. A. Berthold, C. M. Rienstra, and M. A. Schuler (2007) High-yield expression and purification of isotropically labeled cytochrome P450 monooxygenases for solid-state NMR spectroscopy. *Biochim. Biophys. Acta* 1768(12):3061-3070.

60. S. Wagner, M. M. Klepsch, S. Schlegel, A. Appel, R. Draheim, M. Tarry, M. Hogbom, K. J. van Wijk, D. J. Slotboom, J. O. Persson, and J. W. de Gier (2008) Tuning *Escherichia coli* for membrane protein overexpression. *Proc. Natl. Acad. Sci. U. S. A.* 105(38):14371-14376.

61. Y. Y. Londer (2011) Expression of recombinant cytochromes c in *E. coli*. *Methods Mol. Biol.* 705:123-150.

62. J. M. Shifman, B. R. Gibney, R. E. Sharp, and P. L. Dutton (2000) Heme redox potential control in *de novo* designed four-alpha-helix bundle proteins. *Biochemistry* 39(48):14813-14821.

63. I. H. Saraiva, D. K. Newman, and R. O. Louro (2012) Functional characterization of the FoxE iron oxidoreductase from the photoferrotroph *Rhodobacter ferrooxidans* SW2. *J. Biol. Chem.* 287(30):25541-25548.

64. L. P. Vernon, J. H. Mangum, J. V. Beck, and F. M. Shafia (1960) Studies on a ferrous-ion-oxidizing bacterium. II. Cytochrome composition. *Arch. Biochem. Biophys.* 88:227-231.

65. B. A. Blaylock and A. Nason (1963) Electron Transport Systems of the Chemoautotroph *Ferrobacillus Ferrooxidans*. I. Cytochrome C-Containing Iron Oxidase. *J. Biol. Chem.* 238:3453-3462.

66. M. Firer-Sherwood, G. S. Pulcu, and S. J. Elliott (2008) Electrochemical interrogations of the Mtr cytochromes from *Shewanella*: opening a potential window. *J. Biol. Inorg. Chem.* 13(6):849-854.

67. S. Seeliger, R. Cord-Ruwisch, and B. Schink (1998) A periplasmic and extracellular c-type cytochrome of *Geobacter sulfurreducens* acts as a ferric iron reductase and as an electron carrier to other acceptors or to partner bacteria. *J. Bacteriol.* 180(14):3686-3691.

68. K. L. Straub, M. Benz, and B. Schink (2001) Iron metabolism in anoxic environments at near neutral pH. *FEMS Microbiol. Ecol.* 34(3):181-186.

69. W. Stumm and G. F. Lee (1960) The chemistry of aqueous iron. *Schweizerische Zeitschrift für Hydrologie* 22:295-319

70. F. Widdel, S. Schnell, S. Heising, A. Ehrenreich, B. Assmus, and B. Schink (1993) Ferrous iron oxidation by anoxygenic phototrophic bacteria. . *Nature* 362:834-836

71. B. Thamdrup (2000) Bacterial manganese and iron reduction in aquatic sediments. *Advances in Microbial Ecology* 16:41-84.

72. U. Schwertmann and R. M. Cornell (2000) *Iron oxides in the laboratory : preparation and characterization* (Wiley-VCH, Weinheim ; New York) 2nd completely rev. and extended Ed pp xviii, 188 p.

73. C. Ruby, C. Upadhyay, A. Gehin, G. Ona-Nguema, and J. M. Genin (2006) *In situ* redox flexibility of FeII-III oxyhydroxycarbonate green rust and fougerite. *Environ. Sci. Technol.* 40(15):4696-4702.

74. H. K. Carlson, I. C. Clark, S. J. Blazewicz, A. T. Iavarone, and J. D. Coates (2013) Fe(II) oxidation is an innate capability of nitrate-reducing bacteria that involves abiotic and biotic reactions. *J. Bacteriol.* 195(14):3260-3268.

75. Y. Li, O. Raschdorf, K. T. Silva, and D. Schuler (2014) The terminal oxidase cbb3 functions in redox control of magnetite biomineralization in *Magnetospirillum gryphiswaldense*. *J. Bacteriol.* 196(14):2552-2562.

76. Y. Li, E. Katzmann, S. Borg, and D. Schuler (2012) The periplasmic nitrate reductase Nap is required for anaerobic growth and involved in redox control of magnetite biomineralization in *Magnetospirillum gryphiswaldense*. *J. Bacteriol.* 194(18):4847-4856.

Chapter 3: *Purification of putative iron mineral-templating peptides and their interaction with magnetite and magnetite precursors*

3.1. Introduction

Magnetite nanocrystals are co-localized in the magnetosome vesicle with several magnetosome island-derived proteins, including a set of tightly bound small proteins that can only be removed from the mineral upon boiling under denaturing conditions [1]. This family of proteins, called the Mms proteins, includes Mms5 (MamG), Mms6, Mms7 (MamD), MmsF, and Mms13 (MamC) and are located within two adjacent clusters (*mamCDFG* and *mms6*) in the *Magnetospirillum magneticum* AMB-1 island [2]. Sequence analysis of the Mms6 family proteins indicate that these proteins share common properties including an N-terminal hydrophobic portion comprising a putative transmembrane segment and self-assembly related sequence as well as a C-terminal acidic portion that could interact with the mineral. The critical function of the Mms6 family proteins in magnetite biomineralization are supported by genetic studies, which have demonstrated that disruption of these genes lead to shape and size defects in mineralization [3, 4]. It has been suggested that members of the family share some redundant function and control the morphology of the crystal in a cumulative manner [5], a theory which recently has been confirmed by careful analysis of *mms* genetic knockout strains [6]. Further *in vitro* magnetite synthesis studies with Mms6 have shown that the inclusion of the Mms6 protein in a colloidal synthesis leads to tighter size distributions of nanocrystals [7] and that changes in crystal size and morphology compared to purely synthetic magnetite can be observed with high-resolution TEM [8, 9].

Based on their sequence characteristics and *in vitro* and *in vivo* mineralization function, it seems likely that the Mms proteins play an analogous role to templating proteins involved in calcium or silica biomineralization, which can self-assemble using one domain to provide a multimeric array of functional groups on another domain that can stabilize mineral growth by binding interactions [10, 11] (*Figure 3.1*). Therefore, control over magnetite size and shape should be dependent on both N- and C-terminal sequences of the Mms6 family proteins: the C-terminal domain interacts directly with the mineral to template its formation and the N-terminal segment self-assembles to control how the mineral-binding sequence is presented to the growing nanocrystal. We have therefore focused on establishing an *in vitro* biochemical system to study interactions between Mms proteins and magnetite in order to elucidating the design principles that determine size and shape of the nanocrystals. As metal-binding peptides can control the size, shape, crystallinity, and ion composition of nanocrystals, understanding the design principles of the Mms6 family proteins would facilitate efforts to engineer the magnetosome for new synthetic functions.

Despite the challenge of isolating different Mms6 family protein constructs due to their unusual sequence and small size, we have been able to purify many of these proteins to homogeneity for *in vitro* mineral-binding and mineral synthesis studies. In particular, we focused on cloning and purifying the metal-binding C-terminal segment of Mms6 family proteins from species of magnetotactic bacteria that crystallize magnetite with different habits in order to explore the molecular basis for stabilization of different magnetite faces. We also constructed several N-terminal fusions of short amino acids sequences with defined quaternary structure based on either α-helix or β-sheet motifs with the C-terminal mineral binding domain of Mms6 in order to examine the role of the N-terminal sequence in *in vitro* size and shape control. To characterize these protein constructs, we have developed *in vitro* binding studies with purified Mms6 family proteins to show that they are capable of binding and stabilizing non-(111) faces of magnetite and that the N-terminus plays a role in binding to magnetite. We have also used *in vitro* iron mineralization

reactions to show that the Mms6 family proteins can work synergistically with the redox protein MamP to produce mixed-valent iron oxides from soluble Fe(II) species and to control mineral structure.
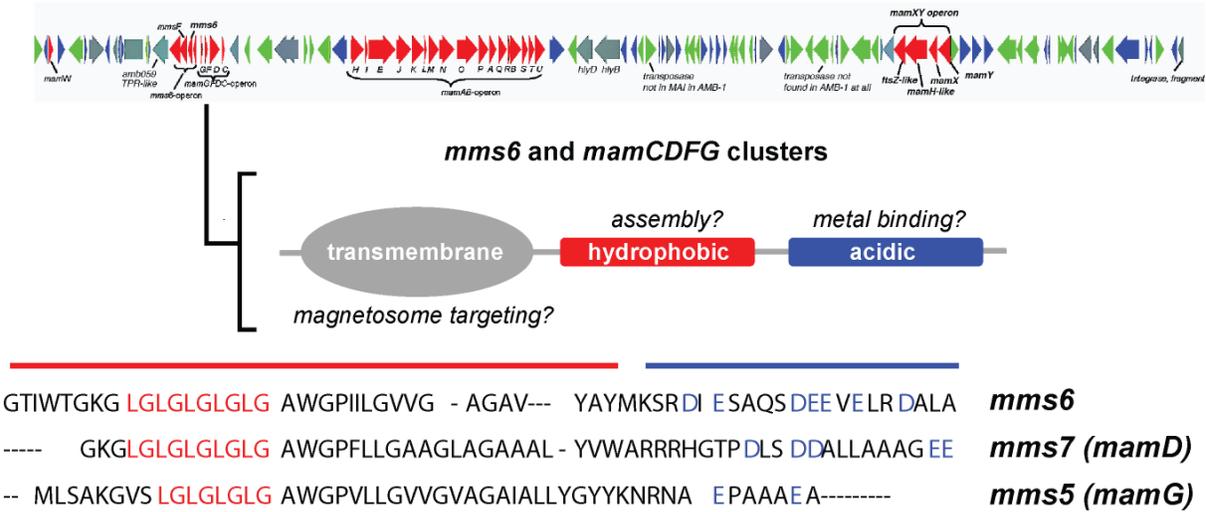

Figure 3.1. The structure of templating proteins from the MamCDFG and Mms6 clusters. Sequence analysis of the Mms proteins indicate that these proteins share common properties including an N-terminal hydrophobic portion comprising a putative transmembrane segment and self-assembly related sequence. The C-terminal segment is highly acidic and likely interacts with the mineral.

3.2. Materials and methods

   Reagent information. Luria-Bertani (LB) Broth Miller, Terrific Broth, LB Agar Miller, sodium thiosulfate, and glycerol were purchased from EMD Biosciences (Darmstadt, Germany). Carbenicillin (Cb), isopropyl-β-D-thiogalactopyranoside (IPTG), phenylmethanesulfonyl fluoride (PMSF), tris(hydroxymethyl)aminomethane base (Tris), sodium chloride (NaCl), dithiothreitol (DTT), 4-(2-hydroxyethyl)-1-piperazineethanesulfonic acid (HEPES), magnesium chloride hexahydrate, potassium chloride, potassium phosphate monobasic, potassium phosphate dibasic, D-sucrose, kanamycin (Km), ethylene glycol, ethylene diamine tetraacetic acid disodium dihydrate (EDTA), bromophenol blue sodium salt, anhydrous sodium acetate, methanol, L-ascorbic acid, sodium acetate, guanidine hydrochloride, and 30% hydrogen peroxide were purchased from Fisher Scientific (Pittsburgh, PA). Chloramphenicol, methylsulfoxide (DMSO), hydrochloric acid, glacial acetic acid, sodium nitrate, potassium nitrate, ammonium hydroxide, potassium hydroxide, and sodium hydroxide (NaOH) were purchased from EMD Millipore (Billerica, MA). β-mercaptoethanol, ammonium bicarbonate, sodium dithionite, sodium phosphate dibasic hepthydrate, N,N,N',N'-tetramethyl-ethane-1,2-diamine (TEMED), ammonium iron(II) sulfate hexahydrate, iron (II) chloride, magnesium sulfate heptahydrate, manganese(II) sulfate monohydrate, cobalt(II) chloride hexahydrate, calcium chloride, zinc sulfate heptahydrate, copper(II) sulfate pentahydrate, aluminum potassium sulfate dodecahydrate, boric acid, sodium molybdate dehydrate, succinic acid, biotin, folic acid, pyridoxine hydrochloride, thiamine hydrochloride, riboflavin, calcium D-(+)-pantothenate, vitamin B-12, *p*-aminobenzoic acid, thioctic acid, nicotinic acid, d-desthiobiotin, diaminopimelic acid (DAP), and sinapic acid were purchased from Sigma-Aldrich (St. Louis, MO). Imidazole and formic acid were purchased from Acros Organics (Morris Plains, NJ). Nitrilotriacetic acid was purchased from Eastman Organic Chemicals. Acrylamide/Bis-acrylamide (30%, 37.5:1), electrophoresis grade sodium dodecyl sulfate (SDS) and ammonium persulfate were purchased from Bio-Rad Laboratories (Hercules, CA). Restriction enzymes, T4 DNA ligase, Antarctic phosphatase, Phusion DNA polymerase, T5 exonuclease, and Taq DNA ligase were purchased from New England Biolabs (Ipswich, MA). Deoxynucleotides (dNTPs) and Platinum Taq High-Fidelity polymerase (Pt Taq HF) were purchased from Invitrogen (Carlsbad, CA). PageRuler™ Plus prestained protein ladder was purchased from Fermentas (Glen Burnie, Maryland). Oligonucleotides were purchased from Integrated DNA Technologies (Coralville, IA), resuspended at a stock concentration of 100 µM in 10 mM Tris-HCl, pH 8.5, and stored at either 4°C for immediate use or -20°C for longer term use. DNA purification kits and Ni-NTA agarose were purchased from Qiagen (Valencia, CA). Recombinant RNAse-free DNAse I and Complete EDTA-free protease inhibitor were purchased from Roche Applied Science (Penzberg, Germany). TEV protease was purchased from the QB3 MacroLab at UC Berkeley. Amicon Ultra 3,000 MWCO and 10,000 MWCO centrifugal concentrators and 5,000 MWCO and 10,000 MWCO regenerated cellulose ultrafiltration membranes were purchased from EMD Millipore (Billerica, MA). Mass spectral analyses were carried out at the College of Chemistry Mass Spectrometry Facility at UC Berkeley.

   Bacterial strains. *E. coli* DH10B-T1^R was used for DNA construction. *E. coli* BL21(DE3) was used for heterologous protein production of Mms6 family proteins. *E. coli* WM3064 was used for conjugative transfer of plasmids into *M. magneticum* AMB-1 wild-type (AK30) and knockout Δ*mamP* (AK69) [*3*, *12*].

   Plasmid construction. Standard molecular biology techniques were used to carry out plasmid

construction. All PCR amplifications were carried out with Phusion DNA polymerase. For amplification of GC-rich sequences from *M. magneticum* AMB-1 (AMB-1), PCR reactions were supplemented with DMSO (5%) with primer annealing temperatures 8-10°C below the melting temperature (T_m) calculated using OligoCalc [13]. Plasmids were assembled either using the Gibson method [14] or restriction digest and ligation. All constructs were verified by sequencing (Quintara Biosciences; Berkeley, CA).

Plasmids for heterologous expression of Mms6 family proteins in *E. coli*. The plasmids for heterologous expression of Mms6 family proteins in *E. coli* were constructed as follows:

pCR2.1-MBPtev.sMms7mat. The sequence for the synthetic gene encoding mature Mms7 (MamD; Mms7mat, residues 260-314 [1]) was optimized for *E. coli* class II codon usage using Gene Designer from DNA 2.0 [15]. The sMms7mat fragment was assembled for a SOE reaction with MBP by extension of two overlapping primers (sMms7.Nt F1/sMms7.Ct R1) in a reaction that included that included the SOE primers (sMms7.SOE F1/sMms7 R1) primers. The MBP fragment was amplified from pSV272.1 with the MBP F1/sMms7.SOE R1 primers. The two individual fragments were then combined in a SOE reaction to produce MBPtev.sMms7mat by rescue with the MBP F1/sMms7 R1 primers. The product was then gel purified and inserted into the pCR2.1 plasmid by TA cloning (Invitrogen).

pET16sx-Strep.MBPtev.sMms7mat. The pET16sx-Strep.MBPtev.sMms7mat plasmid was constructed by amplification of the MBPtev.sMms7mat cassette from pCR2.1-MBPtev.sMms7mat using the MBP F1/sMms7 R1 primers and insertion into the NdeI-SpeI site of pET16sx.

pET16sx-Strep.MBPtev.Mms7ct. The plasmid pET16sx-Strep.MBPtev.Mms7ct was constructed by nested PCR by amplification of the sequence encoding the Mms7 C-terminus (Mms7ct, residues 290-314 [1]) from AMB-1 genomic DNA with the Mms7ct linker/Mms7ct R1 primers followed by amplification of the PCR product with the Mms7ct F1/R1 primers. The product of the second PCR was then inserted into the SacI-SpeI site of pET16sx-Strep.MBPtev.sMms7mat to yield pET16sx-Strep.MBPtev.Mms7ct.

pSV272.1-His$_6$.MBPtev.Mms6mat. The sequence for the synthetic gene encoding mature Mms6 (Mms6mat, residues 98-157 [1]) was optimized for *E. coli* class II codon usage using Gene Designer from DNA 2.0 [15]. The Mms6mat fragment was assembled for a SOE reaction in two pieces. The N-terminal fragment was amplified by primer extension with the primers Mms6mat F1/Mms6mat R1. The C-terminal fragment was amplified by primer extension with the primers Mms6mat F2/Mms6mat R2. The two individual fragments were then combined in a SOE reaction to produce Mms6mat by rescue with the 6mat rescue F1/6mat rescue R1 primers.

pSV272.1-His$_6$.MBPtev.Mms6ct. The sequence for the synthetic gene encoding the putative metal-binding peptide Mms6ct (Mms6ct, residues 128-157 [1]) was optimized for *E. coli* class II codon usage using Gene Designer from DNA 2.0 [15]. The pSV272.1-His$_6$.MBPtev.Mms6ct plasmid was constructed by using primer extension to construct the Mms6 C-terminus with 6ct.AMB1 F1/R1. The gene was inserted in the pSV272.1 expression vector through the KasI-BamHI restriction site.

pSV272.1-His₆.MBPtev.Mms6ct.MSR-1. The sequence for the synthetic gene encoding the C-terminal 30 residue putative metal-binding region of Mms6 from *Magnetospirillum gryphiswaldense* MSR-1 (Mms6ct.MSR-1, residues 130-159 [*16*]) was optimized for *E. coli* class II codon usage using Gene Designer from DNA 2.0 [*15*]. The pSV272.1-His₆.MBPtev.Mms6ct.MSR-1 plasmid was constructed by amplifying Mms6ct.MSR-1 by primer extension with 6ct.MSR1 F1/6ct.MSR1 R1 and inserting into pSV272.1 at the SfoI site.

pSV272.1-His₆.MBPtev.Mms7ct.MSR-1. The sequence for the synthetic gene encoding the C-terminal 27 residue putative metal-binding region of Mms7 from *Magnetospirillum gryphiswaldense* MSR-1 (Mms7ct.MSR-1, residues 288-314 [*16*]) was optimized for *E. coli* class II codon usage using Gene Designer from DNA 2.0 [*15*]. The pSV272.1-His₆.MBPtev.Mms7ct.MSR-1 plasmid was constructed by amplifying Mms7ct.MSR-1 by primer extension with 7ct.MSR1 F1/7ct.MSR1 R1 and inserting into pSV272.1 at the SfoI site.

pSV272.1-His₆.MBPtev.Mms6ct.MV-1. The sequence for the synthetic gene encoding the C-terminal 30 residue putative metal-binding region of Mms6 from *Magnetovibrio blakemorei* MV-1 (Mms6ct.MV-1, residues 48-77 [*17*]) was optimized for *E. coli* class II codon usage using Gene Designer from DNA 2.0 [*15*]. The pSV272.1-His₆.MBPtev.Mms6ct.MV-1 plasmid was constructed by amplifying Mms6ct.MV-1 by primer extension with 6ct.MV1 F1/6ct.MV1 R1 and inserting into pSV272.1 at the SfoI site.

pSV272.1-His₆.MBPtev.Mms7ct.MV-1. The sequence for the synthetic gene encoding the C-terminal 28 residue putative metal-binding region of Mms7 from *Magnetovibrio blakemorei* MV-1 (Mms7ct.MV-1, 188-215 [*17*]) was optimized for *E. coli* class II codon usage using Gene Designer from DNA 2.0 [*15*]. The psv272.1-His₆.MBPtev.Mms7ct.MV-1 plasmid was constructed by amplifying Mms7ct.MV-1 by primer extension with 7ct.MV1 F1/7ct.MV1 R1 and inserting into pSV272.1 at the SfoI site.

pSV272.1-His₆.MBPtev.Mms6ct.MC-1. The sequence for the synthetic gene encoding the C-terminal 26 residue putative metal-binding region of Mms6 from *Magnetococcus marinus* MC-1 (Mms6ct.MC-1, 169-194 [*16*]) was optimized for *E. coli* class II codon usage using Gene Designer from DNA 2.0 [*15*]. The psv272.1-His₆.MBPtev.Mms6ct.MC-1 plasmid was constructed by amplifying Mms6ct.MC-1 by primer extension with 6ct.MSR1 F1/6ct.MC1 R1 and inserting into pSV272.1 at the SfoI site.

pSV272.1-His₆.MBPtev.Mms7ct.Fos001. The sequence for the synthetic gene encoding the C-terminal 29 residue putative metal-binding region of Mms7 from an uncultured magnetotactic bacterium (Mms7ct.Fos001, 117-146 [*2*]) was optimized for *E. coli* class II codon usage using Gene Designer from DNA 2.0 [*15*]. The psv272.1-His₆.MBPtev.Mms7ct.MV-1 plasmid was constructed by amplifying Mms7ct.Fos001 by primer extension with 7ct.Fos001 F1/7ct.Fos001 R1 and inserting into pSV272.1 at the SfoI site.

pSV272.1-His₆.MBPtev.Mms6ct.ΔE. In order to mutate the putative metal-binding glutamate residues to alanines, the pSV272.1-His₆.MBPtev.Mms6ct.ΔE plasmid was constructed by amplifying Mms6ct.ΔE by primer extension with 6ct.ΔE F1/6ct.ΔE R1 and inserting into pSV272.1 at the SfoI site.

pSV272.1-His₆.MBPtev.Mms7ct.ΔE. In order to mutate the putative metal-binding glutamate residues to alanines, the pSV272.1-His₆.MBPtev.Mms7ct.ΔE plasmid was constructed by amplifying Mms7ct.ΔE by primer extension with 7ct.ΔE F1/7ct.ΔE R1 and inserting into pSV272.1 at the SfoI site.

pSV272.1-His₆.MBPtev.FF1.Mms6. The sequence for the synthetic gene encoding a β-sheet fibril-forming peptide (FF1, NSGAITIG [18]) was optimized for *E. coli* class II codon usage using Gene Designer from DNA 2.0 [15] and fused to the N-terminus of Mms6ct. The pSV272.1-His₆.MBPtev.FF2.Mms6 plasmid was constructed by amplifying the pSV272.1-His₆.MBPtev.Mms6mat vector with overlapping primers FF1 F1/FF1 R1 and assembling by the Gibson method [14].

pSV272.1-His₆.MBPtev.FF2.Mms6. The sequence for the synthetic gene encoding a β-sheet fibril-forming peptide (FF2, QQRFQWQFEQQ [19]) was optimized for *E. coli* class II codon usage using Gene Designer from DNA 2.0 [15] and fused to the N-terminus of Mms6ct. The pSV272.1-His₆.MBPtev.FF2.Mms6 plasmid was constructed by amplifying the pSV272.1-His₆.MBPtev.Mms6mat vector with overlapping primers FF2 F1/FF2 R1 and assembling by the Gibson method [14].

pSV272.1-His₆.MBPtev.Melittin.Mms6. The sequence for the synthetic gene encoding an α-helix-forming peptide (truncated Melittin, GIGAVLKVLTTGLPALISWI [20, 21]) was optimized for *E. coli* class II codon usage using Gene Designer from DNA 2.0 [15] and fused to the N-terminus of Mms6ct. The pSV272.1-His₆.MBPtev.Melittin.Mms6 plasmid was constructed by amplifying the pSV272.1-His₆.MBPtev.Mms6mat vector with overlapping primers Mel F1/Mel R1 and assembling by the Gibson method [14].

Plasmids for expression of Mms proteins in *M. magneticum* AMB-1. The plasmids for expression of Mms6 family proteins in *M. magneticum* AMB-1 were constructed as follows:

pAK262Amp-MmsF.Mms6. The pAK262Amp-MmsF.Mms6 plasmid was constructed by amplifying *mmsF* and *mms6* from AMB-1 genomic DNA with the primers MmsF6 F1/MmsF6 R1 and MmsF6 F2/MmsF6 R2, respectively, and inserting into pAC262Amp-MamP at the EcoRI-SpeI site with the Gibson assembly method [14].

pAK262Amp-MmsF. The pAK262Amp-MmsF plasmid was constructed by amplifying *mmsF* from the pAK262Amp-MmsF.Mms6 plasmid with the primers MmsF F1/MmsF R1 and the pAK262Amp backbone from pAK262Amp-MamP with the primers MmsF F2/MmsF R2 and inserting into pAC262Amp-MamP at the EcoRI-SpeI site with the Gibson assembly method [14].

pAK262Amp-Mms6. The pAK262Amp-Mms6 plasmid was constructed by amplifying *mms6* from the pAK262Amp-MmsF.Mms6 plasmid with the primers Mms6 F1/Mms6 R1 and the pAK262Amp backbone from pAK262Amp-MamP with the primers Mms6 F2/Mms6 R2 and inserting into pAC262Amp-MamP at the EcoRI-SpeI site with the Gibson assembly method [14].

Heterologous expression of Mms proteins. TB (5 × 1 L) containing Cb (50 µg/mL) for pET16sx vectors or Km (50 µg/mL) for pSV272 vectors and glucose (0.1% w/v) in a 2.8 L Fernbach baffled shake flask was inoculated to OD₆₀₀ = 0.05 with an overnight TB culture of freshly-transformed *E. coli* BL21(DE3) with the Mms6 family protein expression vector. The

cultures were grown at 37°C at 200 rpm to $OD_{600} = 0.6$ to 0.8 at which point cultures were cooled on ice for 20 min, followed by induction of protein expression with 1 mM IPTG and overnight growth at 16°C. Cell pellets were harvested by centrifugation at $9,800 \times g$ for 7 min at 4°C and stored at -80°C.

Purification of Mms6 family protein constructs. A subset of Mms6 family protein constructs were purified for studies. Frozen cell pellets were thawed and resuspended at 5 mL/g cell paste with lysis buffer (50 mM Tris base pH 8.0, 200 mM NaCl, 1 mM EDTA, 5 mM DTT) supplemented with Complete EDTA-free protease inhibitor cocktail (1 tablet/50 mL, Roche) and PMSF (1 mM). The cell paste was homogenized and DNase I (1 uL/10 mL cell resuspension) was added before lysis by passage through a French Pressure cell (Thermo Scientific; Waltham, MA) at 14,000 psi. The lysate was centrifuged at $15,300 \times g$ for 20 min at 4°C to separate the soluble and insoluble fractions.

The soluble lysate was loaded onto an amylose column (NEB, 1 mL resin/g cell paste) by gravity flow. The column was washed with Buffer A (50 mM Tris base pH 8.0, 200 mM NaCl, 1 mM EDTA, 1 mM PMSF) until the eluate reached an $A_{280\ nm} < 0.05$ or was negative for protein content by Bradford assay (Bio-Rad). The column was eluted with Buffer B (20 mM Tris base pH 8.0, 100 mM NaCl, 0.5 mM EDTA, 10 mM maltose, 1 mM PMSF). The eluate was concentrated to 25-40 mL in a 350 mL Amicon Ultrafiltration Stirred Cell (Millipore) fit with a 10 kDa MWCO YM regenerated cellulose membrane.

To the concentrated amylose eluate, His_6-tagged TEV protease (1 mg TEV per 80-100 mg of MBP fusion) was added. After cleaving overnight at 4°C, guanidine-HCl (6 M) was added to the solution and the pH was adjusted to 10. The sample was then filtered using a 350 mL Amicon Ultrafiltration Stirred Cell with a 10 kDa MWCO YM regenerated cellulose membrane to partially remove Strep-MBP and His_6-TEV. When the volume in the Amicon cell reached ~5 mL, additional buffer (50 mM Tris pH 10.0 containing 6 M guanidine-HCl, 150 mL) was added to wash the membrane of adsorbed Mms7ct. Both filtrates were collected and pooled for purification by HPLC. As the chemical character of the Mms6 family proteins differ, the HPLC column purification was optimized for each protein

Isolation of Mms7ct and Mms7ct homologs. The Zorbax SB C_{18} column (21.2 × 250 mm, 7 μm, Agilent) was equilibrated with 5% v/v HPLC Buffer B (acetonitrile containing 0.1% v/v TFA) in HPLC Buffer A (ddH₂0 containing 0.1% v/v TFA). Acetonitrile was added directly to the sample to a final concentration of 5% v/v before manual loading of the entire filtrate (~500 mL) onto the column through the Buffer A line (10 mL/min). The column was then washed with 5% v/v HPLC Buffer B until the $A_{260\ nm}$ returned to baseline before applying the following steps (22 mL/min): a 5-10% solvent B gradient for 10 min, a 10-40% solvent B gradient for 40 min, a 40-100% solvent B gradient for 5 min and then hold at 100% solvent B for 5 min. The samples corresponding to peaks in the $A_{280\ nm}$ chromatogram were collected and lyophilized. The lyophilized sample was resuspended in ddH₂O. The extinction coefficient of Mms7ct was calculated to be 6990 cm^{-1} M^{-1} at 280 nm by ExPasy ProtParam [22] and used to estimate the concentration. The extinction coefficients for Mms7ct homologs were calculated in the same way (Mms7ct.MSR-1, 6990 cm^{-1} M^{-1}; Mms7ct.MV-1, 5960 cm^{-1} M^{-1}; Mms7ct.Fos001, 4470 cm^{-1} M^{-1}; Mms7ct.ΔE, 6990 cm^{-1} M^{-1}). Because Mms7ct was unable to be visualized by Coomassie staining due to its composition and small size, analytical HPLC

and mass spectrometry were used to confirm the identity and purity of the protein. For Mms7ct from AMB-1, the calculated [M-H$^+$] m/z was 2826.1 and the found [M-H$^+$] m/z was 2826.4.

Isolation of Mms7mat. The Zorbax SB C$_{18}$ column (21.2 × 250 mm, 7 μm, Agilent) was equilibrated with 5% v/v HPLC Buffer B (acetonitrile containing 0.1% v/v TFA) in HPLC Buffer A (ddH$_2$0 containing 0.1% v/v TFA). Acetonitrile was added directly to the sample to a final concentration of 5% v/v before manual loading of the entire filtrate (~500 mL) onto the column through the Buffer A line (10 mL/min). The column was then washed with 5% v/v HPLC Buffer B until the A$_{260\ nm}$ returned to baseline before applying the following steps (22 mL/min): a 5-30% solvent B gradient for 10 min, a 30-60% solvent B gradient for 40 min, a 60-100% solvent B gradient for 5 min and then hold at 100% solvent B for 15 min. The samples corresponding to peaks in the A$_{280\ nm}$ chromatogram were collected and lyophilized. The lyophilized sample was resuspended in ddH$_2$O. The extinction coefficient of Mms7mat was calculated to be 12,490 cm^{-1} M^{-1} at 280 nm by ExPasy ProtParam [22] and used to estimate the concentration. Because Mms7mat was unable to be visualized by Coomassie staining due to its composition and small size, analytical HPLC and mass spectrometry were used to confirm the identity and purity of the protein. For Mms7mat from AMB-1, the calculated [M-H$^+$] m/z was 5542.3 and the found [M-H$^+$] m/z was 5542.0.

Isolation of Mms6ct and Mms6ct homologs. The Zorbax SB C$_{18}$ column (21.2 × 250 mm, 7 μm, Agilent) was equilibrated with 5% v/v HPLC Buffer B (acetonitrile containing 0.1% v/v TFA) in HPLC Buffer A (ddH$_2$0 containing 0.1% v/v TFA). Acetonitrile was added directly to the sample to a final concentration of 5% v/v before manual loading of the entire filtrate (~500 mL) onto the column through the Buffer A line (10 mL/min). The column was then washed with 5% v/v HPLC Buffer B until the A$_{260\ nm}$ returned to baseline before applying the following steps (22 mL/min): a 5-10% solvent B gradient for 10 min, a 10-40% solvent B gradient for 40 min, a 40-100% solvent B gradient for 5 min and then hold at 100% solvent B for 5 min. The samples corresponding to peaks in the A$_{280\ nm}$ chromatogram were collected and lyophilized. The lyophilized sample was resuspended in ddH$_2$O. The extinction coefficient of Mms6ct was calculated to be 2,980 cm^{-1} M^{-1} at 280 nm by ExPasy ProtParam [22] and used to estimate the concentration. The extinction coefficients of the Mms6ct homologs were estimated with the same technique (Mms6ct.MSR-1, 2980 cm^{-1} M$^{-1;}$ Mms6ct.MV-1, 2980 cm^{-1} M^{-1}; Mms6ct.MC-1, 1490 cm^{-1} M^{-1}; Mms6ct.ΔE, 2980 cm^{-1} M^{-1}). Because Mms6ct was unable to be visualized by Coomassie staining due to its composition and small size, analytical HPLC and mass spectrometry were used to confirm the identity and purity of the protein. For Mms6ct from AMB-1, the calculated [M-H$^+$] m/z was 3342.5 and the found [M-H$^+$] m/z was 3342.7.

Isolation of Mms6mat. The Zorbax SB C$_{18}$ column (21.2 × 250 mm, 7 μm, Agilent) was equilibrated with 5% v/v HPLC Buffer B (acetonitrile containing 0.1% v/v TFA) in HPLC Buffer A (ddH$_2$0 containing 0.1% v/v TFA). Acetonitrile was added directly to the sample to a final concentration of 5% v/v before manual loading of the entire filtrate (~500 mL) onto the column through the Buffer A line (10 mL/min). The column was then washed with 5% v/v HPLC Buffer B until the A$_{260\ nm}$ returned to baseline before applying the following steps (22 mL/min): a 5-30% solvent B gradient for 10 min, a 30-60% solvent B gradient for 40 min, a 60-100% solvent B gradient for 5 min and then hold at 100% solvent B for 15 min. The samples corresponding to peaks in the A$_{280\ nm}$ chromatogram were collected and lyophilized. The

lyophilized sample was resuspended in ddH_2O. The extinction coefficient of Mms6mat was calculated to be 13,980 cm^{-1} M^{-1} at 280 nm by ExPasy ProtParam [22] and used to estimate the concentration. Silver-stained SDS-PAGE gel electrophoresis, analytical HPLC, and mass spectrometry were used to confirm the identity and purity of the protein. For Mms6mat from AMB-1, the calculated [M-H+] *m/z* was 5959.8 and the found [M-H+] *m/z* was 5959.7.

MALDI-MS of Mms proteins. The matrix was prepared by dissolving sinapic acid (10 mg/mL) in 70% v/v acetonitrile containing 0.1% TFA. The lyophilized sample was resuspended in ddH_2O and an aliquot (1 µL) was mixed with the matrix solution (10 µL) and spotted on a MALDI plate for analysis after drying in air. The MALDI spectra were collected in positive ion mode.

SDS-PAGE gels. Samples were prepared for loading onto a gel by incubation for 15 min at room temperature with a Laemmli sample buffer with β-mercaptoethanol (4× stock: 0.25 M Tris-HCl, 2% SDS, 40% glycerol, 0.04% bromophenol blue). The sample was analyzed by SDS-PAGE at room temperature following literature protocol [23] on a standard 12 w/v% acrylamide gel at 150 V for approximately 60-80 min. The gels were then stained with Coomassie using standard protocols to visualize total protein content.

Synthesis of $Fe(II)Fe(III)_2O_4$ magnetite. The protocol for the synthesis of magnetite was adapted from literature protocols [24]. A solution of sodium hydroxide (21 mM) in ddH_20 (475 mL) was deaerated with Ar in a 1 L sealed three-neck flask through a glass bubbler with single needle gas outlet (21G × 1.5 in, BD PrecisionGlide). The solution was heated to 37°C under Ar, solid sodium nitrate (0.75 g) was added under argon back pressure, and the resulting solution was deaerated for 1.5 h. Iron (II) chloride (0.380 g) was prepared in a separate round-bottom flask with a stir-bar. The solid was deaerated by 3 × evacuation and refilling by N_2 gas. Deaerated ddH_20 (30 mL) was added to the iron (II) chloride and mixed by stirring. Iron (II) chloride was transferred to the bubbling NaOH solution dropwise via air-tight syringe. The nanoparticles were allowed to mature for 12 h at 37°C before isolation by spinning down in a centrifuge for 15,300 × *g* for 20 min. The nanoparticles were washed with 2 × 300 mL deaerated ddH_2O and resuspended in 100 mL ddH_20. The resuspended particles were frozen in liquid nitrogen and dried on a lyophilizer. The resulting powder was then transferred to anaerobic tubes (15 mL) in single-use batches and deaerated with Ar for storage at -20°C.

Transmission electron microscopy of magnetite samples. Magnetite was resuspended in ddH_2O and the particles were adsorbed onto 400-mesh copper grid coated with Formvar/Carbon (TedPella Inc.) and analyzed using a TECNAI 12 TEM (FEI) operating at 120 kV with a charge-coupled device camera (Gatan UltraScan, University of California at Berkeley Electron Microscope Laboratory). Over 75 nanoparticles were analyzed for each synthesis.

Powder x-ray diffraction of magnetite samples. Powder x-ray diffraction (XRD) samples were characterized on a Bruker AXS D8 Advance diffractometer, which uses an incident Co K_α radiation of 1.79026 Å. The output of the diffractometer is 2Θ or 2 × the angle between the incident ray and the scattering planes. Bragg's Law was used to solve for d, the spacing between the planes in the atomic lattice, with the equation $\lambda = 2dsin\Theta$. The American Mineralologist Crystal Structure Database [25] was compare the d-spacings of the magnetite synthesis to magnetite and maghemite.

Dynamic light scattering (DLS). DLS determined hydrodynamic size was performed at 25°C by dissolving samples in ddH_2O or 0.2 mM potassium phosphate buffer pH 8.5. After brief

sonication of magnetite (0.5 mg/mL) to resuspend, the samples were allowed to aggregate for a set amount of time before briefly resuspending by inversion. The samples were analyzed by a Zetasizer Nanoseries ZS (Malvern Instruments, UK).

Pull-down of Mms6 family proteins by magnetite. Mms proteins were resuspended from lyophilized powder in Magnetite Pull-down Buffer (0.2 mM potassium phosphate pH 8.0) to a stock concentration of 400-800 µM. As Mms7mat and Mms6mat had a tendency to precipitate from solution, all Mms6 family protein solutions were centrifuged at $15,300 \times g$ for 5 min to remove aggregates before introducing protein to the magnetite. Magnetite (8.7 mg/mL) was resuspended in Magnetite Pull-down Buffer and sonicated for 20 min to break up aggregates before immediately distributing to reaction solutions (1 mL) in microcentrifuge tubes (1.5 mL, Eppendorf). Microcentrifuge tubes containing magnetite were sonicated for an additional 20 min before Mms6 family protein or Magnetite Pull-down Buffer was distributed to the tubes to a final concentration of 30 µM. In order to control for the possibility Mms6 family protein self-aggregation over time, it was also added to a tube containing Magnetite Pull-down Buffer without magnetite. The reaction tubes were incubated at 25ºC with rotary shaking (200 rpm) for 3 h and resuspended by inversion every 20 min. After incubation, the reaction tubes were centrifuged at $15,300 \times g$ for 10 min, the supernatant was removed, and the supernatant was re-centrifuged at $15,300 \times g$ for another 10 min.

The absorbance spectra of the supernatant was collected between 200-600 nm on a Beckman Coulter DU800 UV-VIS spectrophotometer fitted with a microcell single-cell holder and a Peltier temperature controller set at 25ºC. The absorbance of the supernatant (100 µL) was measured in a quartz microcell (50 µL; Beckman Coulter, Brea, CA). For each concentration of magnetite, the cell was blanked on the supernatant of the respective magnetite-only reaction tube. The amount of Mms6 family protein bound to magnetite was calculated by subtracting the amount of Mms6 family protein added to the reaction tube from the amount of Mms6 family protein determined from the $A_{280 nm}$ of the supernatant be left in solution. The experiment was performed in triplicate for the same magnetite synthesis and thus same iron oxide surface area. The averages and their standard deviations are reported ($n = 3$).

Synthesis of magnetite in the presence of Mms6 family proteins. A protocol to synthesize magnetite by partial oxidation in the presence of the Mms6 family proteins was adapted from two literature protocols [9, 24]. The pH and redox environment was controlled by potassium hydroxide added to a final concentration of 100 mM and potassium nitrate added to a final concentration of 400 mM in reaction (1 mL total volume) sealed in a glass vial (15×45 mm borosilicate threaded vials, Fisherbrand) with a septum (Sigma-Aldrich Suba-Seal #13). Mms6 family protein (150 µg/mL) was added to the reaction before sealing. The solution was deaerated with Ar by bubbling through a needle ($21G \times 1.5$ in, BD PrecisionGlide) for 20 min. Evaporation was minimized by passing Ar through a bubbler filled with ddH$_2$O between the gas tank and the reaction vial. The glass reaction vials were then heated to 42°C under Ar back pressure and deaerated iron (II) sulfate heptahydrate (30 mM) was added through an air-tight glass syringe. After 12 h incubation without agitation, the reactions were transferred to a microcentrifuge tube and were centrifuged at 15,300 $\times g$ for 5 min. The pellets were washed with 3×1 mL deaerated ddH$_2$O by spinning down the pellet at $15,300 \times g$ for 5 min and resuspending. The pellet was resuspended in ddH$_2$O (200 µL) and an aliquot (2 µL) was deposited and dried onto 400-mesh copper grid coated with Formvar/Carbon (TedPella Inc.) for transmission electron microscopy.

***In vitro* iron mineralization.** MamP (5-25 µM, 500 µL) was exchanged from the phosphate storage buffer into HEPES reaction buffer (50 mM HEPES pH 8.0, 100 mM NaCl) by concentrating and diluting the protein five times in 3,000 MWCO Amicon centrifuge filters (0.5 mL) for a total dilution of ~1:3,125 of the original buffer, as the autooxidation of Fe(II) in phosphate buffer is high. Additional reaction buffer (15 mL) was transferred into a 20 mL borosilicate scintillation vial (Fisherbrand), sealed with a septum (Sigma-Aldrich Suba-Seal #33), and degassed by bubbling Ar gently through the solution with a needle (21G × 1.5 in, BD PrecisionGlide) with a second needle as a purge. Evaporation was minimized by passing Ar through a bubbler filled with ddH_2O between the gas tank and the reaction vial. Ammonium Fe(II) sulfate hexahydrate (125 mg) was used the ferrous iron source because of its air stability in salt form and transferred as a solid into a glass vial (15 × 45 mm borosilicate threaded vials, Fisherbrand) and sealed with a septum (Sigma-Aldrich Suba-Seal #13). The headspace of the vial was then evacuated with Ar using a needle. After 80 min of degassing both the reaction buffer and the solid Fe(II), degassed reaction buffer (2 mL) was introduced to the vial containing the ammonium Fe(II) sulfate solid using an Ar-purged glass syringe to a final concentration of 160 mM and dissolved with gentle agitation.

Empty glass reaction vials (15 × 45 mm borosilicate threaded vials, Fisherbrand) were sealed with septa (Sigma-Aldrich Suba-Seal #9) and degassed with Ar for 30 min using a needle. Reaction buffer (425 µL) was then added with an Ar-purged airtight glass syringe, followed by Fe(II) (150 µL, 40 mM final concentration). All vials were kept under partial Ar pressure after introduction of Fe(II) by delaying the removal of the Ar needle for an additional min after removal of the venting needles from the reaction vials. At this time, undegassed MamP (25 µL) or reaction buffer (25 µL) was immediately introduced via Ar-purged glass syringe to a final concentration of 2.5 µM to initiate the reaction (t = 0 min) and agitated gently to mix. Over the course mineralization reaction, the vials were agitated gently at 10 min intervals and with ambient air (20 µL) was introduced via a glass syringe at t = 10 min and 20 min to turn over MamP.

The conditions were modified slightly for Mms7ct reactions. The final Fe(II) concentration was reduced from 40 mM to 20 mM and the final MamP concentration from 2.5 µM to 1.2 µM . The pH of the reaction buffer was also changed to pH 7.5. The Mms7ct protein was resuspended in reaction buffer (pH 7.5, 100-200 µL) and added to a final concentration of 45 µM to the empty reaction vial prior to sealing with a septum and degassing with Ar using a needle for 30 min. Buffer and Fe(II) was added as described previously before the vial was removed from the Ar tank. Finally, MamP was added to initiate the reaction and ambient air (20 µL) was introduced at t = 5 min and 10 min. The septa were removed at 20 min and replaced with screw tops, which were closed loosely to allow air to circulate freely for the remaining time of the reaction. These were the conditions for all *in vitro* mineralization reaction with Mms6 family proteins unless otherwise noted in the text.

***Magnetospirillum magneticum* AMB-1 cell culture.** AMB-1 was grown using Magnetic Growth (MG) media [3] with Wolfe's mineral solution omitting tartaric acid, Wolfe's vitamin solution, and iron malate (100× stock made from 3 mM $FeCl_3$ and 9 mM DL-malic acid). Solid media was generated by the addition of agar (0.7% w/v) to MG media. For antibiotic selection, carbenicillin (Cb) was used at a final concentration of 20 µg/mL in both liquid and solid media. Plasmids were introduced into AMB-1 strains by conjugative transfer with an *E. coli* WM3064 donor strain using literature methods as described [26]. Cultures for mutant screens, C_{mag}

measurements, and TEM characterization were grown in MG media (10 mL) at 30°C without agitation in seal-capped anaerobic culture tubes (20 mL) after degassing the headspace with Ar.

Transformation of *M. magneticum* AMB-1. Plasmids for complementation or gene disruption were introduced into AMB-1 by conjugative transfer from an *E. coli* WM3064 donor strain using literature methods as described [*26*]. The plasmid to be transferred was first transformed into *E. coli* WM3064 by electroporation and plated for growth overnight at 37ºC on LB agar supplemented with the appropriate antibiotic (Cb, 100 µg/mL) and DAP (300 µM). Individual colonies were inoculated into LB (5 mL) containing antibiotic and DAP and grown overnight at 37ºC with rotary shaking (200 rpm). *E. coli* cell cultures (500 µL) were then pelleted by brief centrifugation ($14,000 \times g$) for 1 min at room temperature. The pellets were washed twice with LB DAP (0.5 mL) before resuspending in LB DAP (200 µL). The AMB-1 recipient strain was prepared by inoculation of cells from a freezer stock into a sealed-cap conical tube (50 mL) containing Magnetic Growth media (MG media, 50 mL). All MG media described in this document is prepared according to literature methods and supplemented with iron malate solution ($100\times$ stock made from 3 mM $FeCl_3$ and 9 mM DL-malic acid) and Wolfe's vitamin solution [*3*]. After 2 d growth at 30ºC without agitation, the entire culture volume was pelleted by centrifugation ($14,000 \times g$) for 15 min at 4ºC and resuspended in MG (600 µL). One-third of the resuspended AMB-1 pellet was added to the resuspended *E. coli* pellet (200 µL), the cells were mixed gently, pelleted by brief centrifugation ($14,000 \times g$) for 10 min at room temperature, and resuspended in MG (200 µL). The cells were plated together onto MG DAP agar. The plates were first incubated at room temperature for 1 h before transferring into a sealed microaerobic jar (Oxoid, Ltd.; Basingstoke, UK) at 30ºC for an additional 2-4 h. The jar was evacuated with vacuum until the pressure valve read -0.6 bar and was then refilled with N_2 to a pressure of +0.2 bar. The positive pressure was relieved by venting before the jar was sealed at 0 bar. After this incubation, cell mixtures were scraped off the MG DAP agar plates with a sterile inoculating loop and streaked onto fresh MG agar plates supplemented with the appropriate antibiotic (Cb, 20 µg/mL). These plates were incubated in the microaerobic jar for 4-6 d until colonies could be visualized. Single colonies were inoculated into microcentrifuge tubes (1.5 mL, Eppendorf) completely filled with MG (1.5 mL) and supplemented with the appropriate antibiotic (Cb, 20 µg/mL) to yield primary cultures within 4-8 d of growth at 30ºC with no agitation. After a cell pellet developed in the primary culture, an aliquot of the primary culture (10 µL) was diluted (1:1000) into sealed anaerobic tubes (20 mL) with MG containing 20 mM HEPES pH 7.2 supplemented with the appropriate antibiotic (10 mL) and grown at 30ºC with no agitation until $OD_{400 \text{ nm}} = 0.1\text{-}0.25$ (approximately 2 d) for the secondary culture.

Characterization of cellular magnetization (C_{mag}). Secondary AMB-1 cultures were grown in MG (10 mL) containing 20 mM HEPES pH 7.2 without agitation at 30°C in seal-capped anaerobic culture tubes (20 mL) with Ar-evacuated headspace to $OD_{400 \text{ nm}} = 0.2$ (~2 d). The culture C_{mag} was determined as previously described [*27*]. Briefly, $OD_{400 \text{ nm}}$ was measured on an Agilent 8000 UV-Visible spectrophotometer with a magnet parallel or perpendicular to the spectrometer beam and the ratio ($C_{mag} = A_{400 \text{ nm, perpendicular}}/A_{400 \text{ nm, parallel}}$) was calculated. The C_{mag} measurements were performed in biological triplicates with two technical replicates per colony using cultures from three independent growths or conjugations.

Transmission electron microscopy of AMB-1 samples. Secondary AMB-1 cultures were grown in MG (10 mL) containing 20 mM HEPES pH 7.2 without agitation at 30°C in seal-capped

anaerobic culture tubes (20 mL) with the headspace evacuated with Ar to $OD_{400\,nm} = 0.25$–0.3 (~2-3 d). An aliquot of cell culture (100–500 µL) was pelleted by brief centrifugation (14,000 × g) for 10 min aerobically at room temperature and resuspended in MG (~10 µL). The cells were adsorbed onto 400-mesh copper grid coated with Formvar/Carbon (TedPella Inc.) and analyzed using a TECNAI 12 TEM (FEI) operating at 120 kV with a charge-coupled device camera (Gatan UltraScan, University of California at Berkeley Electron Microscope Laboratory). In each case, 20–50 cells, each containing 1–20 crystals, were analyzed. For each strain, >300 particles from >20 cells was analyzed for three different colonies from each biological replicate.

3.3. Results and discussion

Comparison of Mms proteins across species. The Mms6 family proteins were first identified from the analysis of proteins tightly bound to magnetite particles in *Magnetospirillum magneticum* AMB-1 species [*28*]. Additional members of the family were then subsequently identified by bioinformatic approaches using the sequences of Mms6 and Mms7 (MamD) from AMB-1 [*29*]. The sequences obtained from this BLAST search were aligned by Clustal W2 (*Figure 3.2A*). All Mms6 family proteins contain an N-terminal hydrophobic portion comprising a putative signal sequence/transmembrane segment which is thought to be removed by *in vivo* processing [*1*]. The mature portion of the Mms6 family proteins includes a self-assembly related sequence with an unusual LGLG repeat motif (hereafter referred to as the N-terminus or N-terminal segment) as well as a C-terminal acidic portion that could interact with the mineral by chelating iron atoms. A short conserved motif of positively charged residues are located between the aggregating segment and the mineral binding segment, and could assist in self-assembly [*10, 19, 30*]. The LGLG repeat motif and motif of positive charged residues are highly conserved in amino acid identity and spacing. However, the metal-binding segment, though acidity is maintained, contains considerable diversity in the number, type, and spacing of amino acids, suggesting that the metal-binding segment could be primed to interact with different lattice spacings and thus different facets of the magnetite.

The sequence diversity of the C-terminal metal-binding segment of the Mms family proteins across different species of bacteria is particularly intriguing, as different species of bacteria crystallize magnetite with different crystal parameters (*Figure 3.2B*). For example, *Magnetospirillum magneticum* AMB-1 crystallizes cubo-octahedral magnetite with (111) and (100) facets while *Magnetovibrio blakemorei* MV-1 crystals have (111) and (110) facets. Where AMB-1 is symmetrical, MV-1 is elongated along an axis, implying that there is some further mechanism of kinetic control over mineral faces to introduce anisotropy.

70

Figure 3.2. *Comparison of Mms proteins and crystal habits in different species of magnetotactic bacteria (A) Mms6 and Mms7 aggregation and mineral-binding sequences found in BLAST and aligned using ClustalW2. (B) Different species of magnetotactic bacteria crystallize magnetite with different morphologies. Synthetic magnetite has octahedral shape and reveals the thermodynamically stable (111) lattice face. Kinetic control over biominerals formation allows non-thermodynamically favorable faces to be revealed and anisotropy in the growth of those faces to elongate crystals in one direction.*

Heterologous expression and purification of Mms proteins. We sought to express and purify Mms6 family variants that allow us to investigate their size and shape control of magnetite as well as to explore the diversity of magnetite habits by engineering both the N- and C-terminal self-assembly and mineral binding functions. We built constructs to test the following variants: (1) native and well-studied Mms6 family proteins from the genetically-tractable AMB-1 species, (2) Mms proteins from AMB-1 in which the acidic residues are mutated to alanine or arginine to test the hypothesis that Asp and Glu are the key residues for mineral binding, (3) Mms proteins from other magnetotactic species with known differences in crystal size and morphology to explore the basis for diversity of crystal habits across species, and (4) synthetic Mms hybrids incorporating engineered N-terminal self-assembly domains with naturally-occurring C-terminal sequences to potentially access different crystal shapes or sizes.

We have developed a heterologous expression platform in *E. coli* that allows us to obtain purified metal-free preparations of Mms proteins either as full N-terminal and C-terminal fusions or individual C-terminal domains (*Figure 3.3*). Since proteins <10-15 kD are often degraded in *E. coli*, the Mms6 family protein variants are expressed as a fusion with maltose-binding protein (MBP). Overall, the Mms6 family fusion constructs expressed quite well after induction with IPTG (500 µM) and overnight incubation. Problematic constructs for expression included the highly hydrophobic Mms6ct.ΔE and Mms6ct.ΔE variants, in which all putative metal-binding acidic residues were mutated to alanine.

Maltose-binding protein can also be used as an affinity tag to isolate the His$_6$.MBP-tagged Mms proteins on an amylose column, allowing us to avoid using the metal-based NiNTA column for isolation of our putative metal-binding peptides. Due to the tendencies to aggregate and solubility issues, especially of Mms6mat and Mms7mat, guanidine hydrochloride (6 M) was added to the protein mixture after cleaving the His$_6$.MBPtev.Mms and Strep.MBPtev.Mms fusions by incubation with His$_6$.TEV protease. To partially remove the His$_6$.MBP (~45 kDa) or Strep.MBP (~44 kDa) and His$_6$.TEV (~27 kDa) from the small Mms proteins (2-6 kDa), the protein was then applied to a 10 kDa MWCO and the eluate collected for preparative HPLC purification. The eluate was loaded on a preparative reverse-phase HPLC column under aqueous conditions (1) to allow all salt and guanidine to be washed completely off the column before running the column into organic solvent and (2) to minimize band widening from the large volume loaded on the column as the relatively hydrophobic peptides would remain stacked up at the front of the column until organic solvent (acetonitrile) is applied. The C-terminal peptides such as Mms7 eluted quite cleanly from the column due to their lack of aggregation and ability to be separated more easily from the larger contaminants (*Figure 3.3B*). However, Mms7mat and Mms6mat needed to be separated on the preparative reverse-phase HPLC from MBP and TEV contaminants (*Figure 3.4*).

The Mms6 family protein variants were then characterized by analytical HPLC and MALDI-TOF MS (*Figure 3.5*). Truncation was an unresolved problem with some variants, such as Mms6ct.MC-1. However, in the case of Mms6ct.MC-1, the charged metal-binding segment was left intact despite truncation, and therefore the purified variant was collected for downstream *in vitro* mineralization experiments. Mms7ct, Mms7mat, Mms6ct, and Mms6mat are the Mms variants were the focus of our studies. A full list of cloned Mms6 family variants and the results of their expression, purification, and characterization can be found in Table 3.1.
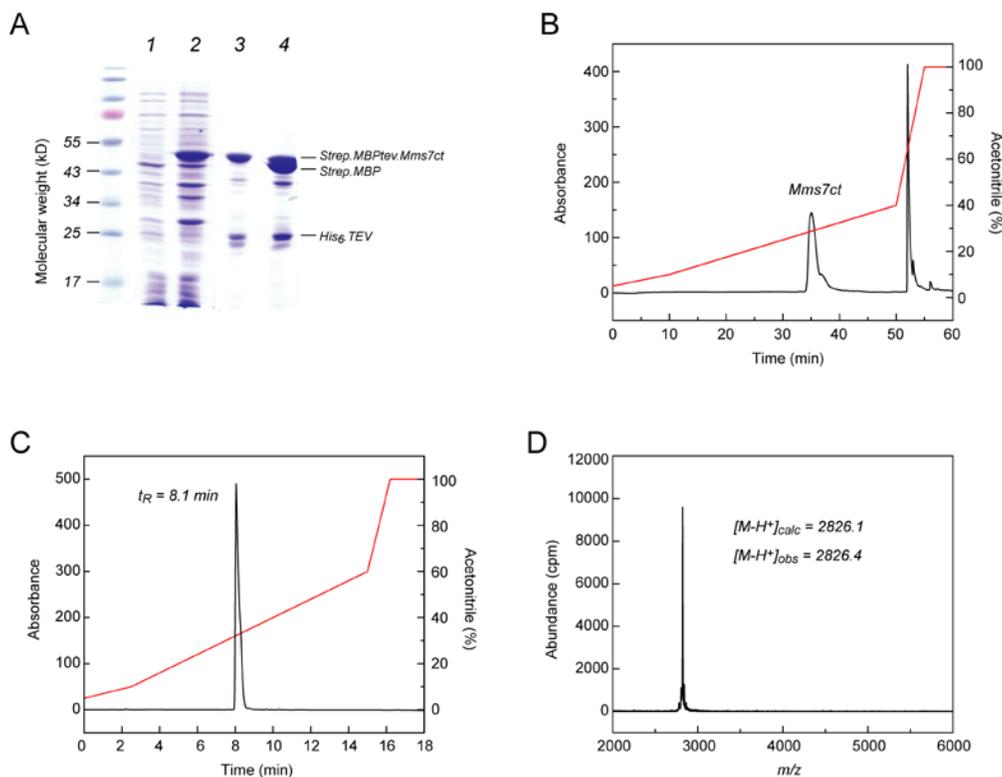
Figure 3.3. *Characterization of Mms7ct purification. (A) SDS-PAGE of a representative Mms7ct purification. Pre-induction of Strep.MBPtev.Mms7ct (lane 1), post-induction (lane 2), post-NiNTA purification of Strep.MBPtev.Mms7ct fusion (lane 3), post TEV cleavage (lane 4). The samples were run on a 12% acrylamide Bis-Tris gel and stained with Coomassie. Please note that Mms7ct is not visualized on this gel due to its size and is instead characterized by HPLC analysis. Molecular weights: Strep.MBPtev.Mms7ct, 49 kD; Strep.MBP, 46 kD, His$_6$.Tev, 27 kD. (B) Preparative HPLC chromatogram of the crude Mms7ct sample monitoring A$_{280\,nm}$. (C) Analytical HPLC trace of purified Mms7ct monitoring A$_{280\,nm}$. The lyophilized sample was resuspended in ddH$_2$O and chromatographed on a Zorbax Eclipse XDB-C$_{18}$ column (3.0 × 150 mm, 3.5 μm, Agilent) using several different steps (0.8 mL/min): a linear gradient of 5-10% Solvent B over 2.5 min, a linear gradient of 10-60% Solvent B over 12.5 min, a linear gradient of 60-100% Solvent B gradient over 1 min, hold at 100% Solvent B for 2 min (Solvent A, 0.1% v/v TFA in ddH$_2$O; Solvent B, acetonitrile containing 0.1% TFA). (D) MALDI-MS of Mms7ct.*
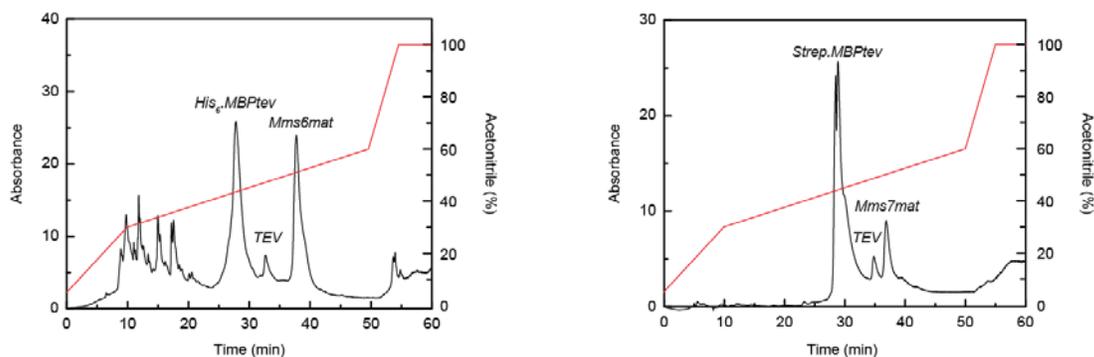
Figure 3.4. *Preparative HPLC of Mms6mat and Mms7mat. Preparative HPLC separates the Mms proteins from His$_6$.TEV (TEV) and His$_6$.MBPtev or Strep.MBPtev. The lyophilized sample was resuspended in ddH$_2$O and chromatographed on a Zorbax SB C$_{18}$ column (21.5 × 250 mm, 7 μm, Agilent) using several different steps (22 mL/min): a linear gradient of 5-30% Solvent B over 10 min, a linear gradient of 30-60% Solvent B over 40 min, a linear gradient of 60-100% Solvent B gradient over 5 min, hold at 100% Solvent B for 15 min (Solvent A, 0.1% v/v TFA in ddH$_2$O; Solvent B, acetonitrile containing 0.1% TFA).*

73
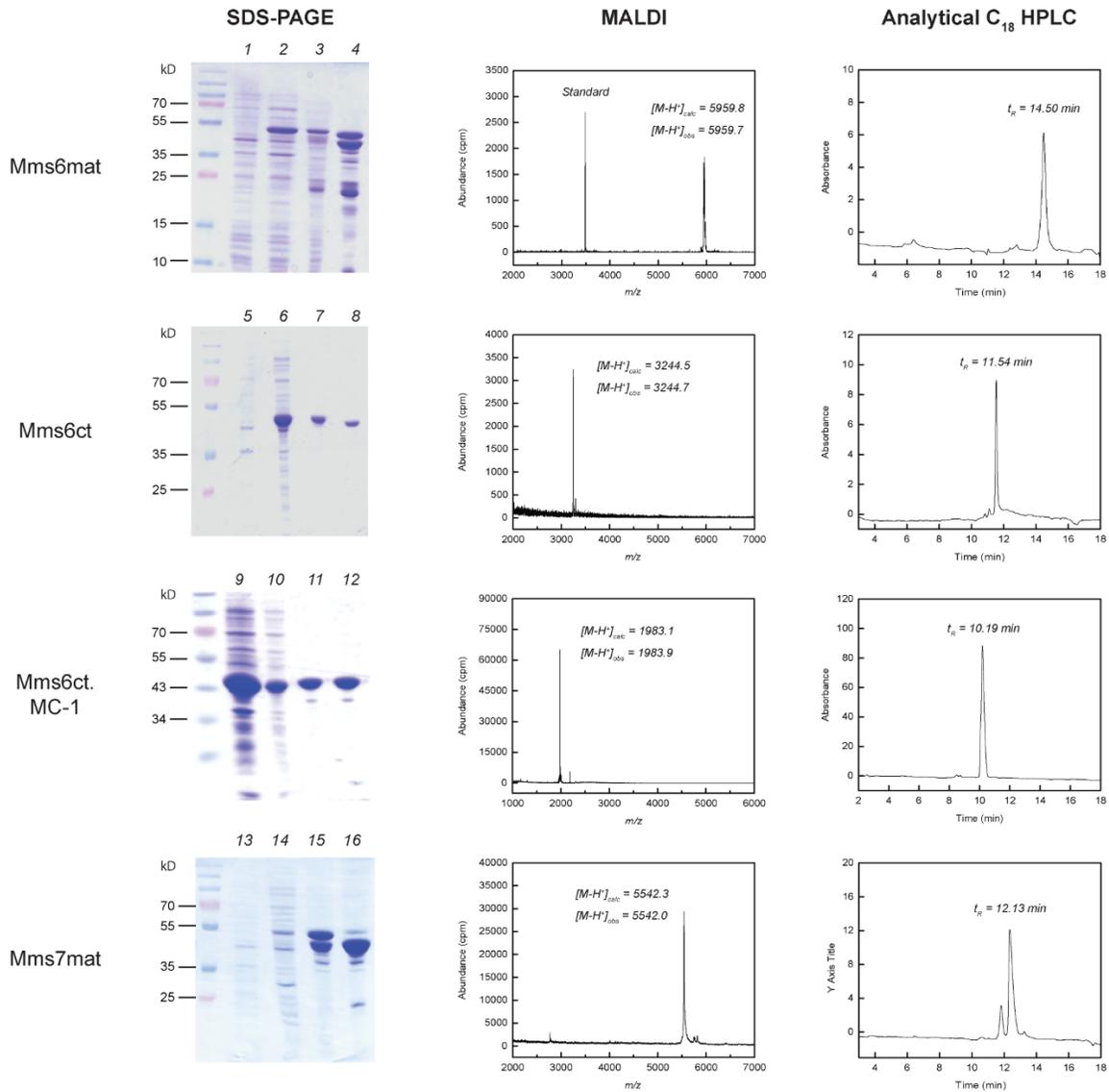
Figure 3.5. *Purification and characterization of key Mms proteins. SDS-PAGE of representative purifications: pre-induction of His6.MBPtev.Mms6mat (lane 1), post-induction (lane 2), post-NiNTA purification of His6.MBPtev.Mms6mat fusion (lane 3), post TEV cleavage (lane 4), pre-induction of His6.MBPtev.Mms6ct (lane 5), post-induction (lane 6), post-NiNTA purification of His6.MBPtev.Mms6ct fusion (lane 7), post TEV cleavage (lane 8), pre-induction of His6.MBPtev.Mms6ct.MC-1 (lane 9), post-induction (lane 10), post-NiNTA purification of His6.MBPtev.Mms6ct.MC-1 fusion (lane 11), post TEV cleavage (lane 12), pre-induction of Strep.MBPtev.Mms7mat (lane 13), post-induction (lane 14), post-NiNTA purification of Strep.MBPtev.Mms7ct fusion (lane 15), post TEV cleavage (lane 14). The samples were run on a 12% acrylamide Bis-Tris gel and stained with Coomassie. Please note that Mms proteins are not visualized on this gel due to their size and are instead characterized by analytical HPLC and MALDI. MALDI MS of Mms6mat, Mms6ct, Mms6ct.MC-1, and Mms7mat are shown. Analytical HPLC trace of purified Mms proteins monitoring A280 nm. The lyophilized sample was resuspended in ddH2O and chromatographed on a Zorbax Eclipse XDB-C18 column (3.0 × 150 mm, 3.5 μm, Agilent) using several different steps (0.8 mL/min): a linear gradient of 5-10% Solvent B over 2.5 min, a linear gradient of 10-60% Solvent B over 12.5 min, a linear gradient of 60-100% Solvent B gradient over 1 min, hold at 100% Solvent B for 2 min (Solvent A, 0.1% v/v TFA in ddH2O; Solvent B, acetonitrile containing 0.1% TFA).*

| Protein	Expresses well in *E. coli*	$[M-H^+]_{calc}$	$[M-H^+]_{obs}$	Completed
Mms7mat	Yes	5542.3	5542.0	Purified
Mms7ct	Yes	2826.1	2826.4	Purified
Mms6mat	Yes	5959.8	5959.7	Purified
Mms6ct	Yes	3244.5	3244.7	Purified
Mms6ct.MSR-1	Yes	*TBD*	*TBD*	Expressed
Mms7ct.MSR-1	Yes	*TBD*	*TBD*	Expressed
Mms6ct.MV-1	Yes	3196.5	3197.0	Purified
Mms7ct.MV-1	Yes	*TBD*	*TBD*	Expressed
Mms6ct.MC-1	Yes	1983.1	1983.9	Purified, truncated
Mms7ct.Fos001	Yes	*TBD*	*TBD*	Expressed
Mms6ct.ΔE	No	*TBD*	*TBD*	Expression needs optimization
Mms7ct.ΔE	Poorly	*TBD*	*TBD*	Expression needs optimization
FF1.Mms6	*TBD*	*TBD*	*TBD*	Cloned
FF2.Mms6	Yes	4779.1	4778.6	Purified
Melittin.Mms6	Yes	TBD	TBD	Expressed

Table 3.1. Expression and purification of Mms constructs

Pull down of Mms proteins by synthetic magnetite. We developed a protocol to investigate the strength of Mms6 family protein interaction with magnetite by incubation and pull-down with synthetic magnetite. As Mms6 family proteins are a set of tightly bound small proteins that can only be removed from the mineral upon boiling under denaturing conditions [*1*], it is likely that they bind magnetite with a high degree of specificity. This assay also allows us to compare Mms6 family proteins from the same species, from different species, with a mutation to the engineered N-terminal domain, or with mutations to C-terminal chelating residue mutants in order to determine how spacing and presentation of acidic/hydrogen-bonding residues affects lattice binding and metal ion selection, which ultimately determines mineral identity.

In order to have a standard magnetite surface area for comparison of binding of different Mms6 family proteins, the same batch of synthesized magnetite was used in all pull down experiments. Bare magnetite was synthesized by partial oxidation of Fe(II) [*24*] in the absence of chelating ligands and characterized by TEM and powder XRD (*Figure 3.6*). As size is important to the mode of peptide binding to nanocrystals and can influence affinity, we chose a synthetic method that crystallizes magnetite nanoparticles within the biological size regime of 20-60 nm [*31-33*]. Analysis of particle size from TEM images showed an average diameter of 36 ± 16 nm, which falls within the range of sizes for magnetite particles biomineralized by *Magnetospirillum* species (Figure). However, close inspection of the TEM images reveals mostly octahedral habits, which suggests the lattice face presented to the Mms6 family proteins for binding will be mostly thermodynamically stable (111) facets (Figure). As biological magnetite formation is likely controlled by peptides binding to and stabilizing unstable facets, this is not ideal and ground geological magnetite should be considered in comparison for further studies [*34*]. Powder XRD d-spacings were consistent with magnetite or with a mixture of magnetite and some maghemite, which has a similar lattice structure as magnetite but is fully oxidized to Fe(III) (*Figure 3.6*).

In order to conduct binding experiments, we set out to find conditions in which the size of the magnetite particles remained on the nanoscale and suspended in solution over the time course of the binding experiment. Bare magnetite nanoparticles have a tendency to aggregate due to van der Waals interactions and weak magnetic forces [*35*]. Traditional strategies to prevent aggregation involve passivating the surface of the particles with capping agents and/or tailoring the surface charges to increase the electrostatic repulsion between particles [*36*]. However, for binding studies, the magnetite must be passivated to prevent aggregation without (1) dramatically changing the surface chemistry of the magnetite or (2) preventing Mms proteins direct interaction with the surface. We used dynamic light scattering (DLS) to monitor the aggregation of magnetite in minimal concentrations of biological buffers over time (*Figure 3.7*). Only 20 min after sonication in ddH$_2$O, magnetite aggregation had a predicted particle radius far outside of the nanoscale regime (>1000 nm). In 0.2 mM potassium phosphate at pH 8.5, magnetite aggregates monitored by DLS were minimized (~100 nm), and magnetite remained suspended in solution. We also tested 5 mM HEPES at pH 8.0 with similar results and found that Mms7ct binding to magnetite was comparable to its binding in 0.2 mM potassium phosphate at pH 8.0 (*Figure 3.7*).

76

A
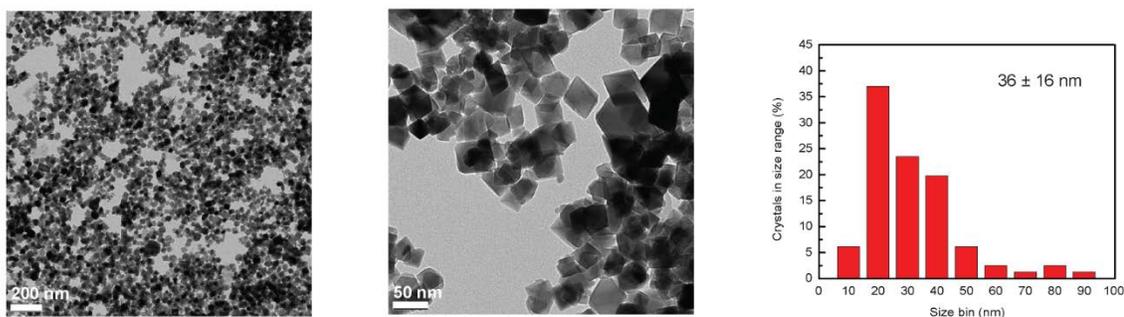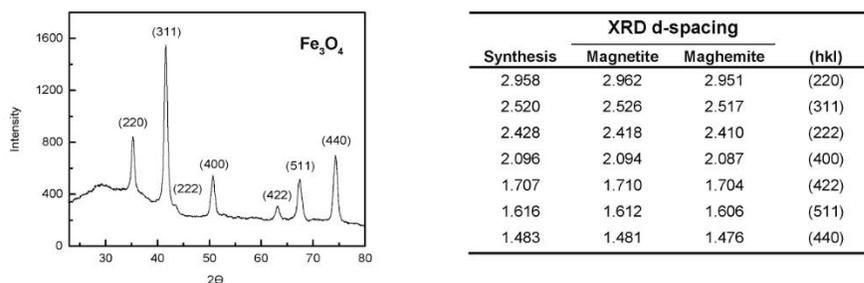
Figure 3.6. *Characterization of magnetite synthesis. (A) Transmission electron microscopy images of synthesized magnetite and histogram of crystal sizes observed in magnetite synthesis (81 nanoparticles with a mean diameter of 36 ± 16 nm). (B) Powder x-ray diffraction of synthesized magnetite from a Bruker AXS D8 Advance diffractometer with an incident Co Kα radiation of 1.79026 Å. The lattice d-spacing (d) of the synthesized iron oxide was calculated using Bragg's law λ= dsinθ where λ is 1.79026 Å and 2θ is the output from the diffractometer. The standard d-spacing for magnetite and the closely related fully oxidized maghemite lattice is from the American Mineralogist Crystal Structure Database. The notation (hkl) corresponds to the Miller index of the observed lattice.*
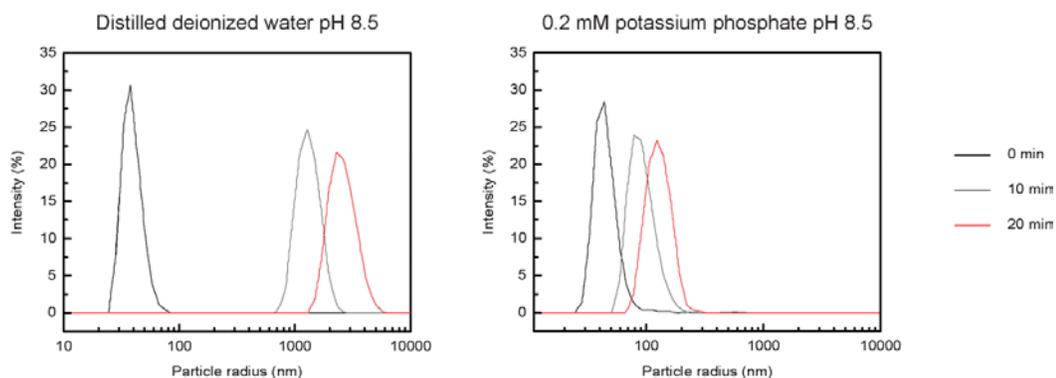
Figure 3.7. *Characterization of magnetite aggregation by dynamic light scattering. DLS determined hydrodynamic size was performed at 25 °C by dissolving samples in ddH2O or 0.2 mM potassium phosphate buffer pH 8.5. After brief sonication of 0.5 mg/mL magnetite to resuspend, the samples were allowed to aggregate for a set amount of time before resuspended briefly by inversion. The samples were analyzed by a Zetasizer Nanoseries ZS (Malvern Instruments, UK). The samples were not analyzed for hydrodynamic radius but used as a qualitative measurement to find a buffer in which magnetite particles were passivated from extensive aggregation.*

77

With nanoscale magnetite and buffer conditions in hand, we set out to compare the Mms6 family proteins' ability to bind magnetite. We suspended solutions of magnetite by sonication in 0.2 mM potassium phosphate pH 8.0 and serially diluted the magnetite into different concentrations. We then added an equal amount of buffer (UV-Vis blank and aggregation control) or Mms6 family protein to each dilution of magnetite. As Mms6 family proteins are predicted to aggregate or self-assemble [8, 28], a protein-only control experiment was also performed: total protein in solution was measured by absorbance at 280 nm (A280) after centrifuging to remove aggregates at the beginning and end of the incubation time. The protein-magnetite solutions were agitated for several hours on a rotary shaker with periodic manual agitation to resuspend particles. The protein-magnetite, magnetite only, and protein only solutions were then spun down carefully and the supernatant collected. The A280 of the supernatant was measured to determine the molar amount of protein left in solution. The relative amount of protein pulled down was determined by subtracting the protein in the supernatant at the end of the incubation time from the total protein added to solution and dividing by the total protein added to solution.

We found that Mms7ct binds magnetite with higher affinity than BSA in both 0.2 mM potassium phosphate and 5 mM HEPES buffers at pH 8.0 (*Figure 3.8*A). We further found that Mms6ct binds magnetite comparably to Mms7ct at concentrations of magnetite below 0.5 mg/mL (*Figure 3.8B*). While the binding curve looks different above a magnetite concentration of 0.5 mg/mL, this result may be an artifact of the low A280 measurements for Mms6ct given the low extinction coefficient of Mms6ct and small amount of protein left in solution. Interestingly, we found that Mms7mat, containing both the aggregating N-terminus and metal-binding C-terminus, binds magnetite quite differently than the metal-binding C-terminus Mms7ct (*Figure 3.8C*). Mms7mat appears to bind magnetite in a linear fashion up to 80% protein bound by magnetite. At first glance, it appears that it reaches saturation at a nearly four-fold higher concentration of magnetite when compared to the total amount of protein added to solution. However, the protein-only control of Mms7mat revealed a significant amount of protein self-aggregates and can be pulled down without magnetite. Adjusting for this fact, Mms7mat reaches 80% of protein bound by magnetite at the same concentration as Mms7ct. This suggests that Mms7mat has a different mechanism of binding than Mms7ct; for example, Mms7mat could first self-assemble and orient the metal-binding C-termini before binding in cluster to the magnetite surface. Self-assembly of proteins and biomolecules to build a matrix prior to metal ion deposition is a common theme in biomineralization, and could introduce another tier of control over magnetite size, shape, and lattice composition [10, 37-40].
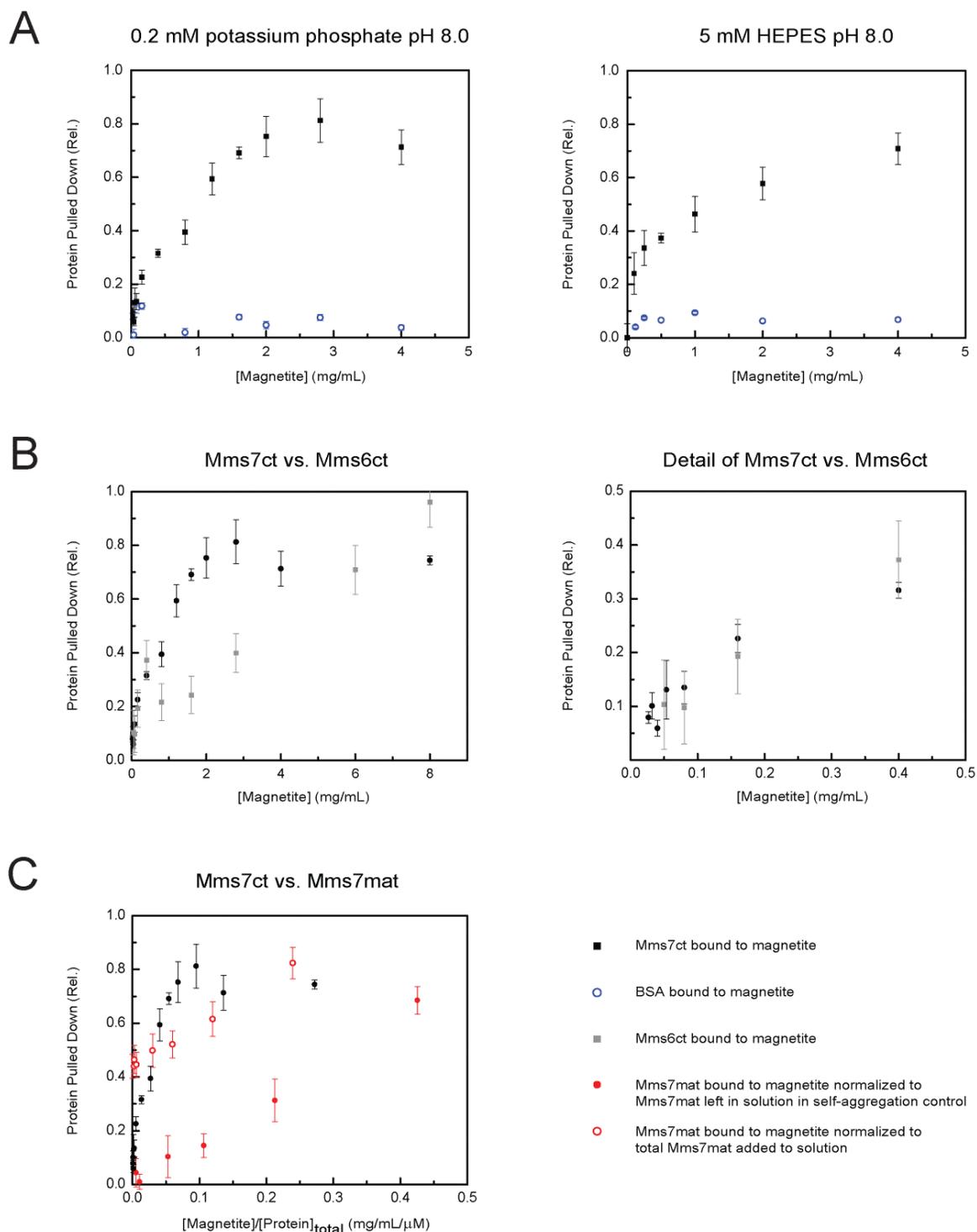
Figure 3.8. *Pull down assays of Mms proteins by magnetite. (A) Comparison of Mms7ct pull down (black squares) by magnetite in 0.2 mM potassium phosphate buffer versus 5 mM HEPES pH 8.0 buffer at pH 8.0. Bovine serum albumin (BSA) binding to magnetite was also evaluated (open blue circles). (B) Comparison of Mms7ct pull down (black squares) and Mms6ct (gray squares) in 0.2 mM potassium phosphate buffer pH 8.0. (C) Comparison of Mms7ct pulled down to Mms7mat protein (red circles normalized to total protein added to solution, open red circles normalized to non-self-aggregating total protein) containing the aggregating segment fused to the N-terminus of Mms7ct in 0.2 mM potassium phosphate buffer pH 8.0.*

Synthesis of magnetite in the presence of Mms proteins. In order to monitor the effect of Mms proteins on *in vitro* mineralization, we prepared synthetic magnetite by partial oxidation of Fe^{2+} [*9, 24, 41, 42*] in the presence and the absence of Mms protein variants and monitored the growth of the crystal with transmission electron microscopy (*Figure 3.9A*). We observe that synthetic magnetite tends to grow as octahedral crystals of irregular size while Mms6 family protein-templated synthesis appears to produce nanocrystals of more uniform size with a rounded appearance by low-resolution TEM. These observations are consistent with previous reports that use high-resolution TEM to show that the rounded appearance at low resolution created by Mms6 family proteins is caused by the introduction new mineral faces to synthetic magnetite, which is otherwise octahedral and fully terminated with the thermodynamically-preferred (111) surfaces [*8, 43*]. This suggests that Mms proteins are capable of binding and stabilizing non-(111) faces of magnetite, thereby initiating the formation of new mineral facets for shape control. However, we see no obvious size or shape differences between magnetite synthesized in the presence of AMB-1 Mms6 family proteins (cubo-octahedral magnetite habit) versus MV-1 Mms6 family proteins (rectangular, elongated magnetite habit). This does not preclude the possibility that different crystal faces would be identified by observing lattice fringes with high-resolution transmission microscopy or that a full species' set of Mms6 family proteins are necessary to build a recognizable crystal habit, but the effects of Mms6 family proteins on growing magnetite under non-environmental conditions (pH > 12, small molecule oxidants, high temperatures) appear to be subtle [*6, 8, 43*].

Figure 3.9. Comparison of magnetite synthesized in vitro and in vivo. (A) In vitro magnetite synthesis by partial oxidation of Fe(II) in the absence and presence of Mms proteins from AMB-1. (B) The knockout of the mms proteins in AMB-1 reveals defects in the shape and size of magnetite crystals. Complementing the knockout with mms6 and mmsF recovers the wild type phenotype.

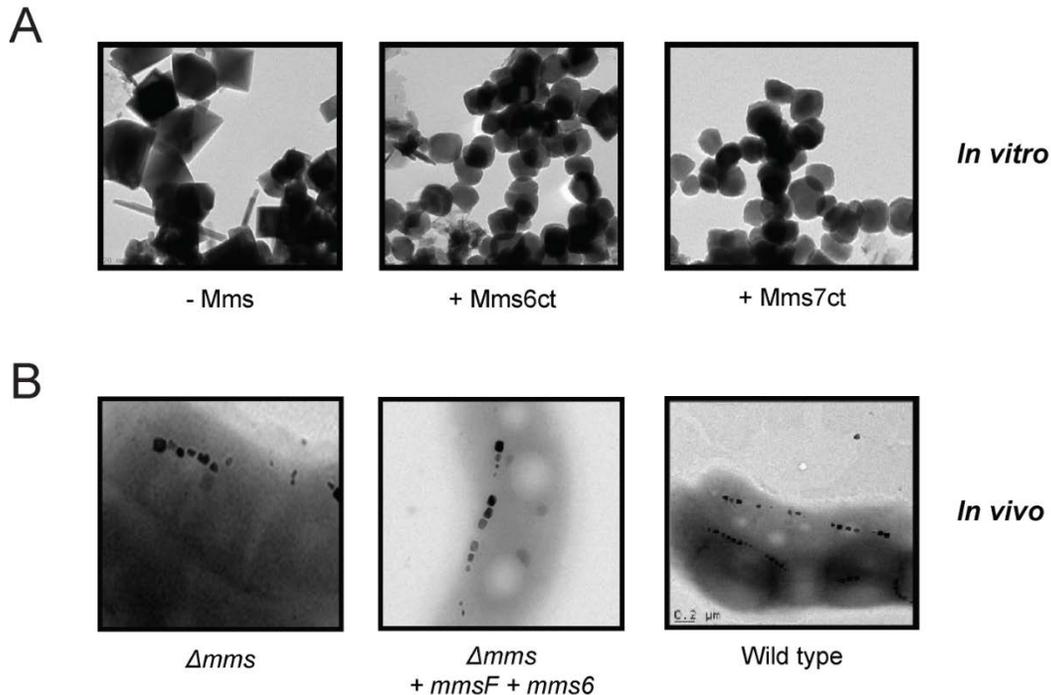***In vitro* mineralization of iron oxides by MamP in the presence of Mms proteins.** Given the competence of MamP to transform soluble iron(II) species to mixed valent Fe(II)/Fe(III) oxide minerals (*Chapter 2*), we were interested to see how the Mms6 family templating proteins might interact with the growing material in the presence of MamP. This experiment was of particular interest given the effects (though subtle) of Mms6 family proteins on *in vitro* magnetite synthesis by partial oxidation under harsh conditions (pH > 12) with powerful small molecule oxidants. In addition to redox partners that are necessary to generate both Fe(II) and Fe(III) to form magnetite, templating proteins such as the Mms6 family proteins could help determine the crystallinity, size, shape, or thermodynamic or kinetic stability of the material.

To explore possible synergy between redox catalysis and structural templating provided by MamP and Mms7, respectively, *in vitro* iron mineralization reactions were run in the presence of both proteins (*Figure 3.10*). In the absence of MamP, the addition of Mms7Ct to soluble Fe(II) and introduction of oxygen did not lead to immediate mineralization. Furthermore, reactions containing both MamP and Mms7ct proceeded similarly to those with MamP alone, with rapid formation of green rust on the same timescale. However, an interesting change in behavior was induced by Mms7ct after mineralization. If the reactions were opened to air, those that did not contain Mms7ct quickly turned orange, which signifies the formation of fully oxidized Fe(III) oxide red rusts and represents the typical endpoint for reactions of Fe(II) with oxygen. In contrast, the green rust remained mostly intact in reactions containing Mms7ct after direct exposure to air, indicating that the mixed-valent Fe(II)/Fe(III) material was somehow being protected from further oxidation (*Figure 3.10A*). This behavior is sensitive to the Fe(II):Mms7ct ratio based on the observation that full protection can be lost at large excess of Fe(II) (>1:1,000). These results suggest that both the redox potential of MamP as well as the structural templating of the Mms proteins control the identity of the mineral being formed. This also suggests that Mms7ct and other Mms proteins may play a more significant role in controlling magnetite mineral structure than previously hypothesized [*5, 44*]. Beyond simple control of size and shape of magnetite, it may also template the crystal lattice of the mineral itself similar to what has been observed with calcium biomineralization, where unstable crystal forms and phases of the mineral are stabilized by interaction with peptides and other macromolecules [*45*]. In fact, acidic residues in magnetite-mineralizing peptides have been hypothesized to be nucleation inhibitors, stabilizing an amorphous intermediate through the coordination of iron [*46*]. The Mms peptides also could be critical to stabilizing a mixed-valent amorphous material, preventing further oxidation before the material's transformation into a functional, magnetic crystal.
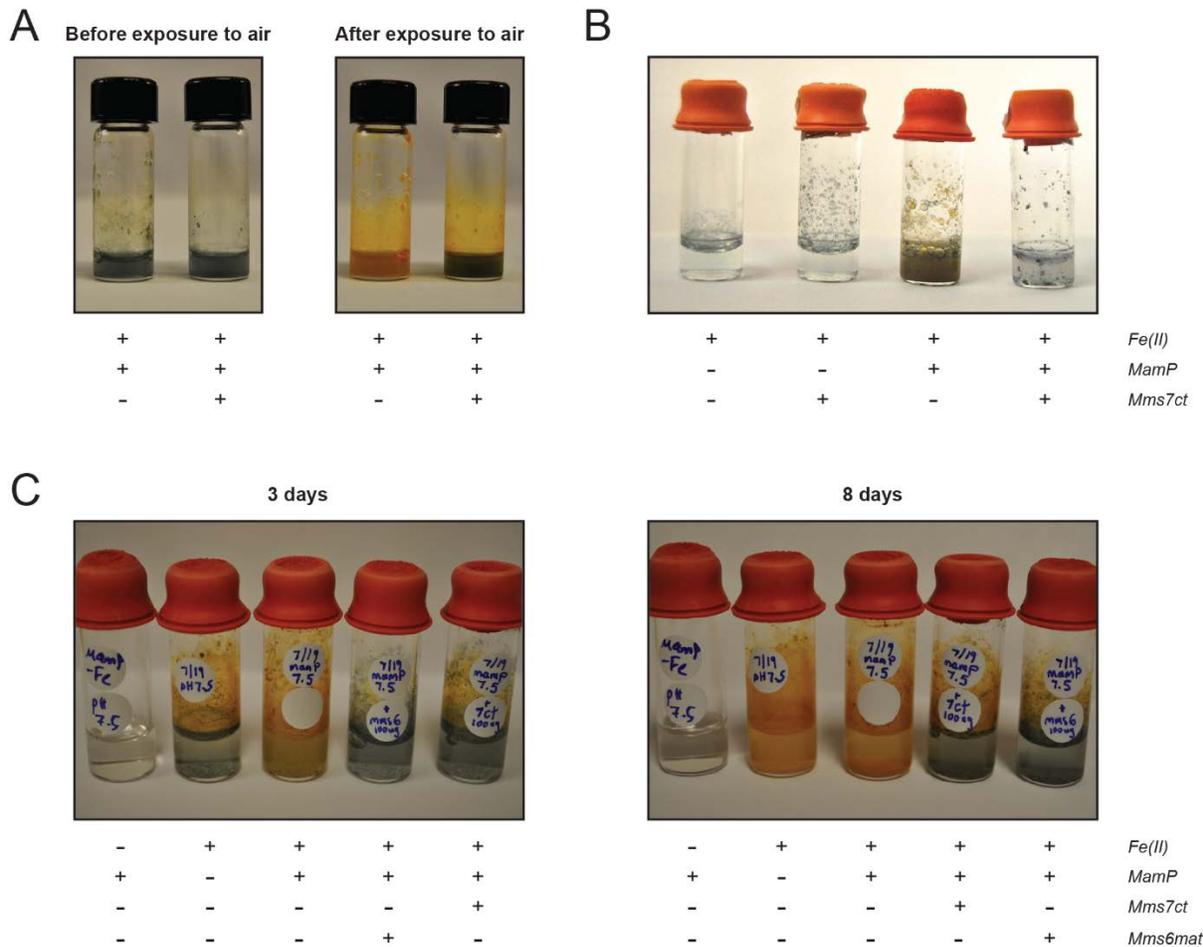
Figure 3.10. Mineralization of iron oxides with Mms proteins. *(A) In vitro iron mineralization reactions containing ammonium Fe(II) sulfate (20 mM) and MamP (1.2 µM) in 50 mM HEPES pH 7.5, 100 mM NaCl with and without Mms7ct (45 µM). After the end of the mineralization reaction, reaction vials were opened to air for 20 min. (B) Reactions with and without Mms7ct proceed at a similar reaction rate and contain no iron precipitates in solution after 3 h at pH 7.5. Reactions with MamP oxidize soluble Fe(II) quickly to green rust, though the reaction containing Mms7ct stops the reaction at a green rust stage. The reactions are performed as described except that no additional injections of air or agitation were carried out after the addition of either MamP or MamP buffer. (C) Reactions were purged with Ar and left without agitation to slowly oxidize over 8 d and highlight the protective ability of the Mms proteins (Mms6mat; Mms7ct).*

3.4. Conclusions

In summary, we developed a system for the heterologous expression and purification of Mms proteins and their variants. In particular, we focused on cloning and purifying the metal-binding C-terminal segment of Mms6 family proteins from species of magnetotactic bacteria that crystallize magnetite with different habits in order to explore the molecular basis for stabilization of different magnetite faces. We also constructed several N-terminal fusions of short amino acids sequences with defined quaternary structure based on either α-helix or β-sheet motifs with the C-terminal mineral binding domain of Mms6 in order to examine the role of the N-terminal sequence in *in vitro* size and shape control. Given the *in vivo* and *in vitro* behavior of these proteins, new magnetite crystal sizes and shapes can be accessed *in vivo* by engineering the Mms6 family proteins to self-assemble and interact with magnetite lattices in different ways.

We use *in vitro* binding and synthesis studies with Mms6 family proteins to show that they are competent to bind and stabilize non-(111) faces of magnetite and that the N-terminus appears to play a role in controlling binding to magnetite. We also use *in vitro* iron mineralization to show that the Mms6 family proteins can work synergistically with the redox protein MamP to produce mixed-valent iron oxides from soluble Fe(II) species and to control mineral structure. Further studies with Mms7ct indicate that it and other Mms6 family proteins may play a more significant role in controlling magnetite mineral structure than previously hypothesized. Beyond simple control of size and shape of magnetite, it may also template the crystal lattice of the mineral itself similar to what has been observed with calcium biomineralization, where unstable crystal forms and phases of the mineral are stabilized by interaction with peptides and other macromolecules.

3.5. References

1.   A. Arakaki, J. Webb, and T. Matsunaga (2003) A novel protein tightly bound to bacterial magnetic particles in *Magnetospirillum magneticum* strain AMB-1. *J. Biol. Chem.* 278(10):8745-8750.
2.   C. Jogler, W. Lin, A. Meyerdierks, M. Kube, E. Katzmann, C. Flies, Y. Pan, R. Amann, R. Reinhardt, and D. Schuler (2009) Toward cloning of the magnetotactic metagenome: identification of magnetosome island gene clusters in uncultivated magnetotactic bacteria from different aquatic sediments. *Appl. Environ. Microbiol.* 75(12):3972-3979.
3.   D. Murat, A. Quinlan, H. Vali, and A. Komeili (2010) Comprehensive genetic dissection of the magnetosome gene island reveals the step-wise assembly of a prokaryotic organelle. *Proc. Natl. Acad. Sci. U. S. A.* 107(12):5593-5598.
4.   D. Murat, V. Falahati, L. Bertinetti, R. Csencsits, A. Kornig, K. Downing, D. Faivre, and A. Komeili (2012) The magnetosome membrane protein, MmsF, is a major regulator of magnetite biomineralization in *Magnetospirillum magneticum* AMB-1. *Mol. Microbiol.* 85(4):684-699.
5.   A. Scheffel, A. Gardes, K. Grunberg, G. Wanner, and D. Schuler (2008) The major magnetosome proteins MamGFDC are not essential for magnetite biomineralization in Magnetospirillum gryphiswaldense but regulate the size of magnetosome crystals. *J. Bacteriol.* 190(1):377-386.

6.   A. Arakaki, A. Yamagishi, A. Fukuyo, M. Tanaka, and T. Matsunaga (2014) Co-ordinated functions of Mms proteins define the surface structure of cubo-octahedral magnetite crystals in magnetotactic bacteria. *Mol. Microbiol.* 93(3):554-567.

7.   T. Prozorov, P. Palo, L. Wang, M. Nilsen-Hamilton, D. Jones, D. Orr, S. K. Mallapragada, B. Narasimhan, P. C. Canfield, and R. Prozorov (2007) Cobalt ferrite nanocrystals: out-performing magnetotactic bacteria. *ACS Nano* 1(3):228-233.

8.   A. Arakaki, F. Masuda, Y. Amemiya, T. Tanaka, and T. Matsunaga (2010) Control of the morphology and size of magnetite particles with peptides mimicking the Mms6 protein from magnetotactic bacteria. *J. Colloid Interface Sci.* 343(1):65-70.

9.   Y. Amemiya, A. Arakaki, S. S. Staniland, T. Tanaka, and T. Matsunaga (2007) Controlled formation of magnetite crystal by partial oxidation of ferrous hydroxide in the presence of recombinant magnetotactic bacterial protein Mms6. *Biomaterials* 28(35):5381-5389.

10.   C. Groger, K. Lutz, and E. Brunner (2008) Biomolecular self-assembly and its relevance in silica biomineralization. *Cell. Biochem. Biophys.* 50(1):23-39.

11.   G. He, S. Gajjeraman, D. Schultz, D. Cookson, C. Qin, W. T. Butler, J. Hao, and A. George (2005) Spatially and temporally controlled biomineralization is facilitated by interaction between self-assembled dentin matrix protein 1 and calcium phosphate nuclei in solution. *Biochemistry* 44(49):16140-16148.

12.   A. Quinlan, D. Murat, H. Vali, and A. Komeili (2011) The HtrA/DegP family protease MamE is a bifunctional protein with roles in magnetosome protein localization and magnetite biomineralization. *Mol. Microbiol.* 80(4):1075-1087.

13.   W. A. Kibbe (2007) OligoCalc: an online oligonucleotide properties calculator. *Nucleic Acids Res.* 35(Web Server issue):W43-46.

14.   D. G. Gibson, L. Young, R. Y. Chuang, J. C. Venter, C. A. Hutchison, and H. O. Smith (2009) Enzymatic assembly of DNA molecules up to several hundred kilobases. *Nat. Methods* 6(5):343-345.

15.   A. Villalobos, J. E. Ness, C. Gustafsson, J. Minshull, and S. Govindarajan (2006) Gene Designer: a synthetic biology tool for constructing artificial DNA segments. *BMC Bioinformatics* 7:285.

16.   M. Richter, M. Kube, D. A. Bazylinski, T. Lombardot, F. O. Glockner, R. Reinhardt, and D. Schuler (2007) Comparative genome analysis of four magnetotactic bacteria reveals a complex set of group-specific genes implicated in magnetosome biomineralization and function. *J. Bacteriol.* 189(13):4899-4910.

17.   D. A. Bazylinski, A. J. Dean, T. J. Williams, L. K. Long, S. L. Middleton, and B. L. Dubbels (2004) Chemolithoautotrophy in the marine, magnetotactic bacterial strains MV-1 and MV-2. *Arch. Microbiol.* 182(5):373-387.

18.   E. Kasotakis, E. Mossou, L. Adler-Abramovich, E. P. Mitchell, V. T. Forsyth, E. Gazit, and A. Mitraki (2009) Design of metal-binding sites onto self-assembled peptide fibrils. *Biopolymers* 92(3):164-172.

19.   A. Aggeli, M. Bell, N. Boden, J. N. Keen, P. F. Knowles, T. C. McLeish, M. Pitkeathly, and S. E. Radford (1997) Responsive gels formed by the spontaneous self-assembly of peptides into polymeric beta-sheet tapes. *Nature* 386(6622):259-262.

20.   T. C. Terwilliger, L. Weissman, and D. Eisenberg (1982) The structure of melittin in the form I crystals and its implication for melittin's lytic and surface activities. *Biophys. J.* 37(1):353-361.

21. T. C. Terwilliger and D. Eisenberg (1982) The structure of melittin. II. Interpretation of the structure. *J. Biol. Chem.* 257(11):6016-6022.

22. M. R. Wilkins, E. Gasteiger, A. Bairoch, J. C. Sanchez, K. L. Williams, R. D. Appel, and D. F. Hochstrasser (1999) Protein identification and analysis tools in the ExPASy server. *Methods Mol. Biol.* 112:531-552.

23. H. Schagger (2006) Tricine-SDS-PAGE. *Nat. Protoc.* 1(1):16-22.

24. K. Nishio, M. Ikeda, N. Gokon, S. Tsubouchi, H. Narimatsu, Y. Mochizuki, S. Sakamoto, A. Sandhu, M. Abe, and H. Handa (2007) Preparation of size-controlled (30-100 nm) magnetite nanoparticles for biomedical applications. *J. Magn. Magn. Mater.* 310(2):2408–2410.

25. R. T. Downs and M. Hall-Wallace (2003) The *American Mineralogist* crystal structure database. *Am. Mineral.* 88:247-250.

26. A. Komeili, H. Vali, T. J. Beveridge, and D. K. Newman (2004) Magnetosome vesicles are present before magnetite formation, and MamA is required for their activation. *Proc. Natl. Acad. Sci. U. S. A.* 101(11):3839-3844.

27. D. Schuler, R. Uhl, and E. Bauerlein (1995) A simple light scattering method to assay magnetism in *Magnetospirillum gryphiswaldense*. *FEMS Microbiol. Lett.* 132:139-145.

28. A. Arakaki, J. Webb, and T. Matsunaga (2003) A novel protein tightly bound to bacterial magnetic particles in *Magnetospirillum magneticum* strain AMB-1. *J. Biol. Chem.* 278(10):8745-8750.

29. S. F. Altschul, T. L. Madden, A. A. Schaffer, J. Zhang, Z. Zhang, W. Miller, and D. J. Lipman (1997) Gapped BLAST and PSI-BLAST: a new generation of protein database search programs. *Nucleic Acids Res.* 25(17):3389-3402.

30. K. Lutz, C. Groger, M. Sumper, and E. Brunner (2005) Biomimetic silica formation: analysis of the phosphate-induced self-assembly of polyamines. *ChemPhysChem* 7(14):2812-2815.

31. M. B. Dickerson, K. H. Sandhage, and R. R. Naik (2008) Protein- and peptide-directed syntheses of inorganic materials. *Chem. Rev.* 108(11):4935-4978.

32. M. Sumper, S. Lorenz, and E. Brunner (2003) Biomimetic control of size in the polyamine-directed formation of silica nanospheres. *Angew. Chem. Int. Ed. Engl.* 42(42):5192-5195.

33. V. Puddu and C. C. Perry (2014) Interactions at the silica-peptide interface: the influence of particle size and surface functionality. *Langmuir* 30(1):227-233.

34. M. M. Tomczak, J. M. Slocik, M. O. Stone, and R. R. Naik (2007) Bio-based approaches to inorganic material synthesis. *Biochem. Soc. Trans.* 35(3):512-515.

35. W. Zhang (2014) Nanoparticle aggregation: principles and modeling. *Adv. Exp. Med. Biol.* 811:19-43.

36. D. Li and R. B. Kaner (2006) Shape and aggregation control of nanoparticles: not shaken, not stirred. *J. Am. Chem. Soc.* 128(3):968-975.

37. S. Weiner and L. Addadi (2011) Crystallization pathways in biomineralization. *Annu. Rev. Mater. Res.* 41:21-40.

38. M. Sumper and E. Brunner (2008) Silica biomineralization in diatoms: the model organism *Thalassiosira pseudonana*. *ChemBioChem* 9(8):1187-1194.

39. A. Arakaki, K. Shimizu, M. Oda, T. Sakamoto, T. Nishimura, and T. Kato (2014) Biomineralization-inspired synthesis of functional organic/inorganic hybrid materials: organic molecular control of self-organization of hybrids. *Org. Biomol. Chem.*

40.   L. Addadi and S. Weiner (1997) Biomineralization - a pavement of pearl. *Nature* 389:912.
41.   F. Vereda, J. de Vicente, M. P. Morales, F. Rull, and R. Hidalgo-Alvarez (2008) Synthesis and characterization of single-domain monocrystalline magnetite particles by oxidative aging of $Fe(OH)_2$. *J. Phys. Chem. C* 112(15):5843–5849.
42.   T. Sugimoto and E. Matijevic (1980) Formation of uniform spherical magnetite particles by crystallization from ferrous hydroxide gels. *J. Coll. Inter. Sci.* 74(1):227-243.
43.   Y. Amemiya, A. Arakaki, S. S. Staniland, T. Tanaka, and T. Matsunaga (2007) Controlled formation of magnetite crystal by partial oxidation of ferrous hydroxide in the presence of recombinant magnetotactic bacterial protein Mms6. *Biomaterials* 28(35):5381-5389.
44.   A. Lohsse, S. Borg, O. Raschdorf, I. Kolinko, E. Tompa, M. Posfai, D. Faivre, J. Baumgartner, and D. Schuler (2014) Genetic dissection of the mamAB and mms6 operons reveals a gene set essential for magnetosome biogenesis in *Magnetospirillum gryphiswaldense*. *J. Bacteriol.* 196(14):2658-2669.
45.   S. Weiner and L. Addadi (2011) Crystallization pathways in biomineralization. *Annu. Rev. Mater. Res.* 41:21-40.
46.   J. Baumgartner, M. A. Carillo, K. M. Eckes, P. Werner, and D. Faivre (2014) Biomimetic magnetite formation: from biocombinatorial approaches to mineralization effects. *Langmuir* 30(8):2129-2136.

Chapter 4: *Synthetic biology approaches to cellular nanomaterials*

4.1. Introduction

Living organisms are capable of carrying out many sophisticated and coordinated operations, such as sensing, directional movement, self-organization, and transformations of small molecules.. However, the scope of innovation found in natural systems is typically limited to naturally abundant elements in their immediate environment. In contrast, human chemists have discovered many novel and tunable properties of matter by extending reaction space beyond the small subset of elements used in biology to the entire periodic table. This diversity in function and composition is especially striking for the chemistry of inorganic elements and materials. We seek to open new doors between synthetic biology and inorganic nanoscience with the overall goal of designing and exploiting novel hybrid functions for living cells at the biotic-abiotic interface. In this chapter, we discuss directions we have explored in utilizing magnetotactic bacteria as a platform for engineering the production of cellular nanomaterials, and we look towards applications to the synthesis and discovery of new nanoscale materials as well as the implantation of novel intracellular devices to alter or control cell behavior.

Magnetospirillum magneticum AMB-1 is a natural host to access transition-metal based biomaterials and functions: it is already competent to mineralize Fe via magnetosome chemistry, encapsulates the functional material in a self-contained compartment, does not require stringent growth conditions, and has methods worked out for gene deletion and replacement [*1*]. In particular, we are interested in and encouraged by the observation that AMB-1 is competent to control the redox state of metal ions to form a mixed-valent material, a competency necessary to form advanced functional materials from transition metal building blocks. Our specific target is the large superfamily of metal oxides (X_nO_m) and spinels ($XZYO_4$) to which magnetite belongs because their structures should be chemically accessible via magnetosome-based chemistry and they also possess a broad range of electronic, magnetic, and optical properties at the nanoscale and macroscale [*2-9*]. Towards this goal, we constructed chimeras of native tightly-bound, templating peptides, Mms6 family proteins, with alternative mineral-binding sequences reported in the literature for other metal oxide minerals [*10-12*]. We also attempted to identify new mineral-binding and mineral-precipitating peptides for target spinels using used established phage display methods [*13-16*]. With new metal oxide-precipitating constructs in hand, we look for new ways to allow non-iron metal ions access to the magnetosome. Previous studies have shown that prokaryotes are able to transport a wide variety of metal ions and main group elements [*17*], but that *M. magneticum* AMB-1 can easily exclude non-specific metal ions from the magnetosome [*18, 19*]. Therefore, we suggest that ionophores can also be used increase the bioavailability of non-iron metal ions [*20*]. The first part of this chapter discusses our efforts in establishing a system to build new metal oxides in AMB-1.

We also seek to take advantage of the natural transition-metal based function of magnetotactic bacteria, response to an external magnetic field. As most biological samples exhibit negligible magnetic susceptibility, magnetic nanoparticles can be used in various biosensing applications from magnetic resonance imaging (MRI) to biomolecule detection with extremely low detection limits and an even lower background signal [*21-23*]. Magnetic biosensors are based on changes in the magnetic properties of a material to detect an analyte and involve functionalized nanostructured materials fabricated at high financial, effort, and energy cost. However, a cell-based magnetic sensor which turns on magnetism with response to an analyte would eliminate both the need for an external nanomaterial synthesis step as well as allow for characterization instrumentation as

simple as a bar magnet. Therefore, the second part of this chapter discusses our efforts towards inducing a magnetic function in AMB-1 in response to an analyte.

4.2. Materials and methods

Reagent information. Luria-Bertani (LB) Broth Miller, LB Agar Miller, sodium thiosulfate, sodium nitrate, and glycerol were purchased from EMD Biosciences (Darmstadt, Germany). Carbenicillin (Cb), isopropyl-β-D-thiogalactopyranoside (IPTG), sodium chloride, tris(hydroxymethyl)aminomethane base (Tris), dithiothreitol (DTT), 4-(2-hydroxyethyl)-1-piperazineethanesulfonic acid (HEPES), magnesium chloride hexahydrate, potassium chloride, potassium phosphate monobasic, potassium phosphate dibasic, D-sucrose, kanamycin (Km), ethylene glycol, ethylene diamine tetraacetic acid disodium dihydrate (EDTA), bromophenol blue sodium salt, anhydrous sodium acetate, methanol, ethanol, and L-ascorbic acid were purchased from Fisher Scientific (Pittsburgh, PA). Methylsulfoxide (DMSO), hydrochloric acid, glacial acetic acid, ammonium hydroxide, potassium hydroxide, and sodium hydroxide were purchased from EMD Millipore (Billerica, MA). β-mercaptoethanol, ammonium bicarbonate, sodium dithionite, sodium phosphate dibasic hepthydrate, N,N,N',N'-tetramethyl-ethane-1,2-diamine (TEMED), ammonium iron(II) sulfate hexahydrate, magnesium sulfate heptahydrate, manganese(II) sulfate monohydrate, cobalt(II) chloride hexahydrate, calcium chloride, zinc sulfate heptahydrate, copper(II) sulfate pentahydrate, aluminum potassium sulfate dodecahydrate, boric acid, sodium molybdate dehydrate, succinic acid, biotin, folic acid, pyridoxine hydrochloride, thiamine hydrochloride, riboflavin, calcium D-(+)-pantothenate, vitamin B-12, *p*-aminobenzoic acid, thioctic acid, nicotinic acid, d-desthiobiotin, diaminopimelic acid (DAP), arabinose, Tween-20, glycine-HCl, bovine serum albumin (BSA), pyrrolidine dithiocarbamate (PDTC), manganese (II) chloride tetrahydrate, zinc (II) chloride, iron (III) chloride hexahydrate, and lithium manganese (III, IV) oxide were purchased from Sigma-Aldrich (St. Louis, MO). Formic acid was purchased from Acros Organics (Morris Plains, NJ). Nitrilotriacetic acid was purchased from Eastman Organic Chemicals. Acrylamide/Bis-acrylamide (30%, 37.5:1), electrophoresis grade sodium dodecyl sulfate (SDS) and ammonium persulfate were purchased from Bio-Rad Laboratories (Hercules, CA). Restriction enzymes, T4 DNA ligase, Antarctic phosphatase, Phusion DNA polymerase, T5 exonuclease,, Taq DNA ligase, and the Ph.D. 7 phage display peptide library kit were purchased from New England Biolabs (Ipswich, MA). Deoxynucleotides (dNTPs) and Platinum Taq High-Fidelity polymerase (Pt Taq HF) were purchased from Invitrogen (Carlsbad, CA). PageRuler™ Plus prestained protein ladder was purchased from Fermentas (Glen Burnie, Maryland). Oligonucleotides were purchased from Integrated DNA Technologies (Coralville, IA), resuspended at a stock concentration of 100 µM in 10 mM Tris-HCl, pH 8.5, and stored at either 4°C for immediate use or -20°C for longer term use. DNA purification kits was purchased from Qiagen (Valencia, CA).

Bacterial strains. *E. coli* DH10B-T1[R] was used for DNA construction. *E. coli* WM3064 was used for conjugative transfer of plasmids into *M. magneticum* AMB-1 wild-type (AK30) and knockouts (Δ*mamP*, AK69; ΔR3, AK36; Δ*mms6*cl, AK124; Δ*mms6*, AK103) strains as previously described [*24*, *25*, *26*]. *E. coli* ER2738 was used for phage display [*13*].

Plasmid construction. Standard molecular biology techniques were used to carry out plasmid construction. All PCR amplifications were carried out with Phusion DNA polymerase. For

amplification of GC-rich sequences from *M. magneticum* AMB-1 (AMB-1), PCR reactions were supplemented with DMSO (5%) with primer annealing temperatures 8-10°C below the melting temperature (T_m) calculated using OligoCalc [27]. Plasmids were assembled using the Gibson method [28]. All constructs were verified by sequencing (Quintara Biosciences; Berkeley, CA).

Plasmids for complementation for new materials. The plasmids for expression of Mms6 peptides with mutated metal-binding segments in *M. magneticum* AMB-1 were constructed as follows:

pAK262Amp-MmsF.MmsTiO₂. The pAK262Amp-MmsF.MmsTiO₂ plasmid was constructed by whole vector amplification of pAK262Amp-MmsF.Mms6 with overlapping primers MmsFTi F1/MmsFTi R1 to change the metal-binding C-terminus of the Mms6 protein to a peptide known to precipitate TiO₂ i*n vitro* under mild, aqueous conditions (Ti-1; RKKRTKNPTHKL) [29]. The vector was assembled by in a one-piece Gibson reaction [28].

pAK262Amp-MmsTiO₂. The pAK262Amp-MmsTiO₂ plasmid was constructed by amplifying MmsF.MmsTiO₂ from pAK262Amp-MmsF.Mms6 with MmsTi F1/R1 and by amplifying the pAK262Amp vector from pAK262Amp-MamP. The two pieces were assembled in a Gibson reaction [28].

pAK262Amp-MmsF.MmsZnO. The pAK262Amp-MmsF.MmsZnO plasmid was constructed by amplifying MmsF.MmsZnO from pAC-MmsF.Mms6 with MmsZn F1/R1 to change the magnetite-binding C-terminus of Mms6 to a peptide known to precipitate ZnO *in* vitro (ZnO-1; EAHVMHKVAPRPGGSC) [30-32]. The pAK262Amp vector was amplified from pAK262Amp-MamP with MmsZn F2/R2, and the two pieces were assembled in a Gibson reaction [28].

pAK262Amp-MmsF.MmsAu. The pAK262Amp-MmsF.MmsAu plasmid was constructed by amplifying MmsF.MmsAu from pAK262Amp-MmsF.Mms6 with overlapping primers MmsAu F1/R1 to change the metal-binding C-terminus of Mms6 to a well-studied peptide known to precipitate gold nanoparticles (A3; AYSSGAPPMPPF) [33, 34]. The pAK262Amp vector from pAK262Amp-MamP with MmsAu F2/R2 and the two pieces were assembled in a Gibson reaction [28].

Plasmids for complementation for inducible magnetite formation. The plasmids for inducible magnetite formation in *M. magneticum* AMB-1 were constructed as follows:

pAK262Amp-LacIq.(T5)MamP. The pAK262Amp-LacIq.(T5)MamP plasmid was constructed by amplifying the repressor gene *lacIq* and the *T5* promoter from pT533-dsbAC with the primers LacR(T5)P F1/F2 and inserting into the SphI-EcoRI restriction site of pAK262Amp-MamP by Gibson assembly [28].

pAK262Amp-AraC.(ara)MamP. The pAK262Amp-AraC.(ara)MamP plasmid was constructed by amplifying *araC* and the *pBAD* promoter from the pBAD18 vector [35] with the primers AraR(ara)P F1/F2 and inserting into the SphI-EcoRI restriction site of pAK262Amp-MamP by Gibson assembly [28].

pAK262Amp-(ara)MamP. The pAK262Amp-(ara)MamP plasmid was constructed by amplifying the *pBAD* promoter from the pBAD18 vector [35] with primers araP F1/ araR(ara)P

R1 and inserting into the SphI-EcoRI site of the pAK262Amp-MamP vector by Gibson assembly [28].

pAK262Amp-golTSB.MamP. The pAK262Amp-golTSB.MamP plasmid was constructed by amplifying the gold-inducible golTSB operon from the genome of *Salmonella enterica* serovar *typhimurium* [36, 37] with primers golMamP F1/R1 and the gold-inducible promoter with golMamP F2/R2 and inserting into the SphI-EcoRI site of the pAK262Amp-MamP vector by Gibson assembly [28].

pAK262Amp-(gol)MamP. The pAK262Amp-(gol)MamP plasmid was constructed by amplifying the gold-inducible promoter from the genome of *Salmonella enterica* serovar *typhimurium* [36, 37] with primers golMamP F2/R2 and inserting into the SphI-EcoRI site of the pAK262Amp-MamP vector by Gibson assembly [28].

pAK262Amp-LacIq.(T5)MamP.GFP$_{sf}$. The pAK262Amp-LacIq.(T5)MamP.GFP$_{sf}$ plasmid was constructed by amplifying GFP$_{sf}$ from pAK262Amp-MamP.GFP$_{sf}$ with P GFPsf F3/R3 and inserting into the pAK262Amp-LacIq.(T5)MamP vector at the SpeI restriction site.

pAK262Amp-AraC.(ara)MamP.GFP$_{sf}$. The pAK262Amp-AraC.(ara)MamP.GFP$_{sf}$ plasmid was constructed by amplifying GFP$_{sf}$ from pAK262Amp-MamP.GFP$_{sf}$ with P GFP sf F3/P GFPsf R3 and inserting into the pAK262Amp-AraC.(ara)MamP vector at the SpeI restriction site.

pAK262Amp-LacIq.(T5)GFP$_{sf}$. The pAK262Amp-LaqIq.(T5)GFP$_{sf}$ plasmid was constructed by amplifying GFP$_{sf}$ from pAK262Amp-MamP.GFP$_{sf}$ with lacGFP F1/P GFPsf R3 and inserting into pAK 262Amp-LacIq.(T5)MamP at the NdeI-SpeI restriction site.

pAK262Amp-AraC.(ara)GFP$_{sf}$. The pAK262Amp-AraC.(ara)GFP$_{sf}$ plasmid was constructed by amplifying GFP$_{sf}$ from pAK262Amp-MamP.GFP$_{sf}$ with araGFP F1/P GFPsf R3 and inserting into pAK262Amp-AraC.(ara)MamP at the NdeI-SpeI restriction site.

Transformation of *M. magneticum* AMB-1. Plasmids for complementation or gene disruption were introduced into AMB-1 by conjugative transfer from an *E. coli* WM3064 donor strain using literature methods as described [1]. The plasmid to be transferred was first transformed into *E. coli* WM3064 by electroporation and plated for growth overnight at 37ºC on LB agar supplemented with the appropriate antibiotic (Km, 100 µg/mL; Cb, 100 µg/mL) and DAP (300 µM). Individual colonies were inoculated into LB (5 mL) containing antibiotic and DAP and grown overnight at 37ºC with rotary shaking (200 rpm). *E. coli* cell cultures (500 µL) were then pelleted by brief centrifugation (14,000 × *g*) for 1 min at room temperature. The pellets were washed twice with LB DAP (0.5 mL) before resuspending in LB DAP (200 µL). The AMB-1 recipient strain was prepared by inoculation of cells from a freezer stock into a sealed-cap conical tube (50 mL) containing Magnetic Growth media (MG media, 50 mL). All MG media described in this document is prepared according to literature methods and supplemented with iron malate solution (100× stock made from 3 mM FeCl$_3$ and 9 mM DL-malic acid) and Wolfe's vitamin solution [25]. After 2 d growth at 30ºC without agitation, the entire culture volume was pelleted by centrifugation (14,000 × *g*) for 15 min at 4ºC and resuspended in MG (600 µL). One-third of the resuspended AMB-1 pellet was added to the resuspended *E. coli* pellet (200 µL), the cells were mixed gently, pelleted by brief centrifugation (14,000 × *g*) for 10 min at room temperature, and resuspended in MG (200 µL). The cells were plated together onto MG DAP agar. The plates were

first incubated at room temperature for 1 h before transferring into a sealed microaerobic jar (Oxoid, Ltd.; Basingstoke, UK) at 30ºC for an additional 2-4 h. The jar was evacuated with vacuum until the pressure valve read -0.6 bar and was then refilled with N_2 to a pressure of +0.2 bar. The positive pressure was relieved by venting before the jar was sealed at 0 bar. After this incubation, cell mixtures were scraped off the MG DAP agar plates with a sterile inoculating loop and streaked onto fresh MG agar plates supplemented with the appropriate antibiotic (Km, 15 µg/mL; Cb, 20 µg/mL). These plates were incubated in the microaerobic jar for 4-6 d until colonies could be visualized. Single colonies were inoculated into microcentrifuge tubes (1.5 mL, Eppendorf) completely filled with MG (1.5 mL) and supplemented with the appropriate antibiotic (Km, 10 µg/mL; Cb, 20 µg/mL) to yield primary cultures within 4-8 d of growth at 30ºC with no agitation. After a cell pellet developed in the primary culture, an aliquot of the primary culture (10 µL) was diluted (1:1000) into sealed anaerobic tubes (20 mL) with MG containing 20 mM HEPES pH 7.2 supplemented with the appropriate antibiotic (10 mL) and grown at 30ºC with no agitation until $OD_{400\,nm} = 0.1$-0.25 (approximately 2 d) for the secondary culture.

Characterization of cellular magnetization (C_{mag}). Secondary AMB-1 cultures were grown in MG (10 mL) containing 20 mM HEPES pH 7.2 without agitation at 30°C in seal-capped anaerobic culture tubes (20 mL) with Ar-evacuated headspace to $OD_{400\,nm} = 0.2$ (~2 d). The culture C_{mag} was determined as previously described [*38*]. Briefly, $OD_{400\,nm}$ was measured on an Agilent 8000 UV-Visible spectrophotometer with a magnet parallel or perpendicular to the spectrometer beam and the ratio ($C_{mag} = A_{400\,nm,\,perpendicular}/A_{400\,nm,\,parallel}$) was calculated. The C_{mag} measurements were performed in biological triplicates with two technical replicates per colony using cultures from three independent growths or conjugations.

Transmission electron microscopy. Secondary AMB-1 cultures were grown in MG (10 mL) containing 20 mM HEPES pH 7.2 without agitation at 30°C in seal-capped anaerobic culture tubes (20 mL) with the headspace evacuated with Ar to $OD_{400\,nm} = 0.25$–0.3 (~2-3 d). An aliquot of cell culture (100–500 µL) was pelleted by brief centrifugation ($14,000 \times g$) for 10 min aerobically at room temperature and resuspended in MG (~10 µL). The cells were adsorbed onto 400-mesh copper grid coated with Formvar/Carbon (TedPella Inc.) and analyzed using a TECNAI 12 TEM (FEI) operating at 120 kV with a charge-coupled device camera (Gatan UltraScan, University of California at Berkeley Electron Microscope Laboratory). In each case, 20–50 cells, each containing 1–20 crystals, were analyzed. For each strain, >300 particles from >20 cells was analyzed for three different colonies from each biological replicate.

Immunostaining. Antibodies to MamP were raised by ProSci Inc. (Poway, CA) in rabbits using a synthetic peptide from MamP (QLEGAPMILAGPRPHGYR) conjugated to a carrier protein. AMB-1 cultures were grown without agitation in MG (10 mL) containing 20 mM HEPES pH 7.2 at 30°C in seal-capped anaerobic culture tubes (20 mL) evacuated with Ar to $OD_{400\,nm} = 0.2$ (~ 2d). Cells were pelleted by centrifugation ($9,800 \times g$) for 15 min and resuspended in 2×Laemmli buffer containing BME (5% v/v) (125 µL for 10 mL of culture at $OD_{400\,nm} = 0.2$). The cell suspension was heated at 70ºC for 15 min and centrifuged ($14,000 \times g$) for 10 min at room temperature to remove particulate matter. Samples (15 µL) were run on a 12% Bis-Tris SDS-PAGE gel at 150 V at 4ºC for 45-80 min. The gel was equilibrated in transfer buffer (50 mM Tris, 192 mM glycine, 20% v/v methanol, 0.05% w/v SDS) for 25 min before transferring at 50 V for 2 h to a pre-wetted PVDF membrane (Bio-Rad) using a BioRad Trans-Blot. All subsequent steps

utilized a rocking agitator to provide mixing. The membrane was blocked for 2 h at room temperature in 5% w/v milk (Apex BioResearch Products, Research Triangle Park, NC) in TBST buffer (50 mM Tris, pH 8.0, 150 mM NaCl, 0.1% w/v Tween-20) followed by incubation with MamP primary antibodies (1:1000 dilution in TBST containing 5% w/v milk) at room temperature for 1.5 h. The membrane was washed in TBST (3×15 min) before incubating with Goat Anti-Rabbit IgG-HRP (Bio-Rad Laboratories,1:5000) at room temperature for 1 h. The membrane was washed again TBST (3×15 min) before visualization with a Western Lightning Plus ECL kit (PerkinElmer; Waltham, MA) using a Bio-Rad Mini Trans-Blot Cell and Quantity One software.

Synthesis of MnFe$_2$O$_4$. The spinel ferrite MnFe$_2$O$_4$ was synthesized by a co-precipitation protocol adapted from literature protocol [39]. In a round-bottom flask (500 mL) with a stir bar, iron (III) chloride hexahydrate (32.44 g) and manganese (II) chloride tetrahydrate (19.79 g) was added and purged of oxygen by applying vacuum and refilling with N$_2$ three times. Next, ddH$_2$O (250 mL) degassed with Ar was added via syringe to the solution and the metal salts were mixed until dissolved. In another round-bottom flask (1 L) with a stir bar, sodium hydroxide (60 g) was dissolved in ddH$_2$O (250 mL) which had been degassed by Ar. The FeCl$_3$/MnCl$_2$ solution was then added dropwise via syringe to the stirring sodium hydroxide solution. Once the metal mixture was added, the flask was heated to 100°C. After 2 h, the flask was cooled and the nanoparticles were isolated by a magnet and washed with 3×500 mL ddH$_2$O. The particles were then resuspended in ddH$_2$O (50 mL), frozen in liquid nitrogen, and lyophilized to obtain a dry powder.

Phage panning against spinel materials. Ph.D. 7 phage display peptide library kit (New England Biolabs; Ipswitch, MA) was used to select for peptides that can strongly bind spinel materials MnFe$_2$O$_4$ (synthesized as described in previous section) and LiMn$_2$O$_4$ (uncoated powder, purchased from Sigma-Aldrich) *in vitro*. Standard protocols were followed closely and are summarized below [16]:

Negative selection panning against polystyrene. The polystyrene 6-well (diameter=34.8 mm) Corning Co-star cell culture dish was used as a panning plate (Sigma-Aldrich; St.Louis, MO). In order to eliminate phage peptides that bind nonspecifically to the panning plate, we performed a negative selection against the plate. The well was washed with 0.5% TBST (50 mM Tris-HCl pH 7.5, 150 mM NaCl with 0.5% Tween-20) and then rinsed with 3×1 mL TBS (50 mM Tris-HCl pH 7.5, 150 mM NaCl). An aliquot of phage (10 μL) from the Ph.D. 7 phage display peptide library kit (New England Biolabs; Ipswitch, MA) in 0.5 mL TBS was added to the plate and incubated for 15 min with agitation on a rotary shaker at 150 rpm. The unbound phage was removed and added directly to *E. coli* ER2738 cells to be amplified (see below) for positive selections against peptide libraries. The plate was washed with 5×0.5 mL 0.5% TBST. Each of these washes was then subsequently added to the same *E. coli* for positive selection. For the negative control, the bound phage were eluted with 0.5 mL of Elution Buffer (0.2 M glycine-HCl, pH 2.2, 1 mg/mL Bovine Serum Albumin) by incubation for 5 min on a rotary shaker followed by neutralization with 150 μL Neutralization Buffer (1 M Tris-HCl pH 9.1). These phage were added to a new aliquot of *E. coli* ER2738 cells (20 mL) grown from an overnight to OD$_{600}$ ~ 0.05 to be propagated as the negative control. Cultures containing the infected cells were grown for 37°C for 4.5 h at 300 rpm. Phage amplification, isolation, and titering yielded a library of 1×10^{11} plaque-forming units per 10 μL (pfu) amplified eluate for phage panning experiments against spinel materials.

Phage amplification and isolation. For amplification of phage, *E. coli* ER2738 was plated on LB agar containing tetracycline (Tc, 20 µg/mL) and grown overnight at 37°C. A single colony was picked and inoculated into a culture tube containing 10 mL LB Tc, which was grown overnight at 37°C with shaking at 200 rpm. The overnight culture was then used to seed a 20 mL LB in a 250 mL baffled flask to $OD_{600} = 0.001$. After growing at 37°C at 200 rpm to $OD_{600} \sim 0.01 - 0.05$, eluate from the panning studies was added and the culture was propagated at 37°C with vigorous shaking (300 rpm) for an addition 4.5 h. The culture was then transferred to a 50 mL centrifuge tube and pelleted at $12,000 \times g$ for 10 min at 4°C. The supernatant was collected, transferred to a new tube, and recentrifuged at $12,000 \times g$ for 10 min at 4°C. The upper 80% of the supernatant was transferred to a new tube and the phage was precipitated overnight by addition of $^1/_6$ vol of 20% (w/v) polyethylene glycol (PEG) in 2.5 M NaCl at 4°C. The precipitated phage was pelleted at $12,000 \times g$ for 15 min at 4°C. The supernatant was removed and discarded before recentrifuging the pellet at $12,000 \times g$ for 1 min at 4°C to remove residual supernatant by pipetting, while carefully avoiding the white phage pellet on the side of the tube. The phage pellet was then resuspended in 1 mL of TBS (50 mM Tris-HCl pH 7.5, 150 mM NaCl), transferred to a microcentrifuge tube (1.5 mL), and centrifuged at $16,500 \times g$ for 5 min at 4°C. The supernatant containing the resuspended phage was transferred to a new microcentrifuge tube (1.5 mL) and the phage were reprecipitated by the addition of $^1/_6$ vol of 20% (w/v) PEG in 2.5 M NaCl and incubation on ice for 30 min. The phage pellet was collected by centrifuging at $16,500 \times g$ for 10 min at 4°C. The supernatant removed and discarded while the dry pellet was resuspended in 200 µL TBS and centrifuged at $16,500 \times g$ for 1 min at 4°C to remove additional insoluble material. The supernatant was then transferred to a clean tube to be used as the amplified eluate for additional rounds of panning.

Phage titering. An accurate determination of the number of phage in the amplified eluate is necessary to determine the amount of eluate to add to the next round of panning. *E. coli* ER2738 was inoculated from a plate into LB (5 mL containing 20 µg/mL Tc) and grown at 37°C at 200 rpm to $OD_{600} \sim 0.5$. The cell suspension (200 µL) was aliquoted into three individual microcentrifuge tubes for tittering (1.5 mL). For infection, the phage solution (10 µL of 10-, 100-, and 1000-fold dilutions of the unamplified phage eluate or 10^8-, 10^9-, and 10^{10}-fold dilutions of amplified phage eluate) was to this aliquot, vortexed briefly, and incubated at room temperature for 5 min. The cells were then transferred to individual culture tubes (50 mL) containing Top Agar (10 g/L Bacto-Tryptone, 5 g/L yeast extract, 0.5 g/L NaCl, 7 g/L Bacto-Agar autoclaved before the addition of 0.5 mM $MgCl_2$ and 2 mM glucose) at 45°C. The Top Agar was then plated on a LB agar plate containing IPTG (50 µg/mL) and X-gal (40 µg/mL) and warmed to 37°C. After overnight incubation at 37°C, plates containing ~100 well-spaced plaques were counted to obtain plaque-forming units (pfu) in 10 µL eluate.

Panning against spinel materials. $MnFe_2O_4$ and $LiMn_2O_4$ (0.5 mg) were added in separate wells and allowed to air dry. The powders were washed once with 0.1% TBST (1 mL) for 10 min on a rotary shaker at 100 rpm. Amplified phage from the negative selection against polystyrene (11 µL) was added in 0.1% TBST (0.5 mL) and incubated for 10 min on a rotary shaker at 100 rpm. The phage was removed by pipet and the powders were washed with $5 \times$ 0.5 mL of 0.1% TBST. Bound phage was eluted with Polystyrene Elution Buffer (0.5 mL) and neutralized with Neutralization Buffer (150 µL). Phage amplification and isolation was performed as described above on the eluted phage before titering. The first panning round with

94

MnFe$_2$O$_4$ yieldedan eluted phage titer of 80×10^9 pfu, while the first panning round with LiMn$_2$O$_4$ gave an amplified phage titer of 192×10^9 pfu.

A second round of panning was performed using the amplified eluate from the first panning round as the starting library. The dried MnFe$_2$O$_4$ and LiMn$_2$O$_4$ (0.5 mg) powders were washed once in their individual wells with 0.2% TBST (1 mL) for 10 min on a rotary shaker at 100 rpm. Amplified phage from the first panning (MnFe$_2$O$_4$, 90 µL; LiMn$_2$O$_4$, 20 µL) was added in 0.1% TBST (0.5 mL) and incubated for 20 min on a rotary shaker at 100 rpm. The phage was removed by pipet and the powders were washed with 10×0.5 mL 0.2% TBST for 1 min per wash on a rotary shaker at 100 rpm. Bound phage was eluted with Polystyrene Elution Buffer (0.5 mL) and neutralized with Neutralization Buffer (150 µL). The second panning round on MnFe$_2$O$_4$ yielded an eluted phage titer of 6×10^{11} pfu, while the second panning round on LiMn$_2$O$_4$ gave an amplified phage titer of 3×10^{11} pfu. These libraries were used for the third round of panning.

A third round of panning was performed using an analogous protocol to the second round except that TBST was increased from 0.2% to 0.5% in all steps (MnFe$_2$O$_4$, 10 µL amplified phage; LiMn$_2$O$_4$, 10 µL amplified phage). Bound phage from this round (Pan 3) were isolated as individual plaques and submitted for sequencing.

Stringency was increased for the fourth and last round of panning by addition of 50 mM sodium acetate to 0.5% TBST in all steps and performed using an analogous protocol to the third round (From Pan 3 libraries: MnFe$_2$O$_4$, 10 µL amplified phage; LiMn$_2$O$_4$, 10 µL amplified phage). Bound phage from this round (Pan 4) were isolated as individual plaques and submitted for sequencing.

Phage sequencing. From a titering plate containing fewer than 100 plaques, individual blue phage plaques were picked with sterile pipette tips and transferred to a culture tube (10 mL) containing 1 mL of *E. coli* ER2738 overnight culture diluted 100-fold in LB and subsequently incubated for 4.5 h at 37°C with shaking at 300 rpm. To isolate phage DNA for sequencing, the culture was centrifuged at $16,500 \times g$ for 30 s in 1.5 mL microcentrifuge tubes. A portion of the supernatant (500 µL) was transferred to a fresh tube and 20% (w/v) PEG in 2.5 mM NaCl (200 µL) was added and mixed by inversion. The tubes were incubated at room temperature for 10 min to preferentially precipitate single-stranded phage DNA and then centrifuged at $16,500 \times g$ for 10 min at 4°C. After removing the supernatant, the pellet was washed with ice-cold 70% (v/v) ethanol (0.5 mL) and air dried briefly before resuspending in TBS buffer (30 µL). The phage peptide tails were sequenced by Quintara Biosciences using the -96 gIII sequencing primer included in the Ph.D. 7 phage display peptide library kit (New England Biolabs; Ipswitch, MA).

Growth curves of *M. magneticum* AMB-1. Single colonies were inoculated into microcentrifuge tubes (1.5 mL, Eppendorf) completely filled with MG (1.5 mL) and supplemented with the appropriate antibiotic (Km, 10 µg/mL; Cb, 20 µg/mL) to yield primary cultures within 4-8 d of growth at 30ºC with no agitation. After a cell pellet developed in the primary culture, an aliquot of the primary culture (10 µL) was diluted (1:1000) into sealed anaerobic tubes (20 mL) with MG containing 20 mM HEPES pH 7.2 supplemented with the appropriate antibiotic (10 mL) and the compound being tested. Zinc (II) chloride or the pyrolidine dithiocarbamate (PDTC) ionophore were added in concentrations from 50-150 µM or 0.5-10 µM, respectively. The

secondary cultures were then degassed by evacuating the headspace with Ar for 15 min and grown at 30ºC with no agitation. The OD_{400} was measured by removing 500 µL via syringe periodically after 24 h of growth using an Agilent 8453 UV-Vis spectrophotometer.

Inducible magnetic response. Experiments for inducible magnetic response were performed on secondary cultures, prepared as described for the transformation of *M. magneticum* AMB-1. After a cell pellet developed in the primary culture, an aliquot of the primary culture (10 µL) was diluted (1:1000) into sealed anaerobic tubes (20 mL) with MG containing 20 mM HEPES pH 7.2 supplemented with the appropriate antibiotic (10 mL). The secondary cultures were then degassed by evacuating the headspace with Ar for 15 min and grown at 30ºC with no agitation. The inducer IPTG (500 µM) was added to the secondary culture of Δ*mamP* containing the plasmid pAK262Amp-LacIq.(T5)MamP once the culture was grown to $OD_{400} = 0.08$. The inducer arabinose (10 mM) was added to the secondary culture of Δ*mamP* containing the plasmid pAK262Amp-AraC.(ara)MamP once the culture was grown to $OD_{400} = 0.08$. Western and C_{mag} for each strain as well as for a control strain to which no inducer was added was performed as described above.

4.3. Results and Discussion

Design of constructs for the synthesis of new materials *in vivo*. Magnetotactic bacteria have a complex system of controls to prevent the uptake of non-iron metal ions into the magnetosome as well as to prevent the precipitation of new materials in the magnetosome [*18, 19*]. Therefore, we have taken several steps to simplify our approach. First, our specific target is the large superfamily of metal oxides (X_nO_m) and spinels ($XZYO_4$) to which magnetite belongs because their structures could be chemically accessible via magnetosome-based chemistry. They also possess a broad range of electronic, magnetic, and optical properties at the nanoscale and macroscale, and thus are of great interest in a wide range of applications [*8, 9, 40, 41*]. Second, though we are interested in the unique control over the valence of metal ions incorporated into the crystalline lattice, for the sake of synthetic simplicity, we chose to first focus on metal oxides that rely on a redox-neutral synthetic approach. For example, titanium dioxide (TiO_2) excites intense interest in its functional properties in different forms as a photocatalyst, semiconductor, solar cell material, and optoelectronic material (LCD and data storage), to name a few [*42*]. As a result, there are many synthetic routes to its synthesis, including biologically-templated [*29, 43-48*] along with redox-neutral and redox-dependent chemical approaches [*42*]. In particular, an aqueous-based synthesis of TiO_2 relies on Ti^{4+} hydrolysis chemistry to arrive at the crystalline product over a wide range of pH and redox conditions. Another interesting metal oxide with redox-neutral synthesis from simple zinc salts is zinc oxide (ZnO) [*32, 49-51*], a common additive to commercially important materials as well as a semiconductor with favorable properties for applications in liquid crystal displays and electronics. Third, we chose materials whose formation can potentially be monitored or screened by optical approaches. For example, though nanoscale Au(0) requires redox chemistry to form from a soluble salt, its formation can easily be monitored by eye due to the intense color of nanoscale Au [*52*]. Thus, many different conditions can be screened quickly.

Fourth but most critically, we chose materials that can be precipitated by a well-characterized peptide. Namely, a peptide sequence has been identified that binds and precipitates the material in water at biological pH or, better yet, robustly over a wide range of conditions. We

chose the Ti-1 peptide (RKKRTKNPTHKL), which can form crystalline anatase titanium dioxide over pH 2-8, for *in vivo* TiO_2 precipitation [*29*]. We chose the Zn-binding peptide (EAHVMHKVAPRPGGSC), which precipitates zinc oxide at room temperature in water, for *in vivo* ZnO crystallization [*30*]. We also included the A3 peptide (AYSSGAPPMPPF) in our study to test for *in vivo* Au(0) formation because it has shown to reduce Au salts in aqueous conditions to form nanoparticles [*33, 34*]. We then replaced the mineral-binding C-terminus of the Mms6 protein with each peptide to form $MmsTiO_2$, MmsZnO, and MmsAu, respectively (*Figure 4.1*). The chimeric protein was cloned behind the *lac* promoter in pAK262Amp for native expression in AMB-1. A second set of constructs with the fusion proteins as well as *mmsF* cloned behind the *lac* promoter in in pAK262Amp for native expression of both proteins in AMB-1, as *mmsF* is shown to be critical for the formation of full-sized magnetic particles in AMB-1 [*26*]. In fact, in the $\Delta mms6_{cl}$ knockout, *mmsF* was found to be the most critical gene in recovering a wild type phenotype, with mms6 having a more subtle finishing effect in wild type sized and shaped nanoparticles [*26*]. However, MmsF was not found to be bound tightly to magnetite particles *in vivo* [*53*]. Therefore, it is unclear what the physiological function is of MmsF and whether it would assist or inhibit the formation of non-magnetite materials.

Figure 4.1. *Mms6 mutants for precipitation of new materials in the magnetosomes of Magnetospirillum magneticum AMB-1. The mineral-binding C-terminus of the Mms6 protein was replaced withTiO₂-, ZnO-, and Au-precipitating peptides (a black box was placed around the residues) to form MmsTiO2, MmsZnO, and MmsAu, respectively. The chimeric protein was cloned behind the lac promoter in pAK262Amp for native expression in AMB-1.*

Expression and characterization of Mms6 chimeras in *M. magneticum* AMB-1. To test the potential ability of non-native mineral-precipitating peptides to inhibit the formation of magnetite *in vivo*, the corresponding *mmsF.mms6*, *mmsF.mmsTiO$_2$*, and *mmsF.mmsZnO* as well as *mmsTiO$_2$* fusions were then expressed from a constitutive *tac* promoter on a pAK(Amp^R)-derived plasmid in the AMB-1 Δ*mms6*$_{cl}$ background [*26*]. Initial characterization of the *mms6* chimeras was carried out using a qualitative assay for cellular magnetization (C$_{mag}$), which measures the ability of an oblong cell to turn in the presence of an external magnetic field using the ratio of light scattered when this field is placed parallel or perpendicular to the axis of the spectrophotometric cell. The parental Δ*mms6*$_{cl}$ strain exhibits a strong magnetic defect with C$_{mag}$ measurement of 1.1, where 1.0 indicates no cellular magnetization and 2.0 represents the characteristic C$_{mag}$ observed for wild-type *M. magneticum* AMB-1 with full magnetite chains [*38*]. This observation is in line with the values for the strain measured by Murat *et al.*, as is the measurements for the complementation of the chromosomal deletion of *mms6*$_{cl}$ with the corresponding plasmid-borne wild-type *mmsF* and *mms6* genes, which rescues cellular magnetization to wild-type levels (C$_{mag}$ = 2.2). In contrast, initial characterization suggests that the MmsTiO$_2$ and MmsZnO peptides lead to some defects in magnetite mineralization, as complementation of *mms6*$_{cl}$ with plasmid borne *mmsF* with *mmsTiO$_2$* or *mmsZnO* mutants leads to C$_{mag}$ values of 1.6 and 1.4, respectively.

Transmission electron microscopy (TEM) analysis of AMB-1 Δ*mms6*$_{cl}$ and AMB-1 Δ*mms6*$_{cl}$ + *mmsF* + *mms6* iron oxide particle size also corresponded well to previously reported values (*Figure 4.2*) [*26*], with a higher percentage of small particles due to imaging the cells at mid-log phase rather than stationary phase. Though iron oxide particles AMB-1 Δ*mms6*$_{cl}$ + *mmsF* + *mmsTiO$_2$* appears to mineralize quite well in TEM with few size or shape defects, it does have a minor defect in C$_{mag}$ value, suggesting that there is a defect other than shape and size leading to imperfect magnetite, such as a defect in crystallinity or redox regulation. Iron oxide particles do not appear to appear to recover wild type size and shape in AMB-1 Δ*mms6*$_{cl}$ + *mmsF* + *mmsTiO$_2$* (*Figure 4.2*). These observations are interesting generalizations, but biological replicates need to be performed for convincing evidence of defects.
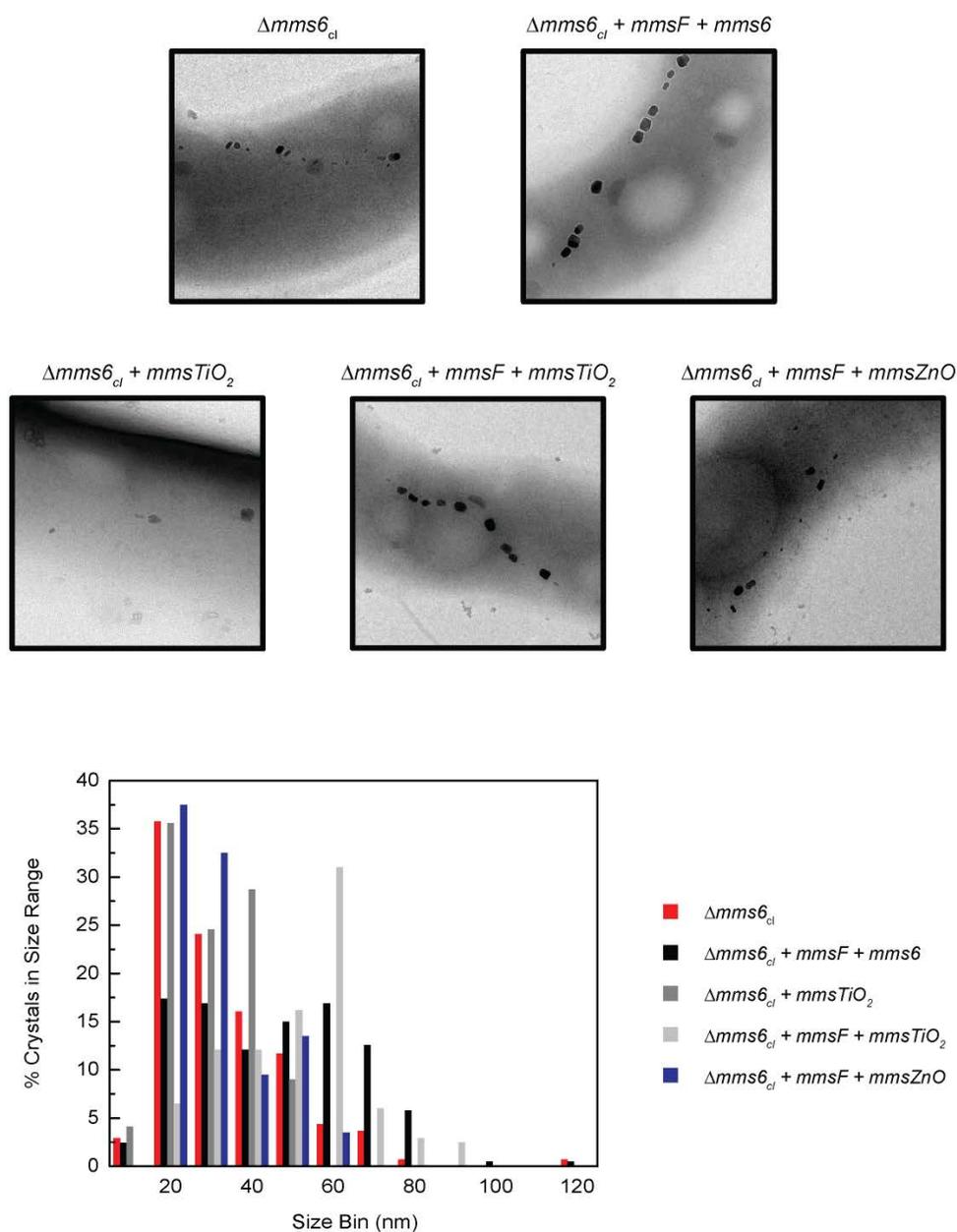
Figure 4.2. Transmission electron microscopy of M. magneticum AMB-1 expressing Mms fusions for new materials. Representative TEM images of M. magneticum AMB-1 $\Delta mms6_{cl}$ strains and $\Delta mms6_{cl}$ complemented with mmsF + mms6, mmsF + mmsTiO$_2$, mmsTiO$_2$, and mmsF + ZnO. Histograms of crystal sizes observed in the M. magneticum AMB-1 control strains ($\Delta mms6_{cl}$, 137 particles; $\Delta mms6_{cl}$ + mmsF + mms6, 207 particles) strains compared to $\Delta mms6_{cl}$ complemented with the different Mms metal-binding variants ($\Delta mms6_{cl}$ + mmsTiO$_2$, 67 particles; $\Delta mms6_{cl}$ + mmsF + mmsTiO$_2$, 54 particles; $\Delta mms6_{cl}$ + mmsF + mmsZnO, 43 particles).

Selection of MnFe₂O₄ and LiMn₂O₄-binding peptide sequences using phage display. Our specific target for forming new materials in the magnetosome is the superfamily of metal oxides (X_nO_m) and spinels ($XZYO_4$) to which magnetite belongs because their structures should be chemically accessible via magnetosome-based chemistry. We focused on accessing TiO_2 and ZnO by because these materials can be precipitated by well-characterized peptides under biological conditions. However, though TiO_2 and ZnO are metal oxides, they are not conservative choices for new material formation in magnetosomes: their lattice structures and their incorporated cations are quite different than magnetite [29, 40]. Therefore, our next step was to attempt to identify peptides that can bind spinel lattices. We chose $MnFe_2O_4$ as our most conservative option for a spinel lattice, where Mn^{2+} is substituted for Fe^{2+} in the crystal lattice. Manganese is also one of the few metal ions that is known to be incorporated into the magnetite lattice in magnetotactic bacteria [54]. We also chose to seek peptides that can bind the spinel $LiMn_2O_4$ due to its importance as a cathode material in low-cost, renewable batteries [55, 56]. We used commercially-available phage-displayed peptide libraries for selection of motifs that bind tightly and specifically to $MnFe_2O_4$ and $LiMn_2O_4$ spinel lattices (New England Biosciences; Ipswitch, MA).

Phage display is a technique that allows for selection of peptides that bind strongly to inorganic materials, organic molecules, biomolecules, or whole cells by panning phage displaying a 7-residue peptide library on the protein coat against the material of interest [13, 16]. The technique allows for selection of strong binding in specific conditions; for inorganic materials, selecting strong binders under aqueous conditions allows for the development of new synthetic methods that eliminate the harsh pressures, temperatures, and solvents often necessary for functional inorganic nanocrystals [10, 13, 16].

In order to remove non-specific binders from the phage library, phage display was first performed against the polystyrene dishes that would serve as the substrate for $LiMn_2O_4$ and $MnFe_2O_4$ nanoparticles in subsequent panning experiments. Phage was applied to the polystyrene and incubated with rotated to allow phage to bind the polystyrene. The polystyrene was washed with $5 \times 0.5\%$ Tween-20 detergent in Tris-buffered saline, and the phage from the washes were amplified in *E. coli* ER2738. The phage was eluted from the polystyrene with an acid wash containing the non-specific protein BSA (0.2 M glycine-HCl, pH 2.2, 1 mg/mL BSA) and these strong polystyrene-binders were removed from the phage library, leaving a library of 1×10^{11} plaque-forming units (pfu) per 10 µL amplified eluate for phage panning experiments against spinel materials.

In order to find peptides that strongly bind nanoscale $LiMn_2O_4$ and $MnFe_2O_4$, the nanoparticles were dried down onto polystyrene dishes and washed with panning buffer before the phage library was applied. After the phage library was incubated with the nanomaterials, the nanomaterials were washed with increasingly stringent conditions to remove phage that bind weakly or bind non-specifically. The strongest binders were eluted with an acidic wash buffer containing a high concentration of bovine serum albumin to help compete bound peptides off the material. The eluted phage was then amplified in cells and isolated from cells to provide the phage library for the next round of panning. The stringency of the washing conditions was increased for each round of panning: 0.1% Tween-20 was used in the first round of panning, 0.2% Tween-20 was used in the second round of panning, and 0.5% Tween-20 was used in the third round of panning. To the fourth round of panning, in addition to washing with 0.5% Tween-20, sodium acetate (50 mM) was added in order to provide additional competition for non-specific binders.

100

After four rounds of panning, we saw changes in the distribution of amino acids towards polar residues and proline (*Figure 4.3*). Though proline can be very important for setting binding topology [*57*, *58*], it has also been suggested that the abundance of proline in phage-displayed peptides originates from the phage secretion mechanism [*59*]. Therefore, binding studies need to be performed to attribute the dramatic increase (up to 12.8%) in proline residues from the original library to specific interactions with the spinels. Phage sequences from the third and fourth pannings also show a 1.2% to 5.0% increase in polar residues compared to the original library. This is interesting in that hydrophobic sequences are prone to non-specifically bind metal oxide nanoparticles under aqueous conditions [*33*]. The emergence of polar motifs suggests specific binding. However, we saw no evidence of amplification of charged residues, which are expected to bind strongly and specifically to metal oxides [*60*]. We theorize that the strongest binders may not have eluted from the materials even under harsh eluting conditions, as transition metal oxides adsorb many different molecules and reagents under biological conditions [*61*]. For example, the Mms6 family proteins could only be removed from magnetite *in vivo* by boiling the particles in detergent [*53*]. The lack of emergence of a consensus sequence also suggests that we are not selecting for the strongest binders and that the wash or elution conditions or both need to be much more stringent.

	MnFe$_2$O$_4$ Pan 3	MnFe$_2$O$_4$ Pan 4	LiMn$_2$O$_4$ Pan 3	LiMn$_2$O$_4$ Pan 4
	V H T T L R N	S E Q M K W I	R P A M H L A	T A I P F T M
	S D H R P S W	V P Y K N S H	S Y L V T M A	I V L P Y P I
	T H H T L F S	W H T A S S P	S P S L L R T	C P P P C S R
	T T P I T V P	S N L W T T G	I A Y Q P L N	G A Y P S P G
	N T N Q P T P	G A G A Q K G	T K T N Q M H	S I L P Y P Y
	T Q H R S P H	G L A D H L R	Q S T T S R A	A P P R T H P
	T L N R P P V	S I L P Y P Y	H Y S P P T P	A S S Q F P S
	V S S E H P S	Y T P S T P N	Q T S P H G K	I P L V T R S
	A H P L M L Y	G N S F R F L	S Q F S R T F	S S H T I S F
	V F P S S S P	T K G P T P S	K T T D W H I	A H S G M Y P
	Y A N W T S M	A T S P T A L	I E P P K P L	A L H Q P S R
	T I A L D A L	A P T T Q F P	T T P P A W E	Y P Q T S T S
	N I S H P R G	S N S S F K W	N S Q L K P Q	Q I I P P P H
	Q G P A P E R	G T W L S R G	A L T Y A P L	Q P Q H Q H L
	L A R E P T S	H Q S S F L H	E Q L R L T P	Q Y L P D A T
	A L M H G T S	G A Q S P R A	V S T D E N Y	T K G P T P S
	Q A A S L M L	L L A T P E K	M T P A A A R	Y H A R M L S
	L P P P S S F	F G Q I Q T E	T P L K I P N	S S A A L A Y
	H H F S R N I	W P N L L A P	L Q S P F T F	N Q D V P L F
			M H A S D Q I	
Hydrogen-bonding residues	+ 2.8	+ 2.8	+ 5.0	+ 1.2
Proline residues	+ 6.8	+ 12.8	+ 7.5	+ 4.5
Hydrophobic minus Proline	- 2.4	- 4.5	- 3.0	- 3.0

Figure 4.3. *Sequencing results of phage display against spinel nanomaterials MnFe$_2$O$_4$ and LiMn$_2$O$_4$. Phage display was performed against MnFe$_2$O$_4$ and LiMn$_2$O$_4$ nanoparticles. Non-specific or weakly binding phage were washed off the nanoparticles with increasing concentrations of Tween-20 detergent culminating in 0.5% Tween-20 washes in pan 3 and 0.5% Tween-20 washes containing 50 mM sodium acetate in pan 4. Strongly bound phage was eluted from the material with 0.2 M glycine-HCl pH 2.2 with 1 mg/mL BSA. Eluted phage were amplified, and individual plaques were picked and sequenced (19-21 sequences per experiment) for round 3 and 4 of panning.*

Optimizing the growth of *M. magneticum* AMB-1 in the presence of zinc(II) and a zinc(II) ionophore. Though prokaryotes are able to transport a wide variety of metal ions and main group elements [*17*], *Magnetospirillum magneticum* AMB-1 appears to exclude metal ions other than iron from the magnetosome [*18, 19*]. In fact, even when flooded with near-lethal concentrations of toxic heavy metals, magnetotactic bacteria will tightly control of the entrance of ions into the magnetosome resulting in different outcomes based primarily on the concentration of iron in solution: (1) in the presence of iron, MTB will precipitate magnetite only, (2) in the presence of low levels of iron, MTB will precipitate magnetite with some small incorporation of certain non-iron cations in the outer sphere of the magnetite crystal [*19*] or (3) precipitate highly toxic ions in the cytoplasm, such as in the case of tellurium, leaving the magnetosome free to crystallize magnetite [*18*], and (4) in the presence of no iron, magnetosomes remain empty. Therefore, it seems that either extensive protein engineering of putative magnetosome ion transporters or an alternate method that bypasses the native machinery is required to mobilize non-iron ions across the magnetosome membrane. We suggest that ionophores, small lipid-soluble molecules that selectively transport ions across bacterial membranes, can also be used increase the bioavailability of non-iron metal ions [*20*].

With a zinc oxide-mineralizing peptide in hand, we chose to focus on utilizing the zinc(II) ionophore, pyrrolidine dithiocarbamate (PDTC), to bypass the magnetosome's tight control of metal uptake. PDTC can inhibit bacterial growth at concentrations as low as 1 µM in sensitive strains and has been used at concentrations up to 400 µM to inhibit growth of *Escherichia coli* in the presence of trace zinc(II) [*62, 63*]. With the addition of $ZnCl_2$ to growth media, inhibitory effects are dramatic, while the addition of $FeCl_2$ or $FeCl_3$ has little to no effect on bacterial growth. In order to evaluate growing conditions for AMB-1 for zinc uptake, we tested the growth effect of PDTC and $ZnCl_2$ on wild type *Magnetospirillum magneticum* AMB-1. We found no inhibition of growth from 1 to 10 µM PDTC, suggesting that AMB-1 grows robustly in the presence of PDTC with trace Zn (*Figure 4.4A*). However, addition of $ZnCl_2$ has an unexpectedly dramatic effect on AMB-1. While previously tested bacteria grow with mild defects in the presence of 100 µM $ZnCl_2$, this concentration of zinc inhibited the growth of magnetotactic bacteria over 48 h (*Figure 4.4B*). At 50 µM $ZnCl_2$, AMB-1 showed no growth defect. However, the magnetic response of the cells (C_{mag}) peaked at 1.55 as opposed to AMB-1 cells grown without zinc (peak $C_{mag} \sim 2.0$), suggesting that zinc may play an inhibitory role in magnetite biogenesis (*Figure 4.4B*). The next step is be to determine growth curves of AMB-1 in the presence of 50 µM $ZnCl_2$ with various concentrations of PDTC to find concentrations in which Zn-PDTC has an effect on growth without killing the cells.

Next, the AMB-2 $\Delta mms6_{cl}$ + *mmsZnO* strain will be grown in the presence of Zn-PDTC and in both the presence and absence of iron. These cells can be characterized by TEM for their ability to grow nanocrystals and the material subject to more detailed physical analysis to determine mineral identity. There are also small molecules which inhibit the efflux of metal ions [*64*]. Introduction of these efflux inhibitors could increase the effectiveness of Zn-PDTC complexes, giving the zinc time to accumulate and be deposited in the magnetosome.
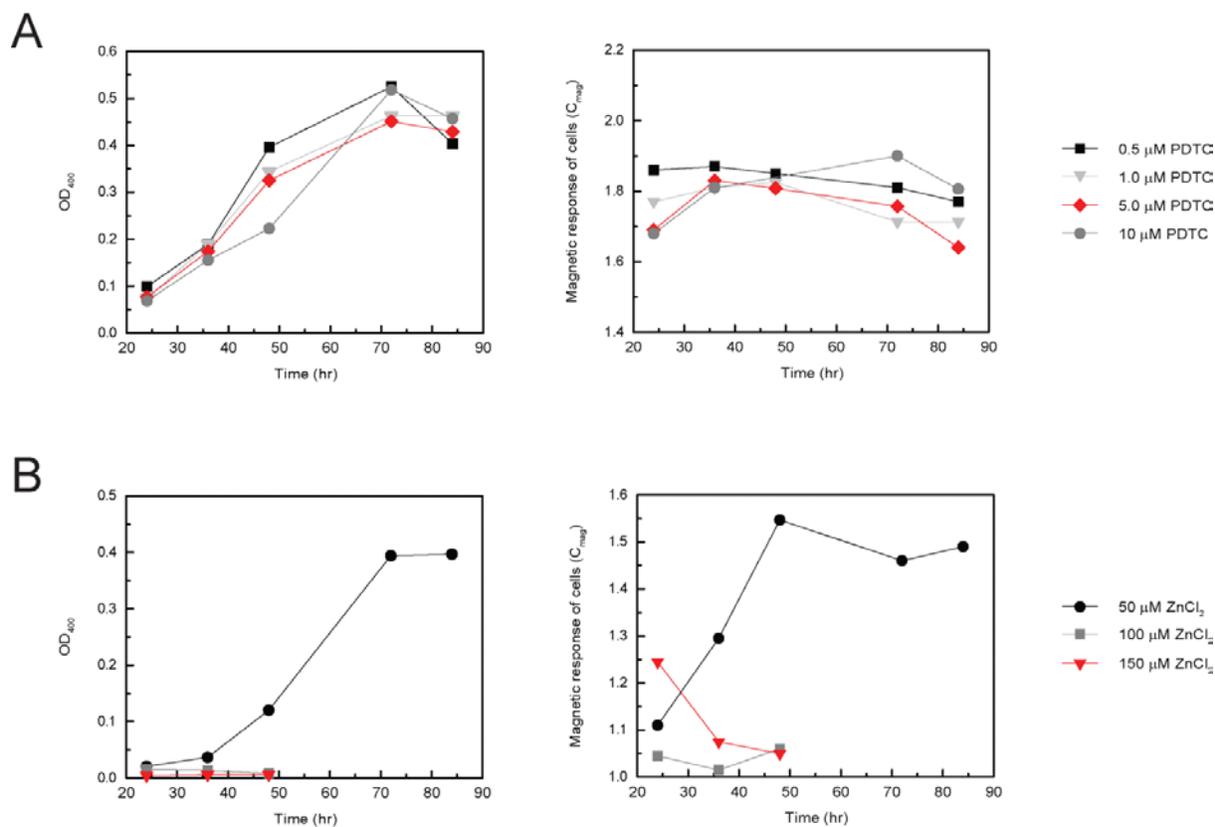
Figure 4.4. *Growth curves for wild type AMB-1 in the presence of zinc and a zinc ionophore. The OD_{400} and the C_{mag} of wild type AMB-1 was monitored for 48-82 hr. (A) AMB-1 were grown in 0.5-10 µM of the zinc ionophore, pyrrolidine dithiocarbamate (PDTC): 0.5 µM (black squares), 1 µM PDTC (light gray triangles), 5 µM PDTC (red diamonds), 10 µM PDTC (dark gray circles). (B) AMB-1 were grown in 50-150 µM of zinc (II) chloride: 50 µM $ZnCl_2$ (black circles), 100 µM $ZnCl_2$ (dark gray squares), 150 µM $ZnCl_2$ (red triangles).*

Inducible magnetic response in AMB-1. We also seek to take advantage of the natural transition-metal based function of magnetotactic bacteria, response to an external magnetic field, to build a cellular biosensor with an inducible magnetic output. By all indications, the protein components of the magnetosome membrane necessary to magnetite biomineralization are pre-assembled and primed to begin biomineralization immediately when the necessary environmental conditions (i.e. the presence of iron) are achieved [*25, 65*]. Therefore, magnetotactic bacteria provide a unique system for a simple biosensor: turning on a key biomineralization gene upstream of the membrane-forming process could also turn on a magnetic moment, an output detected by instrumentation as simple as a bar magnet.

We began by testing promoter-repressor pairs to find a set of responsive elements that are active in *M. magneticum* AMB-1. We began by using *mamP* as an inducible gene due to both the large dynamic range of magnetic response between AMB-1 Δ*mamP* (C_{mag} ~ 1.2) and AMB-1 Δ*mamP* + *mamP* (C_{mag} ~ 2.0) as well as our access to αMamP antibodies and several constructs for MamP expression in AMB-1 (*Chapter 2*). To this end, we expressed *mamP* from bacterial inducible promoters and their cognate respressors on pAK(Amp^R)-derived plasmids in an AMB-1 Δ*mamP* background. We chose to test the common T5 and ara$_{BAD}$ promoters, which are responsive to IPTG and arabinose, respectively [*66*]. We are also interested in testing promoters that can be induced by common environmental contaminants such as heavy metals or steroids, and chose to examine the promoter from the Au-responsive *golTSB* operon in AMB-1 [*36, 37*]. We found that the expression levels of *mamP* in the AMB-1 Δ*mamP* strain background were negligible from the pAK262Amp-LacIq.(T5)MamP and the pAK262Amp-AraC.(ara)MamP plasmids. However, MamP expression from the *gol* promoter in the AMB-1 Δ*mamP* + pAK262Amp-golTSB.MamP strain was high, suggesting that either the promoter has leaky expression or the repressor is not well-expressed/active in AMB-1. The construct also showed a near wild-type C_{mag} of 1.85 (compared to a wild type C_{mag} ~ 2.0), also indicating that MamP expression is high enough to make magnetite particles with a wild type phenotype.

We then tested the ability to induce the expression of MamP (*Figure 4.5*). We added the inducers IPTG (500 µM) to AMB-1 Δ*mamP* + pAK262Amp-LacIq.(T5)MamP and arabinose (10 mM) to Δ*mamP* + pAK262Amp-AraC.(ara)MamP. We found that MamP expression was negligible under the pBAD promoter, suggesting that the promoter is not active in AMB-1 and that higher concentrations of arabinose inducer should be tested. Expression of MamP was induced from the T5 promoter. However, though the expression of MamP was inducible, we were unable to achieve a magnetic response upon complemnetation. Both cells expressing MamP after induction and cells not expressing MamP after induction showed a C_{mag} around 1.30. These results may indicate that the timing of MamP expression could be an important factor in its ability to complement the corresponding genetic knockout and that other genes may be better candidates for biosensor development.

Though *mamP* is a convenient gene for monitoring inducible protein expression in AMB-1, other genes which are critical for the early stages of magnetite formation but do not interfere with magnetosome membrane formation could provide a larger dynamic range of inducible magnetic response. For example, *mamM* and *mamB* are thought to encode cation diffusion facilitator family proteins and probably are involved in iron transport into the magnetsome, while *mamN* is thought to encode a Na+/H+ antiporter, also critical in the early stages of magnetite formation. Knockouts of all three of these genes result in a C_{mag} of 1.0 (no magnetic response) [*25*]. Thus, even poor

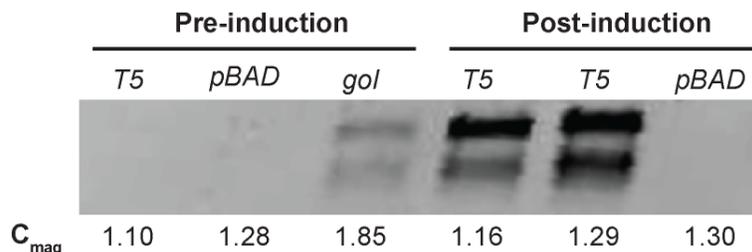formation of magnetite with the induction of these genes could provide a detectable induced magnetic response.

Figure 4.5. *Westerns for inducible expression of MamP in AMB-1 by immunostaining with αMamP. We compared the expression of MamP in complemented with wild-type MamP strains under the control of inducible promoters T5, pBAD, and gol with and without their respective inducer. The strain ΔmamP containing the plasmids pAK262Amp-LacIq.(T5)MamP (pre-induction lane T5), pAK262Amp-AraC.(ara)MamP (pre-induction lane pBAD), and pAK262Amp-golTSB.MamP (pre-induction lane gol) were tested for MamP exrpression without induction. The strain ΔmamP containing the plasmids pAK262Amp-LacIq.(T5)MamP (post-induction lanes T5) and, pAK262Amp-AraC.(ara)MamP (post-induction lane pBAD) were tested for MamP expression by inducing at $OD_{400} = 0.08$ with 500 μM IPTG or 10 mM arabinose, respectively. The C_{mag} was measured at $OD_{400} = 0.18$-0.20 before the cells were prepared for immunostaining.*

4.4. Conclusions

In summary, we have set up and begun testing systems to engineer magnetotactic bacteria for the production of new functional materials. We have replaced the metal-binding C-terminus of native Mms6 family proteins in AMB-1 with peptides known to precipitate metal oxides *in vitro* under mild conditions. Initial characterization of the behavior of these constructs in AMB-1 has been carried out although additional experiments are required to test whether they can enable formation of new materials *in vivo*. Towards this goal, we tested the tolerance of AMB-1 to the first row transition metal Zn, and we suggest that the zinc ionophore pyrrolidine dithiocarbamate could be conducive in bypassing the tightly-regulated metal-uptake systems in AMB-1 to allow transport of different metal ions into the magnetosome for formation of non-iron materials. In a separate goal, we have also discussed developing a cellular biosensor based on the formation of a magnetic material in response to an analyte. We tested common inducible bacterial promoters T5 and pBAD for the expression of magnetosome proteins, and discovered that IPTG can induce MamP expression under the control of the T5 promoter. We believe that inducible magnetism might be achieved by the inducible expression of magnetosome proteins involved in iron uptake.

4.5. References

1. A. Komeili, H. Vali, T. J. Beveridge, and D. K. Newman (2004) Magnetosome vesicles are present before magnetite formation, and MamA is required for their activation. *Proc. Natl. Acad. Sci. U. S. A.* 101(11):3839-3844.
2. M. E. Franke, T. J. Koplin, and U. Simon (2006) Metal and metal oxide nanoparticles in chemiresistors: does the nanoscale matter? *Small* 2(1):36-50.
3. A. Navrotsky (2011) Nanoscale effects on thermodynamics and phase equilibria in oxide systems. *ChemPhysChem* 12(12):2207-2215.
4. C. Yuan, H. B. Wu, Y. Xie, and X. W. Lou (2014) Mixed transition-metal oxides: design, synthesis, and energy-related applications. *Angew. Chem. Int. Ed.* 53(6):1488-1504.
5. J. F. Weaver (2013) Surface chemistry of late transition metal oxides. *Chem. Rev.* 113(6):4164-4215.
6. A. Navrotsky, C. Ma, K. Lilova, and N. Birkner (2010) Nanophase transition metal oxides show large thermodynamically driven shifts in oxidation-reduction equilibria. *Science* 330(6001):199-201.
7. J. Meyer, S. Hamwi, M. Kroger, W. Kowalsky, T. Riedl, and A. Kahn (2012) Transition metal oxides for organic electronics: energetics, device physics and applications. *Adv. Mater.* 24(40):5408-5427.
8. A. Maignan, W. Kobayashi, S. Hebert, G. Martinet, D. Pelloquin, N. Bellido, and C. Simon (2008) Transition-metal oxides with triangular lattices: generation of new magnetic and electronic properties. *Inorg. Chem.* 47(19):8553-8561.
9. B. Keimer (2006) Transition metal oxides: ferroelectricity driven by orbital order. *Nat. Mater.* 5(12):933-934.
10. G. Ahmad, M. B. Dickerson, Y. Cai, S. E. Jones, E. M. Ernst, J. P. Vernon, M. S. Haluska, Y. Fang, J. Wang, G. Subramanyam, R. R. Naik, and K. H. Sandhage (2008) Rapid bioenabled formation of ferroelectric BaTiO$_3$ at room temperature from an aqueous salt solution at near neutral pH. *J. Am. Chem. Soc.* 130(1):4-5.
11. E. M. Krauland, B. R. Peelle, K. D. Wittrup, and A. M. Belcher (2007) Peptide tags for enhanced cellular and protein adhesion to single-crystalline sapphire. *Biotechnol. Bioeng.* 97(5):1009-1020.
12. K. Shiba (2010) Exploitation of peptide motif sequences and their use in nanobiotechnology *Curr. Opin. Biotechnol.* 21(4):412-425.
13. S. R. Whaley, D. S. English, E. L. Hu, P. F. Barbara, and A. M. Belcher (2000) Selection of peptides with semiconductor binding specificity for directed nanocrystal assembly. *Nature* 405(6787):665-668.
14. C. Mao, D. J. Solis, B. D. Reiss, S. T. Kottmann, R. Y. Sweeney, A. Hayhurst, G. Georgiou, B. Iverson, and A. M. Belcher (2004) Virus-based toolkit for the directed synthesis of magnetic and semiconducting nanowires. *Science* 303(5655):213-217.
15. C. Mao, D. J. Solis, B. D. Reiss, S. Kottmann, R. Sweeney, G. Georgiou, B. Iverson, and A. M. Belcher (2004) Virus-based genetic toolkit for the directed synthesis of magnetic and semiconducting nanowires. *Science* 303:213-215.
16. J. Pande, M. M. Szewczyk, and A. K. Grover (2010) Phage display: concept, innovations, applications and future. *Biotechnol. Adv.* 28(6):849-858.

17.   T. J. Park, S. Y. Lee, N. S. Heo, and T. S. Seo (2010) *In vivo* synthesis of diverse metal nanoparticles by recombinant *Escherichia coli*. *Angew. Chem. Int. Ed.* 49(39):7019-7024.

18.   M. Tanaka, A. Arakaki, S. S. Staniland, and T. Matsunaga (2010) Simultaneously discrete biomineralization of magnetite and tellurium nanocrystals in magnetotactic bacteria. *Appl. Environ. Microbiol.* 76(16):5526-5532.

19.   S. Staniland, W. Williams, N. Telling, G. Van Der Laan, A. Harrison, and B. Ward (2008) Controlled cobalt doping of magnetosomes *in vivo*. *Nat. Nanotechnol.* 3(3):158-162.

20.   B. C. Pressman (1976) Biological applications of ionophores. *Annu. Rev. Biochem.* 45:501-530.

21.   Y. Wang, J. Dostalek, and W. Knoll (2011) Magnetic nanoparticle-enhanced biosensor based on grating-coupled surface plasmon resonance. *Anal. Chem.* 83(16):6202-6207.

22.   M. H. Meyer, M. Stehr, S. Bhuju, H. J. Krause, M. Hartmann, P. Miethe, M. Singh, and M. Keusgen (2007) Magnetic biosensor for the detection of *Yersinia pestis*. *J. Microbiol. Methods* 68(2):218-224.

23.   Y. R. Chemla, H. L. Grossman, Y. Poon, R. McDermott, R. Stevens, M. D. Alper, and J. Clarke (2000) Ultrasensitive magnetic biosensor for homogeneous immunoassay. *Proc. Natl. Acad. Sci. U. S. A.* 97(26):14268-14272.

24.   A. Quinlan, D. Murat, H. Vali, and A. Komeili (2011) The HtrA/DegP family protease MamE is a bifunctional protein with roles in magnetosome protein localization and magnetite biomineralization. *Mol. Microbiol.* 80(4):1075-1087.

25.   D. Murat, A. Quinlan, H. Vali, and A. Komeili (2010) Comprehensive genetic dissection of the magnetosome gene island reveals the step-wise assembly of a prokaryotic organelle. *Proc. Natl. Acad. Sci. U. S. A.* 107(12):5593-5598.

26.   D. Murat, V. Falahati, L. Bertinetti, R. Csencsits, A. Kornig, K. Downing, D. Faivre, and A. Komeili (2012) The magnetosome membrane protein, MmsF, is a major regulator of magnetite biomineralization in *Magnetospirillum magneticum* AMB-1. *Mol. Microbiol.* 85(4):684-699.

27.   W. A. Kibbe (2007) OligoCalc: an online oligonucleotide properties calculator. *Nucleic Acids Res.* 35(Web Server issue):W43-46.

28.   D. G. Gibson, L. Young, R. Y. Chuang, J. C. Venter, C. A. Hutchison, and H. O. Smith (2009) Enzymatic assembly of DNA molecules up to several hundred kilobases. *Nat. Methods* 6(5):343-345.

29.   M. B. Dickerson, S. E. Jones, Y. Cai, G. Ahmad, R. R. Naik, N. Kroger, and K. H. Sandhage (2006) Identification and design of peptides for the rapid, high-yield formation of nanoparticulate TiO_2 from aqueous solutions at room temperature. *Chem. Mater.* 20(4):1578-1584.

30.   M. Umetsu, M. Mizuta, K. Tsumoto, S. Ohara, S. Takami, H. Watanabe, I. Kumagai, and T. Adschiri (2005) Bioassisted room-temperature immobilization and mineralization of zinc oxide - the structural ordering of ZnO nanoparticles into a flower-type morphology. *Adv. Mater.* 17:2571-2575.

31.   M.-K. Liang, O. Deschaume, S. V. Patwardhan, and C. C. Perry (2011) Direct evidence of ZnO morphology via the selective adsorption of ZnO-binding peptides. *J. Mater. Chem.* 21:80-89.

32.   P. Golec, J. Karczewska-Golec, M. Los, and G. Wegrzyn (2012) Novel ZnO-binding peptides obtained by the screening of a phage display peptide library. *J. Nanopart. Res.* 14(11):1218.

33.   M. M. Tomczak, J. M. Slocik, M. O. Stone, and R. R. Naik (2007) Bio-based approaches to inorganic material synthesis. *Biochem. Soc. Trans.* 35(3):512-515.

34.   J. M. Slocik, M. O. Stone, and R. R. Naik (2005) Synthesis of gold nanoparticles using multifunctional peptides. *Small* 1(11):1048-1052.

35.   L. M. Guzman, D. Belin, M. J. Carson, and J. Beckwith (1995) Tight regulation, modulation, and high-level expression by vectors containing the arabinose PBAD promoter. *J. Bacteriol.* 177(14):4121-4130.

36.   C. M. Zammit, D. Quaranta, S. Gibson, A. J. Zaitouna, C. Ta, J. Brugger, R. Y. Lai, G. Grass, and F. Reith (2013) A whole-cell biosensor for the detection of gold. *PLoS One* 8(8):e69292.

37.   S. K. Checa and F. C. Soncini (2011) Bacterial gold sensing and resistance. *Biometals* 24(3):419-427.

38.   D. Schuler, R. Uhl, and E. Bauerlein (1995) A simple light scattering method to assay magnetism in *Magnetospirillum gryphiswaldense*. *FEMS Microbiol. Lett.* 132:139-145.

39.   Z. J. Zhang, Z. L. Wang, B. C. Chakoumakos, and J. S. Yin (1998) Temperature dependence of cation distribution and oxidation state in magnetic Mn-Fe ferrite nanocrystals. *J. Am. Chem. Soc.* 128(8):1800-1804.

40.   J. Z. Bloh, R. Dillert, and D. W. Bahnemann (2012) Transition metal-modified zinc oxides for UV and visible light photocatalysis. *Environ. Sci. Pollut. Res. Int.* 19(9):3688-3695.

41.   C. J. Fennie, andD. G. Schlom (2010) Transition-metal oxides: Resistance is not futile. *Nat. Mater.* 9(10):787-788.

42.   X. Chen and S. S. Mao (2007) Titanium dioxide nanomaterials: synthesis, properties, modifications, and applications. *Chem. Rev.* 107(7):2891-2959.

43.   M. B. Dickerson, K. H. Sandhage, and R. R. Naik (2008) Protein- and peptide-directed syntheses of inorganic materials. *Chem. Rev.* 108(11):4935-4978.

44.   H. Chen, X. Su, K.-G. Neoh, and W.-S. Choe (2008) Probing the interaction between peptides and metal oxides using point mutants of a TiO_2-binding peptide. *Langmuir* 24(13):6852-6857.

45.   X. Dang, H. Yi, M.-H. Ham, J. Qi, D. S. Yun, R. Ladewski, M. S. Strano, P. T. Hammond, and A. M. Belcher (2011) Virus-templated self-assembled single-walled carbon nanotubes for highly efficient electron collection in photovoltaic device. *Nat. Nanotechnol.* 6:377-384.

46.   G. Gertler, G. Fleminger, and H. Rapaport (2010) Characterizing the adsorption of peptides to TiO_2 in aqueous solutions by liquid chromatography. *Langmuir* 26(9):6457-6463.

47.   T. M. Gronewold, A. Baumgartner, A. Weckmann, J. Knekties, and C. Egler (2009) Selection process generating peptide aptamers and analysis of their binding to the TiO_2 surface of a surface acoustic wave sensor. *Acta Biomater.* 5(2):794-800.

48.   H. Chen, X. Su, K.-G. Neoh, and W.-S. Choe (2006) QCM-D analysis of binding mechanism of phage particles displaying a constrained heptapeptide with specific affinity to SiO_2 and TiO_2. *Anal. Chem.* 78(14):4872-4879.

49. D. Yan, G. Yin, Z. Huang, M. Yang, X. Liao, Y. Kang, Y. Yao, B. Hao, and D. Han (2009) Characterization and bacterial response of zinc oxide particles prepared by a biomineralization process. *J. Phys. Chem. B* 113(17):6047-6053.

50. A. Stankovic, S. Dimitrijevic, and D. Uskokovic (2013) Influence of size scale and morphology on antibacterial properties of ZnO powders hydrothemally synthesized using different surface stabilizing agents. *Coll. Surf. B Biointerfaces* 102:21-28.

51. M. Raula, M. H. Rashid, T. K. Paira, E. Dinda, and T. K. Mandal (2010) Ascorbate-assisted growth of hierarchical ZnO nanostructures: sphere, spindle, and flower and their catalytic properties. *Langmuir* 26(11):8769-8782.

52. Y. C. Yeh, B. Creran, and V. M. Rotello (2012) Gold nanoparticles: preparation, properties, and applications in bionanotechnology. *Nanoscale* 4(6):1871-1880.

53. A. Arakaki, J. Webb, and T. Matsunaga (2003) A novel protein tightly bound to bacterial magnetic particles in *Magnetospirillum magneticum* strain AMB-1. *J. Biol. Chem.* 278(10):8745-8750.

54. C. N. Keim, U. Lins, and M. Farina (2009) Manganese in biogenic magnetite crystals from magnetotactic bacteria. *FEMS Microbiol. Lett.* 292(2):250-253.

55. H. K. Liu, G. X. Wang, Z. Guo, J. Wang, and K. Konstantinov (2006) Nanomaterials for lithium-ion rechargeable batteries. *J. Nanosci. Nanotechnol.* 6(1):1-15.

56. V. G. Kumar, J. S. Gnanaraj, S. Ben-David, D. M. Pickup, E. R. H. van Eck, A. Gedanken, and D. Aurbach (2003) An aqueous reduction method to synthesize spinel $LiMn_2O_4$ nanoparticles as a cathode material for rechargeable lithium-ion batteries. *Chem. Mater.* 15(22):4211-4216.

57. J. S. Evans, R. Samudrala, T. R. Walsh, E. E. Oren, and C. Tamerler (2008) Molecular design of inorganic-binding polypeptides. *MRS Bulletin* 33:514-518.

58. B. H. Lower, R. D. Lins, Z. Oestreicher, T. P. Straatsma, M. F. Hochella, L. Shi, and S. K. Lower (2008) *In vitro* evolution of a peptide with a hematite binding motif that may constitute a natural metal-oxide binding archetype. *Environ. Sci. Technol.* 42(10):3821-3827.

59. R. Derda, S. K. Tang, S. C. Li, S. Ng, W. Matochko, and M. R. Jafari (2011) Diversity of phage-displayed libraries of peptides during panning and amplification. *Molecules* 16(2):1776-1803.

60. U. O. Seker and H. V. Demir (2011) Material binding peptides for nanotechnology. *Molecules* 16(2):1426-1451.

61. R. R. Naik, S. E. Jones, C. J. Murray, J. C. McAuliffe, R. A. Vaia, and M. O. Stone (2003) Peptide templates for nanoparticle synthesis derived from polymerase chain reaction-driven phage display. *Adv. Funct. Mater.* 14(1):25-30.

62. M. S. Kang, E. K. Choi, D. H. Choi, S. Y. Ryu, H. H. Lee, H. C. Kang, J. T. Koh, K. O. S., Y. C. Hwang, S. J. Yoon, S. M. Kim, K. H. Yang, and I. C. Kang (2008) Antibacterial activity of pyrrolidine dithiocarbamate. *FEMS. Microbiol. Lett.* 280(2):250-254.

63. E. K. Choi, H. H. Lee, M. S. Kang, B. G. Kim, H. S. Lim, S. M. Kim, and I. C. Kang (2010) Potentiation of bacterial killing activity of zinc chloride by pyrrolidine dithiocarbamate. *J. Microbiol.* 48(1):40-43.

64. D. H. Nies (2003) Efflux-mediated heavy metal resistance in prokaryotes. *FEMS Microbiol. Rev.* 27(2-3):313-339.

65. D. Faivre and D. Schuler (2008) Magnetotactic bacteria and magnetosomes. *Chem. Rev.* 108(11):4875-4898.

66. T. Brautaset, R. Lale, and S. Valla (2009) Positively regulated bacterial expression systems. *Microb. Biotechnol.* 2(1):15-30.

Appendix 1: *Plasmids and oligonucleotides*

.

Table A1.1. Plasmid constructs.

Plasmid	Description	Source
pAK344	mamT disruption plasmid	ref. *1*
pAK262	*mamP* (tac), *mob*⁺, Km^R, pBBR1 replicon	ref. *1*
pAK262Amp-MamP	*mamP* (tac), *mob*⁺, Amp^R, pBBR1 replicon	Ch. 2
pAK262Amp-MamP$_{\Delta heme1}$	*mamP$_{\Delta heme1}$* (tac), *mob*⁺, Amp^R, pBBR1 replicon	Ch. 2
pAK262Amp-MamP$_{\Delta heme2}$	*mamP$_{\Delta heme2}$* (tac), *mob*⁺, Amp^R, pBBR1 replicon	Ch. 2
pAK262Amp-MamP$_{\Delta heme}$	*mamP$_{\Delta heme}$* (tac), *mob*⁺, Amp^R, pBBR1 replicon	Ch. 2
pAK262Amp-MamT	*mamT* (tac), *mob*+, Amp^R, pBBR1 replicon	Ch. 2
pAK262Amp-MamT$_{\Delta heme1}$	*mamT$_{\Delta heme1}$* (tac), *mob*⁺, Amp^R, pBBR1 replicon	Ch. 2
pAK262Amp-MamT$_{\Delta heme2}$	*mamT$_{\Delta heme2}$* (tac), *mob*⁺, Amp^R, pBBR1 replicon	Ch. 2
pAK262Amp-MamT$_{\Delta heme}$	*mamT$_{\Delta heme}$* (tac), *mob*⁺, Amp^R, pBBR1 replicon	Ch. 2
pAK262Amp-MamP.FLAG	*mamP.FLAG* (tac), *mob*⁺, Amp^R, pBBR1 replicon	Ch. 2
pAK262Amp-FLAG.MamP	*FLAG.mamP* (tac), *mob*⁺, Amp^R, pBBR1 replicon	Ch. 2
pAK262-MamP.GFP$_{sf}$	*mamP.GFP$_{sf}$* (tac), *mob*⁺, Km^R, pBBR1 replicon	Ch. 2
pAK262-GFP$_{sf}$.MamP	*GFP$_{sf}$.mamP* (tac), *mob*⁺, Km^R, pBBR1 replicon	Ch. 2
pCWOri-OmpA.MamP	*ompA.mamP* (double tac), Amp^R, ColE1 replicon	Ch. 2
pCWOri-OmpA.His$_6$.SUMOtev.MamP	*ompA.His$_6$.SumoTev.mamP* (double tac), Amp^R, ColE1 replicon	Ch. 2
pCWOri-OmpA.His$_6$.NusAtev.MamP	*ompA.His$_6$.NusATev.mamP* (double tac), Amp^R, ColE1 replicon	Ch. 2
pCWOri-OmpA.His$_6$.MOCRtev.MamP	*ompA.His$_6$.MocrTev.mamP* (double tac), Amp^R, ColE1 replicon	Ch. 2
pCWOri-OmpA.His$_6$.TRXtev.MamP	*ompA.His$_6$.TrxTev.mamP* (double tac), Amp^R, ColE1 replicon	Ch. 2
pCWOri-OmpA.His$_6$.MBPtev.MamP	*ompA.His$_6$.MBPTev.mamP* (double tac), Amp^R, ColE1 replicon	Ch. 2
pET29a-OmpA.His$_6$.MOCRtev.MamP	*ompA.His$_6$.MOCRtev.mamP* (T7), Km^R, ColE1 replicon	Ch. 2
pET29a-OmpA.His$_6$.MBPtev.MamP	*ompA.His$_6$.MBPtev.mamP* (T7), Km^R, ColE1 replicon	Ch. 2
pCR2.1-MBPtev.sMms7mat	*MBPtev.mms7mat*, Amp^R, ColE1 replicon	Ch. 3

pET16sx-Strep.MBPtev.sMms7mat	*strepII.MBPtev.mms7mat* (T7), Amp^R, ColE1 replicon	Ch. 3
pET16sx-Strep.MBPtev.Mms7ct	*strepII.MBPtev.mms7ct* (T7), Amp^R, ColE1 replicon	Ch. 3
pSV272.1-His$_6$.MBPtev.Mms6mat	*his$_6$.MBPtev.mms6mat* (T7), Km^R, f1 replicon	Ch. 3
pSV272.1-His$_6$.MBPtev.Mms6ct	*his$_6$.MBPtev.mms6ct* (T7), Km^R, f1 replicon	Ch. 3
pSV272.1-His$_6$.MBPtev.Mms6ct.MSR-1	*his$_6$.MBPtev.mms6ct.MSR-1* (T7), Km^R, f1 replicon	Ch. 3
pSV272.1-His$_6$.MBPtev.Mms7ct.MSR-1	*his$_6$.MBPtev.mms7ct.MSR-1* (T7), Km^R, f1 replicon	Ch. 3
pSV272.1-His$_6$.MBPtev.Mms6ct.MV-1	*his$_6$.MBPtev.mms6ct.MV-1* (T7), Km^R, f1 replicon	Ch. 3
pSV272.1-His$_6$.MBPtev.Mms7ct.MV-1	*his$_6$.MBPtev.mms7ct.MV-1* (T7), Km^R, f1 replicon	Ch. 3
pSV272.1-His$_6$.MBPtev.Mms6ct.MC-1	*his$_6$.MBPtev.mms6ct.MC-1* (T7), Km^R, f1 replicon	Ch. 3
pSV272.1-His$_6$.MBPtev.Mms7ct.Fos001	*his$_6$.MBPtev.mms7ct.Fos001* (T7), Km^R, f1 replicon	Ch. 3
pSV272.1-His$_6$.MBPtev.Mms6ct.ΔE	*his$_6$.MBPtev.mms6ct.ΔE* (T7), Km^R, f1 replicon	Ch. 3
pSV272.1-His$_6$.MBPtev.Mms7ct.ΔE	*his$_6$.MBPtev.mms6ct.ΔE* (T7), Km^R, f1 replicon	Ch. 3
pSV272.1-His$_6$.MBPtev.FF1.Mms6ct	*his$_6$.MBPtev.FF1.mms6ct* (T7), Km^R, f1 replicon	Ch. 3
pSV272.1-His$_6$.MBPtev.FF2.Mms6ct	*his$_6$.MBPtev.FF2.mms6ct* (T7), Km^R, f1 replicon	Ch. 3
pSV272.1-His$_6$.MBPtev.Melittin.Mms6ct	*his$_6$.MBPtev.melittin.mms6ct* (T7), Km^R, f1 replicon	Ch. 3
pAK262Amp-MmsF.Mms6	*mmsF.mms6* (tac), *mob$^+$*, Amp^R, pBBR1 replicon	Ch. 3
pAK262Amp-MmsF	*mmsF* (tac), *mob$^+$*, Amp^R, pBBR1 replicon	Ch. 3
pAK262Amp-Mms6	*mms6* (tac), *mob$^+$*, Amp^R, pBBR1 replicon	Ch. 3
pAK262Amp-MmsF.MmsTiO$_2$	*mmsF.mmsTiO$_2$* (tac), *mob$^+$*, Amp^R, pBBR1 replicon	Ch. 4
pAK262Amp-MmsTiO$_2$	*mmsTiO$_2$* (tac), *mob$^+$*, Amp^R, pBBR1 replicon	Ch. 4
pAK262Amp-MmsF.MmsZnO	*mmsF.mmsZnO* (tac), *mob$^+$*, Amp^R, pBBR1 replicon	Ch. 4
pAK262Amp-MmsF.MmsAu	*mmsF.mmsAu* (tac), *mob$^+$*, Amp^R, pBBR1 replicon	Ch. 4
pAK262Amp-LacIq.(T5)MamP.	*mamP* (T5), *lacIq, mob$^+$*, Amp^R, pBBR1 replicon	Ch. 4
pAK262Amp-AraC.(ara)MamP	*mamP* (ara), *araC, mob$^+$*, Amp^R, pBBR1 replicon	Ch. 4
pAK262Amp-(ara)MamP	*mamP* (ara), *mob$^+$*, Amp^R, pBBR1 replicon	Ch. 4

pAK262Amp-golTSB.MamP	*mamP* (gol), *golTSB, mob*$^+$, Amp^R, pBBR1 replicon	Ch. 4
pAK262Amp-(gol)MamP	*mamP* (gol), *mob*$^+$, Amp^R, pBBR1 replicon	Ch. 4
pAK262Amp-LacIq.(T5)MamP.GFP$_{sf}$	*MamP.GFP$_{sf}$* (T5), *lacIq, mob*$^+$, Amp^R, pBBR1 replicon	Ch. 4
pAK262Amp-AraC.(ara)MamP.GFP$_{sf}$	*MamP.GFP$_{sf}$* (ara), *araC, mob*$^+$, Amp^R, pBBR1 replicon	Ch. 4
pAK262Amp-LacIq.(T5)GFP$_{sf}$	*GFP$_{sf}$* (T5), *lacIq, mob*$^+$, Amp^R, pBBR1 replicon	Ch. 4
pAK262Amp-AraC.(ara)GFP$_{sf}$.	*GFP$_{sf}$* (ara), *araC, mob*$^+$, Amp^R, pBBR1 replicon	Ch. 4
pET29a-OmpA.MamT.strepII	*ompA.mamT.strepII* (T7), Km^R, ColE1 replicon	App. 2
pET29a-OmpA.His$_6$.MBPtev.MamT	*ompA.His$_6$.MBPtev.mamT* (T7), Km^R, ColE1 replicon	App. 2

Table A1.2. Primers used in the construction of plasmids in Table A1.1.

Name	Sequence
pAK MamP F1	gattaagcattggtaactgtcagcgggactctggggttcgaaatgaccgaccaagcg
pAK MamP R1	caggaaggcaaaatgccgcaaaaaagggaataagggcgacacggaaatgttgaatactcatgcgaaacgatcctcatcctg
pAK MamP F2	gaggatcgtttcgcatgagtattcaacatttccgtgtcgcccttattcccttttttgcggcattttgccttcctg
pAK MamP R2	ccccagagtcccgctgacagttaccaatgcttaatcagtgaggcacctatctcagcgatctgtctatttcgttcatccatagttgcc
MamP QC F1	cgtcaatcctcacgaagtgcgcgggccggcggaagccgcggcggtcataaagtgaactagttctagagcggccgccaccgcgg
MamP QC R1	ccgcggtggcggccgctctagaactagttcactttatgaccgccgcggcttccgccggcccgcgcacttcgtgaggattgacg
MamP QC F2	ccccacggctatcgcggcgccgcaaccgatgcggcgcccatcggccaggggttcgagttgacccc
MamP QC R2	ggggtcaactcgaacccctggccgatgggcgccgcatcggttgcggcgccgcgatagccgtgggg
MamP Ex F1	gtagcgcaggccatggcacaggccacgaatacgcag
MamP Ex R1	acagcttatcatcgataagctttcactttatgacgtggcaggc
MamP Ex F2	gagaccatgggtcatcatcatcatcatcacgagctctcttctatggctagcatgtcggactcagaag
MamP Ex R2	gagaaagctttcactttatgacgtggcaggcttcgcacggccc
MamP Ex F3	gagaccatgggtcatcatcatcatcatcacgagctctcttctatgaaatcttctcaccatcaccatc
MamP Ex F4	gagaccatgggtcatcatcatcatcatcacgagctctcttctatgagcaacatgacatacaataatgttttcgac
MamP Ex F5	gagaccatgggtcatcatcatcatcatcacgagctctcttctatgagcgataaaattattcacctgac
MamP Ex R5	gagactcgagtcactttatgacgtggcaggcttcgcacggccc
MamP Ex F6	gagaccatgggccatcatcatcatcatcatcatcatcacggtgcatccggcgg
MamP Ex R3	caccgcctgggactgcgtattcgtggcctgggcgccctgaaaatacaggttttcctcgatcccgaggttgttg
MamP Ex F7	caggccacgaatacgcagtcccaggcggtg
MamP Ex F8	gagatctagaaataattttgtttaactttaagaaggagatatacatatgaaaaagacagctatcgcgattgcagtggcactggctggtttcgc
MamP Ex R4	gagactcgagtcactttatgacgtggcaggcttcgcacggccc
MamP LIC F1	tacttccaatccaatgcacaggccacgaatacgcag
MamP LIC R1	ttatccacttccaatgttattatcactttatgacgtggcag
pAK MamT F1	gacaagaaaggcggcatgagatggcaattatgaactagttctagagcggccgccaccgcg
pAK MamT R1	cgcggtggcggccgctctagaactagttcataattgccatctcatgccgcctttcttgtc
MamT SF1	atgagcatggaggcgccgcg

116

MamT SR1	gacatcgtggtcaaggtgccgg
MamT QC F1	gaagccaggaaccggaatgccgcatccctatgtaggcgatgcaatccaggcagcactgatggtgggcggcccggc
MamT QC R1	gccgggccgcccaccatcagtgctgcctggattgcatcgcctacatagggatgcggcattccggttcctggcttc
MamT QC F2	cgcatccgccggccggacgagcaatcaaagcagcagacatcgtggtcaaggtgccggtggacaagaaaggcg
MamT QC R2	cgcctttcttgtccaccggcaccttgaccacgatgtctgctgctttgattgctcgtccggccggcggatgcg
MamP Flag F1	caatttcacacaggaaacagaattcatgaatagcaaggtggcgcttctggtcgtgggactggc
MamP.Flag R1	tcacttgtcatcgtcatccttgtagtcgatgtcatgatctttataatgaccgtcatggtctttgtagtcctttatgacgtggcaggcttcgcacggccc
MamP Flag F2	gatcatgacatcgactacaaggatgacgatgacaagtgaactagttctagagcggccgccaccgcggtg
MamP Flag R2	catgaattctgtttcctgtgtgaaattgttatccgctc
Flag MamP F1	cgactacaaggatgacgatgacaagatgaatagcaaggtggcgcttctggtc
Flag MamP R1	caccgcggtggcggccgctctagaactagttcactttatgacgtggcaggcttcgcacggccc
Flag MamP F1	tgaactagttctagagcggccgccaccgcggtg
Flag MamP R2	catcttgtcatcgtcatccttgtagtcgatgtcatgatctttataatgaccgtcatggtctttgtagtccatgaattctgtttcctgtgtg
P GFPsf F1	caatttcacacaggaaacagaattcatgaatagcaaggtggcgcttctggtcgtgggactggc
P GFPsf R1	gttcttcacctttagacatggatccctttatgacgtggcaggcttcgcacggccc
P GFPsf F2	cgtgcgaagcctgccacgtcataaagggatccatgtctaaaggtgaagaactgttcaccggtgttgttccgatcctggttgaactggatggtg
P GFPsf R2	caccgcggtggcggccgctctagaactagttcatttgtagagctcatccatgccgtgcgtgatacctgctgcagtaacgaactc
GFPsf P F1	caatttcacacaggaaacagaattcatgtctaaaggtgaagaactgttcaccggtgttgttccgatcctggttgaactggatggtg
GFPsf P R1	gccaccttgctattcatggatcctttgtagagctcatccatgccgtgcgtgatacctgctgcagtaacgaactc
GFPsf P F2	gagctctacaaaggatccatgaatagcaaggtggcgcttctggtcgtgggactggc
GFPsf P R2	caccgcggtggcggccgctctagaactagtcactttatgacgtggcaggcttcgcacggccc
MamT Ex F1	tatacatatgaaaaagacagctatcgcgattgcagtggcactggctggtttcgctaccgtagcgcaggccatggcgatcgggctgggactctattgggaccagctgtcc
MamT Ex R1	gagaggatcctcacttttcgaactgcgggtggctccatgcgctgccacctaattgccatctcatgccgcctttcttgtccac
MamT Ex F2	tttgtttaactttaagaaggagatatacatatgaaaaagacagctatcgcgattgcagtggcactggc
MamT Ex R2	tggtttcgctaccgtagcgcaggccatggcgatcgggctgggactctattgggaccagc
MamT Ex F3	tgggaccagctgtccacg
MamT Ex R3	cataattgccatctcatgccg
MamT Ex F4	cggtggacaagaaaggcggcatgagatggcaattatgaggatccgaattcgagctccg

MamT Ex R4	ggcgttatgccggacggcgtggacagctggtcccaggcgccctgaaaatacaggtttt
MBP F1	gagatatacatatgggttcttctatgaaaatcgaagaaggtaaactggtaatctggattaacggcgataaaggctataac ggtctcgctg
sMms7.Nt F1	gagatatacatatggctaaaggtctgggtctgggtctgggtctgggtgcttggggcccttttcctgctgggtgca gctggcctggcaggtgcgg
sMms7.Ct R1	tatggatccttattcctcacccgccgcagccagcagtgcatcgtcgctcagatcaggggtgccgtgacgacgacgagccc aaacgtacagagccgccgcacctgccaggccagctgc
sMms7 SOE F1	acctgtttcagggcgccgaaaaacctgtattttcagggcgctaaaggtctgggtctgggtctgggtctgggtc
sMms7.SOE R1	gacccagacccagacccagacctttagcgccctgaaaatacaggttttcggcgccctgaaacagg
sMms7 R1	aatactagtatgcatttattcctcacccgccgcagccagcagtgcatcg
Mms7ct F1	ctctgagctcgaacaacaacaacaataacaataacaacaacctcgggatcgaggaaaaacctgtttcagggcgccgaaaac ctgtattttcagggc
Mms7ct R1	attactagtatgcatttattcctcacccgccgcagccagcag
Mms7ct linker	gaggaaaaacctgtttcagggcgccgaaaaacctgtattttcagggctacgtttgggctcgtcgtcgtcacggcacc
6mat.AMB1 F1	attggcgccgaaaaacctgtattttcagggcggtacgatctggacgggcaaaggtctgggtctgggtctg
6mat.AMB1 R1	acaacgcccaggataatcgggccccaggcaccgagacccaggcccagacccagacccagacctttgc
6mat.AMB1 F2	atcctgggcgttgtgggtgccggtgcggtgtacgcttacatgaaaagccgtgatattgaaagcgcaca
6mat.AMB1 R2	attggatcctcacgccagggcgtcgcgcagctcaacttcctcgtcgctctgtgcgctttcaatatcacggc
6mat rescue F1	attggcgccgaaaaacctgtattttca
6mat rescue R1	attggatcctcacgccagggc
6ct.AMB1 F1	gagatataggcgccgaaaaacctgtattttcagggtgccggtgcggtgtacgcttacatgaaaagccgtgatattgaaagc gcacagagcgacgagg
6ct.AMB1 R1	attggatcctcacgccagggcgtcgcgcagctcaacttcctcgtcgctctgtgcgctttcaatatcacggc
6ct.MSR1 F1	gggatcgaggaaaaacctgtattttcagggcgccggtgcggtgtacgcttatatgaaaagccgtgatattgaggcggccca atctgatgaagaggtcgag
6ct.MSR1 R1	gcgcggggagaggcggtttgcgtattgggcgccttagctcagcgcatcacgcagctcgacctcttcatcagattgggccg cctcaatatcacggcttttt
7ct.MSR1 F1	gggatcgaggaaaaacctgtattttcagggcgcctacacgtgggcgcgtcgtcgtcatggtgcaccggacgtgagcgatga cgcg
7ct.MSR1 R1	gcgcggggagaggcggtttgcgtattgggcgccttattcctcaccaaccgccgccagcagcgcgtcatcgctcacgtccg gtgc
6ct.MV1 F1	gggatcgaggaaaaacctgtattttcagggcgccgtgtatggttatgtccgtagccgtaaggcggaacagagccagaccga ggaggagctgg
6ct.MV1 R1	gcgcggggagaggcggtttgcgtattgggcgccttatgcacctgcgatcaccgcagccagttccagctcctcctcggtct ggctctgttccgcctta
7ct.MV1 F1	gggatcgaggaaaaacctgtattttcagggctattacctgtacaatcgtagcaaaaattccgccacgacggatgaggacct gcaa
7ct.MV1 R1	gcgcggggagaggcggtttgcgtattgggcgccttacgccagcgcaccggccagttcattttgcaggtcctcatccgtcg tggc
6ct.MC1 F1	gggatcgaggaaaaacctgtattttcagggcgccgttggctacggtatctatgcgtatatgaagaatcgtggtgagcaggc agatgag
6ct.MC1 R1	gcgcggggagaggcggtttgcgtattgggcgccttagctaatggcctcctccaactcatctgcctgctcaccacgattct tcat

7ct.Fos001 F1	gggatcgaggaaaacctgtattttcagggcgcctatggttatatgcgtcgccgtaaagccgcaggcggtgaatatgacca cagcgaaaccgac
7ct.Fos001 R1	gcgcggggagaggcggtttgcgtattgggcgccttagctcagtgcctcctggatggcgatgtcggtttcgctgtggtcat attcaccgcct
6ct.ΔE F1	gggatcgaggaaaacctgtattttcagggcgccggtgcaggcgcggtttatgcctatatgaaaagccgtgcgattgcgag cgcacaaag
6ct.ΔE R1	gcgcggggagaggcggtttgcgtattgggcgccttacgccagtgctgcacgcagcgccactgccgccgcgctttgtgcgc tcgcaatcgcacggctt
7ct.ΔE F1	gggatcgaggaaaacctgtattttcagggctatgtttgggcgcgtcgtcgtcatggcaccccggcgttgtctgcggcggc cctg
7ct.ΔE R1	gcgcggggagaggcggtttgcgtattgggcgccttaggccgcacccgccgcggccagcagggccgccgcagacaacgccg ggg
FF1 F1	ccaacagcggcgcgatcaccattggcggtgcggtgtacgcttacatgaaaagc
FF1 R2	gccaatggtgatcgcgccgctgttggcgccctgaaaatacaggttttcc
FF2 F1	caacgctttcagtggcagttccaacagcagggtgcggtgtacgcttacatgaaaag
FF2 R1	ctgctgttggaactgccactgaaagcgttgctgggcgccctgaaaatacaggttttc
Mel F1	ctgacgacgggtctgccggcactgatttcttggatcggtgcggtgtacgcttacatgaaaag
Mel R1	tcagtgccggcagacccgtcgtcagcactttcagcaccgcaccgataccggcgccctgaaaatacaggttttcc
MmsF6 F1	attgtgagcggataacaatttcacacaggaaacagaattcatgactgaagctatccttcgcagcacgctcggtg
MmsF6 R1	actccgttggcgatctgagctggcatggatcctgtttccttcagatccggtgggcgacccagctgatcag
MmsF6 F2	tcagctgggtcgcccaccggatctgaaggaaacaggatccatgccagctcagatcgccaacggag
MmsF6 R2	tggagctccaccgcggtggcggccgctctagaactagttcatcaggccagcgcgtcgcgcagttcgacttc
MmsF F1	atgactgaagctatccttcgcagca
MmsF R1	tcagatccggtgggcgac
MmsF F2	ctgcccctgatcagctgggtcgcccaccggatctgaactagttctagagcggccgcca
MmsF R2	cgcaccgagcgtgctgcgaaggatagcttcagtcatgaattctgtttcctgtgtgaaattgttatcc
Mms6 F1	agcggataacaatttcacacaggaaacagaattcatgccagctcagatcgccaa
Mms6 R1	tggagctccaccgcggtggcggccgctctagaactagttcatcaggccagcgcgtcgcgcagttcgacttc
Mms6 F2	tgaactagttctagagcggccgc
Mms6 R2	gaattctgtttcctgtgtgaaattgttatcc
MmsTi F1	attgtgagcggataacaatttcacacaggaaacagaattcatgccagctcagatcgccaacggagttatttgcccc
MmsTi R1	agagcttgtgggtggggttcttcgtgcgcttcttccgctgcgccgattcgatatcacggctcttcatatacgcg
MmsTi F2	cacgaagaacccacccacaagctctgatgaactagttctagagcggccgccaccgcg
MmsTi R2	gaattctgtttcctgtgtgaaattgttatccgctcacaattccacacattatacgagc

119

MmsFTi F1	cacgaagaaccccacccacaagctctgatgaactagttctagagcggccgccaccgcg
MmsFTi R1	agagcttgtgggtggggttcttcgtgcgcttcttccgctgcgccgattcgatatcacggctcttcatatacgcg
MmsFZn F1	attgtgagcggataacaatttcacacaggaaacagaattcatgactgaagctatccttcgcagcacgctcggtg
MmsFZn R1	cctccgggacgcggagccactttgtgcatcacgtgggcctcatcacggctcttcatatacgcgtaaaccgcccc
MmsFZn F1	aggcccacgtgatgcacaaagtggctccgcgtcccggaggtggctcctgctgatgaactagttctagagcggccgccaccgcg
MmsFZn R2	gaattctgtttcctgtgtgaaattgttatccgctcacaattccacacattatacgagc
MmsFAu F1	attgtgagcggataacaatttcacacaggaaacagaattcatgactgaagctatccttcgcagcacgctcggtg
MmsFAu R1	agggggcataggggagcaccgctggagtaagcctgcgccgattcgatatcacggctcttcatatacgc
MmsFAu F2	atcggcgcaggcttactccagcggtgctcccctatgcccctttctgatgaactagttctagagcggccgccaccgcg
MmsFAu R2	gaattctgtttcctgtgtgaaattgttatccgctcacaattccacacattatacgagc
lacR(lac)P F1	aatgcttaatgaattacaacagtttttatgcatgcagataaaatatttgctcatgagcccgaagt
lacR(lac)P R1	cccacgaccagaagcgccaccttgctattcatcatatgtatatctccttcttgagctctgtgtgaa
araR(ara)P F1	aatgcttaatgaattacaacagtttttatgcatgccgccagcaaccgcacctgtggc
araR(ara)P R1	gtcccacgaccagaagcgccaccttgctattcatattagttgatttttcgaactggtg
araP F1	aatgcttaatgaattacaacagtttttatgcatgccagacattgccgtcactgcgtc
golMamP F1	gtcgccttgcgtataatatttgccgctctagaaattttgaatgttctac
golMamP R1	catgctggagttcttcgcccaccccgaggatccctgcatagtgaactcc
golMamP F2	cttaatgaattacaacagtttttatgcatgcctagtctagatatccagaacatgc
golMamP R2	cagaagcgccaccttgctattcatgaattcgaggatccctgcatagtgaactcc
P GFPsf F3	gggccgtgcgaagcctgccacgtcataaagggatccatgagtaaaggagaagaacttttcact
P GFPsf R3	gagctccaccgcggtggcggccgctctagaactagtctatttgtatagttcatccatgccatgtgtaatcc
lacGFP F1	atttcacacagagctcaagaaggagatataggatccatgagtaaaggagaagaacttttcact
araGFP F1	ttttgggctagcgaattcgagctcggtaccgttttagccaccagttcgaaaaaatcaactaatatgagtaaaggagaagaacttttcactggagtt

Table A1.3. Strains used in this work.

Name	Genotype	Source
Escherichia coli		
DH10B	F– *mcr*A Δ(*mrr-hsd*RMS-*mcr*BC) Φ80*lacZ*ΔM15 Δ*lac*X74 *rec*A1 *end*A1 *ara*D139 Δ(*ara leu*) 7697 *gal*U *gal*K *rps*L *nup*G λ– *ton*A	Invitrogen
WM3064	*thrB*1004 *pro thi rpsL hsdS lacZ*Δ*M15* RP4-1360 Δ(*araBAD)567* Δ*dapA*1341::[*erm pir*]	W. Metcalf, UIUC
C43(DE3)	F – *ompT hsdSB (rB- mB-) gal dcm* (DE3)	ref. *2*
BL21(DE3)	*fhuA2 [lon] ompT gal (λ DE3) [dcm]* Δ*hsdS*	Novagen
M. magneticum AMB-1		
Wild type	AK30	ref. *1*
Δ*mamP*	AK69	ref. *1*
ΔR9	AK57	ref. *1*
Δ*mamT*ΔR9	AK155	Ch. 2
ΔR3	AK36	ref. *1*
Δ*mms6*$_{cl}$	AK124	ref. *3*
Δ*mms6*	AK103	ref. *3*

References

1. D. Murat, A. Quinlan, H. Vali, and A. Komeili (2010) Comprehensive genetic dissection of the magnetosome gene island reveals the step-wise assembly of a prokaryotic organelle. *Proc. Natl. Acad. Sci. U. S. A.* 107(12):5593-5598.
2. S. Wagner, M. M. Klepsch, S. Schlegel, A. Appel, R. Draheim, M. Tarry, M. Hogbom, K. J. van Wijk, D. J. Slotboom, J. O. Persson, and J. W. de Gier (2008) Tuning *Escherichia coli* for membrane protein overexpression. *Proc. Natl. Acad. Sci. U. S. A.* 105(38):14371-14376.
3. D. Murat, V. Falahati, L. Bertinetti, R. Csencsits, A. Kornig, K. Downing, D. Faivre, and A. Komeili (2012) The magnetosome membrane protein, MmsF, is a major regulator of magnetite biomineralization in *Magnetospirillum magneticum* AMB-1. *Mol. Microbiol.* 85(4):684-699.

Appendix 2: *Supplementary materials for Chapter 2*

Table of Contents

Supplementary methods

Plasmid construction. Standard molecular biology techniques were used to carry out plasmid construction. All PCR amplifications were carried out with Phusion DNA polymerase. For amplification of GC-rich sequences from *M. magneticum* AMB-1 (AMB-1), PCR reactions were supplemented with DMSO (5%) with primer annealing temperatures 8-10°C below the melting temperature (T_m) calculated using OligoCalc [1]. Plasmids were assembled either using the Gibson method [2] or restriction digest and ligation. All constructs were verified by sequencing (Quintara Biosciences; Berkeley, CA).

Plasmids for heterologous expression of MamT in *E. coli*. The initial plasmid for the heterologous expression of MamT in *E. coli* was constructed in a series of steps designed to make intermediates for testing MamT expression.

pET29a-OmpA.MamT.strepII. The sequence encoding the soluble MamT sequence (residues 21 - 176) predicted by TMHMM program [3] was amplified from the AMB-1 genome with MamT Ex F1/R1. The Gibson overlaps were added with nested PCR by amplifying the isolated mamT gene with the MamT Ex F2/R2 primers. The OmpA.MamT.strepII cassette was then inserted into the NdeI-BamHI site of pET29a.

pET29a-OmpA.His$_6$.MBPtev.MamTt. The sequence encoding a further-truncated soluble MamT (residues 29 - 176) was amplified from pAK262Ap-MamT with MamT Ex F3/R3 primers. The pET29a-OmpA.His$_6$.MBPtev.MamT vector was constructed by amplifying the pET29a-OmpA.His$_6$.MBPtev cassette from pET29a-OmpA.His$_6$.MBPtev.MamP with MamT Ex F4/R4 primers, and using Gibson assembly [2] to insert the *mamT* gene into the vector backbone.

Immunostaining for MamT. Antibodies to MamT were raised by ProSci, Inc. (Poway, CA) in rabbits using a synthetic peptide from MamT (CHDIVVKVPVDKKGGMRWQL) conjugated to a carrier protein. Testing of these antibodies indicated that MamT could be detected to < 20 ng/lane using a 1:1000 dilution. AMB-1 cultures were grown without agitation in MG (10 mL) containing 20 mM HEPES pH 7.2 at 30°C in seal-capped anaerobic culture tubes (20 mL) evacuated with Ar to $OD_{400\ nm} = 0.2$ (~ 2d). Cells were pelleted by centrifugation ($9,800 \times g$) for 15 min and resuspended in 2× Laemmli buffer containing BME (5% v/v) (125 μL for 10 mL of culture at $OD_{400\ nm} = 0.2$). The cell suspension was heated at 70ºC for 15 min and centrifuged ($14,000 \times g$) for 10 min at room temperature to remove particulate matter. Samples (15 uL) were run on a 12% Bis-Tris SDS-PAGE gel at 150 V at 4°C for 45-80 min. The gel was equilibrated in transfer buffer (50 mM Tris, 192 mM glycine, 20% v/v methanol, 0.05% w/v SDS) for 25 min before transferring at 50 V for 2 h to a pre-wetted PVDF membrane (Bio-Rad) using a BioRad Trans-Blot. All subsequent steps utilized a rocking agitator to provide mixing. The membrane was blocked for 2 h at room temperature in 5% w/v milk (Apex BioResearch Products, Research Triangle Park, NC) in TBST buffer (50 mM Tris, pH 8.0, 150 mM NaCl, 0.1% w/v Tween-20) followed by incubation with MamT primary antibodies (1:1000 dilution) in TBST containing 5% w/v milk at room temperature for 1.5 h. The membrane was washed in TBST (3×15 min) before incubating with Goat Anti-Rabbit IgG-HRP (Bio-Rad Laboratories,1:5000) at room temperature for 1 h. The membrane was washed again TBST (3×15 min) before visualization with a Western

Lightning Plus ECL kit (PerkinElmer; Waltham, MA) using a Bio-Rad Mini Trans-Blot Cell and Quantity One software.

Heterologous expression and purification of MamT.strepII. $2 \times$ YT (6×1 L) containing Cb (50 µg/mL) and Cm (35 µg/mL) in a 2.8 L Fernbach baffled shake flask was inoculated with 10 mL of an overnight 50 mL LB culture of freshly transformed *E. coli* C43(DE3) containing the appropriate overexpression plasmid and the cytochrome *c* maturation plasmid, pEC86 [*4*]. The cultures were grown at 37°C and 200 rpm to $OD_{600} \sim 0.7$, at which point cultures were induced to express protein with IPTG (500 µM) and shaken for 6 h at 24°C and 200 rpm with the heme precursor 5-aminolevulinic acid (55 mg/mL). Cell pellets were harvested by centrifugation at $5,524 \times g$ for 7 min at 4°C and immediately lysed for protein purification.

Harvested cell pellets were thoroughly resuspended (5 mL/g wet cell paste) by gentle pipetting in MamT Periplasmic Lysis Buffer (20% w/v sucrose, 0.5 mM EDTA, 100 mM Tris, pH 8.0) supplemented with a Complete EDTA-free protease inhibitor cocktail (1 tablet/50 mL buffer, Roche). A combined lysozyme/osmotic shock strategy was employed to prepare the periplasmic fraction by addition of lysozyme (0.5 mg/mL) and incubation with gentle stirring at 4°C for 1.5 h followed by the addition of an equal volume of cold ddH$_2$O. The soluble periplasmic fraction was separated from the remaining cellular debris by centrifugation at $10,414 \times g$ for 15 min at 4°C. The soluble periplasmic fraction with added avidin (1 mg) was loaded onto a Strep-Tactin Superflow column (IBA GmbH, 6 mL) equilibrated with Strep Resin Wash Buffer (50 mM Tris pH 8.0, 150 mM NaCl, 1 mM PMSF). The resin was washed with 20 CV of Strep Resin Wash Buffer and eluted with 15 CV Strep Resin Elution Buffer (50 mM Tris pH 8.0, 150 mM NaCl, 2.5 mM d-desthiobiotin). The eluate was concentrated to <10 mL in an Amicon Ultrafiltration Stirred Cell (Millipore) fit with a 5 kD MWCO YM regenerated cellulose membrane (Millipore) and then further concentrated to <2 mL in a 3 kD MWCO Amicon Ultra-15 Centrifugal Filter Unit (Millipore) by centrifugation ($5,000 \times g$) at 4°C.

Heterologous expression and purification of MamT from His$_6$.MBP.MamT. $2 \times$ YT (4×1 L) containing Km (50 µg/mL) and Cm (35 µg/mL) in a 2.8 L Fernbach baffled shake flask was inoculated with 10 mL of an overnight 50 mL LB culture of freshly transformed *E. coli* C43(DE3) containing the appropriate overexpression plasmid and the cytochrome *c* maturation plasmid, pEC86 [*4*]. The cultures were grown at 30°C and 200 rpm to $OD_{600} = 0.6$ to 0.7, at which point cultures were induced to express protein with IPTG (250 µM) and shaken overnight at 30°C and 200 rpm. Cell pellets were harvested by centrifugation at $5,524 \times g$ for 7 min at 4°C and immediately lysed for protein purification.

The fusion was purified as described for the His$_6$.MBP.MamP until the TEV cleavage step, using 100 mM NaCl in buffers as opposed to 300 mM. As the cleaved MamT concentrates poorly due to sticking to dialysis membranes and spin filters, steps were taken to eliminate these steps. First, His$_6$.MBP.MamT was concentrated to < 4 mL and then was buffer-exchanged by G25 column (GE Healthcare; 50 mL in 50 mM potassium phosphate pH 8.0, 50 mM NaCl, 10 mM imidazole, 10% glycerol) prior to TEV cleavage. To the G25 eluate, His-tagged TEV protease (~ 1 mg TEV per 20-30 mg of His$_6$.MBP.MamT fusion) and the resulting mixture was loaded onto a DEAE-Sepharose column. The column (~ 20 mL) was run in 4 CV Buffer A and then in a gradient into Buffer B over 5 CV and then in 1 CV in Buffer B (Buffer A, 50 mM potassium phosphate pH 8.0, 50 mM NaCl, 10 mM imidazole, 10% glycerol; Buffer B, 50 mM potassium phosphate pH

8.0, 800 mM NaCl, 10% glycerol). Fractions with high R_z were used as needed or concentrated in filters with very small surface area, losing up to 80% of the protein but leaving enough for analysis

Silver staining of SDS-PAGE gels. Samples were prepared for loading onto a gel by incubation for 15 min at room temperature with a Laemmli sample buffer with β-mercaptoethanol omitted (4× stock: 0.25 M Tris-HCl, 2% SDS, 40% glycerol, 0.04% bromophenol blue). The sample was analyzed by Tricine SDS-PAGE at room temperature following literature protocol [*5*] on a 15 w/v% acrylamide gel. The gel was stained using a SilverQuest Silver Staining Kit (Invitrogen; Carlsbad, CA).

Supplementary results

Expression, isolation, and heme content of MamT from *M. magneticum* AMB-1. Based on the essential role of the heme redox sites of these two cytochromes *in vivo*, we also attempted to confirm the *in vitro* biochemical characterization of MamT, which is both predicted to be anchored to the magnetosome via a transmembrane segment [*6*, *7*]. Towards this goal, we constructed two plasmids for the heterologous expression of the MamT protein from AMB-1 in *Escherichia coli* (*E. coli*) based on our successful MamP expression plasmids. These two plasmids contain the native *mamT* gene encoding the predicted mature sequence of MamT (residues 29 - 176) as well as an N-terminal OmpA tag [*8*] to direct the protein to the periplasm of *E. coli*, which provides an oxidizing compartment needed for the maturation of *c*-type cytochromes [*9*]. The first construct also consists of a C-terminal strepII tag, while the second construct includes a solubilization tag consisting of a fused protein (MBP, maltose-binding protein) flanked by an N-terminal His$_6$-affinity tag and C-terminal Tobacco Etch Virus (TEV) protease cleavage site (*Appendix 1*). Overall, we found that the solubility of MamT was problematic in both variants, though the small amounts we were able to purify confirms that MamT is a heme-loaded c-type cytochrome by UV-VIS and ESI-MS.

MamT.strepII is >90% clean by SDS-PAGE gel electrophoresis, but so little protein was obtained that a silver stain was necessary to visualize the total protein content. The purification gel of MamT from the MBP fusion show partially pure MamT. The UV-VIS shows a characteristic heme absorption Soret peak at 407 nm with an R_z of 5.6. The pure MamT Soret peak should have an R_z greater than or equal to 7.2 or that of MamP's, showing that MamT has not been fully isolated (*Figure A2.1*). The ESI-MS spectrum confirms this. The peak in the ESI mass spectrum for truncated MamT isolated from His$_6$.MBP.MamT is centered at 17,441 Da, as expected for the diheme-loaded protein (calculated: 17,443 Da). The other peak in the spectrum is a contaminant centered at 26,249 kDa and is likely a contaminant from the periplasm of *E. coli*. Despite the problems purifying MamT, *in vitro* analysis does suggest that MamT is a diheme-loaded c-type cytochrome that can act as an electron transfer protein *in vivo*.

Immunostaining for MamT. Antibodies to MamT were raised by ProSci, Inc. (Poway, CA) in rabbits using a synthetic peptide from MamT (CHDIVVKVPVDKKGGMRWQL) conjugated to a carrier protein. Testing of these antibodies indicated that MamT could be detected to < 20 ng/lane using a 1:1000 dilution. However, immunostaining of AMB-1 cell pellets did not detect very high levels of the protein (*Figure A2.2*). It is possible that MamT is not very highly expressed,

that is it highly associated with the magnetite and thus difficult to solubilize to run on the gel, or simply that the protocol has not been optimized well for MamT detection.
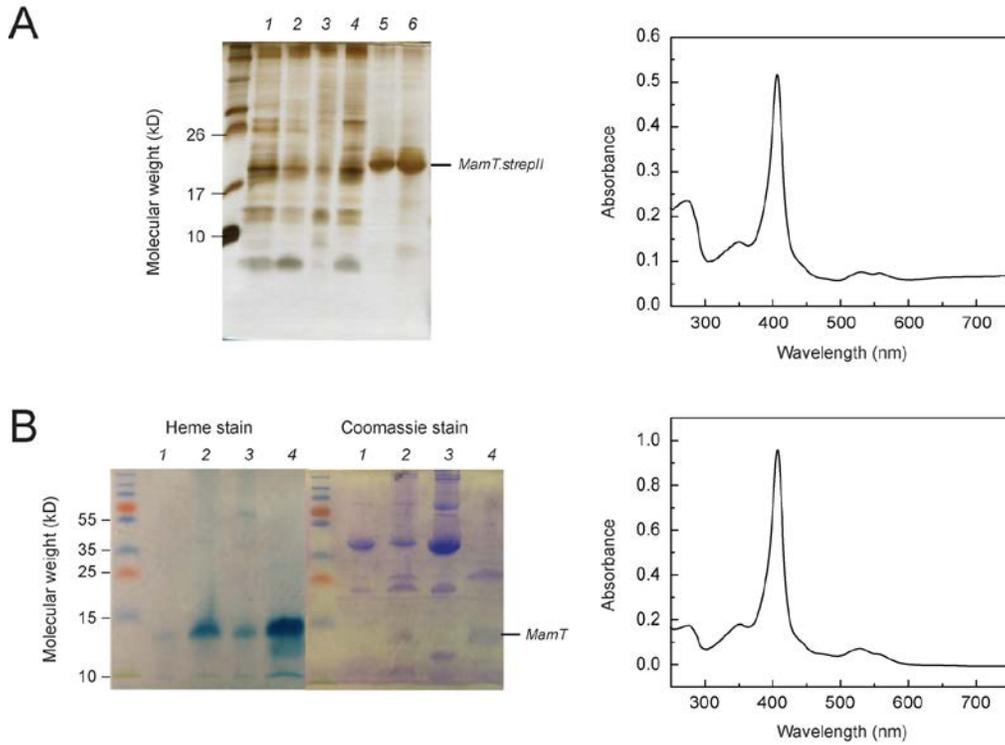

Figure A2.1. Heterologous expression and purification of two MamT constructs. (A) Purification of MamT.strepII.Silver-stained SDS-PAGE gel: pre-induction (lane 1), post-induction (lane 2), periplasm (lane 3), spheroblast (lane 4), strep resin eluate 2x dilution (lane 5), strep resin eluate (lane 6). UV-VIS spectrum of MamT.strepII (B) Purification of MamT from His_6.MBP.MamT. Heme-stained and Coomassie-stained SDS-PAGE gel: post-TEV cleavage (lane 1), DEAE eluate MamT peak (lane 2), DEAE eluate MBP peak (lane 3), DEAE eluate MamT peak after a second NiNTA clean-up (lane 4). UV-VIS spectrum of MamT.
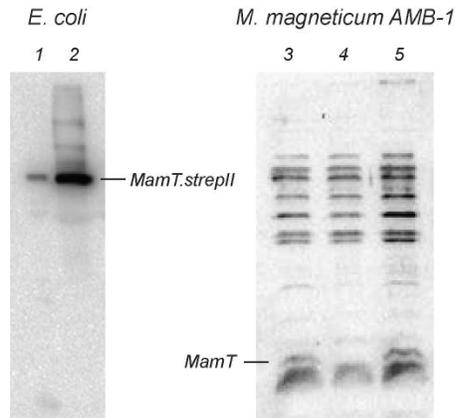
Figure A2.2. *Immunostaining of AMB-1 cell pellets with αMamT. (A) Characterization of the αMamT serum with His₆.MBPtev.MamP. Periplasmic preparation (lane 1), Ni-NTA eluate (lane 2). Based on the concentrations of these samples estimated using the absorption of the Soret peak, the detection limit is < 20 ng per lane for the MamT fusion. (B) Western blot comparing expression of MamP in wild type, ΔmamT, and ΔmamP. Wild-type undiluted (lane 3), wild type (lane 4), ΔmamT (lane 5), ΔmamP (lane 6).*

References

1. W. A. Kibbe (2007) OligoCalc: an online oligonucleotide properties calculator. *Nucleic Acids Res.* 35(Web Server issue):W43-46.
2. D. G. Gibson, L. Young, R. Y. Chuang, J. C. Venter, C. A. Hutchison, and H. O. Smith (2009) Enzymatic assembly of DNA molecules up to several hundred kilobases. *Nat. Methods* 6(5):343-345.
3. A. Krogh, B. Larsson, G. von Heijne, and E. L. Sonnhammer (2001) Predicting transmembrane protein topology with a hidden Markov model: application to complete genomes. *J. Mol. Biol.* 305(3):567-580.
4. E. Arslan, H. Schulz, R. Zufferey, P. Kunzler, and L. Thony-Meyer (1998) Overproduction of the *Bradyrhizobium japonicum* c-type cytochrome subunits of the cbb3 oxidase in *Escherichia coli. Biochem. Biophys. Res. Commun.* 251(3):744-747.
5. H. Schagger (2006) Tricine-SDS-PAGE. *Nat. Protoc.* 1(1):16-22.
6. M. I. Siponen, G. Adryanczyk, N. Ginet, P. Arnoux, and D. Pignol (2012) Magnetochrome: a c-type cytochrome domain specific to magnetotatic bacteria. *Biochem. Soc. Trans.* 40(6):1319-1323.
7. A. Taoka, Y. Eguchi, S. Mise, Z. Oestreicher, F. Uno, and Y. Fukumori (2014) A magnetosome-associated cytochrome MamP is critical for magnetite crystal growth during the exponential growth phase. *FEMS Microbiol. Lett.*
8. M. P. Pritchard, R. Ossetian, D. N. Li, C. J. Henderson, B. Burchell, C. R. Wolf, and T. Friedberg (1997) A general strategy for the expression of recombinant human cytochrome P450s in *Escherichia coli* using bacterial signal peptides: expression of CYP3A4, CYP2A6, and CYP2E1. *Arch. Biochem. Biophys.* 345(2):342-354.

9.   C. Sanders, andH. Lill (2000) Expression of prokaryotic and eukaryotic cytochromes c in *Escherichia coli. Biochim. Biophys. Acta* 1459(1):131-138.